Journal of Quantitative Spectroscopy & Radiative Transfer 277 (2022) 107949

Contents lists available at ScienceDirect

Journal of Quantitative Spectroscopy & Radiative Transfer

journal homepage: www.elsevier.com/locate/jqsrt

The HITRAN2020 molecular spectroscopic database

I.E. Gordon[a,*], L.S. Rothman[a], R.J. Hargreaves[a], R. Hashemi[a], E.V. Karlovets[a], F.M. Skinner[a], E.K. Conway[a], C. Hill[b], R.V. Kochanov[a,c,d], Y. Tan[a,e], P. Wcisło[f], A.A. Finenko[a,g], K. Nelson[a], P.F. Bernath[h], M. Birk[i], V. Boudon[j], A. Campargue[k], K.V. Chance[a], A. Coustenis[l], B.J. Drouin[m], J.–M. Flaud[s], R.R. Gamache[o], J.T. Hodges[p], D. Jacquemart[q], E.J. Mlawer[r], A.V. Nikitin[c], V.I. Perevalov[c], M. Rotger[t], J. Tennyson[u], G.C. Toon[m], H. Tran[L], V.G. Tyuterev[t,d,c], E.M. Adkins[p], A. Baker[n], A. Barbe[t], E. Canè[w], A.G. Császár[y,z], A. Dudaryonok[c], O. Egorov[c], A.J. Fleisher[p], H. Fleurbaey[k], A. Foltynowicz[A], T. Furtenbacher[y], J.J. Harrison[B,C,D], J.–M. Hartmann[v], V.–M. Horneman[E], X. Huang[F], T. Karman[a], J. Karns[a,W,X], S. Kassi[k], I. Kleiner[M], V. Kofman[R], F. Kwabia–Tchana[M], N.N. Lavrentieva[c], T.J. Lee[G], D.A. Long[p], A.A. Lukashevskaya[c], O.M. Lyulin[c], V.Yu. Makhnev[N], W. Matt[a,X], S.T. Massie[H], M. Melosso[x], S.N. Mikhailenko[c], D. Mondelain[k], H.S.P. Müller[I], O.V. Naumenko[c], A. Perrin[L], O.L. Polyansky[u,N], E. Raddaoui[q], P.L. Raston[J,K], Z.D. Reed[p], M. Rey[t], C. Richard[j], R. Tóbiás[y], I. Sadiek[A,O], D.W. Schwenke[G], E. Starikova[c], K. Sung[m], F. Tamassia[w], S.A. Tashkun[c], J. Vander Auwera[P], I.A. Vasilenko[c], A.A. Vigasin[Q], G.L. Villanueva[R], B. Vispoel[T,S,o], G. Wagner[i], A. Yachmenev[U,V], S.N. Yurchenko[u]

[a] Center for Astrophysics |Harvard & Smithsonian, Atomic and Molecular Physics Division, Cambridge, MA 02138, USA
[b] Nuclear Data Section, International Atomic Energy Agency, Vienna International Centre, PO Box 100, Vienna A-1400, Austria
[c] V.E. Zuev Institute of Atmospheric Optics, Laboratory of Theoretical Spectroscopy, Russian Academy of Sciences, Tomsk 634055, Russia
[d] QUAMER laboratory, Tomsk State University, Tomsk 634050, Russia
[e] Hefei National Laboratory for Physical Science at Microscale, University of Science and Technology of China, Hefei, China
[f] Institute of Physics, Faculty of Physics, Astronomy and Informatics, Nicolaus Copernicus University in Torun, Grudziadzka 5, Torun 87-100, Poland
[g] Department of Chemistry, Lomonosov Moscow State University, Moscow 119991, Russia
[h] Department of Chemistry, Old Dominion University, Norfolk VA, USA
[i] German Aerospace Center (DLR), Remote Sensing Technology Institute, Wessling, Germany
[j] Laboratoire Interdisciplinaire Carnot de Bourgogne, Université de Bourgogne Franche-Comté, UMR 6303 CNRS, Dijon Cedex, France
[k] University of Grenoble Alpes, CNRS, LIPhy, Grenoble F-38000, France
[l] Laboratoire d'Etudes Spatiales et d'Instrumentation en Astrophysique, Paris Observatory, CNRS, PSL University, Sorbonne University, Paris, France
[m] Jet Propulsion Laboratory, California Institute of Technology, Pasadena, CA, USA
[n] Division of Astronomy, California Institute of Technology, Pasadena, CA, USA
[o] Department of Environmental, Earth & Atmospheric Sciences, University of Massachusetts, Lowell, MA, USA
[p] Chemical Sciences Division, National Institute of Standards and Technology, Gaithersburg, MD, USA
[q] Sorbonne Université, CNRS, De la MOlécule aux NAno-objets : Réactivité, Interactions et Spectroscopies, MONARIS, Paris 75005, France
[r] Atmospheric and Environmental Research, Lexington MA, USA
[s] Institut des Sciences Moléculaires d'Orsay, CNRS, Université Paris-Sud, Université Paris-Saclay, Orsay F-91405, France
[t] Groupe de Spectrométrie Moléculaire et Atmosphérique, UMR CNRS 7331, BP 1039, Reims Cedex 2 F-51687, France
[u] Department of Physics and Astronomy, University College London, London WC1E 6BT, UK
[v] Laboratoire de Météorologie Dynamique/IPSL, CNRS, École polytechnique, Sorbonne Université, École normale supérieure, PSL Research University, Palaiseau F-91120, France
[w] Dipartimento di Chimica Industriale "Toso Montanari", Università di Bologna, Viale Risorgimento 4, Bologna 40136, Italy
[x] Dipartimento di Chimica "Giacomo Ciamician", Università di Bologna, Via F. Selmi 2, Bologna 40126, Italy
[y] MTA-ELTE Complex Chemical Systems Research Group, Budapest, Hungary
[z] Eötvös Loránd University, Institute of Chemistry, Budapest, Hungary
[A] Department of Physics, Umeå University, Umeå 901 87, Sweden
[B] Department of Physics and Astronomy, University of Leicester, Leicester, UK
[C] University of Leicester, National Centre for Earth Observation, Leicester, UK
[D] University of Leicester, Leicester Institute for Space and Earth Observation, Leicester, UK
[E] Department of Physics, University of Oulu, FIN-90014, Finland
[F] SETI Institute, Mountain View, CA 94043, USA

* Corresponding author.
E-mail address: igordon@cfa.harvard.edu (I.E. Gordon).

https://doi.org/10.1016/j.jqsrt.2021.107949

[G] Planetary Systems Branch, Space Science and Astrobiology Division, NASA Ames Research Center, Moffett Field, CA 94035, USA
[H] University of Colorado, Laboratory for Atmospheric and Space Physics, Boulder CO, USA
[I] I. Physikalisches Institut, Universität zu Köln, Köln 50937, Germany
[J] Department of Chemistry and Biochemistry, James Madison University, Harrisonburg, VA 22807, USA
[K] Department of Chemistry, University of Adelaide, South Australia 5005, Australia
[L] Laboratoire de Météorologie Dynamique/IPSL, CNRS, Sorbonne Université, École normale supérieure, PSL Research University, École polytechnique, Paris F-75005, France
[M] Université de Paris and Univ Paris Est Creteil, CNRS, LISA, Paris F-75013, France
[N] Institute of Applied Physics of Russian Academy of Sciences, Nizhny Novgorod, Russia
[O] Leibniz Institute for Plasma Science and Technology (INP), Greifswald, Germany
[P] Université Libre de Bruxelles, Spectroscopy, Quantum Chemistry and Atmospheric Remote Sensing (SQUARES), C.P. 160/09, Brussels B-1050, Belgium
[Q] Obukhov Institute of Atmospheric Physics, Russian Academy of Sciences, Pyzhevsky per. 3, Moscow 119017, Russia
[R] NASA Goddard Space Flight Center, Greenbelt, MD 20771, USA
[S] Research Unit Lasers and Spectroscopies (LLS), Institute of Life, Earth and Environment (ILEE), University of Namur (UNamur), Namur B-5000, Belgique
[T] Royal Belgian Institute for Space Aeronomy (BIRA-IASB), Brussels 1180, Belgium
[U] Center for Free-Electron Laser Science, Deutsches Elektronen-Synchrotron DESY, Notkestraße 85, Hamburg 22607, Germany
[V] Hamburg Center for Ultrafast Imaging, Universität Hamburg, Luruper Chaussee 149, Hamburg 22761, Germany
[W] Golisano College of Computing and Information Sciences, Rochester Institute of Technology, Rochester, NY 14623, USA
[X] Computer Science Department, State University of New York at Oswego, Oswego, NY 13126, USA

ARTICLE INFO

Article history:
Received 12 March 2021
Revised 15 September 2021
Accepted 17 September 2021
Available online 25 September 2021

Keywords:
HITRAN
Spectroscopic database
Molecular spectroscopy
Spectroscopic line parameters
Absorption cross-sections
Collision-induced absorption
Aerosols
Molecular opacities

ABSTRACT

The HITRAN database is a compilation of molecular spectroscopic parameters. It was established in the early 1970s and is used by various computer codes to predict and simulate the transmission and emission of light in gaseous media (with an emphasis on terrestrial and planetary atmospheres). The HITRAN compilation is composed of five major components: the line-by-line spectroscopic parameters required for high-resolution radiative-transfer codes, experimental infrared absorption cross-sections (for molecules where it is not yet feasible for representation in a line-by-line form), collision-induced absorption data, aerosol indices of refraction, and general tables (including partition sums) that apply globally to the data. This paper describes the contents of the 2020 quadrennial edition of HITRAN. The HITRAN2020 edition takes advantage of recent experimental and theoretical data that were meticulously validated, in particular, against laboratory and atmospheric spectra. The new edition replaces the previous HITRAN edition of 2016 (including its updates during the intervening years).

All five components of HITRAN have undergone major updates. In particular, the extent of the updates in the HITRAN2020 edition range from updating a few lines of specific molecules to complete replacements of the lists, and also the introduction of additional isotopologues and new (to HITRAN) molecules: SO, CH_3F, GeH_4, CS_2, CH_3I and NF_3. Many new vibrational bands were added, extending the spectral coverage and completeness of the line lists. Also, the accuracy of the parameters for major atmospheric absorbers has been increased substantially, often featuring sub-percent uncertainties. Broadening parameters associated with the ambient pressure of water vapor were introduced to HITRAN for the first time and are now available for several molecules.

The HITRAN2020 edition continues to take advantage of the relational structure and efficient interface available at www.hitran.org and the HITRAN Application Programming Interface (HAPI). The functionality of both tools has been extended for the new edition.

1. Introduction

Over the last fifty years, the HITRAN molecular spectroscopic database has provided scientists and engineers with the necessary data to predict and simulate the transmission and emission of electromagnetic radiation in gaseous media. The history of the database was recently reviewed by Rothman [1]. The database is being updated regularly, and official "editions" have been released and described in corresponding papers [2–16]. In the last three decades, the database has been released on a quadrennial basis. This paper describes the new and/or updated data in the HITRAN2020 edition of the database.

There are countless applications of HITRAN in science and industry including, but not limited to, atmospheric, astrophysical, and medical sciences, as well as pollution monitoring. With that being said, the primary goal of HITRAN is to assist interpretation and modeling of spectra in the terrestrial atmosphere. Multiple ongoing (e.g., OCO-2 [17], OCO-3 [18], TES [19], GOSAT [20], ACE [21], TROPOMI [22], GEMS [23]) and upcoming (e.g., FORUM [24], TEMPO [25], MethaneSat [26]) remote-sensing missions rely on the quality of spectroscopic data in the HITRAN database. It is fair to generalize that remote-sensing missions equipped with spectrometers of *any* resolution use HITRAN data in the analyses of their retrievals. However, this point is often overlooked since HITRAN data are often being integrated into radiative-transfer codes that are in turn used by atmospheric scientists. Whereas articles describing the HITRAN database are among the most cited articles in geosciences (recent editions have typically been cited over 2000 times each), it is very often not cited when the radiative-transfer codes are being used, despite their heavy reliance on HITRAN. There are many radiative-transfer codes that have HITRAN data directly integrated or are more flexible and allow the user to input HITRAN-formatted files themselves, including LBLRTM [27], MODTRAN [28], GENLN [29], RFM [30], ARTS [31], GARLIC [32], kCARTA [33] and VLIDORT [34], to name a few. These codes are used not only for monitoring the concentrations and atmospheric profiles of gases but also in climate models.

The second most prominent application of HITRAN is the interpretation and modeling of spectra of planetary atmospheres, including those of exoplanets. Many HITRAN-powered radiative-transfer codes listed above are used for both terrestrial and planetary atmospheres. There are also some planetary-designated codes

(including NEMESIS [35], petitRADTRANS [36], PSG [37], Exotransmit [38] and HELIOS-K [39]) that employ HITRAN data. One should keep in mind that not all of these (or terrestrial) codes employ the most recent versions of HITRAN. Therefore, one needs to be aware of the particular edition of HITRAN that is implemented in their chosen radiative-transfer code.

Naturally, the success of previous/current (for instance, Venus Express [40,41], ExoMars [42,43], Cassini [44], and Hershel [45]) as well as future (including JWST [46] and ARIEL [47]) space missions depend on the quality and extent of reference molecular parameters, including spectral parameters in the HITRAN database. In turn, ground-based telescopes need HITRAN not only to interpret their observations of astrophysical objects, but also to subtract the effect of the terrestrial atmosphere [48]. Keeping the aforementioned applications in mind, HITRAN also plays an integral role in undergraduate and graduate courses on molecular spectroscopy and/or radiative transfer.

The greatly improved observational and retrieval capabilities of terrestrial and planetary remote-sensing missions have thus placed critical new requirements on HITRAN. Among the needs are: improved accuracy of all spectroscopic parameters, global consistency of line intensities, improved line-shape parameters (and the means by which they are represented), the addition of missing molecular bands and trace gas species, representation of phenomena that are impacting the retrievals including collision-induced absorption (CIA) bands, advanced line-shape formalisms, line-mixing, and pressure broadening by gases different than “air” and “self”.

The HITRAN project is rising to the challenge through an extensive scientific collaboration among spectroscopists, atmospheric scientists, and data scientists. State-of-the-art theoretical and experimental values have been rigorously evaluated, and semi-empirical procedures have been developed for where the data were not available. The data have gone through validation against alternative sources, laboratory and field data when available. Fig. 1 in the HITRAN2012 paper [15] provides an overview of the typical validation process. In this current paper, we describe the updates and extension of the database and associated software tools towards meeting the goals of remote sensing and planetary communities, and in parallel, assisting many other applications. For instance, atmospheric scientists would be interested in improved quality of spectroscopic parameters of ozone, which, as described in Section 2.3 will yield better consistency between different spectral regions. They will also appreciate the addition of parameters associated with the broadening of spectral lines by ambient pressure of water vapor [49] described in multiple subsections. This will also be welcomed by the exoplanetary community that models spectra of exoplanets with “steamy” atmospheres. In general, the planetary community and combustion researchers will be interested in learning about the extension of the number of gases that now have broadening parameters due to ambient pressure of H_2, He, CO_2, and H_2O. Medical experts who analyze human breath for markers of different diseases will appreciate improved relative intensities of the ^{14}NO and ^{15}NO transitions described in Section 2.8 and the addition of the CS_2 molecule described in Section 2.53. Cometary scientists will also appreciate the latter. These are just a few relatively random examples of the gargantuan extent of the updates in this edition and the rationale for doing these updates.

Before the release of the HITRAN2016 edition [16], we had restructured the database into a relational database format in order to accommodate the need for additional parameters and flexibility of their representation [50,51]. Many of these parameters can already be retrieved from the dynamic and user-friendly web interface HITRAN*online* (at www.hitran.org), which as of early September, 2021 has over 20 700 registered users in the initial six years of it being made available. This new versatility allows one to request either the familiar HITRAN-format ASCII files (for those users that will not require advanced parameters), but also user-defined formats that can accommodate new features and parameters. The HITRAN Application Programming Interface (HAPI) [52] that was released with HITRAN2016 has also been updated for increased capabilities and speed of calculations.

The HITRAN compilation in its current state comprises five components that encompass different parametrizations of various molecular phenomena required as spectroscopic input into the radiative-transfer models. The updates to these five portions of HITRAN, as well as the underlying system of data structure with accompanying internet user interface and an application programming interface (API), will be discussed in the following sections: (1) Section 2 is dedicated to the line-by-line section, the original and most popular component, which provides spectroscopic parameters for high-resolution molecular absorption and radiance calculations (from the microwave through to the ultraviolet region of the spectrum). (2) A second component described in Section 3 relates to experimental (mostly infrared) absorption cross-sections. These cross-sections are generally representing absorption by molecules that have very dense spectra or many low-lying vibrational modes. (3) Collision-induced absorption datasets for multiple collisional pairs are described in Section 4. (4) Tables of aerosol refractive indices are described in Section 5. (5) Global data that apply in a general manner to the archive is another important part of the database and are described in Section 6. This includes its particular component, Total Internal Partition Sums (TIPS), as well as updates to the HITRAN website, underlying structure and HAPI, which are also described in Section 6.

The high temperature, HITEMP, database described by Rothman et al. [53] was established to provide substantially more transitions (compared to HITRAN), which become necessary for modeling radiative transfer of high-temperature environments [54]. These additional transitions are not required for typical atmospheric applications and are therefore not included in HITRAN. Recently, the number of molecules available through HITEMP (see www.hitran.org/hitemp/) has been extended to include nitrogen oxides [55] and methane [56]. An in-depth description of HITEMP is beyond the scope of this work; nevertheless, it is often the case that updates of HITRAN and HITEMP are performed at the same time using the same data sources (such as for NO [55]). Therefore, a brief description of corresponding HITEMP updates are included in Section 2 for N_2O, CH_4, NO, NO_2, and OH.

In order to better understand the discussion in this paper it is important to understand the HITRAN definitions of the parameters and formalisms, which can be found in the documentation section of the HITRAN website https://hitran.org/docs/definitions-and-units/. For a complete description of quantum number identifications of energy levels or states provided for each molecule in the line-by-line section of the HITRAN database, users are referred to the Supplementary Material of this work. The global and local quanta are described in Tables S1 and S2, respectively, and these supplementary tables supersede those previously described in HITRAN2004 (i.e., Tables 3 and 4 of Ref. [13]). New users of the database should also be aware that all of the HITRAN editions (including this one) do not strictly adhere to the Système International (SI) for both historical and application-specific reasons. Thus cm^{-1} (reciprocal centimeter, the unit of the quantity wavenumber) is seen throughout, as is atm (atmosphere) for pressure (in SI units of Pascals, 101,325 Pa = 1 atm). Also, the symbol ν is used throughout for line position in cm^{-1}, thereby dropping the tilde ($\tilde{\nu}$) that is the official designation of wavenumber. The HITRAN unit for intensity is traditionally expressed as cm^{-1}/(molecule cm^2) rather than simplifying to the equivalent cm $molecule^{-1}$. However, both notations are used throughout this paper.

A number of abbreviations have been used throughout this paper when describing data, instruments, and methods that have been used to update the HITRAN database. These are described in the text when used, but a list of these abbreviations is also provided in Appendix A.

2. Line-by-line modifications

An overview of changes and additions to the line-by-line section for each isotopologue in the database with respect to the HITRAN2016 edition is provided in Table 1. Isotopologues are given in order of their descending abundance for each individual molecule. The molecular abundance values in HITRAN are calculated based on the terrestrial atomic abundances selected from Ref. [57]. It is important to remember that the intensities in the HITRAN database are scaled by these abundances. Note that although for many molecules the amount of lines and spectral ranges have not changed, many parameters were updated or added. In the subsequent subsections dedicated to individual molecules, detailed accounts of those changes are provided.

The definitions of the uncertainty indices used in HITRAN for spectral parameters in the line-by-line representation are defined in Table 2. Uncertainty and reference indices are now given for all parameters in HITRAN except for the Einstein-A coefficients (which usually share the same source and uncertainty as the intensities), lower-state energies and quantum numbers. It should be remarked that the code 0 in Table 2 might lend itself to two different meanings in the case of line position or air pressure-induced shift. It means that either the uncertainty in the shift reported is greater than 1 cm^{-1} or was not reported. The word “default” or “constant” (code 1 in Table 2) means a constant value, and the word “average” or “estimate” (code 2 in Table 2) means an average or empirical value. This table will be frequently referred to across different subsections of Section 2.

2.1. H_2O: water vapor (molecule 1)

Considering that water vapor is the major absorber of light in the terrestrial atmosphere, it is difficult to overstate the importance of the quality and extent of spectroscopic parameters for this molecule in HITRAN. The details surrounding the previous (HITRAN2016) water-vapor compilation can be found in the corresponding paper [16]. To briefly summarize, the wavelength range has now been extended to approximately 238 nm (42,000 cm^{-1}), and the study used *ab initio* calculated line lists as its initial starting point. Whenever possible, line positions were replaced with accurate experimental data or wavenumbers generated from a MARVEL-based [58,59] set of empirical energy levels [60]. The bulk of the intensities were of *ab initio* origin, but in many places experimental data were used (taken most notably from Refs. [61–72]). This approach substantially reduces the number of missing lines (from an atmospheric perspective) in all isotopologues and, in general, it enhances the quality of the line parameters. Similar to the two earlier editions (HITRAN2008 [14] and HITRAN2012 [15]), HITRAN2016 [16] continued to utilize the “Diet” algorithm [73] for broadening parameters, supplemented with the newest experimental data. Moreover, parameters determined for the advanced Hartmann-Tran (HT) profile [74,75] were incorporated into the database, where available from Ref. [66]. Remote-sensing experiments in the IR region have identified that the HITRAN2016 water-vapor compilation results in smaller residuals when compared with previous editions (see Ref. [76] for instance). Nevertheless, a number of issues have been found. One of the sources of discrepancies predominantly manifests itself in the NIR to visible parts of the spectrum and is associated with erroneous broadening and shifting parameters of experimental origin. Unfortunately, one of the “Diet” algorithm features that was designed to eliminate outliers was inadvertently turned off in the HITRAN2016 edition. This has resulted in some of the issues reported in the visible region by Baker et al. [77]. Another problem concerned the incorrect quantum assignment of certain transitions, which, while not having adverse affects on atmospheric retrievals, were not accurate from a spectroscopic perspective. In the new edition, these issues have been eliminated. Moreover, the water database was extended into the UV region, and the general quality of the parameters was improved overall. The details of the HITRAN2020 update are given below.

2.1.1. $H_2^{16}O$

The water-vapor line lists for HITRAN2020 have received a significant update compared to HITRAN2016 [16]. The entire process of developing the HITRAN2020 line list for the principal isotopologue is presented as a flowchart in Fig. 1. Within the text below, we will describe the steps in significantly more detail.

In Ref. [78], an *ab initio* dipole moment surface (DMS), underpinned by high-level electronic-structure calculations, was developed and designed to create highly-accurate spectra extending all the way to the dissociation limit in the near ultraviolet. The motivation for this work came in part from the forthcoming launch of NASA’s TEMPO (Tropospheric Emissions Monitoring of Pollution) satellite [25], which carries a short-wavelength instrument (operating between 290–740 nm) that aims to accurately monitor the chemical composition in the air across the North American continent. TEMPO will retrieve water-vapor column densities in the 440–450 nm spectral interval, a region that is often used for water retrievals [79–81]; however, the interference of water-vapor absorption features in the near ultraviolet needs to be accounted for when targeting trace gases such as formaldehyde.

Atmospheric observations from Lampel et al. [82] indicate that the “POKAZATEL” [83] line list underestimates the magnitude of absorption features at near-ultraviolet wavelengths (363 nm) by a factor of 2.6, a potential source of error for TEMPO retrievals. A noteworthy point is that the HITRAN2016 line list extends only to 400 nm and the source of transition intensities that underpins a large portion of the visible transitions are variational in nature and these use a similar DMS [84] to that was used in the creation of the POKAZATEL line list, hence the requirement to update the transition frequency limit and *ab initio* data sources.

Conway et al. [85] calculated $H_2^{16}O$ and $H_2^{18}O$ line lists that extended to the HITRAN2016 frequency limits and compared the new *ab initio* intensities against a large quantity of experimental sources, most of which feature in the HITRAN2016 line list. It became evident that the new *ab initio* spectra from Conway et al. [85] provide more accurate and reliable transition intensities than other available *ab initio* line lists, particularly at short wavelengths. More recently, Conway et al. [86] created a new near-ultraviolet line list that extends to dissociation and this provides the correct amount of absorption at 363 nm, while also adhering to the upper limit absorption thresholds proposed by Lampel et al. [87] through atmospheric observations, and to that of Wilson et al. [88] through experimental measurements. What cannot be replicated by the *ab initio* spectra are the measured spectra of Du et al. [89] and Pei et al. [90]. The magnitude of the water-vapor cross sections reported both by Du et al. and Pei et al. are significantly larger than the *ab initio* predictions; meaning, for example, that they would adversely perturb atmospheric retrievals of ozone.

To create the HITRAN2020 $H_2^{16}O$ line list we started with the *ab initio* spectra from Conway et al. [86]. While semi-empirical potential energy surfaces (PES) capable of predicting energy levels to a hundredth [92] and even a thousandth of a wavenumber are gradually appearing [93], they are still far less accurate than their experimental counterparts, which make use of, for ex-

Table 1
Molecules and isotopologues represented in the line-by-line portion of HITRAN.

Molecule	Isotopologue	Abundance[a]	HITRAN2016		HITRAN2020	
			Spectral Range[b]	# of lines	Spectral Range[b]	# of lines
(1) H_2O	$H_2^{16}O$	9.973×10^{-1}	0–25 711	146 878	0–42 000	319 886
	$H_2^{18}O$	2.000×10^{-3}	0–19 918	39 903	0–19 992	42 178
	$H_2^{17}O$	3.719×10^{-4}	0–19 946	27 544	0–19 946	27 544[c]
	$HD^{16}O$	3.107×10^{-4}	0–19 936	56 430	0–19 935	56 430
	$HD^{18}O$	6.230×10^{-7}	0–10 729	10 664	0–10 729	10 664
	$HD^{17}O$	1.159×10^{-7}	0–10 703	6360	0–10 703	6360
	$D_2^{16}O$	2.420×10^{-8}	0–12 797	23 488	0–12 797	23 195[c]
(2) CO_2	$^{12}C^{16}O_2$	9.842×10^{-1}	158–14 076	173 024	158–19 909	174 446
	$^{13}C^{16}O_2$	1.106×10^{-2}	332–13 735	70 577	332–13 735	69 870
	$^{16}O^{12}C^{18}O$	3.947×10^{-3}	1–12 678	127 850	1–12 678	122 140
	$^{16}O^{12}C^{17}O$	7.340×10^{-4}	0–12 727	77 941	0–12 727	73 942
	$^{16}O^{13}C^{18}O$	4.434×10^{-5}	2–9213	43 782	2–9213	41 058
	$^{16}O^{13}C^{17}O$	8.246×10^{-6}	9–8062	25 175	9–8062	23 607
	$^{12}C^{18}O_2$	3.957×10^{-6}	482–8163	10 522	482–8163	10 498
	$^{17}O^{12}C^{18}O$	1.472×10^{-6}	491–8194	15 878	498–8194	14 623
	$^{12}C^{17}O_2$	1.368×10^{-7}	535–6933	6518	535–6933	6493
	$^{13}C^{18}O_2$	4.446×10^{-8}	2245–4751	2916	539–6687	2926
	$^{18}O^{13}C^{17}O$	1.654×10^{-8}	549–4915	4190	549–4915	3980
	$^{13}C^{17}O_2$	1.538×10^{-9}	575–3615	1501	575–3615	1501
(3) O_3	$^{16}O_3$	9.929×10^{-1}	0–6997	289 340	0–6997	304 262
	$^{16}O^{16}O^{18}O$	3.982×10^{-3}	0–2768	44 302	0–3165	57 907
	$^{16}O^{18}O^{16}O$	1.991×10^{-3}	1–2740	18 887	1–2740	18 887
	$^{16}O^{16}O^{17}O$	7.405×10^{-4}	0–2122	65 106	0–2122	65 467
	$^{16}O^{17}O^{16}O$	3.702×10^{-4}	0–2101	31 935	0–2102	31 022
(4) N_2O	$^{14}N_2^{16}O$	9.903×10^{-1}	0–7797	33 074	0–7797	33 265
	$^{14}N^{15}N^{16}O$	3.641×10^{-3}	5–5086	4222	5–5086	4222
	$^{15}N^{14}N^{16}O$	3.641×10^{-3}	4–4704	4592	4–4704	4592
	$^{14}N^{14}N^{18}O$	1.986×10^{-3}	0–4672	116 694	0–10364	116 694
	$^{14}N_2^{17}O$	3.693×10^{-4}	550–4430	1705	550–4430	1705
(5) CO	$^{12}C^{16}O$	9.865×10^{-1}	3–14 478	1344	3–14 478	1344[c]
	$^{13}C^{16}O$	1.108×10^{-2}	3–12 231	1042	3–12 231	1042[c]
	$^{12}C^{18}O$	1.978×10^{-3}	3–12 205	920	3–12 205	920[c]
	$^{12}C^{17}O$	3.679×10^{-4}	3–10 295	800	3–10 295	800[c]
	$^{13}C^{18}O$	2.223×10^{-5}	3–8078	674	3–8078	674[c]
	$^{13}C^{17}O$	4.133×10^{-6}	3–8168	601	3–8168	601[c]
(6) CH_4	$^{12}CH_4$	9.883×10^{-1}	0–11 502	313 943	0–11 502	309 863
	$^{13}CH_4$	1.110×10^{-2}	0–11 319	77 626	0–11 319	77 597
	$^{12}CH_3D$	6.158×10^{-4}	7–6511	54 076	7–6511	54 076
	$^{13}CH_3D$	6.918×10^{-6}	959–1695	4213	959–1695	4213
(7) O_2	$^{16}O_2$	9.953×10^{-1}	0–57 028	15 263	0–57 028	15 505
	$^{16}O^{18}O$	3.991×10^{-3}	1–56 670	2965	1–56 670	2975
	$^{16}O^{17}O$	7.422×10^{-4}	0–14 537	11 313	0–14 538	11 313
(8) NO	$^{14}N^{16}O$	9.940×10^{-1}	0–9273	103 701	0–23 727	251 898
	$^{15}N^{16}O$	3.654×10^{-3}	1609–2061	699	0–15 630	67 370
	$^{14}N^{18}O$	1.993×10^{-3}	1602–2039	679	0–15 503	65 037
(9) SO_2	$^{32}S^{16}O_2$	9.457×10^{-1}	0–4092	72 460	0–4160	549 425
	$^{34}S^{16}O_2$	4.195×10^{-2}	0–2500	22 661	0–3465	141 665
	$^{33}S^{16}O_2$	7.464×10^{-3}	–	–	0–2625	75 785
	$^{16}O^{32}S^{18}O$	3.792×10^{-3}	–	–	0–2793	208 183
(10) NO_2	$^{14}N^{16}O_2$	9.916×10^{-1}	0–3075	104 223	0–7978	171 058
	$^{15}N^{16}O_2$	3.646×10^{-3}	–	–	1500–1660	5860
(11) NH_3	$^{14}NH_3$	9.959×10^{-1}	0–10 349	65 828	0–10 349	76 605
	$^{15}NH_3$	3.661×10^{-3}	0–5180	1320	0–5180	13 791
(12) HNO_3	$H^{14}N^{16}O_3$	9.891×10^{-1}	0–1770	950 864	0–1770	950 864
	$H^{15}N^{16}O_3$	3.636×10^{-3}	0–923	58 108	0–923	58 108
(13) OH	^{16}OH	9.975×10^{-1}	0–19 268	30 772	0–43 408	55 698
	^{18}OH	2.000×10^{-3}	0–329	295	0–329	295
	^{16}OD	1.554×10^{-4}	0–332	912	0–332	912
(14) HF	$H^{19}F$	9.998×10^{-1}	24–32 351	8090	24–32 351	8090
	$D^{19}F$	1.557×10^{-4}	13–20 829	11 920	13–20 829	11 920
(15) HCl	$H^{35}Cl$	7.576×10^{-1}	8–20 231	8892	8–20 231	8892
	$H^{37}Cl$	2.423×10^{-1}	8–20 218	8908	8–20 218	8908
	$D^{35}Cl$	1.180×10^{-4}	5–15 265	17 762	5–15 265	17 762
	$D^{37}Cl$	3.774×10^{-5}	5–15 246	17 690	5–15 246	17 690
(16) HBr	$H^{79}Br$	5.068×10^{-1}	13–16 033	3039	13–16 033	3039
	$H^{81}Br$	4.931×10^{-1}	13–16 031	3031	13–16 031	3031
	$D^{79}Br$	7.894×10^{-5}	7–8780	1455	7–8780	1455
	$D^{81}Br$	7.680×10^{-5}	7–8777	1455	7–8777	1455
(17) HI	$H^{127}I$	9.998×10^{-1}	10–13 907	3161	10–13 907	3161
	$D^{127}I$	1.557×10^{-4}	5–7625	1590	5–7625	1590
(18) ClO	$^{35}Cl^{16}O$	7.559×10^{-1}	0–1208	5721	0–1208	5721
	$^{37}Cl^{16}O$	2.417×10^{-1}	0–1200	5780	0–1200	5780
(19) OCS	$^{16}O^{12}C^{32}S$	9.374×10^{-1}	0–7822	18 264	0–7822	21 776
	$^{16}O^{12}C^{34}S$	4.158×10^{-2}	0–7796	6846	0–7796	7424

(*continued on next page*)

Table 1 (*continued*)

	$^{16}O^{13}C^{32}S$	1.053×10^{-2}	0–6660	3275	0–6660	3395
	$^{16}O^{12}C^{33}S$	7.399×10^{-3}	0–6631	3005	0–6632	3005
	$^{18}O^{12}C^{32}S$	1.880×10^{-3}	0–4046	1640	0–4046	1640
	$^{16}O^{13}C^{34}S$	4.675×10^{-4}	–	–	1951–2039	221
(20) H_2CO	$H_2{}^{12}C^{16}O$	9.862×10^{-1}	0–3100	40 670	0–3100	40 670[c]
	$H_2{}^{13}C^{16}O$	1.108×10^{-2}	0–117	2309	0–117	2309[c]
	$H_2{}^{12}C^{18}O$	1.978×10^{-3}	0–101	1622	0–101	1622[c]
(21) HOCl	$H^{16}O^{35}Cl$	7.558×10^{-1}	1–3800	8877	1–3800	8877
	$H^{16}O^{37}Cl$	2.417×10^{-1}	1–3800	7399	1–3800	7399
(22) N_2	$^{14}N_2$	9.927×10^{-1}	11–9355	1107	11–9355	1107
	$^{14}N^{15}N$	7.478×10^{-3}	11–2578	161	11–2578	161
(23) HCN	$H^{12}C^{14}N$	9.851×10^{-1}	0–17 586	58 108	0–17 586	131 031
	$H^{13}C^{14}N$	1.107×10^{-2}	2–3405	652	0–8000	22 599
	$H^{12}C^{15}N$	3.622×10^{-3}	2–3420	646	2–3420	646
(24) CH_3Cl	$^{12}CH_3{}^{35}Cl$	7.489×10^{-1}	0–3198	110 462	0–3198	110 462
	$^{12}CH_3{}^{37}Cl$	2.395×10^{-1}	0–3198	109 113	0–3198	109 113
(25) H_2O_2	$H_2{}^{16}O_2$	9.950×10^{-1}	0–1731	126 983	0–1731	126 983
(26) C_2H_2	$^{12}C_2H_2$	9.776×10^{-1}	13–9890	22 866	13–10 737	74 335
	$H^{12}C^{13}CH$	2.197×10^{-2}	613–6589	285	613–9857	2120
	$H^{12}C^{12}CD$	3.046×10^{-4}	1–789	7512	1–789	7512
(27) C_2H_6	$^{12}C_2H_6$	9.770×10^{-1}	225-3001	54 460	225-3071	63 516
	$^{12}CH_3{}^{13}CH_3$	2.195×10^{-2}	285–919	7107	285–919	7107
	$^{12}C_2H_5D$	9.131×10^{-4}	–	–	681–3207	39 271
(28) PH_3	$^{31}PH_3$	9.995×10^{-1}	0–3602	22 190	0–3660	104 759
(29) COF_2	$^{12}C^{16}O^{19}F_2$	9.865×10^{-1}	725–2002	168 793	697–2002	168 793
	$^{12}C^{16}O^{19}F_2$	1.108×10^{-2}	686–815	15 311	687–815	15 311
(30) SF_6	$^{32}S^{19}F_6$	9.502×10^{-1}	580–996	2 889 065	319–965	336 027
(31) H_2S	$H_2{}^{32}S$	9.499×10^{-1}	2–11 330	36 561	3–11 330	36 556[c]
	$H_2{}^{34}S$	4.214×10^{-2}	5–11 227	11 352	6–11 227	11 452[c]
	$H_2{}^{33}S$	7.498×10^{-3}	5–11 072	6322	6–11 072	6220[c]
(32) HCOOH	$H^{12}C^{16}O^{16}OH$	9.839×10^{-1}	10–1890	62 684	10–1890	187 596
(33) HO_2	$H^{16}O_2$	9.951×10^{-1}	0–3676	38 804	0–3676	38 804
(34) O	^{16}O	9.976×10^{-1}	68–159	2	69–159	2
(35) $ClONO_2$	$^{35}Cl^{16}O^{14}N^{16}O_2$	7.496×10^{-1}	763–798	21 988	763–798	21 988
	$^{37}Cl^{16}O^{14}N^{16}O_2$	2.397×10^{-1}	765–791	10 211	765–791	10 211
(36) NO^+	$^{14}N^{16}O^+$	9.940×10^{-1}	3–2531	1270	4–2531	1270
(37) HOBr	$H^{16}O^{79}Br$	5.056×10^{-1}	0–316	2177	0–316	2177
	$H^{16}O^{81}Br$	4.919×10^{-1}	0–316	2181	0–316	2181
(38) C_2H_4	$^{12}C_2H_4$	9.773×10^{-1}	620–3243	59 536	620–3243	59 536
	$^{12}CH_2{}^{13}CH_2$	2.196×10^{-2}	614–3181	18 095	615–3181	18 095
(39) CH_3OH	$^{12}CH_3{}^{16}OH$	9.859×10^{-1}	0–1408	19 897	0–1408	19 897
(40) CH_3Br	$^{12}CH_3{}^{79}Br$	5.010×10^{-1}	794–1706	18 692	794–1706	18 692
	$^{12}CH_3{}^{81}Br$	4.874×10^{-1}	796–1697	18 219	795–1697	18 219
(41) CH_3CN	$^{12}CH_3{}^{12}C^{14}N$	9.739×10^{-1}	890–946	3572	890–946	3572
(42) CF_4	$^{12}C^{19}F_4$	9.889×10^{-1}	582–1519	842 709	582–1519	842 709
(43) C_4H_2	$^{12}C_4H_2$	9.560×10^{-1}	0–1303	251 245	0–1303	251 245
(44) HC_3N	$H^{12}C_3{}^{14}N$	9.633×10^{-1}	0–760	180 332	0– 3361	248 273
(45) H_2	H_2	9.997×10^{-1}	15–27 185	3480	15–27 185	3480[c]
	HD	3.114×10^{-4}	3–36 406	5129	3–36 406	11 575
(46) CS	$^{12}C^{32}S$	9.396×10^{-1}	1–2586	1088	1–2586	1088
	$^{12}C^{34}S$	4.168×10^{-2}	1–1359	396	1–1359	396
	$^{13}C^{32}S$	1.056×10^{-2}	1–1331	396	1–1331	396
	$^{12}C^{33}S$	7.417×10^{-3}	1–156	198	1–156	198
(47) SO_3	$^{32}S^{16}O_3$	9.434×10^{-1}	0–2825	14 295	0–2825	14 295
(48) C_2N_2	$^{12}C_2{}^{14}N_2$	9.708×10^{-1}	200–307	71 775	200–307	71 775
(49) $COCl_2$	$^{12}C^{16}O^{35}Cl_2$	5.664×10^{-1}	793–900	164 437	793–900	164 437
	$^{12}C^{16}O^{35}Cl^{37}Cl$	3.622×10^{-1}	800–892	145 477	800–892	145 477
(50) SO	$^{32}S^{16}O$	9.479×10^{-1}	–	–	0-12 631	42 916
	$^{34}S^{16}O$	4.205×10^{-2}	–	–	0-372	671
	$^{32}S^{18}O$	1.901×10^{-3}	–	–	0-363	677
(51) CH_3F	$^{12}CH_3{}^{19}F$	9.884×10^{-1}	–	–	1067–1291	1499
(52) GeH_4	$^{74}GeH_4$	3.652×10^{-1}	–	–	648–2270	12 209
	$^{72}GeH_4$	2.741×10^{-1}	–	–	649–2270	12 141
	$^{70}GeH_4$	2.051×10^{-1}	–	–	649–2271	12 092
	$^{73}GeH_4$	7.755×10^{-2}	–	–	649–2270	12 170
	$^{76}GeH_4$	7.755×10^{-2}	–	–	648–2270	12 266
(53) CS_2	$^{12}C^{32}S_2$	8.928×10^{-1}	–	–	23–6467	45 758
	$^{32}S^{12}C^{34}S$	7.921×10^{-2}	–	–	196–4543	7237
	$^{32}S^{12}C^{33}S$	1.409×10^{-2}	–	–	611–4567	3401
	$^{13}C^{32}S_2$	1.003×10^{-2}	–	–	1–4426	27 024
(54) CH_3I	$^{12}CH_3{}^{127}I$	9.884×10^{-1}	–	–	693–3274	178 247
(55) NF_3	$^{14}N^{19}F_3$	9.963×10^{-1}	–	–	2–2201	2 717 795

[a] Abundances are calculated from terrestrial atomic abundances in Ref. [57]. Line intensities in the HITRAN database have been scaled by these isotopologue abundances.

[b] Spectral ranges are given in cm^{-1}.

[c] Although spectral ranges and amount of lines is unchanged with respect to HITRAN2016, there are changes to spectral parameters of lines for these isotopologues.

Table 2
The uncertainty codes used by the HITRAN database (as presented in HITRAN*online*) are based on Table 5 of the HITRAN2004 paper [13]. There are two types of uncertainty code corresponding to absolute uncertainty in cm^{-1} (used for the line position and pressure-induced line shift parameters) and relative uncertainty in % (used for the line intensity and line-shape parameters).

Code	Absolute uncertainty range	Code	Relative uncertainty range
0	≥ 1 or Unreported	0	Unreported or unavailable
1	≥ 0.1 and < 1	1	Default or constant
2	≥ 0.01 and < 0.1	2	Average or estimate
3	≥ 0.001 and < 0.01	3	$\geq 20\%$
4	≥ 0.0001 and < 0.001	4	$\geq 10\%$ and $< 20\%$
5	≥ 0.00001 and < 0.0001	5	$\geq 5\%$ and $< 10\%$
6	≥ 0.000001 and < 0.00001	6	$\geq 2\%$ and $< 5\%$
7	≥ 0.0000001 and < 0.000001	7	$\geq 1\%$ and $< 2\%$
8	≥ 0.00000001 and < 0.0000001	8	$< 1\%$
9	≥ 0.000000001 and < 0.00000001		

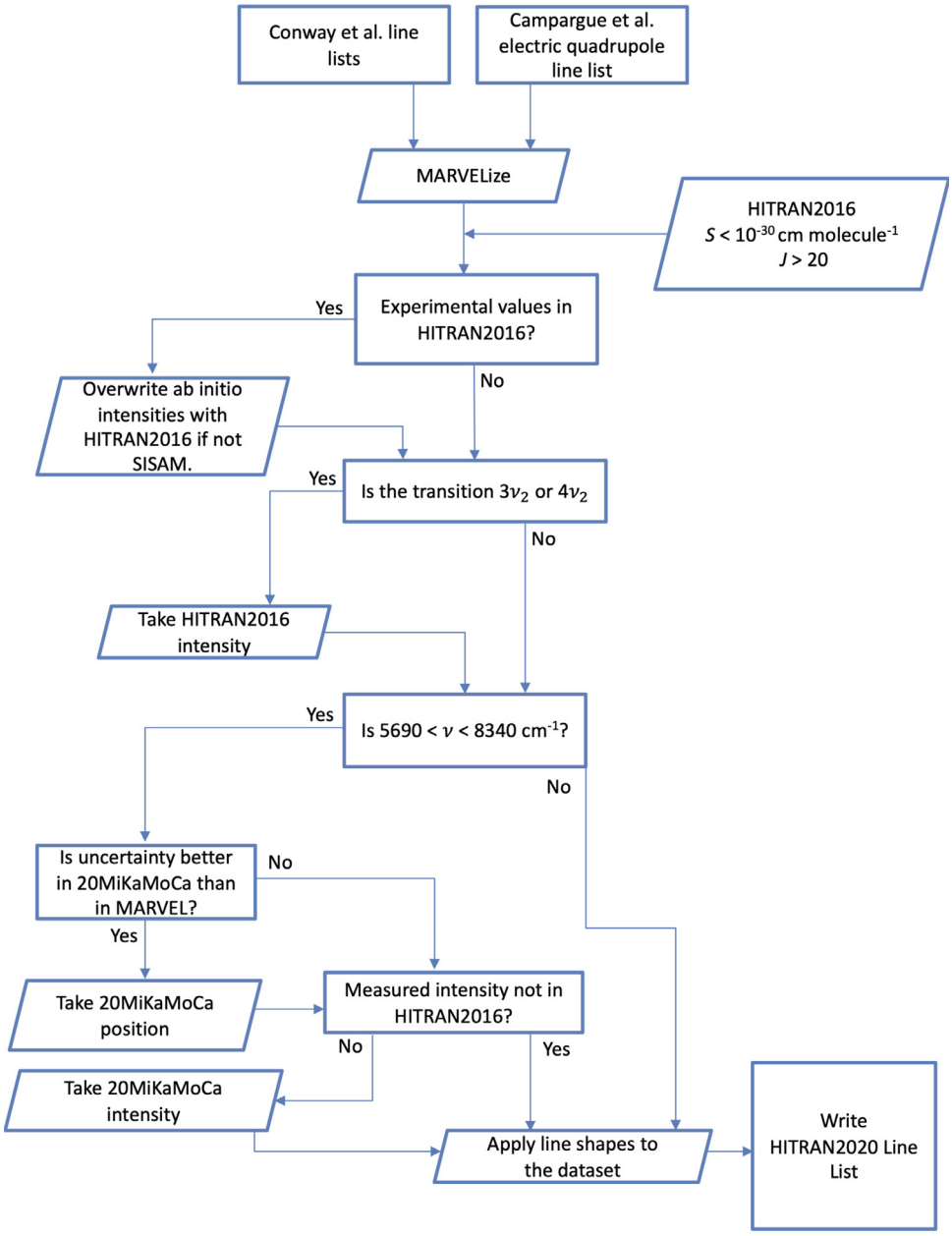

Fig. 1. A flowchart describing the development of the HITRAN2020 line list for the principal isotopologue of water vapor. The Mikhailenko et al. [91] line list is abbreviated to "20MiKaMoCa" within the chart shown above.

ample, frequency-comb and Lamb-dip techniques. The MARVEL (Measured Active Rotational-Vibrational Energy Levels) methodology [58,59] utilizes the framework provided by spectroscopic networks [94] and high-quality experimental measurements of line positions. Highly-accurate experimental measurements of line positions [95] were utilized during the latest MARVEL attempts to analyze water spectra. These accurate measurements can simultaneously improve the accuracy of the majority of energy levels [95] involved in connected transitions. Furtenbacher et al. released a much improved set of highly accurate $H_2^{16}O$ energy levels [96,97], named the "W2020" dataset, containing 19,225 empirical energy levels derived from 286,987 non-redundant experimental ro-vibrational transitions. Utilizing the labels and the transition wavenumbers of the W2020 set the information in the *ab initio* line list was updated. Conway et al. [98] recently applied the Hose–Taylor theorem [99] to theoretical spectroscopy and showed that the projection of the total angular momentum (J) onto the body fixed axis (k) can be considered a good quantum number once the square of the projected component's wave-function amplitude is greater than one-half ($\Psi_k^2 > 0.5$). The theory was tested using the DVR3D [100] nuclear motion code on the water and ozone molecules. The asymmetric-top quantum numbers K_a and K_c were determined to a high degree of fidelity up to dissociation. We used these results to label states in the visible and near ultraviolet where MARVEL does not yield this information.

Mikhailenko et al. [91] also released an empirical line list that spans 5690 – 8340 cm^{-1}, and we compared their results to the *ab initio* calculations of Conway et al. [85]. It was found that high overtones of ν_2, notably $3\nu_2$ and $4\nu_2$, were not accurately represented in the new *ab initio* calculations. Hence, for these bands, we replaced the calculated results of Conway et al. with what was already present in HITRAN2016. We also detected a small number of discrepancies in the transition frequencies created by the latest empirical (MARVEL) energy levels to those present in the empirical line list. In such cases, we chose the source that has the lowest uncertainty associated with it and also considered the type of experiment used to derive the value in the empirical line list.

In the next step, we focused on overwriting the *ab initio* intensities with high-quality experimental measurements wherever it was deemed appropriate. Experimental measurements in the IR which were performed at the Deutsches Zentrum für Luft und Raumfahrt (DLR) [66,102,103] were analyzed by Birk et al. [104] and deficiencies were observed in the *ab initio* data of Lodi et al. [84], particularly in the ν_1 band. The same deficiencies in ν_1 are present in the Conway et al. *ab initio* data but improvements are evident in many other bands [85], especially for those near 1 μm. Differences between the experimental [66] and the new *ab initio* data were found in the relative intensities for ν_2 (ca. 1%) and $2\nu_2$ (ca. 1.5%). The differences occur in the upper wavenumber range of the bands and increase with wavenumber. In the case of the ν_3 fundamental, the average difference changes from 0.18% with the calculation of Lodi et al. [84] to −1.08% with the *ab initio* data of Conway et al. [85]. The $3\nu_3$ band also showed similar behavior, with the mean residuals increasing from −0.7% using the Lodi et al. [84] line list to −3.9%. The latter one is the only band in the 1-μm region where no improvement was observed. Utilizing the high-quality measured intensity data, scaling factors were derived for the *ab initio* data from Conway et al. in the corresponding bands. These factors were then applied to scale the *ab initio* intensities for all lines in these bands, with an intention to improve the accuracy of the transitions (in these bands) where no measurement is available. Further investigations indicated that the underlying electronic structure calculations were the culprit of such irregularities [105] and Conway et al. [85] showed for the ν_2 fundamental how changing the spectrum-fitting profile can result in different transition parameters – in particular, intensities.

All experimental intensity measurements present in the HITRAN2016 line list, with the exception of the SISAM (Spectromètre Interférentiel à Sélection par l'Amplitude de la Modulation) data [61] (excluding any $3\nu_2$ and $4\nu_2$ measurements), are transcribed into HITRAN2020 [62–72]. Comparisons [85] between the new *ab initio* intensities and the intensity measurements within the SISAM data set in the infrared region exhibited a skewed appearance. This is not the first instance of such a structure being attributed to Kitt Peak water-vapor spectra [63,104,106]. If we detected an experimentally determined value for an intensity in the empirical list of Mikhailenko et al. [91], the *ab initio* intensity was overwritten by the experimental datum.

For the first time, electric quadrupole (E2) transitions for the water molecule were identified in experimental spectra, made possible by the availability of an E2 *ab initio* line list [107,108]. The E2 transitions have now been added to the HITRAN2020 line list (only for the principal isotopologue). This room temperature E2 line list for $H_2^{16}O$ ranges from 0 to 10,000 cm^{-1} and contains 6227 lines with intensities stronger than 10^{-30} cm/molecule. It was generated using MARVEL line positions and lower-state energies and theoretical transition intensities computed using a high-level *ab initio* electric quadrupole moment and a state-of-the-art variational approach [109,110]. The character in the last field of lower-state rotational ("local") quanta (i.e. preceding the error code for the line positions) in the traditional 160 character ".par" format will carry a label "q" to denote these transitions (see the Supplementary Material of this paper for the description of the upper- and lower-state quanta in the ".par" format). It should be noted that E2 type transitions are typically 6–8 orders of magnitude weaker than electric dipole transitions [107].

The HITRAN2016 line list included a large number of highly-accurate transition wavenumber measurements from the SISAM data set. Comparisons of these data to derived MARVEL transition frequencies indicated that the transition wavenumbers derived from the most recent version of the MARVEL data [97] match the SISAM values to within their uncertainty. The predicted MARVEL line positions are therefore selected as the preferable source of data because, apart from their validated accuracy, they also would provide consistency throughout the database. Hence, where possible, we overwrite the *ab initio* energy levels and transition frequencies with the MARVEL data.

The accuracy of the HITRAN2020 line list in the visible region is significantly better than that of its predecessor, HITRAN2016. Harder et al. [101] reported water-vapor absorption spectra in the 22,100–22,700 cm^{-1} interval through atmospheric observations. Using the HITRAN Application Programming Interface (HAPI) [52], we have generated cross sections at a temperature of 288 K using the Voigt profile at a resolution of 0.03 cm^{-1}. In Fig. 2, it becomes clear that the HITRAN2020 line list is significantly better suited for retrieving water in the visible region. It has already been reported that the HITRAN2016 water line list has spectroscopic errors in the visible range [111] and the HITRAN2020 edition offers substantial improvements. These errors were attributed to a collection of irregularities in line shape parameters and inaccurate *ab initio* transition intensities.

To extend this comparison between HITRAN2020 and HITRAN2016 in the visible between 9000 and 20 000 cm^{-1}, we generated two telluric models using the Planetary Spectrum Generator (PSG) [37], each generated with the two respective line lists, and compared these models to a high SNR telluric spectrum extracted from solar observations detailed in Baker et al. [77]. The atmospheric profile used to generate the model was evaluated for the appropriate location and elevation of the observation site in Göttingen, Germany as well as the corresponding observation time of June 17, 2015 UTC 10:50:30.5. The water-vapor abundance and surface pressure were adjusted by fitting the model to a subset

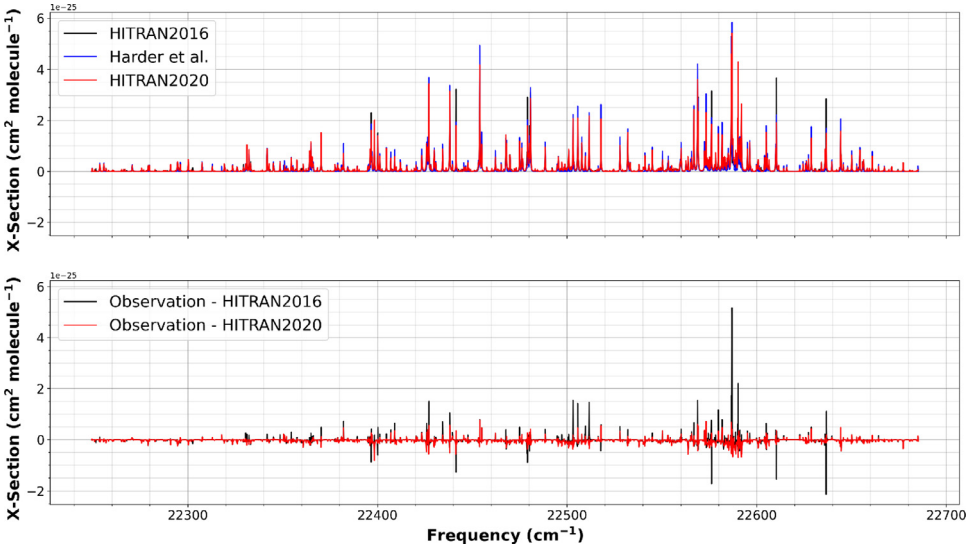

Fig. 2. Comparison of the HITRAN2020 and HITRAN2016 [16] line lists against the observed water-vapor cross sections reported by Harder et al. [101].

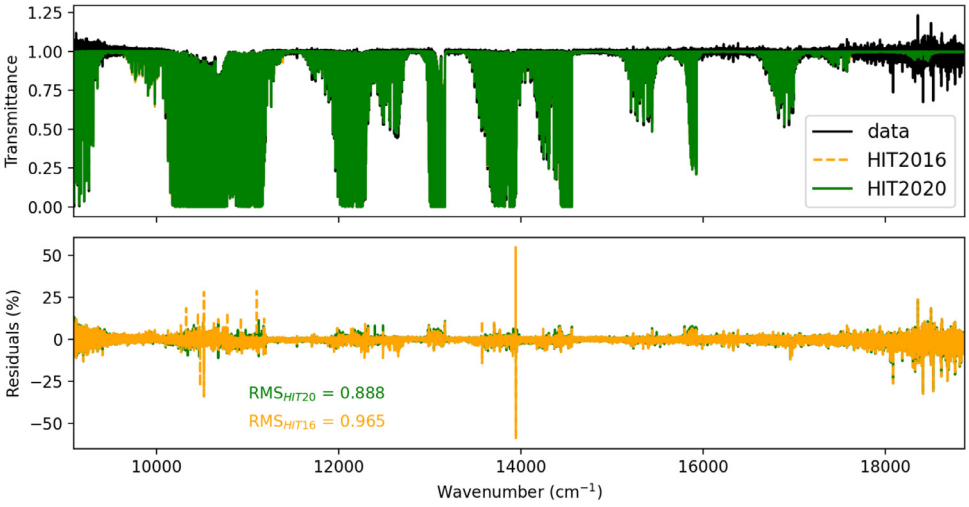

Fig. 3. Comparison of the HITRAN2020 and HITRAN2016 [16] water vapor line lists through modeling the terrestrial atmospheric transmittance. Models were generated with the Planetary Spectrum Generator (PSG) [37] and compared to a telluric spectrum extracted from a high-resolution solar spectrum as described by Baker et al. [77].

of the data between 13,679.89 and 13,698.63 cm^{-1}. The results of this comparison are shown in Fig. 3. The residual root mean square (RMS) for each model comparison shows overall improvements in HITRAN2020. This is partly due to the completeness of the HITRAN2020 line list, which now includes transitions that were missing in HITRAN2016, some of which were identified by Baker et al. [77] and partly due to improvements in the line-shape algorithm described below. Similar results are found by redoing this analysis using a transmission spectrum of the atmosphere at Kitt Peak [112] also derived from solar observations, but extracted using a different method to that used in Baker et al. [77]. The majority of transition intensities within Fig. 3 are from *ab initio* calculations and the line-shape parameters are often estimated, therefore the residuals could be improved with new high quality experimental measurements.

2.1.2. $H_2^{18}O$

The HITRAN2020 line list for $H_2^{18}O$ also begins with the *ab initio* line list from Conway et al. [85], which extends to 20,000 cm^{-1}. In their comparisons against the experimental transition intensities present in the HITRAN2016 line list, discrepancies were observed that were not evident in any of the $H_2^{16}O$ comparisons. A large amount of scatter was observed in intensity comparisons to measurements in the SISAM data [61], while a large, 20% shift was observed in the Tanaka et al. [113] intensities present in HITRAN2016. No such discrepancies were detected for the principle isotopologue covering the same regions. Considering that the *ab initio* line lists for $H_2^{16}O$ and $H_2^{18}O$ were calculated using very similar PESs and the same DMS, the source of the discrepancies is more likely to be associated with experiments. Therefore, the Tanaka et al. data is not included in the HITRAN2020 release.

Comparisons against new experimental spectra measured by Mikhailenko et al. [114] between 16,400 and 17,200 cm^{-1}, that was not present in HITRAN2016, were also performed [85]. While Mikhailenko et al. noticed that the HITRAN2016 data missed particularly strong transitions in the region, most from *ab initio* calculations [115], the new *ab initio* calculations were not missing such transitions.

In addition to releasing a much improved set of $H_2^{16}O$ energy levels, Furtenbacher et al. [97] also released an updated set of empirical energy levels for both $H_2^{18}O$ and $H_2^{17}O$ as part of their W2020 dataset. Hence, to develop the $H_2^{18}O$ line list for HITRAN2020 we considered the *ab initio* line list from Conway et al. and updated the *ab initio* energy levels with the latest MARVEL

data. Furtenbacher et al. also utilized the method of Polyansky et al. [116] to generate so-called pseudo-experimental energy levels. Use of these semi-empirical levels for both $H_2^{18}O$ and $H_2^{17}O$ will be considered as a possible further improvement in a future release.

Following this, we proceeded to update the calculated transition intensities with the measured data present in HITRAN2016 [63,68–71,117], with the exception of the SISAM (aside from the measured $3\nu_2$ and $4\nu_2$ bands) and Tanaka et al. data. In addition, we also supplement the line list with newly measured intensities from Mikhailenko et al. [114].

2.1.3. $H_2^{17}O$

The HITRAN2016 $H_2^{17}O$ line list possessed several small issues [97], mostly related to spectroscopic assignment of states. There were forbidden transitions between ortho–para states, rotational parity was equal for several upper and lower-states, and the list possessed several duplicate transitions. To address these issues, we have updated the energy levels (hence the transition frequencies) with the latest MARVEL data and remedied these transition assignments.

2.1.4. $HD^{16}O$, $HD^{18}O$ *and* $HD^{17}O$

The HITRAN2016 $HD^{16}O$, $HD^{18}O$ and $HD^{17}O$ line lists also possessed several issues related to forbidden transitions. To address these issues, we have updated the transition assignments. Positions and intensities have not been altered from HITRAN2016.

2.1.5. $D_2^{16}O$

The $D_2^{16}O$ line list in HITRAN2016 was based on a preliminary version of the line list from Kyuberis et al. [118]. This preliminary list was found to contain some incorrect quantum assignments and therefore for HITRAN2020 the published list from Kyuberis et al. [118] was used.

2.1.6. Line-shape parameters for water vapor

Line-shape parameters, including the half-width, γ, and the line shift, δ, their associated errors, and the temperature dependence of these parameters have been added to the water-vapor transitions discussed above. The algorithm becomes rather involved due to the fact that the data availability and uncertainties vary greatly with spectral bands and isotopologues but basically follows the "Diet" procedure of Gordon et al. [73]. Line-shape parameters for H_2O-air and self-collision systems were added for all the isotopologues of water vapor, although for self-collisions only the half-widths are considered. It is important to note that for HITRAN2020, only values associated with the power law of temperature dependencies were considered for water vapor. When the shift does not change sign over the temperature range of the calculations (see below), the power law temperature dependence, m, was also determined. However, when possible, the temperature dependence of the half-width and the line shift were generated using the Gamache–Vispoel double power law (DPL) model [119] and will be considered for the database update in the future. The infrastructure for this is already setup [120] but large effort is required to validate and populate these parameters as mentioned in Section 7.1.1.

The "Diet" procedure takes line-shape data from a number of sources and prioritizes the data for addition to HITRAN. Beginning with an updated version of the measurement database of Gamache and Hartmann [121], which contains data for the seven water-vapor isotopologues in HITRAN, data of known high quality for γ and δ were extracted and put into a "priority" data file. It is important to emphasize that the priority data are from laboratory measurements or line shape parameters determined from the fits of the atmospheric spectra. For instance, Mlawer et al. [122] have identified issues with broadening parameters for a couple of dozen of lines in the FIR region and have suggested alternative values based on the retrievals. These values form the priority data file for the HITRAN2020 update.

Next, an intercomparison of the measurement data was performed, and the inconsistent references and individual outliers were filtered from the air-broadening database. The intercomparison of H_2O-air data and H_2O-H_2O data were redone and average values from the intercomparison of data were determined and transitions with less than 5% standard deviation for the intercomparison are retained and stored in files for the half-widths and the line shifts. Then, all the lines for which an intercomparison could not be performed, i.e., a single datum for a transition, were written to separate files for the half-widths and the line shifts.

Next in the sequence, theoretical calculations of the line-shape parameters were considered. Taking the Modified Complex Robert–Bonamy (MCRB) calculations of Vispoel et al. [123] for the H_2O-N_2 collision system and similar calculations for the H_2O-O_2 collision system, the line-shape information for the H_2O-air collision system were produced by $\gamma_{air} = 0.79\gamma_{N_2} + 0.21\gamma_{O_2}$ with a similar formula for the line shift. Note the calculations considered 13 temperatures from 200-3000 K; γ and δ were determined for these 13 temperatures so that the temperature dependence could be determined. These MCRB calculations were made for 10,782 rotational transitions for the rotational band and for bands with one to four ν_1, ν_2, and ν_3 vibrational quanta exchanged, giving some 140,000 calculated transitions. These data make up the calculated H_2O-air line-shape files for the $H_2^{16}O$, $H_2^{18}O$, $H_2^{17}O$ isotopologues. For these three isotopologues, the self-broadening Complex Robert–Bonamy calculations that were added to previous HITRAN databases were used. For the HDO and D_2O isotopologues self-broadened data are from the calculations in Refs. [124–126].

Next in the algorithm was the use of accurate predicted values of γ, δ, and the temperature dependence of each. Gamache and Hartmann, working from Robert–Bonamy theory, derived a formula that can accurately predict γ and δ [127] at any temperature. Plots showing the agreement of these predictions with the experimental data from the ν_2 band are provided in Supplementary Material. This routine has been successfully applied to H_2O-air [128], CO_2-x, where x = N_2, O_2, air, CO_2 [129], H_2O-H_2 [130], and H_2O-N_2 [131], and the predicted values agree well with the calculated or measured values with a standard deviation of about 5% for the H_2O studies. A prediction routine was developed based on the H_2O-air MCRB data ($H_2^{16}O$, $H_2^{18}O$, $H_2^{17}O$) and the prediction coefficients determined at the 13 temperatures allowing the temperature dependence to also be determined. These data make the predicted part of the H_2O-air database.

Lastly, for transitions that are not in the above databases, the half-width is estimated by using the rotation band value if it is available, i.e. neglecting the vibrational dependence. However, there are a large number of H_2O transitions in the HITRAN database that do not have attributions. These are transitions generally taken from *ab initio* calculations where only the rotational quantum number J and parity are "good" quantum numbers. For these transitions, the rotation band calculations were taken and half-widths as a function of J'' were determined. These data were extrapolated to J''= 50 (keeping HITEMP in mind). Note, because of the very strong vibrational dependence of the line shift, no comparable average values can be determined.

This general procedure was done in three groups: ($H_2^{16}O$, $H_2^{18}O$, $H_2^{17}O$), ($HD^{16}O$, $HD^{18}O$, $HD^{17}O$) and ($D_2^{16}O$) for air- and self-collisions, producing the isotopologue-dependent files, which are added to HITRAN2020 in the following priority scheme: (1) priority data, (2) intercomparison data, (3) single measurement data, (4) MCRB data, (5) predicted data, and (6) J-average data. It was possible to do the temperature dependence of the J-average values only for the first group. This procedure assumes that the line-shape

data for the oxygen-16, 18, and 17 species of water are the same, which has been well demonstrated by measurement and calculation [121].

These data sets are summarized in more detail in the Table provided in the Supplementary Material. From these data the Python dictionaries were made using the ro-vibrational quantum numbers as the key. A Python algorithm was written that loads into memory, for all isotopologues of H_2O, the database dictionaries described above and then reads the HITRAN2020 water-vapor line file and selectively adds the line-shape data to each transition in the prioritized scheme discussed above.

It is important to note that all the parameters described above are for the Voigt line shape. However, non-Voigt line shapes and specifically HT profile have also been accommodated. HITRAN2016 already contained many of these parameters, but more have been added for the HITRAN2020 edition, specifically in the 2.3 μm region. The data are based on the new H_2O/HDO database in the spectral range 4190–4340 cm^{-1} (2.39–2.30 μm) that was generated within the framework of the ESA project SEOM-IAS (Scientific Exploitation of Operational Missions — Improved Atmospheric Spectroscopy Databases), ESA/AO/1-7566/13/I-BG [103,132]. This work has already been partially reported in HITRAN2016 [16], but only line intensities were entered into the database.

In the 4190–4340 cm^{-1} region, several Fourier-Transform transmittance spectra of pure and air-broadened water vapor at low and high temperatures were measured and analyzed. These measurements were dedicated to water-vapor parameters to be used in TROPOMI/S5-P retrievals. The analysis was based on a multi-spectrum fit using the HT profile. Line positions, intensities, self- and air-broadened line-shape parameters including speed-dependence and Dicke narrowing parameters as well as their temperature dependence were retrieved in the analysis. The line-shape parameters are available in the HITRAN2020 database. The data as well as the measurements can also be downloaded from Zenodo [103,132].

The new 2.3 μm H_2O data together with the new 2.3 μm CH_4 data described in Section 2.6 have been validated by ground-based solar occultation measurements by Frank Hase, KIT, Karlsruhe, Germany. Fig. 4 shows residuals applying HITRAN2012, HITRAN2016, and the new database. The residuals are smallest for the new database. Remaining residuals are caused by imperfect modeling of solar lines.

2.2. CO_2: carbon dioxide (molecule 2)

Current and planned atmospheric remote sensing instruments set a very challenging level of 0.3% accuracy on the retrieved CO_2 column [133], which in turn places stringent requirements on the quality of spectroscopic parameters for this molecule.

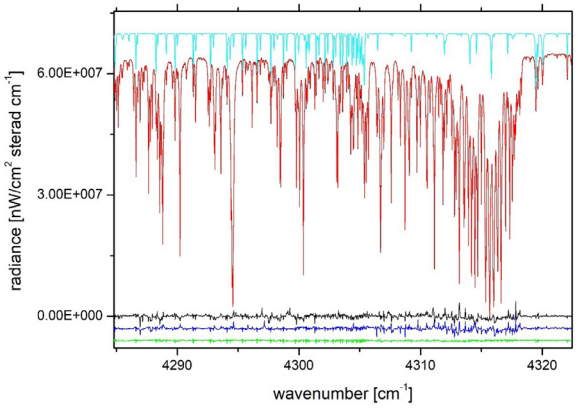

Fig. 4. Solar occultation spectrum (red) and residuals for different spectroscopic databases, green: new line list, black: HITRAN2012, blue: HITRAN2016, light blue: solar transmission spectrum. Courtesy Frank Hase, KIT, Karlsruhe, Germany.

The HITRAN2016 line list for the twelve stable isotopologues of carbon dioxide has proven to be an overall improvement over the previous editions of the database (see, for instance, Ref. [76]). However, a number of remaining or new issues were identified as described below. For the HITRAN2020 database, these issues were addressed while a number of previously missing bands above 8000 cm^{-1} were added.

2.2.1. CO_2 line positions and intensities

The details of the update for line positions and intensities are provided in a dedicated publication in this special issue [134]. Here we briefly summarize important points. Before describing the new data, it is worth recalling that, below 8000 cm^{-1}, the line positions for CO_2 transitions in HITRAN2016 were predominantly based on the update to the 2015 version of the Carbon Dioxide Spectroscopic Database (CDSD-296) [135]. The line intensities were mostly of *ab initio* origin [136] based on the work of Zak et al. [137–139] except for the bands that were identified as "sensitive" [137], where CDSD intensities were preferred.

2.2.2. Improved line positions and "new" bands

The majority of the CO_2 line positions in the HITRAN2020 database were updated using the line positions from the recent 2019 version of CDSD-296 for atmospheric applications [140]. It should be noted that the slightly corrected and updated version of the CDSD-296 database uploaded at ftp.iao.ru as `pub/CDSD-296/cdsd-296_version_1.rar` was used. The differences with CDSD-296 published in Tashkun et al. [140]: 1. $\Delta P = 6$ region ($P = 2V_1 + V_2 + 3V_3$ is the polyad number, V_i are the vibrational quantum numbers) of the $^{16}O^{12}C^{18}O$ isotopologue was recalulated using the new set of effective dipole moment parameters; 2. A total of 226 lines with $\Delta l_2 = 4$ of the $^{12}C^{16}O_2$, $^{13}C^{16}O_2$, and $^{16}O^{12}C^{18}O$ isotopologues were added. The lower-state energies and the uncertainty codes of the line positions were also transferred from CDSD-296 [140] to HITRAN2020.

The line parameters for the principal isotopologue above 8000 cm^{-1} were extended by including the new bands from the high-temperature line list from Yurchenko et al. [141] (with appropriate intensity cutoff). The assignments for these CO_2 lines were achieved by using the CDSD-296 [140] and NASA Ames [142] databases. The vibrational assignments were replaced with "-2-2-2-20" when the states were not assigned. Uncertainty codes 3 for the line positions and 4 for the line intensities (see Table 2) were used in the case of the newly added CO_2 lines.

Also, the 30022–00001 and 30023–00001 bands of the $^{16}O^{12}C^{18}O$ isotopologue, missing in HITRAN2016 [16] and CDSD-296 [140], were included in the HITRAN2020 line list. The line positions for these bands were computed up to $J = 34$ using the spectroscopic constants obtained by the fit to the measured line positions from Karlovets et al. [143]. In Ref. [143], it was also shown that the R-branch intensities of the 00041–01101 band of the $^{12}C^{16}O_2$ isotopologue are in good agreement with the Ames values while HITRAN2016 values are largely overestimated. This band is missing in CDSD2019 [140] and included in HITRAN2016 from an old version of CDSD [144]. The line intensities for the three bands described above were updated using the NASA Ames database [142]. Uncertainty code 4 for line positions and uncertainty code 4 for line intensities (see Table 2) were updated for these bands in the HITRAN2020 CO_2 line list. An overview of the HITRAN2020 line lists for all 12 isotopologues of carbon dioxide in natural abundance is plotted in Fig. 5.

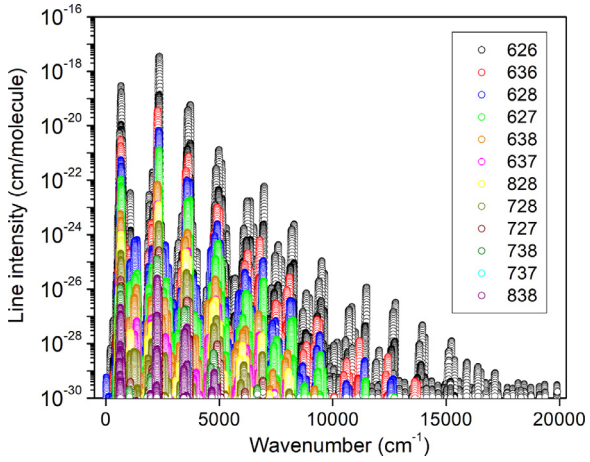

Fig. 5. Overview of the HITRAN2020 line lists for all 12 naturally abundant isotopologues of carbon dioxide.

2.2.3. Addressing the issues found in HITRAN*2016*

Most of the HITRAN2016 CO_2 issues were identified by comparisons against laboratory and atmospheric spectra obtained with Fourier Transform Spectrometers (FTS) at the Kitt Peak National Observatory, MkIV balloon, and Total Carbon Column Observing Network (TCCON) [145,146]. In particular, it was shown that:

- Comparisons with the Kitt Peak laboratory spectrum demonstrated 10-15% rotationally dependent errors in the *ab initio* intensities of the 40002–01101 band of $^{12}C^{16}O_2$ isotopologue near 4800 cm^{-1}. This region is probed by the OCO-2 instrument [147], so it is important, although it is worth pointing out that the intensities of this hot band are about two orders of magnitude weaker than the strongest lines in that region. This comparison helped to identify a systematic issue in the *ab initio* calculations [137] when calculating intensities for the transitions that involve either of the interacting 40002 and 21113 vibrational states which are affected by Coriolis interaction.
- In the 1800–2000 cm^{-1} region, the amount of CO_2 retrieved with HITRAN2016 is about 5% larger than that retrieved with previous line lists [14,15]. The biggest deviations in this region were observed for the 11102–00001 band. Two bands 11101–00001 and 11102–00001 borrow the intensities from the strong 00011–00001 band via Coriolis interaction. The CDSD-296 [135] line positions and intensities were used in the previous line lists [14,15] while HITRAN2016 used the UCL *ab initio* line intensities [137]. It was shown in Ref. [140] that the *ab initio* AMES line intensities [142] for the 11101–00001 band deviate considerably from the observations. The same conclusion is valid for the UCL *ab initio* line intensities [137] of this band.
- The TCCON spectra cover the 3950 cm^{-1} to 9500 cm^{-1} region. The HITRAN2016 line lists reduce the CO_2 retrieved from the 6220 cm^{-1} and 6338 cm^{-1} windows by 0.5% and 1.5% respectively, raising additional concerns of consistency at the required level of accuracy. This issue is associated with the line intensities in the 30012–00001 band and is discussed below.

Critical validation tests for the spectroscopic data were carried out to find problems due to insufficient accuracy of line parameters in some of the bands in the CO_2 line list using available experimental works and the existing theoretical and semi-empirical databases, including NASA Ames [142], UCL [137–139], and CDSD-296 [140]. All updates for the CO_2 line positions and intensities described above are discussed in Ref. [134].

In the HITRAN2016 line list below 8000 cm^{-1}, a number of inconsistencies in the rotational structure in the so-called "sensitive bands" (as defined by Zak et al. [137]) due to the mixing of CDSD [135] and UCL [137–139] line intensities were revealed in Cavity Ring-Down Spectroscopy (CRDS) measurements of ^{18}O- and ^{13}C-enriched and "natural" CO_2 near 1.74 μm [148–150]. They concern the perpendicular bands of the $\Delta P = 9$ series of transitions. It leads to apparent inconsistency in the rotational structure with strong intensity variation between successive J values or even missing transitions (due to falling below the intensity cutoff) as shown, for example, in Fig. 9 of Ref. [148]. Validation tests were carried out for the bands from Refs. [148–150] and the other bands affected by this problem due to the mixing of CDSD and *ab initio* intensities in the HITRAN line list using literature values and those from the different CO_2 databases. Alternative sources of data for each problematic band were identified. See more details in Ref. [134].

2.2.4. New experimental data with sub-percent uncertainty

A number of very accurate measurements have become available after the release of HITRAN2016. Here we make use of the most recent CRDS measurements from NIST [151,152] and FTS measurements from DLR (reported in this special issue by Birk et al. [153] with the corresponding measurements and line parameter database made available on Zenodo [154]). The results of these works were used to improve the HITRAN line intensities for several NIR bands of the principal isotopologue of CO_2. It is interesting to note that in these works it was found that for these particular bands (discussed below) the rotational distribution of the *ab initio* intensities from Zak et al. [137] used in HITRAN2016 was very accurate; however different band scaling factors were recommended. In Refs. [151,152], the reported intensity uncertainty is better than 0.1%. Fleurbaey et al. [151] showed that a constant scaling of 1.0069±0.0002 of HITRAN2016 values in the 20013–00001 band of CO_2 ($\lambda = 2.06$ μm) is consistent with experiment, therefore we have performed this scaling in HITRAN2020. Similarly accurate line intensity measurements for the 3001i–00001 (i = 2-4) bands reported by Long et al. [152] were used to improve the CO_2 line intensities near 1.6 μm. It was shown in Ref. [152] that their results and the *ab initio* calculations of Zak et al. [137] agree at the 0.06% level for the 30013–00001 (also targeted by the OCO-2 mission) and 30014–00001 bands, but there is a systematic discrepancy of about 1.1% for the 30012–00001 band. Following these results, the HITRAN2016 line intensities were scaled to the experimental band-dependent scaling factors from Long et al. [152]. Uncertainty code 8 (see Table 2) for the line intensities was given for the corresponding bands in the HITRAN2020 line list.

Ambient temperature FTS measurements of pure CO_2 have been conducted at the German Aerospace Center (DLR) with a Bruker IFS 125HR in the range 6000–7000 cm^{-1} [153]. Line intensity accuracies of 0.15% have been reported for the strongest bands in that spectral region. They also covered the 3001i–00001 bands, but this time including the 30011–00001 band. The corresponding factor 1.0061 was used to scale the intensities of the 30011–00001 band of the $^{12}C^{16}O_2$ isotopologue according to DLR measurements [153]. Good agreement between measurements of intensities of the 30013–00001 and 30014–00001 bands in Refs. [152,153] were found. Nevertheless, for the 30012–00001 band the differences outside of the stated uncertainties were reported. However, these differences are still small, <0.5%. Further investigations will be carried out for future updates of the database. Although this band is not being targeted by the OCO-2 mission, it is used in LIDAR applications (see Ref. [155], for instance), therefore it is important to minimize possible uncertainties.

The line intensities of the 00031–00001 band of the principal isotopologue near 1.4 μm came from CDSD-296 [135] in the HITRAN2016 edition, because this band was identified as "sensitive" in the *ab initio* calculations [137]. The comparison of the CDSD line

intensities with the DLR measurements [153] showed rotationally dependent deviations up to 4% for the 00031–00001 band. In the HITRAN2020 line list, the UCL line intensities [137] of the 00031–00001 band were scaled by the factor of 1.1217 to match the line intensities measured by Birk et al. [153]. Also, the HITRAN2016 line intensities of the 10032–10002 and 01131–01101 relatively weak hot bands located near 6900 cm^{-1} were compared to the DLR measurements [153]. It was found that the line intensities of the 10032–10002 band in HITRAN2016 should be scaled by a factor of 1.1346 while the line intensities of the 01131–01101 band should be scaled by a factor of 1.0022.

2.2.5. Introduction of magnetic dipole transitions

All previous editions of HITRAN provided only electric dipole transitions for CO_2. In this edition, the line parameters of the $\nu_2 + \nu_3$ magnetic dipole band of the $^{12}C^{16}O_2$ isotopologue were introduced into HITRAN for the first time. These new data will help spectral studies of CO_2-rich planetary atmospheres. This band is forbidden in electric dipole absorption, but it is allowed in electric quadrupole and in magnetic dipole absorptions. The first observation of the $\nu_2 + \nu_3$ band of $^{12}C^{16}O_2$ at 3.3 μm was made in the atmosphere of Mars (Trokhimovskiy et al. [156]) by the ExoMars Trace Gas Orbiter ACS instrument (Korablev et al. [42]). This band is located in a CO_2 transparency window and identified as a magnetic dipole band (Perevalov et al. [157]). Detailed spectroscopic studies of this band providing the selection rules for the vibration-rotation transitions, as well as the line position and intensity measurements are given in Refs. [156,157]. The vibrational transition magnetic dipole moment of the $\nu_2 + \nu_3$ band was fit to the line intensities measured with a Bruker IFS 125 HR FTS and a 30 m base multipass gas cell of the V. E. Zuev Institute of Atmospheric Optics SB RAS (Borkov et al. [158]). Using the obtained vibrational transition magnetic dipole moment and the set of the effective Hamiltonian parameters (Majcherova et al. [159]), the line positions and intensities of this band were generated. The maximum line intensities are on the order of 3×10^{-28} cm/molecule. The calculated line intensities for five R-branch lines of this band (R26-R32 and R36) are in a good agreement with the values measured independently by CRDS [160]. In the HITRAN2020 database, the calculated line parameters of this band are presented up to $J = 64$ corresponding to the intensity cutoff 10^{-30} cm/molecule at 296 K. The line position uncertainty code 4 and line intensity uncertainty code 4 (see Table 2) are used for this band. It should be noted that line intensities of this band retrieved from laboratory spectra [158] are about two times smaller than those recovered from Martian atmosphere spectra [156]. To distinguish these transitions in the HITRAN2020 CO_2 line list, a letter "m" is introduced into the quantum notation of these magnetic dipole CO_2 transitions in the field dedicated to upper state rotational ("local") quanta (see the Supplementary Material of this paper for the description of the upper- and lower-state quanta in the ".par" format).

2.2.6. CO_2 line-shape parameters

The approach we have taken to populate the line-shape parameters of CO_2 broadened by air and CO_2 (self-broadening) is described in the study by Hashemi et al. [161], where different comparisons of the parameters and various validation tests are carried out to demonstrate how the appropriate data sets were chosen for the HITRAN2020 edition. In this section, we highlight these updates and we explain the slight modification (regarding Ref. [161]) based on the new measurements.

The update to the line-shape parameters of CO_2 in the HITRAN2020 edition can be summarized in three components:

- Revising the Voigt profile (VP) [162] parameters that belong into the ".par" format file.
- Addition of the air and self speed-dependent Voigt (SDV) [163–165] parameters for all the transitions of CO_2.
- Updating the already-existing CO_2 line-mixing package developed by Lamouroux et al. [166], and addition of the first-order line-mixing to the database.

These parameters are listed in Table 3 for the Voigt profile (VP) and speed-dependent Voigt (SDV) parameter group in two separate sets.

2.2.7. Revising the Voigt profile parameters

The Voigt air- and self-broadened half-widths (γ_{air} and γ_{self}, respectively) of CO_2 lines and their temperature exponent parameters were re-assessed since the vibrational dependence of the line widths was found to be excessive for some of the CO_2 bands in the HITRAN2016 line list. The concern was that the line widths, calculated for the HITRAN2016 edition, were influenced by some of the less accurate measurements. Additionally, the Lorentzian widths, were retrieved using various line-shape profiles for different bands, and were used in the algorithm [129]. This discrepancy in the line widths using different line-shape models, which can alternate by about 5% [167–169], may have been inadvertently ascribed to a large vibrational dependence of the width parameters. For the bands probed by the OCO-2 mission (1.6 μm and 2.06 μm regions), the HITRAN2016 half-widths belonged to the experimental values of Ref. [170] obtained with the SDV profile without supplying the speed-dependent parameters in the database. To investigate the magnitude of the vibrational-dependence of the broadening parameters in HITRAN2016, the laboratory-measured widths and theoretical values for several bands were collected and examined for CO_2 lines using the VP [161]. Not uncommon for a linear molecule, a relatively weak vibrational dependence was revealed. Accordingly, with regard to updates of the line widths and their temperature dependences for the HITRAN2020 edition, the vibrational dependence of these parameters was ignored, and new values were produced for the air- and self-broadening parameters based on the measured data in Refs. [171,172] using semi-empirical models (the Padé approximants) described in Ref. [161]. In general Padé approximants (Eq. (1)) of the third and fourth-order are used extensively in this edition for many molecules.

$$\gamma(|m|) = \frac{(a_0 + a_1|m| + a_2|m|^2 + a_3|m|^3 + a_4|m|^4)}{(1 + b_1|m| + b_2|m|^2 + b_3|m|^3 + b_4|m|^4)}, \quad (1)$$

where the rotational running index m was introduced to treat simultaneously the P-, Q- and R- branch transitions with the following relations to the rotational quanta:

$$\begin{array}{ll} \text{P-branch:} & m = -J'' \\ \text{Q-branch:} & m = J'' \\ \text{R-branch:} & m = J'' + 1 \end{array} \quad (2)$$

Moreover, the air- and self-shifts (δ_0) in HITRAN2016 (calculated using the semi-classical routine in Ref. [129]) for P- and R-branches were not asymmetric. To produce the rotational and vibrational dependence of shift parameters, the empirical model introduced by Hartmann [173] is implemented to determine the air- and self-shifts of lines for all the vibrational bands of CO_2. With regard to this approach, the shifts of CO_2 lines can be obtained from the available measured shift parameters for one band and, after properly determining the fitting coefficients explained in Refs. [161,173], the shift values can be expanded to the non-measured bands and transitions.

2.2.8. Air and self speed-dependent Voigt parameters

To reach the accuracy that is required in atmospheric CO_2 retrievals, it is imperative to include more refined line-shape parameters such as the air and self speed dependence of the line

Table 3
The VP and SDV line-shape parametrization and their notation in HITRAN*online* and HAPI[a].

VP parameters[b]	Common notation	Symbol (units)	Database notation
Half-widths	γ_{air}	γ_{air} ($cm^{-1}atm^{-1}$)	gamma_air
	γ_{self}	γ_{self} ($cm^{-1}atm^{-1}$)	gamma_self
Temp. dep. half-widths	n_{air}	n_{air} (unitless)	n_air
	n_{self}	n_{self} (unitless)	n_self
Line shifts	δ_{air}	δ_{air} ($cm^{-1}atm^{-1}$)	delta_air
	δ_{self}	δ_{self} ($cm^{-1}atm^{-1}$)	delta_self
First-order line-mixing	Y_{air}	Y_{air} (cm^{-1})	Y_air
	Y_{self}	Y_{self} (cm^{-1})	Y_self
SDV parameters[b]	**Common notation**	**Symbol (units)**	**Database notation**
Half-widths	γ_0-air(SDV)	$\gamma_{SDV\_0\_air}$ ($cm^{-1}atm^{-1}$)	gamma_SDV_0_air_296
	γ_0-self(SDV)	$\gamma_{SDV\_0\_self}$ ($cm^{-1}atm^{-1}$)	gamma_SDV_0_self_296
Temp. dep. half-widths	n_{γ_0}-air(SDV)	n_{SDV_air} (unitless)	n_SDV_air_296
	n_{γ_0}-self(SDV)	n_{SDV_self} (unitless)	n_SDV_self_296
Speed dep. half-widths	γ_2-air(SDV)	$\gamma_{SDV\_2\_air}$ ($cm^{-1}atm^{-1}$)	gamma_SDV_2_air_296
	γ_2-self(SDV)	$\gamma_{SDV\_2\_self}$ ($cm^{-1}atm^{-1}$)	gamma_SDV_2_self_296
Temp. dep. speed dep.	n_{γ_2}-air(SDV)	$n_{\gamma_{SDV\_2\_air}}$ (unitless)	n_gamma_SDV_2_air_296
	n_{γ_2}-self(SDV)	$n_{\gamma_{SDV\_2\_self}}$ (unitless)	n_gamma_SDV_2_self_296
Line shifts	δ_0-air(SDV)	$\delta_{SDV\_0\_air}$ ($cm^{-1}atm^{-1}$)	delta_SDV_0_air_296
	δ_0-self(SDV)	$\delta_{SDV\_0\_self}$ ($cm^{-1}atm^{-1}$)	delta_SDV_0_self_296
First-order line-mixing	Y_{air}(SDV)	Y_{SDV_air} (cm^{-1})	Y_SDV_air_296
	Y_{self}(SDV)	Y_{SDV_self} (cm^{-1})	Y_SDV_self_296
Temp. dep. first-order	n_Y-air(SDV)	$n_{Y_{SDV\_air}}$ (unitless)	n_Y_SDV_air_296
line-mixing	n_Y-self(SDV)	$n_{Y_{SDV\_self}}$ (unitless)	n_Y_SDV_self_296

[a] The notations presented here are common notations often encountered in this paper (although sometimes they slightly differ, for instance (SDV) is dropped if there is a dedicated SDV section where parameter is presented), symbols/notation that users can select on HITRAN*online*, and "database notation" (referring to actual names of the parameters in the SQL structure). The latter are used by HAPI for instance to download a particular parameter.

[b] The speed dependence and the temperature dependence of the line shift parameters are not presented in this table because of the lack of accurate measurements for these parameters.

broadening and shift parameters together with their temperature dependences. The air-broadening parameters of CO_2 were determined from requantized classical molecular dynamics simulations (rCMDS) [174] using the SDV profile as presented in Table 1 of the supplemental files from Ref. [161] with adequate coverage of the rotational transitions and an extensive set of the required SDV parameters. The results were extrapolated using the Padé approximants and applied to all the bands of CO_2 for the air-broadening, air-speed dependence of width (γ_2-air), and their temperature dependences. Isotopic dependence of the broadening parameters was ignored and therefore the same approach was used for all 12 isotopologues. Comparison of the temperature dependence of the half-widths and the temperature dependence of the speed-dependent parameter in Ref. [161] revealed that the temperature exponents for γ_0 and γ_2 parameters were not the same. Using HAPI, the SDV parameters were checked by modeling the laboratory spectra, and the corresponding residuals (experiment-calculations) confirmed the validity of the parameters [161]. It is noteworthy that for verifying the parameters, we have also examined the measurements which were issued after the release of the Ref. [161] data and in general very good agreement was found between HITRAN2020 and these measurements. See for example Ref. [175].

For updating the self-broadening half-widths (γ_0-self) of CO_2 and the self speed dependence (γ_2-self) of CO_2 using the SDV profile originally, the measured self-broadening by Predoi-Cross et al. [176] and the self speed-dependence measured by Daneshvar et al. [177] were used in Ref. [161]. However, for the HITRAN2020 edition, the very recent high-accuracy measurements for several bands in the 1.6 μm region by Birk et al. [153] were used. These data potentially allow for assessing the vibrational dependence of the self-half-width parameters. Fig. 6 presents the self-broadening parameters as a function of m for different bands. The agreement between the measured self-broadening in Ref. [176] and the measured data by Birk et al. [153] for the 30013–00001 band is apparent. The measured self-broadening of Ref. [177] for the 21102–00001 band is also comparable with those of 30013–00001 band values.

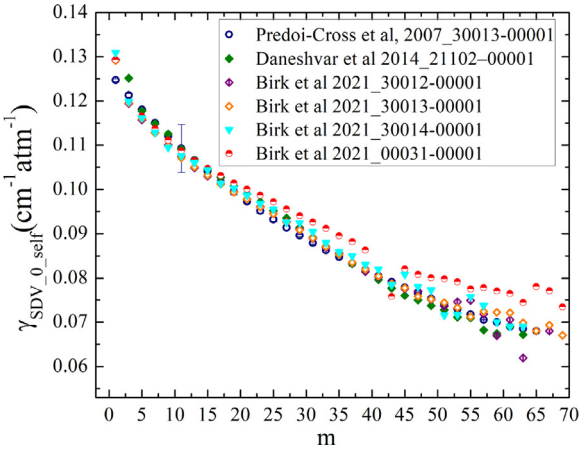

Fig. 6. The self-broadening parameters for CO_2 transitions at 296 K using the SDV profile. The values by Predoi-Cross et al. [176] are compared with the measurement of Ref. [177]. The Birk et al. [153] values are also presented for different bands.

Among the various bands measured in Ref. [153], for the 30011–00001, 30012–00001, 30013–00001, and 30014–00001 bands the vibrational dependence is principally smaller than 1%. However, several data fall outside of the regular pattern for the lines with $J > 30$ of the 00031–00001 band. An appreciable difference of about 10% for the self-broadening parameters, when comparing the 00031–00001 and 30013–00001 band lines, indicates the vibrational dependence of the self-widths. Therefore for HITRAN2020, the $3\nu_3$ band was treated separately, and for all other

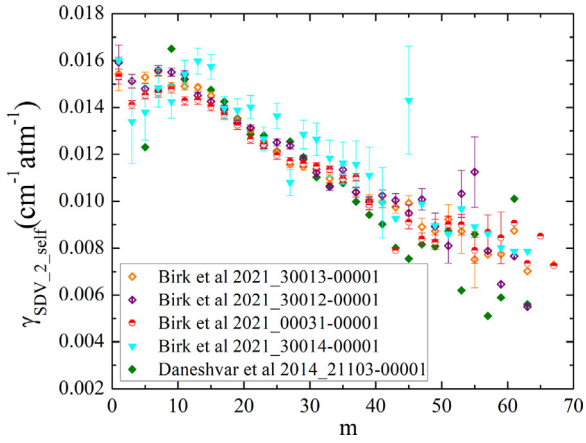

Fig. 7. The self speed-dependence of width parameters for CO_2 transitions at 296 K using the SDV profile. The measured values for different bands by Birk et al. [153] and Daneshvar et al. [177] are compared.

bands no vibrational dependence has been assumed at the moment and the 30013–00001 band results were used. The measured self-shifts of Ref. [153] were used to update the self-shifts for the measured bands and were also used to improve the prediction algorithm for the bands that were not measured.

Similarly, for updating the self speed-dependence of widths, the measured data of Ref. [153] were used to avoid mixing the data from different sources. Fig. 7 displays the γ_2-self parameters for different bands and, as can be seen after $m > 35$, the values deviate from each other. The Padé approximants (Eq. (1)) were used for extrapolating the 30013–00001 band results from Ref. [153] to all the bands except for the 00031–00001 band. After more high-quality experiments become available in various bands, it would be worth attempting to determine the vibrational dependence of the self-broadened half-widths, their temperature, and speed-dependencies.

2.2.9. *Updating the CO_2 line-mixing package*

The FORTRAN code by Lamouroux et al. [166] is used for predicting the line-mixing effect in all the bands of CO_2 either accounting for the full line-mixing (using the VP) or the first-order approximation (using the VP and SDV profiles). The update to the CO_2 line-mixing package is specified in Ref. [161] and the modifications to the line positions, intensities [134] and the relevant line-shape parameters [161] for the HITRAN2020 edition were addressed to update the package. Also, the partition functions were calculated employing TIPS2017 [178]. Moreover, the first-order line-mixing and its temperature dependence were implemented in HAPI to be taken into account with different line-shape profiles [52]. Based on the analyses performed using the measured laboratory spectra in Ref. [161], similar residuals were obtained when the transmission spectra were generated using i) the VP accounting for full line-mixing, and ii) the SDV modeled with first-order line-mixing. For instance, for the examined regions when only the P- and R-branch lines were present, the difference was on the order of 0.1% at 296K. Compared to HITRAN2016, an improvement of about 0.5% in the calculated residuals was achieved when using the new spectroscopic parameters and including line-mixing (implied by Fig. 13, 16, 18, and 19 of Ref. [161]).

For the purpose of atmospheric validation, the CO_2 line-mixing package was used to calculate the absorption coefficients (ABSCO-formatted tables) in the 4700–5100 cm^{-1} region corresponding to the so-called “strong band” in the OCO-2 mission. The ABSCO tables are produced using both Voigt profile accounting for the first-order and full line-mixing, and the speed-dependent Voigt including the first-order line-mixing which are available at Zenodo [179]. The preliminary ABSCO-formatted tables were tested by the OCO-2 science team through comparison of modeled spectra to TCCON measurements of atmospheric transmission and the results showed substantial improvement over those generated with HITRAN2016 as discussed in Ref. [180].

All of the verification investigations [161] confirmed that including the first-order line-mixing parameters is a quick method for calculating the cross-sections with a reasonable improvement in the residuals. Nevertheless, wherever the Q-branch lines are present, the first-order approximation fails to correctly model the spectra, and ultimately, it creates negative absorption coefficients. Therefore, for the more compact spectral regions, the application of full line-mixing is recommended. The current form of the line-mixing code does not support the formulation of the SDV profile accounting for the full line-mixing effect because of the complexity of the calculation. This issue will be studied for the forthcoming releases of the database. Furthermore, for future editions, we plan to add the HT profile [74] parameters to the database of carbon dioxide parameters, which will be valuable in enhancing the retrieval accuracy if the proper functional forms are adopted in the radiative transfer codes.

2.2.10. *Introducing water-vapor broadening parameters*

The predominant importance of water vapor in the terrestrial atmosphere, and its key role in the Earth's climate system, mean the water spectrum has been the subject of numerous studies. At the same time the collisional broadening effects introduced by water vapor on other molecules are required in order to accurately characterize and model spectra of the atmospheres with significant amounts of water vapor. Furthermore, the collisional broadening of spectral lines by water vapor is much larger than that by nitrogen and oxygen. Therefore, we introduced the pressure-broadening parameters including the temperature-dependent exponents due to water vapor in the HITRAN database through semi-empirical models based on the third- to fourth-order Padé approximants (Eq. (1)). The first part of this work was reported for the lines of CO_2, N_2O, CO, CH_4, O_2, NH_3, and H_2S [49].

The water-vapor broadening parameters (γ_{H_2O}) and their temperature dependence exponents (n_{H_2O}) for CO_2 transitions were determined using a semi-empirical approach by fitting accurate parameters to a Padé approximant. The collected data sets included early theoretical calculations from Rosenmann et al. [181,182] and the more recent experimental results from Sung et al. [183–185]. The fitted half-widths of water-vapor broadening are valid up to $J \leq 121$. The new Padé function approach is advantageous over extend the standard polynomial functions as it overcomes the convergence issues for high rotational J transitions, which can become significant at high temperatures. Meanwhile, the temperature-dependent exponents for water vapor broadening of CO_2 are also included in the updating water-vapor broadening parameter data sets.

2.3. O_3: *ozone (molecule 3)*

Ozone plays a crucial role in the chemistry of the terrestrial atmosphere. Its concentrations and vertical distribution are among key factors that drive the quality of human life on Earth, a protector from harmful UV radiation but also a pollutant. Not surprisingly, it is actively monitored by satellite [19,21,22,186], balloon [187,188], and ground-based spectrometers [189] operating from the MW to UV parts of the spectrum.

Although ozone was one of the first gases introduced into HITRAN, and there is no lack of laboratory measurements (see, for instance, the review by Barbe et al. [190]) or theoretical calculations, it remains one of the most challenging line lists in the database. In

particular, a major challenge is related to obtaining self-consistency in band intensities of ozone in various spectral intervals. This is mandatory to avoid discrepancies in the atmospheric ozone retrieval using different spectral windows. In this context, the previously available line-by-line compilations were not fully satisfactory, as shown by laboratory and atmospheric validations (see for instance, [191,192]).

The IR measurements of line intensities of ozone are very challenging. Usually, relative uncertainties in line intensities obtained via fits of observed spectra with effective spectroscopic models could be significantly smaller than the absolute uncertainties. This is because the dynamic range in line intensities is very large, making it necessary to use spectra obtained at different pressure/path length conditions in the fit. As ozone is an unstable species, the partial pressure conditions are difficult to control precisely, which is one of the main factors contributing to inconsistencies between absolute band intensities in different spectral intervals. Related issues for laboratory measurements have been discussed in Refs. [193–198] and references therein. Therefore simultaneous measurements in the MW or UV regions are usually carried out, because the intensities of low-J MW lines can be directly linked to the permanent dipole moment of the molecule, which is known very precisely. The UV standards were considered to be well-calibrated. Also, due to relatively small rotational constants, the IR spectra of ozone are quite congested. Consequently, only a restricted number of the non-blended lines could be accurately measured. Complete line lists for a given band system are typically produced by calculations using empirically-fitted parameters of the effective Hamiltonian (EH) and effective dipole transition moment (EDTM) parameters [190,199]. This implies the increase of uncertainties for extrapolated/interpolated ranges.

As described in the previous section devoted to carbon dioxide, modern *ab initio* calculations allow the determination of precise intensity values for many molecules, except for so-called "sensitive" bands or lines that for molecules like carbon dioxide are not very frequent. Unfortunately, for ozone, it is not always the case, and although a great many calculated intensities are of very good quality, the amount of lines where intensities can not be calculated reliably from first principles is quite large due to severe resonance perturbations, many of which are caused by the "dark" states [190]. Nevertheless, as will be shown below, *ab initio* calculations can be employed for many transitions or serve as a validation tool.

Ozone data in HITRAN2016 [16] weres a substantial improvement compared to previous editions in many spectral regions [76]. Following the release of HITRAN2016, Ref. [195] measured the MW and IR bands at 10 μm simultaneously and found an excellent consistency (better than 1%) between these bands when using HITRAN2016. Assuming that the intensities of the strongest lines in the pure rotational band should be known at a sub-percent level, Ref. [195] concluded that the intensities in the 10- μm band in HITRAN2016 are therefore also of excellent quality. However, Birk et al. [200] have shown that the MW intensities in HITRAN were too weak by ~3.8%, which in the context of the conclusions of Ref. [195] implies that the same scaling should apply to the 10-μm band. These findings have paved the way to an extensive international campaign for remeasuring and recalculating spectral parameters of ozone in all spectral regions from the MW to UV. Although not all of these works have been published, the new data have gone through intensive evaluation procedures, including comparisons with laboratory, ground-based, satellite, and balloon measurements. It was concluded that a combination of data from new laboratory and theoretical sources yield much better consistency of the intensities of ozone bands and also increase the quality of all parameters of individual lines. This is undoubtedly one of the highlights of HITRAN2020. Below we describe three sets of experimental and theoretical data in the IR region and how they were combined, based on the validations, to form the HITRAN2020 ozone line list. UV data are still only available in cross-sections, and that new dataset is described in Section 3.2.1.

2.3.1. New "S&MPO_2020d" line list

In December 2020, a new update for the S&MPO Reims-Tomsk line list (http://smpo.iao.ru, http://smpo.univ-reims.fr) [194] was made, featuring substantial changes in line intensities [201,202] and line positions [203] not only for the principal but also for minor isotopologues [204,205]. The line positions and lower-state energies in S&MPO are based on empirical Hamiltonian models, while the intensities are mostly empirical or semi-empirical, which in the new edition often includes corrections based on *ab initio* calculations.

2.3.1.1. $^{16}O^{16}O^{16}O$: ab initio intensity corrections and empirical line positions. Ab initio calculations of ozone have significantly advanced over the years, which enables one to improve the modeling of collisional processes [206,207] and of vibrational dynamics [208,209] using the PES [210] obtained at a high level of electronic structure theory. Recently, it was shown [201] that line intensity calculations by variational method from the *ab initio* dipole moment surfaces (DMS) of Tyuterev et al. [211] can help to resolve controversies among previously reported $^{16}O^{16}O^{16}O$ data sets in the MW, 5- and 10-μm ranges.

A comparison of results from Ref. [211] with very accurate FTS intensity measurements of Barbe et al. (GSMA, Reims) and preliminary data from Refs. [196,197] in the 5- and 10-μm ranges and with Stark-effect data in the MW [212] have shown an average agreement within 0.3–1.0% for strong lines between *ab initio* theory and these experiments. The tight scatter in these results made it evident that the HITRAN2016 intensities must be increased by 2.5% to 4.5% in the corresponding regions. This was also consistent with the results reported in Refs. [195,198,200]. For the 2020 update of the S&MPO line list (and ultimately HITRAN2020 in selected spectral regions), we have extended *ab initio* intensity corrections for 31 bands including 14 cold and 17 hot bands in the range from 0 to 4300 cm^{-1} using the DMS from Ref. [211]. The corresponding details of calculations are described in the dedicated publication by Tyuterev et al. [202] in this special issue. The summary of changes in line intensities between S&MPO_2020d and HITRAN2016 is shown in Fig. 8.

The target accuracy of line intensities for unstable species like ozone is currently considered as being within 1% for strong and

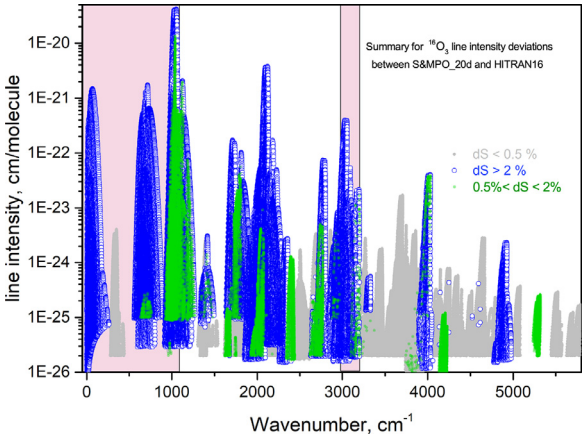

Fig. 8. Summary for the line intensity deviations. $dS = [S(\text{S\&MPO\_20d}) - S(\text{HITRAN2016})]/S(\text{HITRAN2016})$ in % for the ozone $^{16}O_3$ transitions in the 0–5791 cm^{-1} range. Most of changes with $dS > 2\%$ correspond to the *ab initio* intensity correction as described in Ref. [202]. Shaded areas correspond to the spectral regions where S&MPO_20d was not used for the HITRAN2020 ozone database.

Table 4
New (with respect to HITRAN2016) bands added to HITRAN2020 adapted from S&MPO_20d for the principle isotopologue of ozone in "natural" abundance. Minimum and maximum wavenumbers ν_{min} and ν_{max}, number of lines N and sum of line intensities within individual bands S_ν.

v'	v''	ν_{min}, cm^{-1}	ν_{max}, cm^{-1}	N	S_ν, cm/mol
2 2 0	0 2 1	1139.984	1187.006	164	4.218E-24
3 0 0	0 0 2	1155.052	1208.551	12	2.628E-25
2 2 0	1 1 0	1761.375	1817.097	92	3.032E-24
2 0 2	0 0 2	1994.841	2105.185	82	2.899E-24
2 0 2	0 3 0	2011.499	2043.890	2	4.439E-26
2 3 0	2 0 0	2015.029	2062.849	5	1.524E-25
0 5 0	0 2 0	2020.866	2073.526	4	6.219E-25
3 0 1	1 0 1	2154.827	2159.443	6	1.271E-25
0 2 2	0 0 1	2320.650	2365.711	191	2.514E-24
1 2 1	0 0 1	2423.376	2435.536	29	4.182E-25
2 2 0	1 0 0	2476.903	2484.720	15	1.717E-25
0 5 0	0 1 0	2718.726	2771.609	4	6.880E-25
2 2 0	0 1 0	2794.977	2922.083	488	2.933E-23
0 5 0	0 0 0	3419.165	3472.267	4	2.591E-25
3 0 2	0 0 1	4069.803	4143.464	905	5.364E-23
3 0 2	1 0 0	4109.876	4143.008	3	3.816E-26

about 3 or 5% for weak transitions. At this level of accuracy, the best *ab initio* calculations can be competitive with precise experimental measurements [201]. However, it is well known that *ab initio* calculations for multi-electron molecules are not able to achieve experimental high-resolution accuracy in line positions (0.001–0.0001 cm^{-1}) because this corresponds to relative precision requirements in wavenumbers of 10^{-7} or 10^{-8}. In a previous release of the S&MPO database [194], the line positions were computed from empirically-fitted EH parameters except for the cases where effective models do not provide experimental accuracy because of the large number of strongly coupled bands and "dark states" perturbations [190]. Empirical corrections to line positions and energy levels must then be accounted for. Detailed explanations on the improvements in the line positions are provided in Ref. [203] and only brief summary is provided here. Part of these changes corresponded to a simple update of old EH parameters from the previous S&MPO releases by more recent ones: this concerns MW and ν_2 ranges, as well as the 4000 cm^{-1} range [213].

Furthermore, a new list including both line positions and intensities was generated for the strongest ν_1/ν_3 bands using EH and EDTM parameters [203] obtained from the analyses of GSMA/Reims spectra at 10 μm. In particular, the line positions with large ($K_a > 20$) rotational quantum numbers were improved for the ν_3 band. The third type of change concerns empirical corrections of line positions near 2700 cm^{-1} and in the 2900–5500 cm^{-1} range. Following the recent analysis of Ref. [213], the most significant corrections concern the complex band system (103)/(004)/(310)–(000) near 4000 cm^{-1} and in the corresponding hot bands. Some other corrections concern "exotic" accidental resonance perturbations like those involving the (040) and (050) states. Note that a line position correction in one range resulted in many more "induced" corrections in other ranges via the shifts in energy levels. Finally, a limited number of line intensities were empirically adjusted, particularly in the ranges near 3000 cm^{-1} and 5000 cm^{-1} [203]. Overall, in the spectral range of 0–5791 cm^{-1}, the S&MPO_20d list contains 312,669 lines. There are 25 newly generated weak hot bands in that list, 16 of which (above 1180 cm^{-1}) were adapted to HITRAN2020. A summary of these 16 bands is presented in Table 4. A global Table including band statistics for all the bands versus HITRAN2016 is given in the Supplementary Materials.

A summary of line position corrections and new lines is given in Fig. 9. A detailed description will be presented in a dedicated publication in this special issue [203].

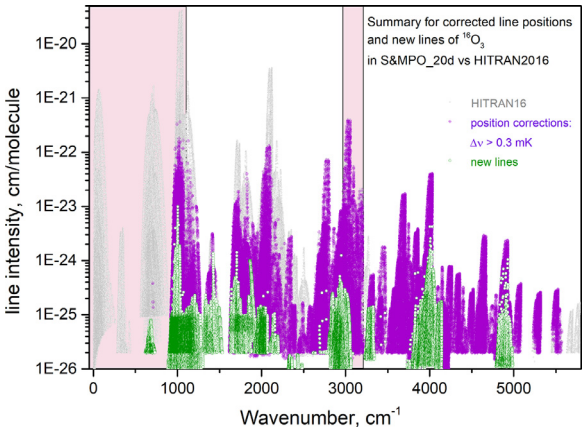

Fig. 9. Summary for newly added (with respect to HITRAN2016) hot bands (in green) and line position corrections [203] for HITRAN2020. The transitions for the $^{16}O_3$ ozone in the 0–5791 cm^{-1} range corrected by more than $d\nu = \nu$(S&MPO_20d) $- \nu$(HITRAN2016) > 0.0003 cm^{-1} are indicated in magenta. Shaded areas correspond to the spectral regions where S&MPO_20d was not used for the HITRAN2020 ozone database.

An example of an improvement for the transmittance calculation near 4000 cm^{-1} using the S&MPO_20d (and hence HITRAN2020 in this region) list including recent results of analysis [213] with the subsequent *ab initio* corrections for intensities [202] is given in Fig. 10.

It is instructive to compare the S&MPO_20d line list with other recent data based on accurate laboratory intensity measurements. Tables 5 and 6 show an excellent agreement for RMS and mean deviations in line-by-line intensities with the DLR list described in Section 2.3.2 in the 10-μm range. On the full sample of the common lines of these lists, the sum of intensities S_ν gives very close values with a deviation of only 0.07% for the strongest ozone band ν_3 and of 0.25% for ν_1 (see Table 5). A systematic offset is almost negligible – between 0.1% and 0.2% for the mean intensity values. For the strong and medium lines, the RMS deviation is significantly smaller for the dominant band ν_3 within about 0.25% (Fig. 11). The deviation increases to an RMS of 0.5% when extending to medium lines including the sample of 1000 transitions (see Table 6). As expected, the scatter increases for weak lines, though many of these weak lines have not been experimentally measured and rely on extrapolations.

Another accurate set of intensities in the 5=and 10μm ranges have been recently obtained in Refs. [196,197]. Preliminary comparison between the *ab initio* and empirical list fitted to LERMA spec-

Table 5
Comparison of integrated intensities for the cold bands in the 10 μm range between S&MPO_20d and DLR line lists for the principle isotopologue, for the common sample of transitions.

Band	N	ν_{min}	ν_{max}	S&MPO S_ν	DLR S_ν	$\Delta(S_\nu)$
ν_3	6212	980.042	1219.990	1.398E-17	1.397E-17	0.07 %
ν_1	5991	980.126	1219.838	5.287E-19	5.274E-19	0.25 %

Table 6
Comparison of RMS and mean intensity deviations between S&MPO_20d and DLR $^{16}O_3$ line lists for strong lines of the ν_1 and ν_3 bands

Band	N	S_{min}	S_{max}	RMS(S), %	Mean(S), %
ν_3	500	9.4E-21	4.2E-20	0.24	0.08
	1000	2.0E-21	4.2E-20	0.50	0.15
ν_1	500	3.0E-22	3.4E-21	0.60	0.23
	1000	1.6E-22	3.4E-21	0.88	0.13

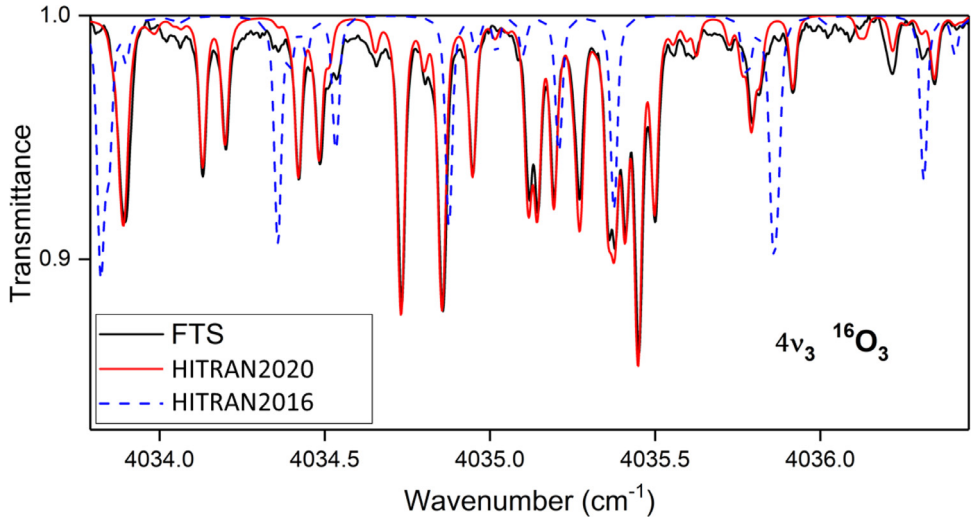

Fig. 10. Example of an improvement of the line list of ozone when compared to the experimental FTS laboratory spectra. It is clear that S&MPO_20d (hence HITRAN2020 in this region) line list in the range of the $4\nu_3$ band is superior to that from HITRAN2016.

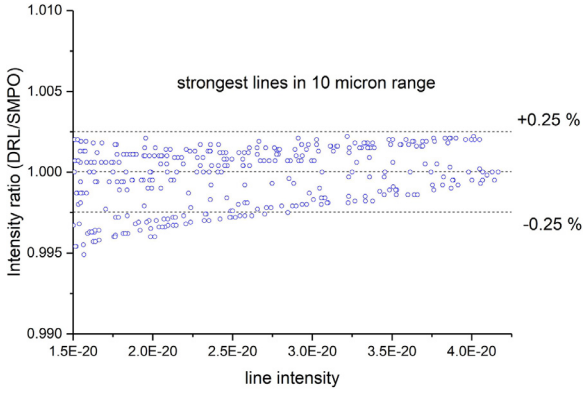

Fig. 11. Ratio of intensities S(DLR)/S(S&MPO_20d) for the strongest lines in the 10-μm range. Note that the DLR data are used in HITRAN2020 in this spectral region.

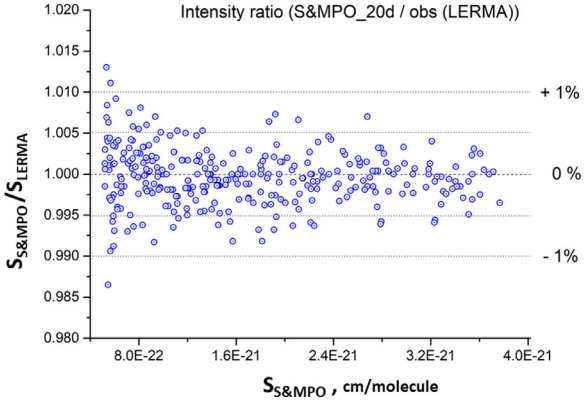

Fig. 12. Ratio of intensities S(S&MPO_20d) / S(LERMA_obs) for the strongest lines in the 5-μm range. Note that the S&MPO data are used in HITRAN2020 in this spectral region.

tra [197] was reported in Ref. [201] where only 50 of the strongest transitions were included. Table 7 summarizes the results of an extended statistical comparison with a complete set of experimental lines determined by Jacquemart et al. [197] from LERMA spectra using a speed-dependent line profile. The comparison for individual strong lines is shown in Fig. 12. Excellent agreement is obvious from these comparisons.

Interestingly, on the common sample of measured lines, the LERMA(obs) gives almost exactly the same ratio $S_\nu(10\,\mu m)/S_\nu(5\,\mu m)$ as the S&MPO_20d line list testifying to a perfect intensity consistency of the two data sets between these spectral ranges, which are of primary importance for atmospheric applications.

Table 7
Comparison of RMS, mean and integrated deviations for line intensities between the S&MPO_20d list and experimental values from LERMA [197] in the 10- and 5- μm ranges for (^{16}O3)

Range	Bands	N	$\Delta(S_\nu)^a$	RMS(S)	Mean (S)
10 μm	ν_3, ν_1, $\nu_2+\nu_3-\nu_2$	497	0.28 %	0.78%	0.26%
5 μm	$\nu_1+\nu_3$, $2\nu_3$	319	-0.04%	0.37%	-0.02%

[a]relative deviations of sums of all line intensities for the range

2.3.1.2. $^{16}O^{16}O^{18}O$ isotopologue. About thirty ozone spectra enriched with ^{18}O were recorded with the GSMA FTS spectrometer using different cell lengths, ^{18}O/^{16}O oxygen isotopic mixtures, and different pressures varying from 4 to 20 Torr. The analyses of the spectra in the range between 900 and 3850 cm^{-1} allowed Ref. [205] to extend substantially the information about ro-vibrational transitions and energy levels of the $^{16}O^{16}O^{18}O$ isotopologue, belonging to the C_s point group. The assignment and modeling have been carried out using EH and EDTM operators with the help of theoretical predictions of the band centers, rotational constants and some coupling parameters. The latter ones have been derived from an *ab initio* potential energy surface (PES) [210] using the MOL_CT code [214] in the standard format of the EH [194,215] of the S&MPO system. We fixed the coupling term values to the predicted ones for the complete polyads of observed bands below 2500 cm^{-1} to characterize the intensity transfer among the observed bands. Above 2500 cm^{-1}, our effective models include only those coupling terms, which correspond to the observed perturbations. In total, 9976 ro-vibrational transitions belonging to the 15 bands of $^{16}O^{16}O^{18}O$ were assigned and modeled with average accuracy of the order of 10^{-3} cm^{-1}. The set of 7030 corresponding upper-state ro-vibrational energy levels were determined. Overall a line list of 49,148 transitions is provided for the HITRAN2020 database for 13 observed bands of $^{16}O^{16}O^{18}O$

Table 8
HITRAN2020 ozone update summary: isotopologues $^{16}O^{16}O^{18}O$, $^{16}O^{16}O^{17}O$ and $^{16}O^{17}O^{16}O$

Isotopologue	Band	N	Region, cm^{-1}	S_ν, cm·mol^{-1}
$^{16}O^{16}O^{18}O$	001-000	3694	961.88–1117.65	5.122E-20
	100-000	7216	973.69–1187.47	4.017E-21
	020-000	505	1342.89–1398.80	7.706E-25
	011-000	2474	1644.36–1720.54	2.033E-22
	110-000	4188	1663.38–1894.67	6.376E-23
	002-000	8149	1897.41–2113.39	6.941E-22
	101-000	3468	2017.37–2113.59	3.889E-21
	200-000	8635	2063.76–2274.12	2.354E-22
	111-000	1910	2701.72–2767.50	9.528E-23
	111-010	2166	2015.15–2084.74	3.835E-27
	003-000	1562	2930.52–3011.53	4.316E-22
	102-000	3241	2965.77–3123.18	1.221E-22
	201-000	1940	3103.03–3164.88	3.782E-23
	Total	49148	961.88–3164.88	6.101E-20
$^{16}O^{16}O^{17}O$	101-000	2135	2045.82–2121.62	6.078E-22
$^{16}O^{17}O^{16}O$	001-000	1157	968.30–1054.70	4.857E-21
	100-000	107	1082.60–1124.24	3.571E-23
	101-000	820	2029.66–2101.31	2.674E-22
	Total	2084	968.30–2101.31	5.160E-21

up to $\Delta\nu = 3$. The corresponding information is summarized in Table 8.

2.3.1.3. $^{16}O^{16}O^{17}O$ and $^{16}O^{17}O^{16}O$ isotopologues. The 5- and 10-μm ranges of the ^{17}O-substituted ozone isotopologue were reinvestigated using GSMA Fourier spectra. The line positions for 15 transitions in the ν_3 band in HITRAN2016 data for the $^{16}O^{17}O^{16}O$ isotopomer were shifted by an order of 10^{-3} cm^{-1} with respect to the experimental spectrum. The spectral line parameters for this isotopic species have been available in the HITRAN database for almost two decades: the ν_1 and ν_3 bands from Ref. [216] and $\nu_1 + \nu_3$ from Ref. [217]. In these calculations, different parameters for the ground state have been used. In Ref. [204], the ν_1, ν_3 and $\nu_1 + \nu_3$ bands of the $^{16}O^{17}O^{16}O$ isotopomer were modeled simultaneously to improve the parameters of the ground state energy level. The analysis of the $\nu_1 + \nu_3$ bands of $^{16}O^{16}O^{17}O$ was also extended. The parameters allowed for the generation of new line lists in the corresponding spectral ranges (see Table 8).

2.3.2. O_3 *DLR database*

New mid-infrared ozone measurements in the range 600–1200 cm^{-1} were carried out within the framework of the ESA project SEOM-IAS, ESA/AO/1-7566/13/I-BG. A detailed publication is in preparation [198]. The goal of this task was to resolve discrepancies in retrieved atmospheric ozone amount between observations in the mid-infrared (MIR) and ultraviolet (UV). An important output of this effort is the new data described in this section and in the section on UV absorption cross-sections for O_3 (see Section 3.2.1).

The new FTS transmittance measurements were carried out with a Bruker IFS 125 HR high resolution spectrometer in combination with a coolable four-window single-pass cell [218] of pathlength 22.15 cm which was also used for the UV measurements utilizing a different window pair. The same four-window cell was used under reproducible conditions for both the UV and MIR measurements, and absorption spectra were recorded under sealed-off conditions. Ozone was prepared from O_2 in a silent discharge and purified and handled using procedures similar to those given in Ref. [219]. Because decomposition of ozone was negligible at the low temperatures considered, the sample number densities could be derived from absolute pressure and temperature measurements. The new measurements were recorded with high-column amounts and different temperatures (23 mbar at 293 K, 11 mbar at 234 K). These measurements were combined with four previously published ambient temperature measurements [219] with lower column amount, which were complementary to the new measurements. The availability of a new multi-spectrum fitting tool (see Ref. [66] and reference cited therein) motivated re-analysis of the previous measurements and yielded improved results, especially when combined with the new measurements.

Four N_2-broadened and three O_2-broadened ozone measurements at ambient temperature from Ref. [219] were re-analyzed with the multi-spectrum fitting tool, also yielding air-broadening and shift parameters.

2.3.2.1. Self-broadened spectra. The primary goal of the line fitting was new line positions and intensities of the main isotopologue. The analysis has shown that for this purpose self-broadening and self speed-dependence have to be considered. All self-broadened spectra were analyzed simultaneously using multi-spectrum fitting. The initial guess was HITRAN2016. The measurements were individually frequency-calibrated against HITRAN2012 ozone line positions. Lines were fitted in the intensity range 1.0×10^{-23} to 4.0×10^{-20} cm/molecule with statistical line intensity uncertainties $<$10% for the weakest lines. The weaker lines are especially important for limb-sounding space instruments measuring ozone. An EH approach was applied to fit line positions and intensities of the fundamentals ν_1 and ν_3 simultaneously. Hot bands in the ν_3 region were also considered in the intensity analysis. Using the parameters from this analysis, the line positions and intensities were calculated, avoiding extrapolation. The calculated data were used to replace the HITRAN2016 values. In the case of ν_2, a scalar (1.014) was fitted to match HITRAN2016 intensities to the experimental ones. All ν_2 intensities were replaced by scaled HITRAN2016 values. Experimental line positions for hot bands in the ν_3 region were used in the database for isolated lines when the line intensity statistical error was less than 10% and the difference to the HITRAN2016 line position was less than 0.02 cm^{-1}. In the case of the most abundant isotopologue, and lines in the ν_3/ν_1 region where no predictions from the EH were available, the intensities were scaled by (1.023+1.017)/2. The two values were obtained by weighted fitting of the experimental line intensities against HITRAN for the ν_1 and ν_3 bands.

Data are given for three different regions: 700–800 cm^{-1} (ν_2), 980–1070 cm^{-1} (mainly ν_3), 1070–1180 cm^{-1} (mainly ν_1). Line positions and intensities of ozone isotopologues were fitted but not used for the final database. The isotopologue abundance differs from the natural abundance by more than 10% due to the kinetics in the ozone production in the silent discharge. Therefore, no reliable line intensities were available from the line fitting.

Previous sections already implied an excellent agreement of both DLR and Janssen et al. [196,197] with S&MPO data, and there is naturally an excellent agreement between these two experimental datasets. It should be noted that the DLR experimental data contain lines up to 100 times weaker than those of Janssen et al.

The measurement and line parameter databases can be downloaded from Ref. [220].

2.3.2.2. N_2- and O_2-broadened spectra. Ambient temperature N_2- and O_2-broadened spectra were presented and analyzed in Ref. [219]. The air-broadened values were taken from polynomial representations and the resulting air-broadening parameters are given in the editions HITRAN2004 (and with some corrections in HITRAN2008) through HITRAN2016. These measurements had considerable self-broadening contributions. The new measurements at high ozone pressure together with the old pure ozone measurements allowed for the determination of the self-broadening parameters to be more accurate than in the old analysis. The multi-spectrum fitting was thus applied for the N_2- and O_2-broadened

measurements using the new self-broadening data to determine N_2- and O_2-broadening parameters on an individual line basis. In case of the weaker ν_1 and ν_2 bands, the data were too noisy but still confirmed the validity of the polynomials mentioned above. For the stronger ν_3 band, more accurate values are available. As in Ref. [219], a simple Voigt profile was used, neglecting speed dependence. Air-broadening parameters were calculated for the strong lines in the ν_3 region when the statistical uncertainty for the N_2- and O_2-broadening parameter was better than 4% and 8%, respectively.

N_2- and O_2-pressure shifts were obtained for several lines in the ν_3 region. Since absolute frequencies were not available, the shifts were calibrated with the accurate shifts of two lines determined by Minissale et al. [221]. Among the eight lines where Minissale et al. determined air-pressure shifts, two were also available in the DLR data set with sufficient precision. The calibration is accurate to 0.00024 cm^{-1}/atm. A second-order polynomial in $\gamma_{0,air}$ was found to be a reasonable representation of the shifts. In the case where the N_2- and O_2-pressure shifts both had smaller statistical uncertainties than 0.001 cm^{-1}/atm, their resulting air shift was added into the database. For all other transitions in the ν_3 fundamental, the value calculated from the polynomial was entered.

2.3.2.3. Error considerations. Line position accuracy is the same as for HITRAN2012 through HITRAN2016 given for most lines (10^{-4}–10^{-3} cm^{-1}). For line intensity, several error sources have to be considered: number density, absorption path, temperature, instrumental line shape, line model, EH approach. The excellent agreement with Janssen et al. data validates overall accuracy <1% for at least the stronger lines. Definitely, the integrated band intensities have accuracies <1% too. From comparison of experimental and predicted line intensities, it was assumed that for lines with intensities $>3\times10^{-23}$ the error was <1%. Since the ν_2 band has no Coriolis perturbation in contrast to the ν_1/ν_3 pair, the relative intensities in the ν_2 band in HITRAN2016 should be better than 1% for lines $>3\times10^{-23}$. All new EH approach predictions in the ν_1/ν_3 band $<3\times10^{-23}$, and the ν_2 HITRAN2016 intensities $<3,\times10^{-23}$ were assigned 1–2% errors. For all other lines in the ν_1/ν_3 region, which are scaled HITRAN2016, the error was set to 2–5%.

The error for $\gamma_{0,air}$ in HITRAN2016 for lines based on the polynomial representation of Ref. [219] was 2–5%. The same error was given for the new data. It should be noted that this error bar is quite conservative and includes statistical and systematic uncertainties. Due to ignoring speed dependence, the broadening could be systematically too small by ~2%.

For all lines in the ν_3 band, where the air shift was updated, an error of 10^{-4} to 10^{-3} cm^{-1}/atm was estimated.

2.3.3. O_3 *UCL line intensities*

A synthetic line list calculated at University College London (UCL) for the principle isotopologue of ozone has been recently presented in Ref. [222]. Variational calculation using a semi-empirical PES [223] and *ab initio* DMS [211] produced very accurate values for the line intensities for the intense cold bands ν_1 and $\nu_1 + \nu_3$ as compared to recent measurements performed in LERMA [196,197], respectively, at 10 and 5 μm. However, variational line positions are far away from their experimental values and complete assignment of rotational and vibrational quantum numbers are missing from the variationally calculated line list. Corrections for intensities distorted by resonances in the variational calculation with *ab initio* DMS due to the artificial intensity stealing has been developed and applied [222]. When resonances occur between levels, the distribution of the line intensities between the transitions involving the resonant levels is often incorrectly represented in variational calculations [115], but the sum of intensities is correct. As a consequence, based on the sum of variationally calculated intensities, the distribution has been corrected using the intensity distribution from HITRAN2016 for the transitions involved.

In the work of Ref. [222], the complementary nature of EH models used in HITRAN2016 [16] (with full vibrational and rotational assignment and accurate line positions) and variational calculated intensities has been used to generate a line list between 0 and 4930 cm^{-1} for the main isotopologue. Only transitions with an intensity cutoff of 10^{-24} cm/molecule at 296 K and with J values below 60 have been generated. Note that for 5% of the transitions generated for the line list (77,819 total transitions), the variationally-calculated intensities were corrected using the intensity distribution from HITRAN2016.

As already noted, the variationally-calculated line intensities have been found to be in very good agreement with recent measurements [196,197] at 10 and 5 μm: sub-percent average discrepancies (as well as sub-percent standard deviation associated with the averages values) are reached for the ν_1 and $\nu_1 + \nu_3$ bands for 476 and 316 common transitions respectively. The whole comparison file is available as supplemental data to Ref. [222]. An interesting case has been noticed concerning the $2\nu_1$–ν_3 band in the 10-μm region. Indeed for this band, the average deviation between variational and HITRAN2016 intensities reaches 28% whereas recent measurements from Birk et al. [220] leads to intensities in better agreement with the variational calculation (average deviation 5.2%). In this region HITRAN2016 is based on the EH model from Flaud et al. [224] constructed when no measurements were available for this band. When accounting for the recent measurements by Birk et al. [220] in an EH model, the average discrepancy between the variationally calculated intensities and the EH calculated intensities from Flaud [225] (that were ultimately employed in HITRAN2020) is 3.3% (with a standard deviation of 2.1%). The $2\nu_1$–ν_3 band provides another example that variationally-calculated intensities could provide a better alternative for the bands where no reliable experimental or semi-empirical information exists.

In order to be tested against atmospheric validations, a HITRAN2016 type line list has been generated where HITRAN2016 line intensities were replaced by the variationally calculated ones (eventually corrected as discussed in Ref. [222]) for transitions presented in Ref. [222].

2.3.4. O_3 *atmospheric validations and choices for* HITRAN*2020*

The three line lists presented above were rigorously validated against laboratory, TCCON, and balloon spectra by Toon [226]. The quality was assessed based on minimal RMS in selected spectral windows and consistency of the amount of ozone from window to window. It is important to stress again that not only intensities are different in the new line lists. With respect to HITRAN2016, the S&MPO line list contains new bands, updated line positions and intensities for four isotopologues, including the principal isotopologue; however line-shape parameters are the same as in HITRAN2016. It is the most complete list and yields the most consistent retrieved amount of ozone over all spectral windows. It is therefore used as a base line list for HITRAN2020, with parts of it being replaced, where appropriate, with other line lists based on the atmospheric validations. The DLR line list contains new line positions, intensities and line-shape parameters; however the isotopologue information is that from HITRAN2016. The UCL line list contains only new intensity information. It was found that in overlapping spectral ranges in most cases all three line lists supersede the HITRAN2016 line list in quality. An exception is only the region of the ν_2 fundamental, where the intensities in the S&MPO and UCL line lists seem to be inferior to those in HITRAN2016 and especially the DLR line list. Based on the validations presented in Ref. [226] and findings in Ref. [200], the following wavenumber-

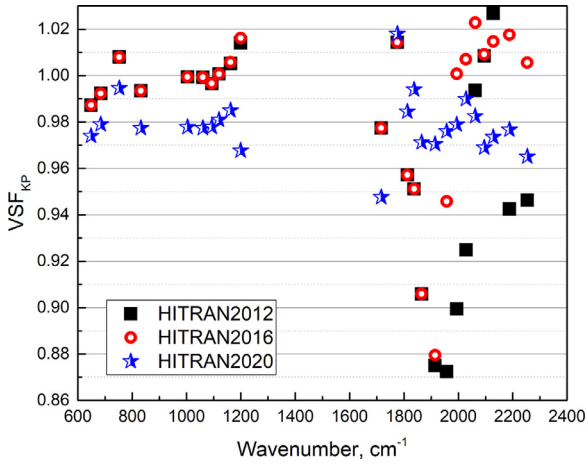

Fig. 13. Volume mixing ratio scaling factors (VSF) obtained in different IR spectral windows from the analyses of the FTS spectra from Kitt Peak laboratory. The absolute values are not definitive as it is hard to control the partial pressure of ozone in the cell. Note the much improved consistency of the retrieved amount of ozone in 5 and 10 μm regions.

dependent selections have been made for the MW-IR transitions of ozone:

1. In the region of pure rotational transitions of all HITRAN isotopologues of ozone, the values from the JPL catalogue [227] were chosen. To take advantage of increased precision of MW transitions, it should be noted that the wavenumber format for ozone in the traditional ".par" format has been updated to F12.9 for transitions below 1.0 cm^{-1}, F12.8 for transitions 1.0–10.0 cm^{-1}, and F12.7 for transitions 10.0–100.0 cm^{-1} (as previously implemented for HNO_3, PH_3, O_2 and NO^+).
2. Between 280 and 600 cm^{-1} the HITRAN2016 line list is retained for HITRAN2020.
3. Between 600 and 1180 cm^{-1} the DLR line list is used.
4. Above 1180 cm^{-1} and up to 5791 cm^{-1} the new S&MPO line list is used except for the 2975–3205 cm^{-1} region, where the RMS of the UCL line list are the lowest. Therefore in that window the UCL line list is used. However, one should be aware that the retrieved amount of ozone with the latter list is noticeably lower compared to other regions.
5. Above 5791 cm^{-1} the HITRAN2016 line list is retained for HITRAN2020.

Fig. 13 demonstrates the improved consistency in the ozone amounts retrieved from the Kitt Peak laboratory spectra in the 5- and 10-μm regions.

2.4. N_2O: *nitrous oxide (molecule 4)*

Due to its prominent presence in the terrestrial atmosphere, nitrous oxide (N_2O) has been the subject of many spectroscopic studies in different spectral ranges, enabling the remote-sensing measurements of N_2O concentrations. In HITRAN2020, intensities of the NIR bands have been updated, while a complete overhaul of the line-shape parameters has been carried out.

2.4.1. N_2O *intensities in NIR*

An update to the near-infrared N_2O line intensities has been performed based upon recent frequency-agile, rapid-scanning cavity ring-down spectroscopy measurements of the 4200–0000 and 5000–0000 bands near 1.6 μm [228]. A band-wide fit of these measurements has allowed for the range of $|m|$ included for these bands to be increased from $|m| \leq 46$ to $|m| \leq 85$. Furthermore, these measurements led to combined standard uncertainties near 1%, which is roughly a factor of five lower than the values found in HITRAN2016 [16], which were based on measurements from Toth [229]. We note that these new measurements (and hence HITRAN2020 intensity values for these bands) are roughly 5% greater than the values found in HITRAN2016 [16]. With that being said, good agreement was observed with the Fourier-transform spectroscopy measurements of Daumont et al. [230].

2.4.2. N_2O *line shapes*

In the description of the atmospheric retrievals by ACE-FTS (Atmospheric Chemistry Experiment–Fourier transform spectrometer), Boone et al. [231] have stressed the need for a revision of line-shape parameters for certain bands in HITRAN and the importance of including the non-Voigt parameters. This issue has been attended in the 2020 edition of the database, where we updated the N_2O-air and N_2O-N_2O line-shape parameters using the Voigt and speed-dependent Voigt parameters, including the first-order line-mixing parameters [232] as presented in Table 3 of Section 2.2.

In updating the line-shape parameters of N_2O, we used the approach similar to the one used for updating the line-shape parameters of CO_2. This approach enabled providing both Voigt and the speed-dependent Voigt parameters (including first order line-mixing) for each transition (see Ref. [233] for more details).

The air- and self-broadening parameters (using VP), their temperature dependence, and the pressure shifts of N_2O in the HITRAN2016 database were based on the earlier studies from Refs. [234–237]. The vibrational dependence of the line widths was assumed negligible. The parameters were revised based on the recent high-quality experimental data from Adkins et al. [228]. The new NIST spectroscopic parameters were measured in the near-IR region for the 4200–0000 and 5000–0000 bands obtained using their Multi-spectrum Analysis Tool for Spectroscopy (MATS) [238] using the line-shape functions defined in HAPI. The non-measured transitions were given an approximated value, estimated from the results reported in Ref. [233], where the Padé approximant functions (Eq. (1)) were applied as a smoothing function over the measured transitions and extrapolated to the higher J lines in all the bands. The reported error codes for the measured lines correspond to the combined error type A (statistical) and B (systematic) error in the measurement. The temperature exponents of the air-broadening parameters were also updated using the Padé approximants fit to the data from Ref. [236]. For the self-broadening (VP) parameters, there were not many measurements of N_2O available in the literature. In HITRAN2016, these values were produced from the study by Toth [235]. For HITRAN2020, a fit of the recent measurement of γ_0-self half-widths by Werwein et al. [239] for the 0002–0000 band was used to extrapolate the results for all the transitions in all the bands [233].

The speed-dependent parameters were not provided in HITRAN2016 except for the ν_3 band of N_2O-air [240], which were obtained from a multi-spectrum fit of FTS measurements. Note that these parameters were present under the HT profile parametrization in the HITRAN2016 edition. We used the air-broadened parameters measured by NIST [228] for the 5000–0000 band and expanded them for all the bands except for the ν_3 band, where the data from Ref. [240] were used for updating the air-broadening, air speed-dependence of width, air-shift, and the first-order line-mixing parameter for the measured transitions. Based on the uncertainties of the parameters reported by NIST, in smoothing the collisional air-broadening (for the SDV) and air-speed-dependence, only data with $|m| \leq 40$ were included in the fit. For the temperature dependence of the air-broadening, we used Ref. [233] data to produce the temperature exponent for the SDV line widths. Also, in the the absence of the measurement of the temperature exponent of γ_2 (i.e., n_{γ_2}), the predicted ones for the the half-width parameters were used.

With a similar fitting approach, we produced the results for the γ_0-self and γ_2-self (for the SDV profile) parameters based on the high-accuracy measured self-broadening using a diode laser spectrometer in Ref. [241] for eight transitions in the $3\nu_1 + 2\nu_2$ band, acquired at room-temperature. In Ref. [233], it is described how the γ_0-self and γ_2-self were generated for the lines where these parameters were not measured.

We used the method proposed by Hartmann [173], which was successfully tested for the CO_2-air and CO_2-CO_2 systems [161], to calculate the pressure shifts of the transitions of air- and self-broadened N_2O bands. Because there were not many measurements available for educating the model with the SDV and VP shifts for different bands, we used the same air- and self-shifts for the VP and SDV profiles to populate the database. The fitting coefficients were presented in Ref. [233]. >

The first-order line-mixing parameters of the N_2O lines were calculated using the Exponential Power Gap law (EPG) approximation [242] explained in Ref. [233] and provided for every transition in HITRAN separately for the VP and SDV profiles for N_2O broadened by air and N_2O [233]. It should be noted that the line-shape parameters were not updated for the $^{14}N_2^{18}O$ isotopologue in the HITRAN2020 line list because of the ambiguities in assignments for some of the NIR bands discussed in the HITRAN2016 paper.

HAPI was used to validate the results against the laboratory spectra. By taking into account the line-mixing effect, the absorption coefficient for the mixture of N_2O-air at specific temperature T and pressure P was obtained. Using the new NIST parameters led to improvements in calculating the spectra both for the VP and SDV profiles as shown in Ref. [233].

Finally, every transition of N_2O now has γ_{H_2O} and n_{H_2O} parameters as described in Ref. [49].

2.4.3. N_2O *in HITEMP*

The addition of N_2O to HITEMP is described in Ref. [55]. This N_2O line list was based on the Nitrous Oxide Spectroscopic Data Bank at 1000 K (NOSD-1000) [243]. Comparisons to PNNL spectra [244] in the region of the 1000–0110 band of $^{14}N_2O$ required a correction to the effective dipole moment used to calculate intensities for NOSD-1000 (see Fig. 1 of Ref. [55]). To create the line list for HITEMP, a recalculated version of the NOSD line list was then merged with the N_2O data in HITRAN2016 [16].

The N_2O line list was added to HITEMP prior to the updates for HITRAN2020 described in Sections 2.4.1 and 2.4.2. To maintain consistency, updates to HITRAN will be incorporated into HITEMP in due course. Readers should refer to Ref. [55] for a full description of the HITEMP line list for N_2O.

2.4.4. *Forthcoming updates*

In its present status, the HITRAN line list for N_2O has room for improvement above 8000 cm^{-1}. Data relative to the main isotopologue are limited to FTS data below 7796 cm^{-1}, mostly from the Toth database [229,245] and correspond to an intensity cutoff of 2×10^{-25} cm/molecule at 296 K. The inclusion in the HITRAN dataset of the calculated line list of the $^{14}N_2^{18}O$ isotopologue from Ref. [246] with an intensity cutoff of 1×10^{-29} cm/molecule leads to a somewhat unusual situation. In spite of it being only forth in abundance, $^{14}N_2^{18}O$ has the largest amount of transitions in the HITRAN N_2O list, extending up to 10,363 cm^{-1}, while many NIR bands of the principal isotopologue are missing. This situation was illustrated in a recent CRDS study in the 8325–8622 cm^{-1} region where the HITRAN line list includes only $^{14}N_2^{18}O$ transitions (see Fig. 7 in Ref. [247]). In addition, there are no $^{14}N^{15}N^{16}O$ and $^{15}N^{14}N^{16}O$ transitions in the HITRAN and HITEMP lists (in the considered region) while the $4\nu_3$ band of the $^{14}N^{15}N^{16}O$ isotopologue is dominant in the 8500–8550 cm^{-1} interval. Fortunately, many of these bands have been accurately measured in the recent literature, in particular by CRDS [245,248–256]. Spectroscopic data available in the literature will be gathered and critically evaluated in order to significantly extend and improve the N_2O lists of the first four isotopologues in the next editions of the HITRAN and HITEMP databases.

2.5. CO: *carbon monoxide (molecule 5)*

The HITRAN2016 [16] line list for carbon monoxide was based on the semi-empirical line list from Li et al. [257]. For the purpose of inclusion into HITRAN2016, the line list was truncated, and the line positions were replaced with updated calculation or state-of-the-art experimental data (see HITRAN2016 paper [16] for details). For the HITRAN2020 edition, the line positions have not been changed, but the intensity and line-shape data have been updated.

2.5.1. CO *intensities*

Intensities in Li et al. [257] were calculated using the piecewise dipole moment function fitted to existing experimental and *ab initio* data. Therefore, it is not surprising that the values of the intensities are primarily driven by the quality of the experimental data used as input. Recent state-of-the-art experiments have either confirmed the quality of CO intensities in HITRAN or have issued recommendations for improvements.

Despite the fundamental band being by far the strongest band of CO, experimental and theoretical data for its intensities in the literature do not agree well. Devi et al. [258] found that the intensities of the principal isotopologue of CO in HITRAN differ by about two percent when compared to their measurements. For the HITRAN2020 edition, the intensities of the $\Delta v = 1$ transitions of all isotopologues of CO in HITRAN were reduced by 2% following the recommendation of Ref. [258]. In the meantime, it is highly desirable that more experiments are carried out in this band.

Intensities of the second overtone in Li et al. [257] were primarily driven by the experimental values reported in Ref. [259] with sub-percent uncertainty. Recently the authors of Ref. [259] revised their experimental procedure, and their new measurements [260] suggest that HITRAN2016 intensities in this band are underestimated by about 2.6%. This assessment was corroborated by independent FTS measurements by Borkov et al. [261]. Therefore, in the HITRAN2020 edition, the intensities of the $\Delta v = 3$ transitions of all isotopologues of CO in HITRAN were increased by 2.6%.

Another recent paper by Borkov et al. [262] is devoted to the third overtone of CO. There the authors find that although HITRAN intensities are within respective error bars, they may be systematically off by about 2%. However, an independent CRDS study by Bordet et al. [263] has confirmed HITRAN values for this band to better than 1%. Therefore, the intensities in this band remain unchanged.

In the future, a better way to address the intensities in the fundamental and second overtone bands would be to refit the dipole moment function from Li et al. [257] with new experimental data and recalculate intensities. Ref. [257] notes that although their procedure should yield the same quality of results for all isotopologues (assuming no Born-Oppenheimer breakdown), comparisons with different experimental values yield different deviations for each of the six isotopologues. New experiments reported in Refs. [259,261–263] do not resolve this issue. One possible explanation is that none of the experiments had a way of measuring the relative abundance of isotopologues in the sample. Experiments with controlled abundance are highly desirable to resolve this issue.

2.5.2. CO *line shapes*

The line broadening and the pressure-shift parameters of transitions of CO perturbed by air and by CO itself have been re-

vised mainly based on a review performed in Ref. [233] on a variety of measurements. Compared to the HITRAN2016 line list, which included the speed-dependent parameters for only transitions of the 2–0 band (up to $J_{max} = 29$), in the 2020 edition of the CO line list, every line includes the speed-dependent Voigt and the Rozenkranz line-mixing parameters [232] for both air- and self-broadened lines. The importance of including non-Voigt line shapes in atmospheric retrievals of CO has been highlighted by Hochstaffl et al. [264,265]. Furthermore, the CO line-shape parameters for the important planetary broadeners such as CO-H_2, CO-He, and CO-CO_2 were revised [266], while parameters associated with broadening by H_2O were introduced for the first time as described in Ref. [49]. A summary of these modifications for the HITRAN2020 edition is given below:

1. *The* CO-*air broadened parameters:*
   (a) For the air half-widths (the VP parameters), to evaluate the effect of vibration, the relative difference of the broadening parameters for various measured bands were calculated and the average difference was well below 1% for different band values. Therefore, the broadening parameters were considered to be vibrationally independent. Then, the Padé approximants model (Eq. (1)) was employed to fit all the measured air-broadening data for several bands, including Ref. [267] for the 1–0 band, Ref. [268] for the 2–0 band, and Ref. [269] for the 3–0 band simultaneously [233]. The fit coefficients are provided in Ref. [233] and the resulting broadening parameters were expanded to all the transitions of CO perturbed by air.
   (b) The update of the speed-dependent Voigt line-shape parameters heavily relies on the semi-empirical Padé approximant fits to the experimental data of Ref. [270]. For the air broadening (the SDV parameters), and the temperature dependence of the air-broadening parameters, the 2–0 band data measured by Devi et al. [270] were used in the fit, and the approximated values from the model were expanded for lines of every band. The air speed dependence of line widths were fitted as well using the same data source, and the corresponding γ_2-air parameters were estimated and attributed to each transition. Wherever the measured SDV parameters were available, the original experimental results were used in populating the database. For instance, the Ref. [258] data were used for the lines of the 1–0 band and the measured parameters of Ref. [271] were used for updating the 2–0 band lines for different isotopologues of CO.
2. *The* CO-CO *broadened parameters:*
   (a) To find the values for the self-broadened half-widths (using the VP) for the high-*J* transitions, the measurements for different bands were used (i.e., 1–0 band [272], 2–0 band [273–275], 3–0 band [276]). All these data were fitted simultaneously to estimate the self-broadening parameters for the lines that were not measured for all the bands except for the measured transitions in the 2–0 band, where the data from Ref. [273] were used for the update.
   (b) The self-broadening parameters, their temperature exponents, and the speed-dependence of the broadening (the SDV profile parameters) were approximated using the measured line widths of Ref. [270] fitted to the Padé approximants model, and we imported the experimental values for different isotopologues reported in Refs. [258,271] for the 1–0 and 2–0 bands, respectively.
3. *The* CO-*air and* CO-CO *pressure shifts:*
   The air and self shifts (for both VP and SDV) were calculated by employing the sophisticated vibrational-dependent approach of Hartmann [173] for all the transitions. The quality of the calculated shifts were validated by comparison of the shifts in different bands [233]. The measured air shifts for the transitions in the 1–0, 2–0, and 3–0 bands remained unchanged as they were reported in HITRAN2016. Also it should be emphasized that measured pressure self shifts of CO for the 1–0 [272], 2–0 [270], 3–0 [269] and 4–0 [263] bands were written into the database directly for the measured lines.
4. *The* CO-*air and* CO-CO *first-order line-mixing:*
   The first-order line-mixing parameters were calculated based on the EPG formalism [242] using both the VP and SDV broadening parameters and provided for every transition. For the 2–0 band of the main isotopologue, the CO-air and CO-CO line-mixing were taken from the measurement of Ref. [270].
5. *Planetary perturbers:*
   Broadening parameters due to pressure of "planetary" (H_2, CO_2, He) gases were first introduced in HITRAN in 2016, based on the procedure described by Li et al. [257]. In this edition we updated these parameters. For the update of the CO-H_2 broadening parameters and their temperature dependence, the data from Refs. [273,277] were taken into the semi-empirical fitting models [266] and the results were extrapolated for every CO line. The line-shape parameters of CO perturbed by helium were also modified, based on Refs. [278–282], and the CO_2 pressure broadening and the temperature dependence of the broadening parameters of CO were generated from extrapolating the data from Ref. [283]. Finally, the pressure shift parameters for all three broadeners of CO were obtained based on the Hartmann semi-classical routine [173] and the values agree well with the available experimental data [266].

2.6. CH_4: *methane (molecule 6)*

HITRAN2016 provided substantial improvements in methane spectroscopy (with respect to previous editions) in many spectral regions (see, for instance, the validation of the ACE-FTS experiment [76]). In general, the line positions and intensities were considerably improved, and the spectral coverage increased. Nevertheless, the spectroscopy of methane is still far from perfect. In this edition, several spectral regions have been improved. However, one of the largest issues that remain is the quality of the line shape parameters. In particular, the tetradecad region targeted by GOSAT and MethaneSat requires revision (as indicated, for instance, in Ref. [284]). A major global revision of the methane line shape parameters is currently underway for Voigt and speed-dependent Voigt parametrizations, as well as the inclusion of line-mixing parameters. At present, this work is still ongoing and will not form part of the current update for methane. The improvements for HITRAN2020 concern updating line-shapes of individual transitions where major issues have been identified. Nevertheless, several spectral regions have received significant updates and are described below.

2.6.1. *3760–4100* cm^{-1}

A new line list from Rodina et al. [285] was used to completely replace HITRAN data for the principal isotopologue in this spectral region. This line list is based on the analyses of the FTS experimental spectra recorded in Reims under different thermodynamic conditions. This line list improves the quality of spectroscopic parameters in this spectral region and contains assignments for all lines, enabling easier conversion between temperatures.

2.6.2. *4190–4315* cm^{-1}

This spectral region is important in remote sensing as it is used by TROPOMI and by TCCON to monitor both methane and carbon monoxide. Lorente et al. [286] evaluated HITRAN2008, HITRAN2016, and SEOM-IAS [103] databases against retrievals from TROPOMI. The sensitivity tests did not indicate an improved data

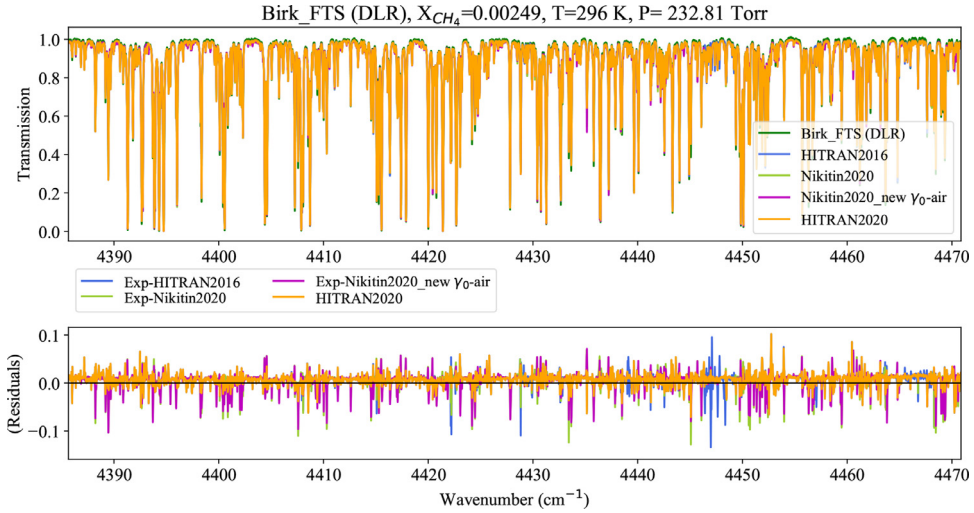

Fig. 14. The FTS transmission spectrum at P = 232.81 Torr, T = 296 K, and volume mixing ratio X_{CH_4} = 0.00249 (for a CH_4-air mixture) in the octad region measured at DLR. Transmission spectra calculated using HAPI for four different line lists are also presented. In the lower panel, the residuals (experiment-calculation) are shown for: i) HITRAN2016 line list, ii) the Ref. [287] line list, iii) the Ref. [287] line list when using the line broadening from Ref. [289], and iv) the HITRAN2020 line list.

quality when either of the spectroscopic databases was used. However, the RMS and χ^2 values were much improved with HITRAN2016 over HITRAN2008, with the SEOM-IAS data giving the best results. Indeed the SEOM-IAS [103] database is a very accurate line list, which, apart from accurate line positions and intensities, provides advanced line-shape parameters including line-mixing. However, it is not completely assigned, and some of the existing assignments contradict the assignments in HITRAN and variational line lists. In addition, the line-mixing formalism used in that work is not yet adapted in HITRAN. This is the reason why only 122 lines from Ref. [103] were adapted for HITRAN2016. For HITRAN2020 substantially more lines from Ref. [103] were assigned and incorporated into HITRAN using the recent HITEMP line list [56]. This, however, has both advantages and disadvantages. On the one hand, assignments allow one to use correct lower-state energies, which provides better applicability of the line list at different temperatures. On the other hand, parameters determined in a multi-spectrum fit of experimental data in Ref. [103] are somewhat correlated; therefore, the changes in lower-state energies could now conflict with other parameters determined in that study. In general, the specifics of the data proposed in Ref. [103] requires a dedicated software or precalculated cross-sections to be used successfully in radiative-transfer codes. The authors of the SEOM-IAS database are working on this approach.

2.6.3. 4315–4600 cm^{-1}

The recent line list from Nikitin et al. [287] was examined to update the methane line list in this spectral region. This line list was based on FTS measurements in Reims and the SOLEIL Synchrotron in France for different pressures and temperatures. To verify the quality of this line list, HAPI was used to calculate transmission spectra to compare with the laboratory measurments. For the air-broadening and shift parameters, the suggested values from Ref. [287] were used. Fig. 14 presents the experimental transmission spectra measured at DLR [132,288], compared to those calculated based on the new line list from Nikitin et al. [287], the HITRAN2016 line list, and the Nikitin et al. [287] line list supplemented with the broadening half-widths from Predoi-Cross et al. [289]. The last set is the HITRAN2020 line list, which is, in principle, the same as the HITRAN2016 line list with the broadening half-widths substituted with the measured values from Predoi-Cross et al. [289], and a few spectral intervals that have been updated using the line positions and intensities from the Ref. [287] line list for the weaker spectral lines.

As can be seen, the Nikitin et al. [287] line list itself did not improve the quality of spectroscopic parameters compared to the HITRAN2016 list in this region for most of the lines. However, using the broadening values from Ref. [289] reduced the residuals slightly. The lowest residuals were achieved when utilizing the proposed line list for the HITRAN2020.

Another validation analysis was performed using the FTS spectra measured at the Jet Propulsion Laboratory (JPL). Fig. 15 shows the transmission spectra and residuals for similar calculations being described in Fig. 14, in a slightly extended spectral range but at lower temperature. This also allows evaluation of the temperature dependence of the widths and reliability of spectroscopic assignments, i.e., lower-state energies. These validation examinations also confirm the effectiveness of the procedure for constructing the HITRAN2020 methane line list in this region.

2.6.4. 8850-9180 cm^{-1}

A new line list from Nikitin et al. [290] was used to update HITRAN for the principal isotopologue of methane in this spectral region. This line list is based on the analyses of FTS spectra that were recorded in Tomsk with a cell path length of 2.2 m under different thermodynamic conditions. This line list improves the quality of spectroscopic parameters in this spectral region and provides substantially more quantum assignment information than the HITRAN2016 list in this region, making conversions between temperatures more reliable.

2.6.5. Line-shape parameters

As was already mentioned, a major revision of methane line-shape parameters is underway and will feature as an update to HITRAN2020. At the moment, only individual parameters from selected lines (that were deemed to be definite outliers) have been updated. Moreover, in the tetradecad region, the air-broadening half-widths were updated using the measured parameters of Refs. [291,292] averaged with the line-broadening values in the so-called “HITRAN2016 Beta” list, which are based on the GOSAT2014 [293] line list for methane. Validation against laboratory spectra showed improved residuals (with a smaller RMS value) when calculating the transmission using the HITRAN2016 line list when introducing the newly averaged line widths (see Fig. 16).

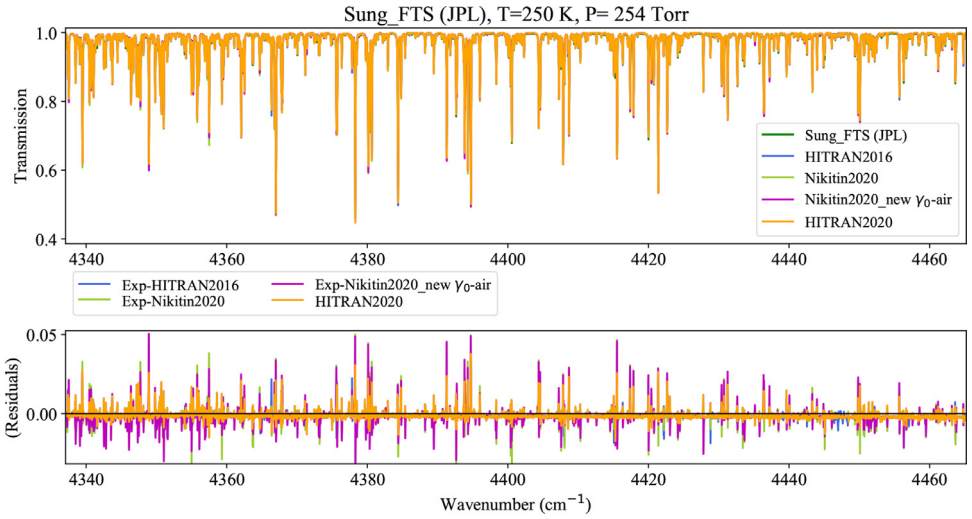

Fig. 15. The FTS transmission spectrum for CH_4 in the octad region at $P = 254$ Torr, $T = 250$ K, and $X_{CH_4} = 0.0572$ (for a CH_4-air mixture) measured at JPL. The description for the lower panel is the same as in Fig. 14.

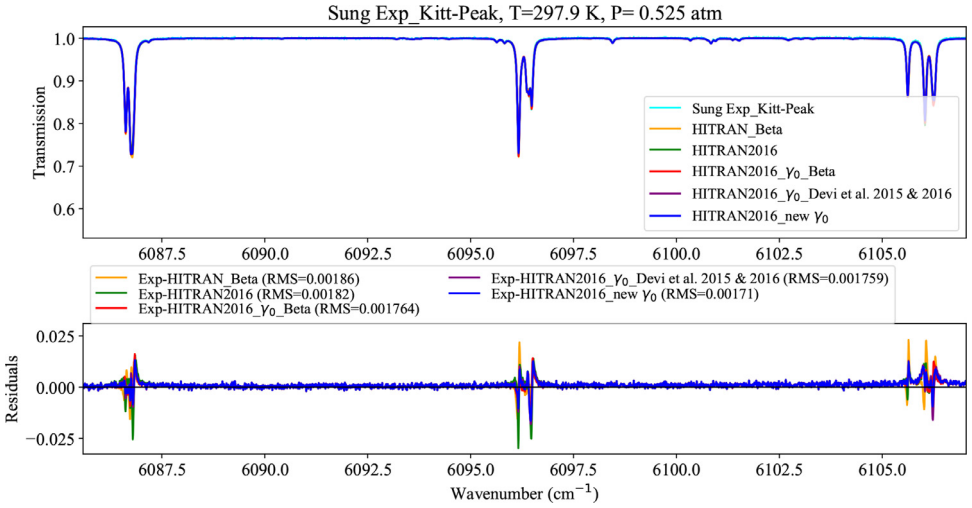

Fig. 16. The FTS transmission spectrum of CH_4 in the tetradecad region at $P = 0.525$ atm, $T = 297.9$ K, and $X_{CH_4} = 0.01$ (for a CH_4-air mixture) measured at Kitt Peak National Solar Observatory (NSO). The top panel also shows calculated transmission spectra employing HAPI and the following data: i) the "HITRAN2016 Beta" line list, ii) the HITRAN2016 line list, iii) the HITRAN2016 line list with the broadening values collected from the "HITRAN2016 Beta" list, iv) the HITRAN2016 line list with the broadening parameters collected from Refs. [291,292], and v) the HITRAN2016 line list with the average broadening values obtained from Refs. [291,292]. The latter line list was eventually used for the HITRAN2020 update. The lower panel shows the differences between the experimental spectra and calculated transmission spectra using these line lists.

Note that for every line of methane, HITRAN2020 features the inclusion of the half-widths (and their temperature dependencies) due to the ambient pressure of water as explained by Tan et al. [49].

2.6.6. Future work

Many other new experimental works on spectroscopy of different isotopologues of the methane molecule exist, which could benefit the HITRAN database, including (but not limited to) Refs. [294–306]. A very extensive effort is underway to evaluate new data against current HITRAN data and experimental and atmospheric spectra. Methane is a very complex molecule from the spectroscopic standpoint and it is not straightforward to make choices for individual parameters of individual lines. One interesting example is a pure rotational spectrum of CH_3D. In the HITRAN2016 paper an argument was made regarding updating the intensity of these lines with results from Bray et al. [307]. Since then, the authors of this work have revised these values [308] but these data still disagree with *ab initio* calculations and other theoretical works, which are not in agreement between themselves either. More work is needed to understand these discrepancies.

The high-temperature theoretical line list for $^{12}CH_4$ produced by Rey et al. [309] (and available online as part of the TheoReTS project [310]) has been used to create a line list suitable for HITEMP [53]. The approach involved merging Ref. [309] with the HITRAN2016 $^{12}CH_4$ data [16]. A method was devised to compress the weak underlying *ab initio* transitions into "effective lines" so that the complete HITEMP line list can be used directly in radiative transfer calculations. For a full description of the HITEMP line list of $^{12}CH_4$, including validation against experimental works, readers are referred to Ref. [56], which describes the addition to HITEMP. Users should be mindful that this HITEMP update was carried out before the $^{12}CH_4$ updates described above for HITRAN2020. To maintain consistency, these updates will be incorporated into HITEMP in due course.

2.7. O_2: molecular oxygen (molecule 7)

Due to the dominant presence and uniform mixing of oxygen in the terrestrial atmosphere, its spectral lines are often used as a benchmark for intensity calibration of atmospheric spectra taken by satellite and ground-based instruments. Although there is over a century of measurements and calculations of spectral parameters of oxygen, their quality and extent was still not able to achieve the sub-percent goal (in retrieved oxygen amount) in many important spectral bands. In this edition, major revisions of the oxygen line lists have been carried out.

2.7.1. 1.27 μm region

Spectroscopy of the $a^1\Delta_g$ – $X^3\Sigma_g^-$ band at 1.27 μm is more complex [311] than that of the A-band at 0.76 μm. It has more branches, a denser spectrum with overlapping lines, stronger underlying collision-induced absorption, and interfering emission features (air-glow) at the top of the terrestrial atmosphere due to the production of oxygen in the $a^1\Delta_g$ state through photo-dissociation of ozone. Nevertheless, it is located closer (on the spectral scale) to the bands of CO_2 and CH_4 that are targeted by the remote-sensing missions and therefore has better benchmarking characteristics to remove systematic errors. In fact, the Total Carbon Cycle Observing Network (TCCON) [312], which is less sensitive to the emission contamination from the top of the atmosphere, already employs this band. Sun et al. [313] have demonstrated that emission features could also be modeled accurately, and therefore, if one knows the spectroscopic parameters to the necessary degree of accuracy, this band can be used in remote sensing and is intended to be used by upcoming satellite missions, including MicroCarb [314] and MethaneSAT [26].

A major overhaul of the spectroscopic parameters for the $a^1\Delta_g$–$X^3\Sigma_g^-$ band of the $^{16}O_2$ and $^{16}O^{18}O$ isotopologues was carried out for this edition. The details for the calculations of line positions and intensities will be provided in a separate paper [315], but a general overview is provided below.

The $a^1\Delta_g$–$X^3\Sigma_g^-$ band consists of nine magnetic dipole (M1) branches (with $\Delta J = 0, \pm1$) and 15 electric quadrupole (E2) branches (with $\Delta J = 0, \pm1, \pm2$, nine of these branches overlap with M1 ones). Typically E2 transitions are about six orders of magnitude weaker than M1 transitions. However, as explained in Gordon et al. [311], intensities of the E2 lines in this particular band are enhanced due to mixing of the different spin-components of the $X^3\Sigma_g^-$ state with the $b^1\Sigma_g^+$ state at around 13,000 cm^{-1} and to a lesser extent with much higher-lying $^1\Pi$ states. These contributions affect each branch differently, and it is very hard to model these overlapping transitions. Therefore, in HITRAN2012 [15] and HITRAN2016 [16] only those E2 transitions with $\Delta J = \pm2$ were included based on measurements reported in Ref. [311] and a model proposed by Mishra et al. [316]. The E2 lines overlapping with M1 lines were not included, therefore creating difficulty in modeling absorption due to M1+E2 lines on a sub-percent level as E2 contribution to the total intensity should be considered almost negligible for some of the bands, but up to 1.5% for others.

Gordon et al. [315] make use of an extensive campaign of new measurements carried out in Grenoble and NIST. These measurements are a continuation of published works [317–319] that take advantage of the extremely sensitive CRDS setup equipped with frequency combs. Intensities with the lowest uncertainties were used in the fit to the model [316] for E2 transitions and the modified model [320] for M1 transitions. Modifications are connected to the Herman-Wallis-like rovibronic deviations that were modeled by introducing polynomials as a function of rotational quanta to the groups of transitions that are connected to the same spin component in the ground state.

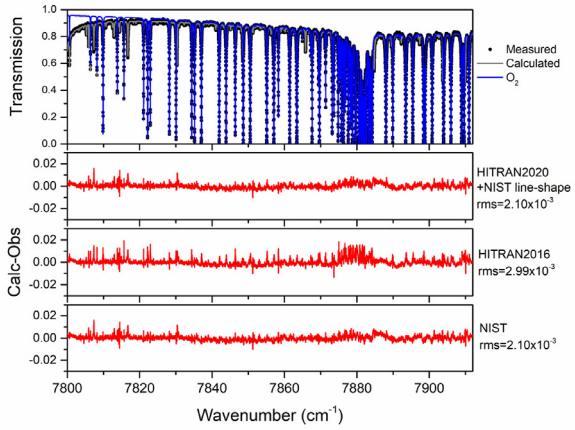

Fig. 17. Comparison between measured transmissions from Park Falls FTS and simulations using different versions of the database.

Frequency comb-calibrated line positions from the new Grenoble and NIST experiments were also used to refit all the $^{16}O_2$ and $^{16}O^{18}O$ data involving the $a^1\Delta_g$ and $X^3\Sigma_g^-$ states simultaneously. Effectively, a systematic change by about 2×10^{-4} cm^{-1} (slightly larger at $J'' \geq 29$) was introduced with respect to the HITRAN2016 values that were based on Ref. [321].

The Voigt line shapes were taken from the analyses of the Grenoble data carried out in Ref. [318], while advanced line-shape parameters, including first-order line-mixing, are from the new study in NIST that updates data from Mendonca et al. [319]. No new studies have been carried out for the temperature dependencies of the width, but in order to satisfy TCCON retrievals, the previous values in HITRAN were multiplied by a factor of 0.93.

Fig. 17 demonstrates how spectroscopic parameters in HITRAN affect the residuals of the TCCON spectra in Park Falls, WI (USA). The use of the HITRAN2020 line list clearly reduces the residuals to a sub-percent level.

2.7.2. A-band region

Updates to O_2 in the A-band region reflect ongoing efforts to improve the balance between line-mixing and collision-induced absorption that have been shown to bias surface pressure retrievals [322,323]. The effort [323] which drives this update does not improve the precision of line positions which may be correlated with self-shift parameters [324]. Therefore this HITRAN update retains the positions produced from the updated global model of Yu et al. [321] and additional uncertainty is recommended for the self-shift parameters. Line intensities are changed up to 5% at higher J values due to a re-assessment of the high-J data [325] used to determine Herman-Wallis terms utilized in the last two HITRAN editions [326]. Intensities in the present update, see Fig. 18, reflect a median value found in the FTS and CRDS datasets analyzed for production of ABSorption COefficient (ABSCO) tables used for the OCO missions [323]. The present adjustment appears larger with respect to HITRAN2016 than in comparison to HITRAN2012. Direct measurements of intensities have been performed subsequently by NIST after mitigating biases associated with the CRDS signal digitization, and found the ABSCO table intensities to be consistent to approximately better than 1%. The intensity changes are largest for the weakest features, such that the total band intensity is less variant, changing 0.92% from ABSCO 5.0 [327] (HITRAN2016) to ABSCO 5.1 [323] (HITRAN2020).

Changes in the air-broadened half-width and its temperature-dependence parameter (both Voigt and speed-dependent Voigt) are subtle, the latter showing increases of a few percent at low m and decreases of a few percent at high m, whereas the for-

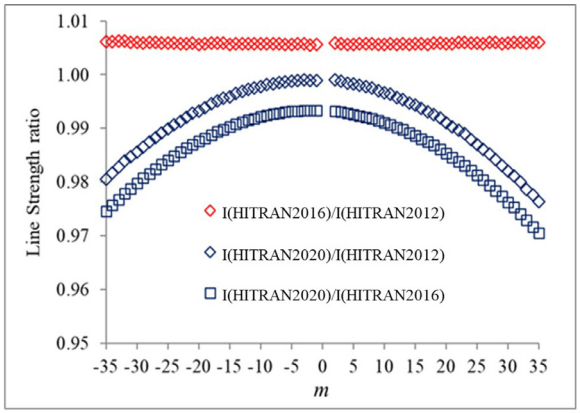

Fig. 18. Ratios of intensities from HITRAN2020 (ABSCO 5.1) [328] compared with HITRAN2016 and HITRAN2012. The HITRAN2016 update, which utilized a prior ABSCO release (5.0), [327], kept the Herman-Wallis factors from HITRAN2012 fixed. The changes are due to band scaling and the application of new Herman-Wallis factors.

mer generally increases and exhibits more variability. Changes in air-induced pressure shifts follow the same trends as the air-broadened half-width, but with a clearer monotonic structure now presented in the P-branch. All of these air-induced line-shape parameters show significant deviations from monotonic behavior near the band head of the R-branch, where there are strong interactions with line-mixing model parameters. It is likely that the subtle *J*-dependent changes in widths and shifts are also attributable to the modified line-mixing model which re-proportioned the odd and even elements of the relaxation matrix. The allocation of a small weight (instead of zero weight) to the odd elements produces a notable zigzag effect in the first-order Rosenkranz parameters provided with the HITRAN2020 database. The median of these elements closely traces prior Rosenkranz parameters except for a stronger slope in the R-branch vs. *m*.

2.7.3. Corrections to the line-broadening parameters for the O_2 B-band

The speed-dependent Voigt line-broadening parameters of the O_2 B-band adopted in the HITRAN2016 database from Domysławska et al. [329,330] were treated as half-widths (while apparently the full-widths were reported in the original papers). This discrepancy was discovered by Sung et al. [331] and the speed-dependent Voigt parameters have now been corrected for this band.

2.7.4. Water-vapor broadening parameters

A variety of experimental methods have been applied to study the water-vapor broadening of O_2 lines including early O_2 Q-branch Raman spectroscopic studies for a wide temperature range (460–990 K) [332]. The pure rotational and A-band transitions have been studied using laser-based photoacoustic spectroscopy [333], frequency-multiplier spectrometers with a Zeeman-modulated absorption cell [334], radio-acoustic detection spectrometers [335], as well as Fourier transform (FT) spectroscopy [336]. A complete analysis for all collected experimental data were presented in Ref. [49]. The Padé approximant (Eq. (1)) was applied to fit the collected data for transitions $N'' \leq 35$. There is an exception with $N'' = 1$ which is treated separately due to the large spin splitting in the lowest rotational level.

2.7.5. Future improvements in the 60 GHz band

The band of oxygen at 60 GHz represents the manifold of transitions between spin components within the same rotational levels. It is an important band from an atmospheric perspective, and although line-positions, intensities, and to a lesser extent Voigt parameters in HITRAN are of very high quality, the close proximity of transitions requires advanced line-shape parameterizations that include line-mixing. The recent study by Koshelev et al. [337] is considered to potentially introduce advanced line-shape parameters for these "fine-structure" transitions.

2.8. NO: *nitric oxide (molecule 8)*

Nitric oxide (NO) plays a key role in tropospheric chemistry [338] and contributes significantly to air pollution [339]. Spectroscopic NO emissions from the upper-atmosphere require the consideration of high rotational transitions in radiative-transfer models due to non-local thermodynamic equilibrium conditions [340].

Hargreaves et al. [55] provide a detailed description of the NO update for HITRAN2020 and HITEMP [53], therefore only a summary is provided here. In HITRAN2016 [16], the $^{14}N^{16}O$ line list contained transitions within the electronic ground state $X^2\Pi_{\Omega'}$–$X^2\Pi_{\Omega''}$ (with $\Omega = 1/2$ and 3/2) for vibrational bands up to $\Delta v = 5$ (with $v'' = 5$). For $^{15}N^{16}O$ and $^{14}N^{18}O$, only 699 and 679 lines of the 1–0 band were provided, respectively.

The comprehensive semi-empirical "NOname" line list [341], part of the ExoMol project [342], contains six isotopologues of NO ($^{14}N^{16}O$, $^{15}N^{16}O$, $^{14}N^{18}O$, $^{14}N^{17}O$, $^{15}N^{17}O$, $^{15}N^{18}O$). For $^{14}N^{16}O$, the NOname line list was created using an effective Hamiltonian by fitting to available experimental energies (with $J < 99.5$, $v < 28$) and combined with *ab initio* intensities. To allow extension to higher rotational levels and vibrational bands, a second variational model was also built by fitting to experimentally-obtained energy levels and positions using the *Duo* program for diatomic molecules [343].

The HITRAN and HITEMP update for $^{14}N^{16}O$ was built around the NOname line list, but some adjustments were necessary. Discontinuities at the stitching point of the two methods used to create the NOname line lists, and intensity issues observed for $\Delta v = 0$ (see Fig. 6 of Ref. [55]), required the effective Hamiltonian to be extended to higher rotational levels for the $\Delta v = 0$ and $\Delta v = 1$ bands [55]. Furthermore, comparisons to experimental observations required the NOname intensities for the $\Delta v = 4$, $\Delta v = 5$ and $\Delta v = 7$ bands to be scaled by a factor of 1.35, 1.30 and 0.55, respectively.

For the 0–0 and 1–1 bands, positions and intensities from the Cologne Database for Molecular Spectroscopy (CDMS) [344] replace the corresponding lines in the adjusted NOname line list. Any lines of the 0–0, 1–1, 1–0, 2–1, 2–0, and 3–1 bands with hyperfine splitting from HITRAN2016 (that were not replaced by CDMS data) have been retained. Further details for transitions with $J \geq 99.5$ are given by Hargreaves et al. [55]. In addition, magnetic dipole transitions (identified by "m" in the local upper-state quanta in the HITRAN line-transition format) for the 0–0 band remain unchanged.

For HITRAN2020, an intensity threshold for nitric oxide has been applied. Lines that remain less than 1.0×10^{-99} cm/molecule, or do not exceed 1.0×10^{-31} cm/molecule (at 100, 296, 500, 1000 or 2000 K) have been omitted from the HITRAN2020 line list. However, readers should be aware that the full $^{14}N^{16}O$ line list is available via HITEMP [55]. Fig. 19 provides an overview of the update for $^{14}N^{16}O$, which highlights the expanded spectral range (up to 23,727 cm^{-1}) and the increase in vibrational band coverage (up to $\Delta v \leq 14$, $v' \leq 26$), when compared to HITRAN2016. To take advantage of the increased precision of MW transitions, it should be noted that the wavenumber format for NO has been updated to F12.9 for transitions below 1.0 cm^{-1}, F12.8 for transitions 1.0 to 10.0 cm^{-1}, and F12.7 for transitions 10.0 to 100.0 cm^{-1} (as previously implemented for HNO_3, PH_3, O_2 and NO^+).

Air- and self-broadening parameters of NO in HITRAN and HITEMP have been refit to available measurements, and are described in detail by Hargreaves et al. [55]. The air-broadening

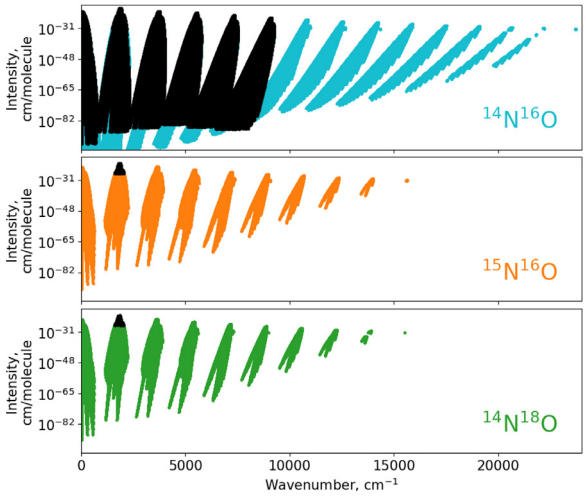

Fig. 19. Overview of the $^{14}N^{16}O$ (top), $^{15}N^{16}O$ (middle) and $^{14}N^{18}O$ (bottom) line lists in HITRAN2020, when compared to HITRAN2016 (indicated by black points).

(where $\gamma_{air} = 0.79\gamma_{N_2} + 0.21\gamma_{O_2}$) is calculated from rotationally-dependant N_2 and O_2 half-widths provided by separate Padé functions (Eq. (1)) for the $\Omega = 1/2$ and 3/2 components. The HITEMP update includes transitions with maximum $J = 184.5$, so care was taken to ensure good performance at high-J. The self-broadening half-widths were also revised as part of the HITRAN and HITEMP updates and were fit to the same functional form. The coefficients of Eq. (1) for N_2-, O_2- and self-broadening of the $\Omega = 1/2$ and 3/2 components of NO are given in Table 3 of Ref. [55].

In addition, the pressure-induced line shifts for air (δ_{air}) that are measured for the fundamental vibrational band [345] have been extended to additional vibrational bands (up to $\Delta v = 6$) using the method outlined by Hartmann and Boulet [346]. This same method was previously applied to CO [257] for HITRAN2016.

The HITRAN2020 update for NO also includes the NOname line lists of $^{15}N^{16}O$ and $^{14}N^{18}O$, with the same intensity thresholds as $^{14}N^{16}O$ applied. The extended coverage when compared to HITRAN2016 is also shown in Fig. 19. Isotopologue analysis of human breath [347] highlighted issues for the intensities of $^{15}N^{16}O$ in HITRAN2016. The present update contains intensities from NOname for each isotopologue and is therefore expected to address this issue. The NOname line lists for the minor isotopologues $^{14}N^{17}O$, $^{15}N^{18}O$ and $^{15}N^{17}O$ (with abundances of 3.7×10^{-4}, 7.3×10^{-6} and 1.4×10^{-6}, respectively) have not been added to HITRAN at this time as they are not expected to contribute significantly to terrestrial atmospheric spectra.

NO also absorbs strongly in the near ultraviolet. In particular, in the 200–230 nm (44,000–50,000 cm^{-1}) region its spectrum overlaps those of ammonia, O_2 and O_3. Qu et al. have recently developed a spectroscopic model which covers the β, γ and δ bands of NO [348] and associated line list [349] which will be considered for future inclusion in the database.

2.9. SO_2: sulfur dioxide (molecule 9)

Sulfur dioxide is an abundant pollutant in the terrestrial atmosphere, being produced by natural (such as volcanoes [350]) and anthropogenic (including coal burning [351]) sources. Characterization of SO_2 is necessary for atmospheric chemistry and climate models, due to its large effect on sulfate aerosols [350]. It is present on Venus, contributing to the Venusian sulfur cycle [352], and SO_2 is also being actively searched for in the atmosphere of Mars [353,354] as it is believed to play an important role in the atmospheres of rocky planets, including exoplanets [355]. The recently selected NASA DaVinci+ mission to Venus will be equipped with the Tunable Laser Spectrometer (TLS), which will be specifically targeting transitions of different isotopologues of SO_2 to obtain information on sulfur isotope ratios [356]. It is therefore important to expand the amount of the isotopologues of this molecule in HITRAN.

2.9.1. Description of new line lists

Recent developments in SO_2 spectroscopy have laid the groundwork for a major update and expansion of the corresponding line list in HITRAN. In particular, semi-empirical line lists from Huang et al. [357], and Naumenko et al. [358], have been identified as major sources for the potential improvement. Both line lists actively employed *ab initio* intensities (sometimes adjusted with empirical values) and systematically verified energy levels available from MARVEL analyses. In the MARVEL work on the SO_2 molecule [58,59], three sulfur isotopologues, $^{32}S^{16}O_2$, $^{33}S^{16}O_2$, and $^{34}S^{16}O_2$, were analyzed, resulting in 15,130, 5852, and 10,893 validated empirical ro-vibrational energy levels, respectively [359]. The $^{32}S^{16}O_2$, $^{33}S^{16}O_2$, and $^{34}S^{16}O_2$ MARVEL datasets, collated from the literature, contain 40,269, 15,628, 31,080 ro-vibrational lines, respectively [359]. Both Huang et al. [357], (hereafter referred to as Ames) and Naumenko et al. [358] (hereafter referred to as Naumenko) line lists and their evaluations against available laboratory spectra are briefly described below.

From 2014 to 2016, NASA Ames-296K *ab initio* IR line lists were published for $^{32}S^{16}O_2$, $^{33}S^{16}O_2$, $^{34}S^{16}O_2$ [360,361], and $^{16}O^{32}S^{18}O$ [362]. They were computed on a PES empirically refined with selected lines taken from HITRAN2012 with line position uncertainty codes $\geq$4 (see Table 2) [15] (unchanged in HITRAN2016 [16]), and an original *ab initio* dipole moment surface determined at the CCSD(T)/aug-cc-pV(Q+d)Z level of theory. Compared to the bands in HITRAN2012 [15], the agreement for intensities was usually better than 90-95% [360,361]. The consistency of the Ames-296K line lists has been systematically investigated to explore the possibility of further improvements [363,364]. Using the same potential and dipole surfaces, Underwood et al. [365] reported a hot $^{32}S^{16}O_2$ line list containing 1.3 billion lines. With more complete calculations at higher J values and extending to a higher energy range, the list was expected to provide the most complete coverage for 0-8000 cm^{-1} and temperatures up to 2000 K.

Although line position predictions from the *ab initio* works described above have matched recent experiments with σ_{RMS} = 0.01–0.02 cm^{-1}, this accuracy is not sufficient for atmospheric applications. In order to improve the line positions, experimental line positions and Effective Hamiltonian (EH) models based upon ro-vibrational energy levels published between 2009 and 2017 were collected and analyzed for $^{32}S^{16}O_2$ [366–373], $^{33}S^{16}O_2$ [374,375], $^{34}S^{16}O_2$ [376–379], and $^{16}O^{32}S^{18}O$ [380–384]. With $J \leq 75$ (the limit of the Ames-296K line lists) and $S_{296K} \geq 10^{-26}$ cm/molecule, 26,464, 25,089, 20,820 lines can be matched for $^{32}S^{16}O_2$, $^{34}S^{16}O_2$, and $^{16}O^{32}S^{18}O$, respectively. These "New Line Sets" and other $^{32}S^{16}O_2$ and $^{34}S^{16}O_2$ data from HITRAN2016 [16] were updated with reliable ground state EH models [371,384,385]. A complete list of observed and calculated energy levels of $^{33}S^{16}O_2$ [386] was incorporated at this stage. The resulting energy levels and other published EH model based levels were taken as the "corrected" reference energy set. Transitions were extracted from the Ames-296K line lists if their lower and upper state energy levels could be matched and replaced by the reference set values. Those extracted lines formed the "Expanded Line Sets". These contain 195,425/162,403/242,889/123,441 lines for $^{32}S^{16}O_2$/$^{34}S^{16}O_2$/$^{16}O^{32}S^{18}O$/$^{33}S^{16}O_2$, in the range of 0–4151/3465/2974/2625 cm^{-1}, with maximum $K_a'' = 42/39/32/35$ for 16/13/11/6 vibrational states and 79/59/39/20 bands. Similarly, an "Ames+MARVEL" line set was extracted from the Ames-296K

line lists by matching to the published MARVEL level set. These include 195 882/159 729/79 927 lines for $^{32}S^{16}O_2/^{34}S^{16}O_2/^{33}S^{16}O_2$, with maximum $K_a'' = 35/29/22$. Uniform criteria were adopted for both line sets: 1) line position difference $\leq$0.10 cm^{-1} (for E', E'', and transition wavenumber), 2) ro-vibrational quantum numbers match, 3) $S_{296K} \geq 10^{-26}$ cm/molecule. Compared to HITRAN2016 [16], many more $^{32}S^{16}O_2$ bands have been added up to 4200 cm^{-1}. However, the $3\nu_1$, $2\nu_1+\nu_3$, and $\nu_1+2\nu_3$ bands of $^{32}S^{16}O_2$ are still missing from the Ames line sets. See more details in Huang et al. [357].

The Ames line sets did not actively utilize the published experimental EH models (or the EH models published along with the MARVEL analysis) to derive a complete energy level set and use it in the match analysis, except for those of the ground states and $^{33}S^{16}O_2$. For example, the $^{34}S^{16}O_2$ EH models of the $3\nu_2$ and $2\nu_1+\nu_3$ states were published by Lafferty and Flaud [387] but they are not available in the Ames line set (nor the MARVEL level set). Therefore, in addition to the S_{296K} and J/K_a cutoffs, the effective coverage and quality are further restricted by the number and accuracy of reported measured lines and EH-based levels. Levels extrapolated from outdated EH models may coexist with those derived from the latest experiments. This potentially would result in a 0.001–0.01 cm^{-1} discrepancy within the "Expanded Line Set". Future updates to the Ames lists are planned that will fix such minor inconsistencies, enable provision of reliable uncertainty indices to line positions, and re-evaluate the intensities of the major isotopologues with an even more accurate dipole moment surface. Additional Ames-296K line list information for other isotopologues with combinations of isotopes ^{17}O, ^{18}O, ^{33}S, ^{34}S, ^{35}S, and ^{36}S [363,364] is available at huang.seti.org/SO2/so2.html, including an "Expanded Line Set" reported for $^{32}S^{18}O_2$ [357].

The Naumenko $^{32}S^{16}O_2$ line list is based primarily on the experimental energy levels derived in the aforementioned MARVEL work by Tóbiás et al. [359]. Moreover, additional experimental energy levels obtained from the identification of the FTS spectra of SO_2 from Vasilenko et al. [388] and Naumenko et al. [389] were also utilized. The uncertainty of the majority of the transition wavenumbers determined this way correspond to HITRAN uncertainty code 4 (see Table 2). For completeness, effective Hamiltonian calculations performed in Tóbiás et al. [359] were used for the rest of the lines which in turn have uncertainties in the range 0.001–0.01 cm^{-1} (code 3).

The Naumenko et al. [358] line list employs *ab initio* intensity values from Underwood et al. [365]. Exceptions are for the $\nu_1+\nu_2$, $\nu_2+\nu_3$, $\nu_1+\nu_3$ and $\nu_1+\nu_2+\nu_3$ bands, where intensity values are from the recent experimental data from Ulenikov et al. [383] and Borkov et al. [390]. The estimated uncertainties of the intensities are around 5–10% on average. Overall, the Naumenko et al. [358] line list ranges from 0.025 and 4159 cm^{-1} and consists of 549,200 transitions with a 10^{-30} cm/molecule intensity cutoff.

2.9.2. Validation

Both $^{32}S^{16}O_2$ line lists (Naumenko and Ames) were converted into the HITRAN format. This includes addition of air- and self-broadening data (as well as temperature dependence of the former) using the procedure derived by Tan et al. [391]. The Ames intensities were scaled by the HITRAN isotopic abundance 0.9457 (note that only the two most abundant isotopologues were available in HITRAN prior to the present edition). The Naumenko line list contains only the principal $^{32}S^{16}O_2$ isotopologue.

In addition, there were further requirements when generating the Ames $^{32}S^{16}O_2$ line list following recommendations in that article. It was suggested using the $^{32}S^{16}O_2$ "Ames+MARVEL" line list which uses MARVEL levels matched to Ames lines. Then supplement the $^{32}S^{16}O_2$ "Ames+Marvel" line list with other transitions from the $^{32}S^{16}O_2$ "Expanded" line list which uses matched Experimental and HITRAN Effective Hamiltonian (EH) model levels to Ames lines. The article also recommended applying cutoffs for $J \leq 50$ and $K_a \leq 25$ for the most reliable Ames-296K intensity. All recommendations were applied for the $^{32}S^{16}O_2$ Ames line list [357] prior to comparisons with laboratory data. Line-to-line comparisons of all the $^{32}S^{16}O_2$ spectral bands were generated to evaluate the position, intensity and lower-state energy differences between the Naumenko line list [358], the $^{32}S^{16}O_2$ Ames line list [357] and the $^{32}S^{16}O_2$ HITRAN2016 [16] line list.

The Naumenko and Ames line lists were compared against PNNL [244] laboratory data at 5°C, 25°C and 50°C with nitrogen as the buffer gas for each data set at a pressure of 1 atm. There is a degree of uncertainty for these comparisons in that the PNNL data are N_2-broadened and HITRAN does not contain N_2-broadening for SO_2, therefore air-broadening has been used. Also, the PNNL [244] measurements are limited to frequencies $\gtrsim$ 600 cm^{-1}, making far-IR comparisons unavailable. In addition to the PNNL comparisons, the line lists were validated at high resolution against an FTS experimental spectrum of SO_2 recorded at Old Dominion University (ODU) in 2015 (using the experimental setup previously described for CH_4 [392]). This spectrum covered the $\nu_1+\nu_3$ and $2\nu_3$ bands of SO_2 with a sample pressure of 10 Torr (0.0132 atm), temperature of 297 K, and resolution of 0.015 cm^{-1}.

The result of the $^{32}S^{16}O_2$ line list comparisons showed that in the majority of the bands where HITRAN had data, both line lists exhibited an improvement in residuals and contained multiple bands not previously available in HITRAN. The only exception is the ν_1+3ν_2 band which was only available in HITRAN2016 and missing from the Naumenko and Ames $^{32}S^{16}O_2$ line lists; therefore this band is being retained for HITRAN2020. The Ames line list [357] lacked some observable transitions. This is due to the $J \leq 50$ and $K_a \leq 25$ limits and a cutoff for intensities beyond 10^{-26} cm/molecule. Sample comparisons to PNNL [244] laboratory data is available in Figs. 20 and 21. These figures include data from $^{32}S^{16}O_2$,$^{34}S^{16}O_2$ in HITRAN2016 [16], $^{32}S^{16}O_2$, $^{34}S^{16}O_2$ from Huang et al. [357], $^{32}S^{16}O_2$ from Naumenko et al. [358] supplemented by the $^{34}S^{16}O_2$ Huang et al. [357] line list. Overall, the final HITRAN2020 $^{32}S^{16}O_2$ line list contains data from Naumenko et al. [358] supplemented by a single band from HITRAN2016 (ν_1+3ν_2) along with some position changes in the 1337-1376 cm^{-1} region where the Ref. [358] values were changed to HITRAN2016 values after detailed comparisons to laboratory spectra.

The $^{34}S^{16}O_2$ isotopologue line list generated by Huang et al. [357] is available in several line list sets. One is labeled the "Expanded" set and another is labeled the "Ames+Marvel" set. As recommended by the article in Huang et al. [357], the following cutoffs were applied for $J \leq 50$ and $K_a \leq 25$. In following the recommendations by the authors, the "Ames+Marvel" set was supplemented with other transitions from the "Expanded" set to generate the final $^{34}S^{16}O_2$ Huang et al. [357] line list.

The resulting $^{34}S^{16}O_2$ line list was evaluated by first converting it into the HITRAN format and then scaling the intensities by the HITRAN isotopic abundance 4.195×10^{-2}. Next, line-by-line comparisons of the available ground state to ground state, ν_1, $\nu_1+\nu_3$ and ν_3 bands in HITRAN were used to evaluate the position, intensity and lower-state energy differences between the $^{34}S^{16}O_2$ Huang et al. [357] line list and the HITRAN2016 [16] $^{34}S^{16}O_2$ line list. From these comparisons and from comparisons against PNNL data, it was determined that the HITRAN2016 main bands had more reliable intensity and position data. HITRAN2016 also contained some transitions that were missing from the $^{34}S^{16}O_2$ Huang et al. [357] line list. Therefore, for the ground state to ground state, ν_1, $\nu_1+\nu_3$ and ν_3 bands, HITRAN2016 data are retained while all other $^{34}S^{16}O_2$ Huang et al. [357] bands are added.

As was the case for the principal isotopologue, the procedure derived by Tan et al. [391] was used to populate line-shape pa-

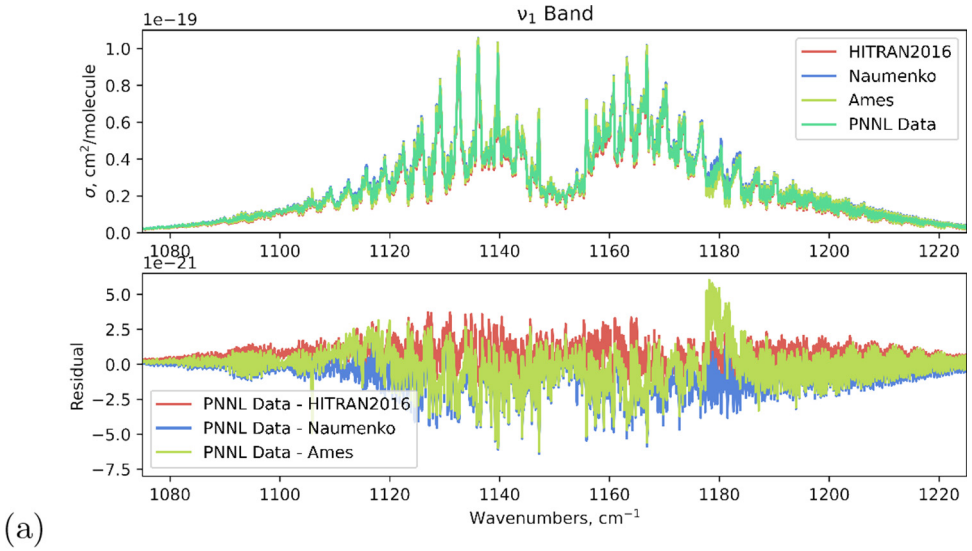

(a)

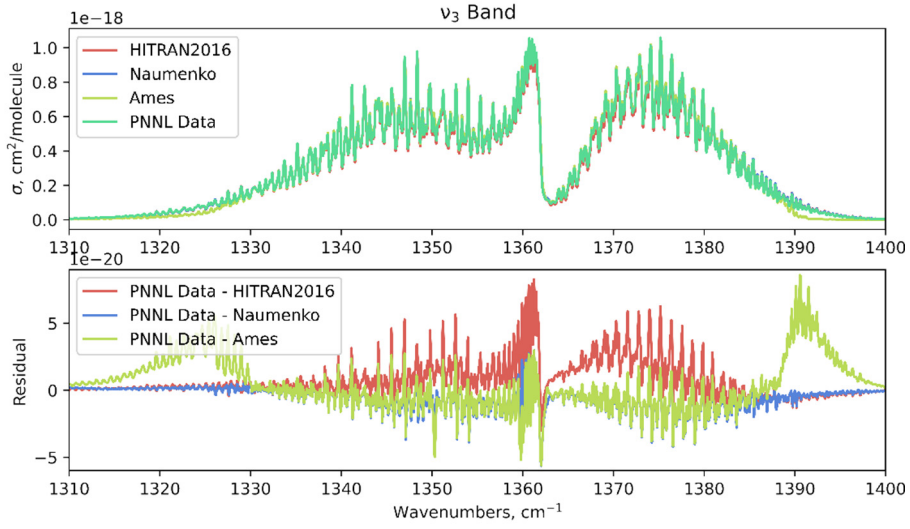

(b)

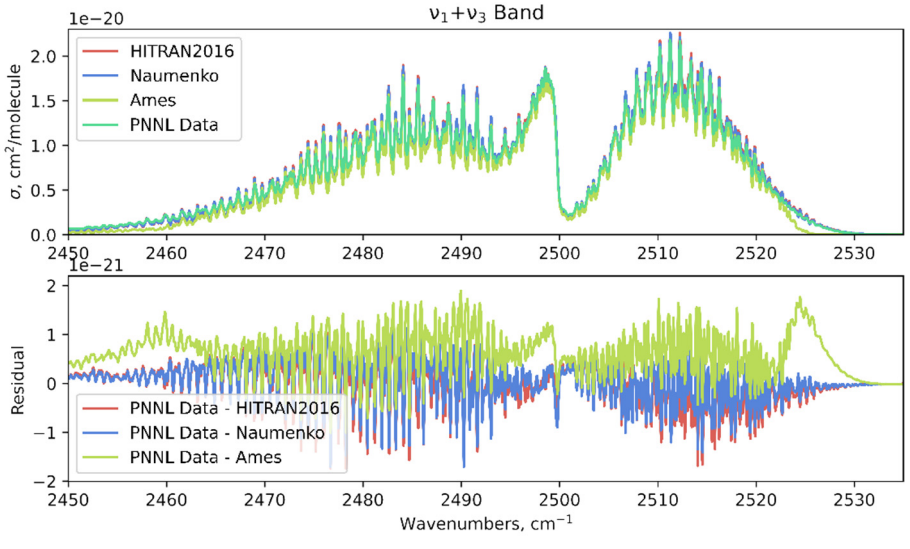

(c)

Fig. 20. Validation of calculated absorption cross sections (σ) covering the ν_1, ν_3 and $\nu_1+\nu_3$ vibrational bands against PNNL laboratory data [244]. In each panel; $^{32}S^{16}O_2$, $^{34}S^{16}O_2$ HITRAN2016 data [16], $^{32}S^{16}O_2$, $^{34}S^{16}O_2$ Ames data [357], and $^{32}S^{16}O_2$ Naumenko data [358] (supplemented by the $^{34}S^{16}O_2$ Huang et al. [357] line list) have been compared to the PNNL SO_2 spectrum at 25°C and 1 atm (N_2 buffer gas). Note that the final HITRAN2020 SO_2 data consists of the following; the $^{32}S^{16}O_2$ isotopologue provided by Naumenko et al. [358] with ν_1+3ν_2 band from HITRAN2016 being retained, the $^{34}S^{16}O_2$ isotopologue provided by Huang et al. [357] in addition to several strong bands from HITRAN2016, the $^{33}S^{16}O_2$ and $^{16}O^{32}S^{18}O$ isotopologues provided by Huang et al. [357].

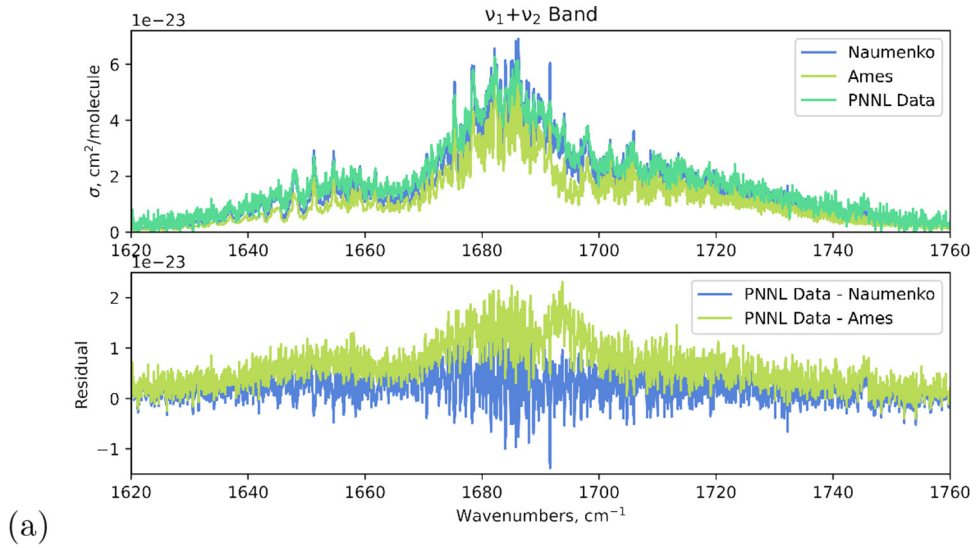

(a)

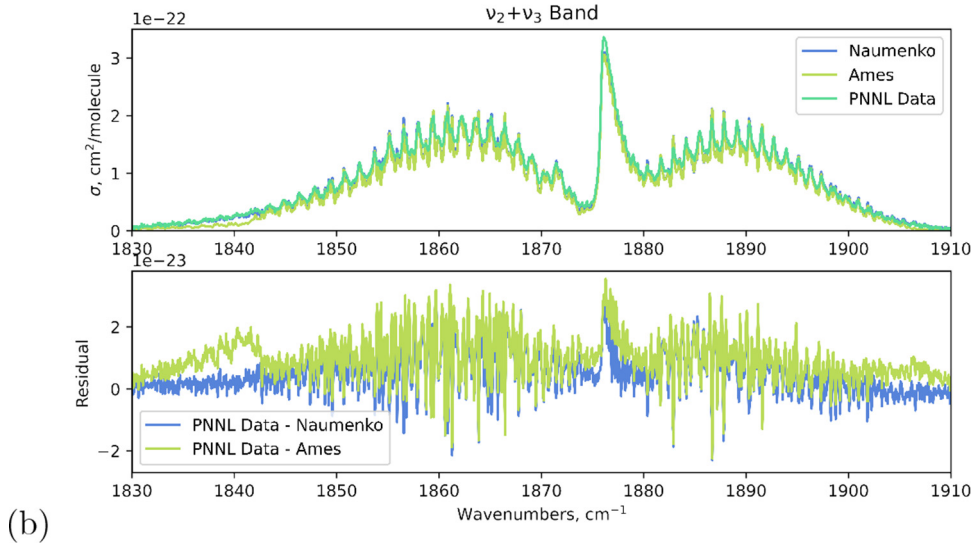

(b)

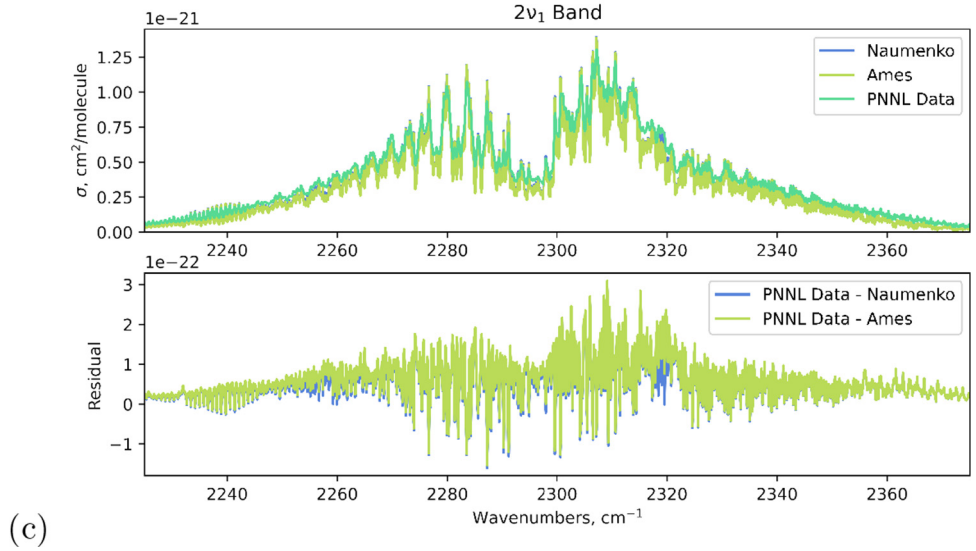

(c)

Fig. 21. Validation of calculated absorption cross sections (σ) covering the $\nu_1+\nu_2$, $\nu_2+\nu_3$ and $2\nu_1$ vibrational bands against PNNL laboratory data [244]. These bands were not previously included in HITRAN2016 [16]. In each panel, spectra calculated from $^{32}S^{16}O_2$, $^{34}S^{16}O_2$ Ames data [357], and $^{32}S^{16}O_2$ Naumenko data [358] (supplemented by the $^{34}S^{16}O_2$ Huang et al. [357] line list) have been compared to the PNNL laboratory SO_2 spectra at 25°C and 1 atm (N_2 buffer gas). Note that the final HITRAN2020 SO_2 data consists of the following; the $^{32}S^{16}O_2$ isotopologue provided by Naumenko et al. [358] with ν_1+3ν_2 band from HITRAN2016 being retained, the $^{34}S^{16}O_2$ isotopologue provided by Huang et al. [357] in addition to several strong bands from HITRAN2016, the $^{33}S^{16}O_2$ and $^{16}O^{32}S^{18}O$ isotopologues provided by Huang et al. [357].

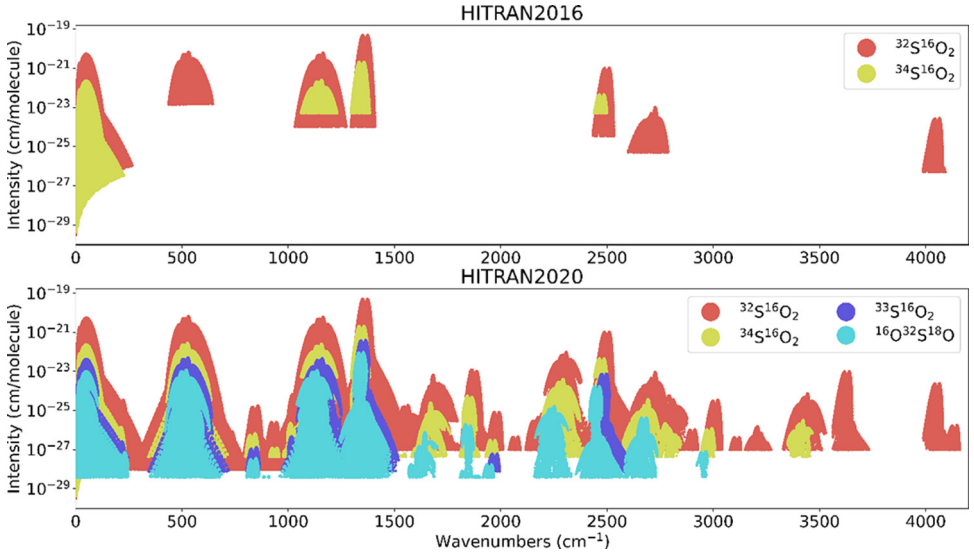

Fig. 22. The HITRAN2016 SO_2 line list [16] is shown in the upper panel, which can be compared to the spectral coverage of the new HITRAN2020 SO_2 line list (using data from Refs. [357,358] shown in the lower panel. These intensities have been scaled to their "natural" abundance (see Table 1) per HITRAN convention.

rameters. Additionally, the $^{34}S^{16}O_2$ Huang et al. [357] line list was supplemented into the $^{32}S^{16}O_2$ Huang et al. [357] line list prior to validations against the PNNL [244] and the ODU laboratory data. HITRAN2016 [16] contains only a few bands for this isotopologue, which is evident from these comparisons. However, the $^{34}S^{16}O_2$ Huang et al. [357] line list contains many more transitions/bands and therefore provide a more complete $^{34}S^{16}O_2$ line list.

The $^{33}S^{16}O_2$ isotopologue is available in several line list sets generated by Huang et al. [357]. One labeled the "Expanded" set and another labeled the "Ames+Marvel" set. As recommended by Huang et al. [357] the line list was limited to $J \leq 50$ and $K_a \leq 25$. The "Ames+Marvel" set was used as a basis and then supplemented with additional transitions from the "Expanded" set to generate the final $^{33}S^{16}O_2$ line list for HITRAN.

The resulting intensities of the $^{33}S^{16}O_2$ line list were scaled by the HITRAN isotopic abundance 7.464×10^{-3}. The $^{33}S^{16}O_2$ isotopologue was not included in HITRAN2016 [16], therefore the $^{33}S^{16}O_2$ line list from Huang et al. [357] was added to HITRAN2020.

The $^{16}O^{32}S^{18}O$ isotopologue was available in the "Expanded" line list generated by Huang et al. [357]. As recommended, the line list was limited to $J \leq 50$ and $K_a \leq 25$ and the resulting $^{16}O^{32}S^{18}O$ intensities were scaled by the HITRAN isotopic abundance 3.793×10^{-3}. The $^{16}O^{32}S^{18}O$ isotopologue was not included in HITRAN2016 [16], therefore the $^{16}O^{32}S^{18}O$ line list from Huang et al. [357] was added to HITRAN2020.

As was the case for the two most abundant isotopologues, the air-broadening coefficients (and their temperature dependence), as well as self-broadening coefficients, were applied to the $^{33}S^{16}O_2$ and $^{16}O^{32}S^{18}O$ Huang et al. [357] line list using the procedure described by Tan et al. [391].

The half-widths of the SO_2 lines by the ambient pressure of CO_2 and their temperature dependence, introduced to HITRAN2016 by Wilzewski et al. [393] have been revised. The new values are based on the semi-empirical algorithm originally developed in Ref. [394]; however for the inclusion into HITRAN2020 this algorithm was updated to account for recent experimental measurements by Borkov et al. [390].

Finally, Fig. 22 compares the new HITRAN2020 line list for SO_2 (for all isotopologues) against the previous SO_2 line list in HITRAN2016 [16] and demonstrates the significant increase in spectral coverage.

2.10. NO_2*: nitrogen dioxide (molecule 10)*

Nitrogen dioxide (NO_2) plays an important role in the photochemistry of Earth's atmosphere. Combustion of fossil fuels at high temperatures (particularly from diesel engines), along with biomass burning and soil emissions are primary contributors to tropospheric NO_2 [395]. NO_2 also impacts air quality and is detrimental to human health [396]; therefore concentrations are routinely monitored, such as during COVID-19 restrictions [397].

For HITRAN2020, the NO_2 spectral coverage has been significantly extended. Fig. 23 (left panel) displays an overview comparison of the $^{14}NO_2$ line lists of HITRAN2016 and HITRAN2020. While HITRAN2016 contained only lines below 3074.153 cm^{-1}, the present version has been extended into the NIR. Selected data from NDSD-1000 [398,399] up to 4775 cm^{-1} (with an intensity threshold of $S = 1.0 \times 10^{-25}$ cm/molecule) have been added for HITRAN2020. Comparisons to PNNL absorption cross sections [244] over the 4060–4775 cm^{-1} spectral region necessitated a scaling of the NDSD-1000 intensities by a factor of 3.5 in this region (see Ref. [55] for further details).

Data obtained from extensive CRDS measurements [400–408] in the 5800–8000 cm^{-1} region has also been added for HITRAN2020. The CRDS measured line positions and intensities were used to fit effective Hamiltonian and effective dipole moment parameters for the separate groups of interacting bands [400–408]. The obtained sets of effective parameters were presently used for the generation of the HITRAN2020 lists. As illustrated in Fig. 23 (right panel), different intensity cutoffs were applied depending on the study (in some cases, the addition to HITRAN has been extrapolated beyond the observed data). The smallest intensity for this region is $S = 1.0 \times 10^{-29}$ cm/molecule and the total number vibrational bands that are included in HITRAN for $^{14}NO_2$ has increased to 48.

For the added bands, semi-empirical approaches [409,410] were used for the calculation of the self- and air-broadening coefficients as well as their temperature exponents [398]. The empirical parameters used in these approaches were fitted to the measured self-broadening coefficients [411] and to the measured N_2- and O_2-broadening coefficients [412]. The vibrational dependence of the line-broadening coefficients was found to be small (less than 4%) [398] and thus neglected in the production of the NO_2 line list.

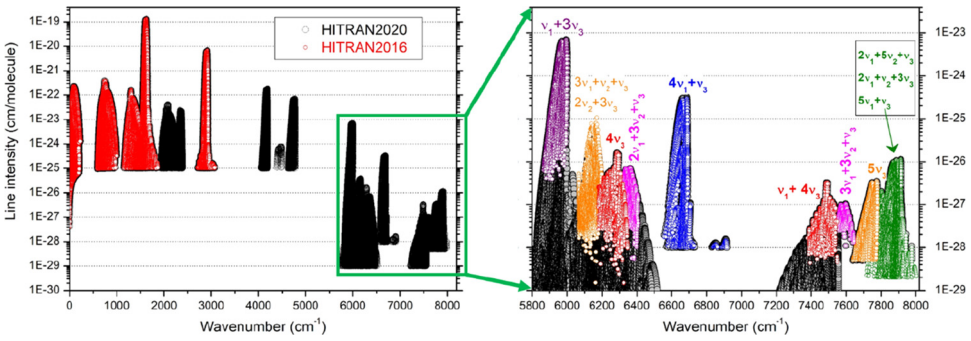

Fig. 23. Overview of the NO_2 line list for the main isotopologue, $^{14}N^{16}O_2$. *Left panel*: Comparison of the HITRAN2016 and HITRAN2020 versions (red and black circles, respectively). *Right panel*: Enlargement of the 5800-8000 cm^{-1} region that has been updated using CRDS measurements. The HITRAN2020 update (black circles) has been overlaid by the original CRDS data for each band system [400–408], which are identified by color.

It is worth noting that the minimum intensity of the $^{14}NO_2$ line list is different below and above 5000 cm^{-1}. However, the HITRAN list is not complete in both regions as some relatively strong bands are not provided due to the lack of measurements. New observations, such as of the $\nu_1+\nu_2+\nu_3$ band near 3600 cm^{-1} [413], will help to improve the completeness for future editions of HITRAN.

Finally, it should be mentioned that the statistical weights of the lower and upper states and the Einstein-*A* coefficients for the NO_2 HITRAN2016 bands with unresolved hyperfine structure were corrected.

2.10.1. Addition of $^{15}N^{16}O_2$

$^{15}N^{16}O_2$ is the second most abundant isotopologue of nitrogen dioxide, with a 0.003646 concentration of total NO_2 [57]. The ν_3 band of $^{15}N^{16}O_2$ is centered at 1582.1029 cm^{-1} and becomes the first band of this isotopologue to be included into HITRAN.

The $^{15}N^{16}O_2$ data included for HITRAN2020 contain 5860 transitions between 1500.73 and 1660.45 cm^{-1} for the ν_3 fundamental band. These transitions have a maximum intensity of 2.0×10^{-26} cm/molecule, with $N_{max}=77$ and $K_a=0$–15. The line positions and intensities were generated during two analyses: Ref. [414] used laboratory FTS spectra recorded at high-resolution (0.006 cm^{-1} unapodized) to generate a preliminary line list, which was later refined by Perrin et al. [415]. The $^{15}N^{16}O_2$ line list was restricted to the strong ν_3 band, although the resonances that couple the strong ν_3 band with the very dark $2\nu_2$ and ν_1 bands were explicitly accounted for. Experimental data concerning absolute line intensities are presently unavailable for $^{15}N^{16}O_2$; therefore the line intensity calculation was performed using the transition moment constants which are quoted for the ν_3 band of $^{14}N^{16}O_2$ in Ref. [416]. The total internal partition sums for $^{15}N^{16}O_2$ have been calculated for HITRAN2020 [417] and are described in Section 6.4.

Perrin et al. [415] have used this line list to detect atmospheric $^{15}N^{16}O_2$ for the first time from balloon-borne solar occultation spectra measured by the JPL MkIV FTS. Their retrieved $^{15}NO_2/^{14}NO_2$ ratio is within 5% of the expected 0.00364 isotopic value (at an altitude of 15–35 km) and validate the calculated intensities. Over the same altitude range the RMS spectral fitting residuals reduce significantly as a result of including the new $^{15}N^{16}O_2$ line list. Thus improving the accuracy of retrievals for all gases that absorb in the 1550–1650 cm^{-1} region (e.g., $^{14}NO_2$, H_2O, HDO, O_2).

Future improvements for the NO_2 line list can be achieved by using the line list for the 1153–4775 cm^{-1} spectral region [413] generated from recently recorded high-resolution FTS measurements (and added to the GEISA database [418]). For the 1500–1750 cm^{-1} and 2780–2920 cm^{-1} spectral regions, Jacquinet-Husson et al. [418] fully updated the line lists for the first hot bands ($\nu_2+\nu_3-\nu_2$ and $\nu_1+\nu_2+\nu_3-\nu_2$, respectively) and also included the ν_3 and $\nu_1+\nu_3$ bands of $^{15}N^{16}O_2$. Several weak cold bands in the 2000–4500 cm^{-1} region together with several higher order hot bands in the 1500–1750 cm^{-1} and 2780–2920 cm^{-1} spectral regions are also included for $^{14}N^{16}O_2$, whenever possible. Finally, Perrin et al. [413] performed a validation of this new line list and inter-comparisons with the NO_2 lists present in the HITRAN and HITEMP [55] databases. The most significant differences concern vibration-rotation bands that have a weak IR signature for typical terrestrial atmospheric conditions, but for hot bands may have an impact for NO_2 in high-temperature gas conditions.

2.10.2. NO_2 added to HITEMP

The HITEMP database [53] has been expanded to include NO_2 [55] and is based on the NDSD-1000 line list [398,399]. NO_2 was added to HITEMP prior to the 5800–8000 cm^{-1} ($^{14}NO_2$) and $^{15}NO_2$ HITRAN additions described above. To maintain consistency, these updates will be incorporated into HITEMP in due course. Readers should refer to Ref. [55] for a full description of the HITEMP line list for NO_2.

2.11. NH_3: ammonia (molecule 11)

Ammonia (NH_3) is integral to global agriculture through its use as an industrial fertilizer [419]. Consequently, anthropogenic emissions are a large contributor to the atmospheric abundance [420], but enhancements can also occur through natural events such as wildfires [421]. The abundance of NH_3 impinges on air quality [422] and its abundance can now be monitored over urban [423], industrial [424], and rural [425] regions using satellite and ground-based observations. Furthermore, NH_3 is a well known constituent of gas giants atmospheres and recent measurements from the Juno mission demonstrate complex weather processes with large-scale NH_3 variability [426,427]. The absorption of NH_3 is also expected to contribute to the opacities of cool brown dwarfs [428] and exoplanets [429].

The “CoYuTe” *ab initio* line list has been calculated as part of the ExoMol project based on a spectroscopically determined PES and an *ab initio* DMS [430]. CoYuTe spans transitions with wavenumbers up to 20,000 cm^{-1} and is designed for use at temperatures up to 1500 K [431]; even before improvement of the energy levels using MARVEL, it is significantly more accurate than the BYTe line list [432] used to populate earlier versions of HITRAN. In parallel there was an extensive update of the $^{14}NH_3$ MARVEL database [433] which considered 46,115 transitions up to 7500 cm^{-1} yielding 4936 unique, labeled empirical ro-vibrational energy levels. These MARVEL energy levels were used in the CoYuTe line list to ensure experimental accuracy in the wavenumbers of the vast majority of transitions lying below 7000 cm^{-1} and above the

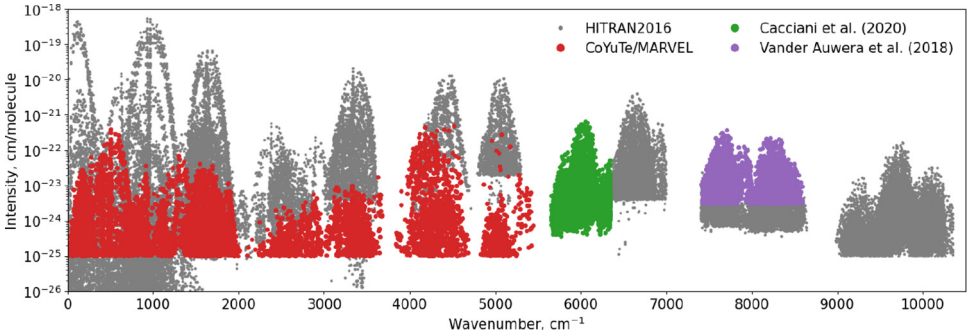

Fig. 24. Overview of the $^{14}NH_3$ data in HITRAN2020. The location of the retained HITRAN2016 data and new additions from CoYuTe/MARVEL, Cacciani et al. [437] and Vander Auwera and Vanfleteren [438] have been indicated.

HITRAN2016 intensity cutoff. These new MARVEL energy levels and the CoYuTe line list were used to complement the HITRAN2016 dataset in which a significant number of lines were missed in the 4000–7000 cm^{-1} region.

2.11.1. Addition of selected bands from the CoYuTe/MARVEL line list

The performance of the CoYuTe/MARVEL line list at modeling room-temperature experimental FTS spectra (0.01 cm^{-1} resolution) between 2400 and 5500 cm^{-1} [434,435] and 4800–7500 cm^{-1} [436] (as well as lower resolution cross-sections from PNNL [244]), has been compared to HITRAN2016 [16]. Throughout these spectral regions there were instances where CoYuTe/MARVEL provided position and/or intensity improvements when compared to HITRAN; however, there were also a number occasions when the HITRAN2016 data were favorable, with many instances where the performance were comparable. A more intensive and thorough assessment of the line-by-line improvements provided by the CoYuTe/MARVEL line list is planned for the future. At this time, only transitions from vibrational bands not previously contained in HITRAN are considered for inclusion. For NH_3, the lower-state energies in HITRAN refer to the lowest allowed lower-state energy and values in the CoYuTe/MARVEL line list have been reduced by 0.7934 cm^{-1}: the energy difference between the symmetric and anti-symmetric $J'' = K'' = 0$ levels of the ground vibrational state.

A previous lack of assignments for NH_3 in the 5500–6350 cm^{-1} spectral region means that the CoYuTe/MARVEL line list is missing the majority of transitions recently observed by Cacciani et al. [437]. Of the weak transitions in this range that were included in the CoYuTe/MARVEL list, the predicted intensities appeared to be overestimated when compared to measured values. Therefore, only the CoYuTe/MARVEL transitions of selected bands < 5500 cm^{-1} (with intensities $> 1.0 \times 10^{-25}$ cm/molecule) were included as part of HITRAN2020. Fig. 24 summarizes the new CoYuTe/MARVEL additions to HITRAN below 5500 cm^{-1}.

The CoYuTe/MARVEL lines that were not included as part of the present update will be thoroughly evaluated as a subsequent update to HITRAN2020. In addition, the intensities for the 50–660 cm^{-1} spectral region measured by Sung et al. [439] will also be considered.

2.11.2. The 5500–6350 cm^{-1} region

In previous editions of HITRAN, this spectral region contained very limited transitions of NH_3 due to a lack of measurements, but this region is part of the 1.6 μm atmospheric transparency window and allows for additional opportunities for NH_3 retrievals. Recently, Cacciani et al. [437] have analyzed an archived FTS spectrum of NH_3 (1.8 Torr at 21.5°C) between 5500 and 6350 cm^{-1} recorded at Kitt Peak NSO in 1991 with a resolution of 0.01 cm^{-1}. A multi-line fitting procedure was used to obtain the positions and intensities of 2779 lines, of which 1762 lines were assigned to 29 vibrational bands.

A small number of transitions (between 6300 and 6350 cm^{-1}) partially overlap the data provided by Sung et al. [440], which was included as part of HITRAN2012 [15]. Comparison of these intensities showed a systematic offset of ~10–15% (within the uncertainty of the experiment), but a good agreement was found when compared to *ab initio* line intensities [431] for many more lines (see Fig. 9 of Ref. [437]). Therefore, the positions and intensities from Cacciani et al. [437] have been added to HITRAN, and replace the previous values [440] for the 6300–6350 cm^{-1} overlap region. For inclusion to HITRAN, the lower-state energies in Ref. [437] have been reduced by 0.7934 cm^{-1} to account for the lowest allowed lower-state energy.

2.11.3. The 7400–8600 cm^{-1} region

Relying on two high-resolution Fourier-transform spectra recorded at room temperature, the positions and intensities of 1936 lines of ammonia were measured in the range 7400–8600 cm^{-1} [438]. These lines are not assigned and lower-state energies are therefore not available. The line positions were calibrated using 145 water-vapor lines observed in the ranges 5255–5536 cm^{-1} and 7054–7398 cm^{-1} and reference line positions reported by Toth [61] and available in HITRAN2016 [16]. The accuracy of the calibrated line positions was estimated to range from 0.001 to 0.002 cm^{-1} from the lower to the upper limits of the spectral range considered, while the accuracy of the line intensities was estimated to be around 10% or better. Line positions and intensities measured in the range 6800–7000 cm^{-1} of the same two spectra with measurements reported by Sung et al. [440] agreed within these estimated accuracies (see Figs. 2 and 3 of Ref. [438]). Partially-assigned lines measured in the 7400–8640 cm^{-1} range of a FTS spectrum recorded at NSO by C. De Bergh in 1980 [441] were incorporated in HITRAN2016 [16]. Comparisons of these line positions and intensities with the new measurements [438] put forward discrepancies within the uncertainties stated in HITRAN2016 [16] for the line positions, but (significantly) larger for the intensities of strong lines ($S > 10^{-22}$ cm/molecule; see Figs. 6 and 7 of Ref. [438]). Note that less-accurately measured positions and intensities of 1985 lines were also reported in the range 7400–8600 cm^{-1} [438], leading to a combined total of 3921 lines.

The Vander AuweraT.Vanfleteren [438] positions and intensities were compared to the empirical line list of Ref. [436]. Empirical lower-state energies have been matched to 578 lines of Ref. [438] to improve the temperature extrapolation of this spectral range. For all other lines, a default value is used ($E'' = 333$ cm^{-1}). The performance of the Vander Auwera and Vanfleteren [438] line lists (all 3921 lines) was validated against HITRAN2016 by modeling a FTS spectrum of NH_3 (5.0 Torr at 21.5°C and recorded at the NSO in 1980). This same spectrum was previously analysed

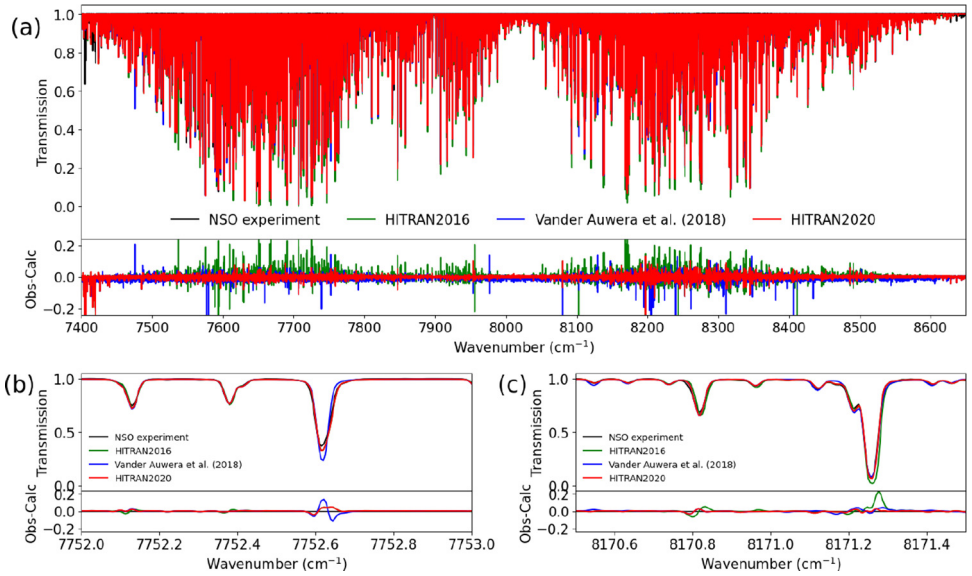

Fig. 25. A demonstration of the improvements for the NH_3 line list in HITRAN2020 over the 7400–8600 cm^{-1} spectral region (a), with zoomed in examples of when HITRAN2016 (b) or Vander Auwera and Vanfleteren [438] (c) contribute to the HITRAN2020 data. In each upper panel, a FTS NSO spectrum with 5.0 Torr of NH_3 at 21.5°C is compared to calculated spectra using HITRAN2016 (using the data of Ref. [441]), Ref. [438] and the combined HITRAN2020 line lists. The lower panels display the obs–calc residuals.

by Barton et al. [441] and the corresponding data added to HITRAN2016 [16]. This reanalysis for this work demonstrated that Ref. [438] provided many improvements, such as for strong lines (as shown in Fig. 25c), but these comparisons also demonstrated that some blended features were better modeled by HITRAN2016 (Fig. 25b). The vast majority of transitions in this region are unassigned; therefore the calculated spectra were assessed in their ability to reproduce the experimental observations. The residuals were analysed on a line-by-line basis, and those parameters from each list (either HITRAN2016 or Ref. [438]) that provided the smallest residual were used for HITRAN2020. The NH_3 line list for HITRAN2020 is also included in the comparison plots of Fig. 25 and can be seen to have the smallest residual in each case.

Additional FTS spectra (10.0 Torr of NH_3 combined with a 0.5 m path length) measured by Beale et al. [436] also cover the 7400–8600 cm^{-1} region. However, the SNR for this region was not sufficient to provide detailed comparisons. Nevertheless, the overestimation of strong line intensities identified by Vander Auwera and Vanfleteren [438] for HITRAN2016 (and shown in Fig. 25c) were clearly observed when comparing calculated spectra, with the HITRAN2020 calculated spectrum providing the smallest residual.

2.11.4. Additional updates and broadening parameters for $^{14}NH_3$

The lower-state energies of 12 transitions were noted to give an incorrect temperature extrapolation when used at higher temperatures [434]. To correct this issue, the lower-state energies of these transitions have been reverted to values from HITRAN2008 [14] and the assignment removed. Provisional comparisons to atmospheric and laboratory spectra highlighted 8 lines near 4415 cm^{-1} (with intensities greater than 10^{-21} cm/molecule), which were absent in previous editions of HITRAN. These transitions were assigned using Ref. [433] and added to HITRAN (with appropriate lower-state energy).

In addition, it was noted by Yurchenko [442] that 3 lines at 5014.4776, 5084.8734, 5104.2963 cm^{-1} identified as belonging to $^{15}NH_3$ had intensities overestimated by (at least) an order of magnitude. These anomalous intensities are due to stronger coincident $^{14}NH_3$ transitions and they have therefore been attributed to $^{14}NH_3$ and the assignment has been removed.

The air- and self-broadening coefficients and temperature dependence from Nemtchinov [443] have been applied to all new transitions. For the current work, the functions used to calculate air-broadening have been extended to improve comparisons with atmospheric and laboratory spectra. For transitions with $J \geq 9$ (and $K \leq 9$), the coefficients are fixed at the values used for and corresponding value of $KJ = 9$. For transitions with $J \geq 9$ and $K > 9$, a constant value of 0.0906 cm^{-1}/atm is used.

To support the application of HITRAN data to modeling of planetary atmospheres, H_2-, He- and CO_2-broadening parameters were introduced for NH_3 as part of HITRAN2016 [393]. In addition, H_2O-broadening parameters have since been added to HITRAN by Tan et al. [49]. These parameters are necessary for accurate modelling of the atmosphere of Jupiter and have been validated against experimental measurements under Jovian conditions [444]. As part of this work, the self-broadening parameter for the $R(0)$ ground-state transition at 4.67463 cm^{-1} was empirically adjusted to 0.250 cm^{-1}/atm, for better agreement with observation.

2.11.5. $^{15}NH_3$

Notwithstanding the recognized important role of $^{15}NH_3$ in the determination of the $^{15}N/^{14}N$ ratio in space [445] where ammonia is abundant in various environments and objects, the extent and quality of spectroscopic information contained in HITRAN2016 for this isotopologue was not on par with that of $^{14}NH_3$ (with the exception of the MW region).

Recently, the spectroscopic analysis of *a* and *s* inversion levels of the bending states up to about 3000 cm^{-1} has been completed for $^{15}NH_3$ at experimental accuracy [446,447], as a result of new high-resolution spectra recorded using the FTS at the Canadian Light Source (CLS) synchrotron and the Bomem DA8 interferometer in Bologna. Overall, 13,288 inversion-rotation-vibration transitions in the ν_2, $2\nu_2$, ν_4, $3\nu_2$, and $\nu_2+\nu_4$ cold bands, in the $2\nu_2 \leftarrow \nu_2$, $2\nu_2 \leftarrow \nu_4$, $\nu_4 \leftarrow \nu_2$, $\nu_4 \leftarrow 2\nu_2$, $3\nu_2 \leftarrow \nu_2$, $3\nu_2 \leftarrow 2\nu_2$, $3\nu_2 \leftarrow \nu_4$, $3\nu_2 \leftarrow \nu_2+\nu_4$, $\nu_2+\nu_4 \leftarrow \nu_2$, $\nu_2+\nu_4 \leftarrow 2\nu_2$, $\nu_2+\nu_4 \leftarrow 3\nu_2$ and $\nu_2+\nu_4 \leftarrow \nu_4$ hot bands, and the inversion-rotation transitions in the studied excited states have been assigned and analyzed [446,447].

This analyses allowed creating a model that can reproduce the line positions of the assigned transitions well within experimen-

tal uncertainties. This was achieved through a fit with an effective Hamiltonian that included all symmetry-allowed interactions between (and within) the studied excited states. This Hamiltonian is derived according to the most recent results of the principal isotopologue of ammonia [448,449]. In both studies [446,447] the experimental values have also been compared with their corresponding *ab initio* values calculated in Ref. [442].

The line positions calculated using the effective Hamiltonian are now included as part of HITRAN2020. The line intensity of each transition is calculated from the *ab initio* Einstein-*A* coefficients computed in Ref. [442] for $J \leq 18$. The lower-state energies of Refs. [446,447] have been reduced by 0.7577 cm^{-1} for HITRAN to account for the energy difference between the symmetric and antisymmetric $J'' = K'' = 0$ levels of the ground vibrational state. Isotopologue dependence of the line shape parameters was ignored, and the same algorithms that were used for the principal isotopologue for self-, air- [443], H_2, He, CO_2 [393], and H_2O [49] broadening (and associated temperature dependencies) have also been applied for for $^{15}NH_3$.

It should be noted, that the quantum number notation used for $^{15}NH_3$ is currently dissimilar to the principal isotopologue in HITRAN. The global quantum number notation used for $^{14}NH_3$ was updated in HITRAN2012 [15] to: ν_1, ν_2, ν_3, ν_4, L_3, L_4, L, Γ_{vib} (refer to Table 7 of Ref. [15] for parameter descriptions, but note that the order of the parameters in the ".par" file is as specified here). However, the global quantum number notation for $^{15}NH_3$ remains as: ν_1, ν_2, ν_3, ν_4, S (parameter descriptions are given in Table 7 of Ref. [13]). For future editions of HITRAN, the consistency of the quantum number notation between ammonia isotopologues will be addressed.

2.11.6. *Future expansion above 12,000* cm^{-1}

The HITRAN2020 NH_3 data extend up to 10,349 cm^{-1}, but recent spectroscopic analyses have provided line lists into the NIR and visible regions. These works [450,451] will be considered for future updates of the database and are briefly summarized below.

Near 12,500 cm^{-1}, the positions and intensities of 1114 ammonia lines observed in the 12,491–12,810 cm^{-1} region have been measured [450] using FTS absorption spectra.

In addition, Zobov et al. [451] have reported analysis of the green and red bands of NH_3 for the 15,200–15,700 cm^{-1} and 17,950–18,250 cm^{-1} spectral regions, respectively, based on reanalysed Kitt Peak archive absorption spectra from 1980. Assignments were made up to $J = 7$ and were used to refine the PES [430] used for the CoYuTe line list [431]. Irwin et al. [452] used the CoYuTe line list to model low- to medium-resolution spectra of Jupiter at visible wavelengths with promising results, although application to high-resolution studies is not recommended

2.12. HNO_3: *nitric acid (molecule 12)*

Unchanged.

2.13. OH: *hydroxyl radical (molecule 13)*

The OH radical is a key species in atmospheric science. In the terrestrial troposphere, OH is the most important oxidizing agent for organic molecules, and in the upper atmosphere produces prominent airglow emission. Atmospheric OH abundances are measured by pure rotational transitions [453,454], vibration-rotation transitions (Meinel bands) [455], and by the $A^2\Sigma^+$–$X^2\Pi$ electronic transition [456]. OH is also prominent in many astronomical objects [457,458] and is a strong emitter in high-temperature sources such as flames [459]. The line positions of the Meinel bands ($X^2\Pi$ vibration-rotation bands) of ^{16}OH were updated using mainly calculated values from the PGOPHER [460] fit of Brooke et al. [461] for $\nu = 0$–13 based on the earlier [462] analysis. Many data sources were included from the literature including some $B^2\Sigma^+$–$X^2\Pi$ bands for the high vibrational levels ($\nu > 10$). The maximum rotational levels reported were extrapolated to 5-10 J values beyond the last observed level and range from 60.5 for $\nu = 0$ to 13.5 for $\nu = 13$.

Noll et al. [455] analyzed Meinel band airglow spectra recorded with the astronomical echelle spectrograph UVES at the European Southern Observatory. The line positions agreed very well with the line list provided by Brooke et al. [461] except for some transitions involving higher rotational levels of $\nu = 5$ and 6. The observed lines of Noll et al. were then included in the Brooke et al. fit using the same number of line parameters. The spectroscopic constants changed slightly, and a new line list was created with PGOPHER for HITRAN2020.

The line positions for the $A^2\Sigma^+$–$X^2\Pi$ electronic transition of ^{16}OH in HITRAN2020 are based on the analysis of Yousefi et al. [463]. Data from the literature was used for $v' = 0$–4 in the $A^2\Sigma^+$ state, and the $X^2\Pi$ state constants for $v'' = 0$–9 were held constant at the values determined by Brooke et al. [461]. The primary source of these data was the $A^2\Sigma^+$–$X^2\Pi$ 0–0, 1–1, and 2–2 bands analyzed by Stark et al. [464] from FT emission spectra and recalibrated using the frequency comb measurements of Fast et al. [465]. PGOPHER was used to make a line list for all *A*–*X* bands with $\Delta v \leq 5$ and extrapolated to 5-7 *J*'s higher than the observed values which range from $J = 12.5$ ($v' = 4$) to 30.5 ($v' = 0$).

The line strengths for the Meinel bands are those calculated by Brooke et al. [461] from two *ab initio* dipole moment functions and the RKR potential curve. The Herman-Wallis effect was taken into account by calculating *N*-dependent dipole matrix elements using LeRoy's LEVEL program [466]. LEVEL does not include electron spin (Hund's case (b) matrix elements) while PGOPHER uses *J*-dependent matrix elements (Hund's case (a)) as input. As described by Brooke et al., the LEVEL output was transformed into the Hund's case (a) dipole matrix elements for PGOPHER. The line list intensities were validated by comparison with the observed Herman-Wallis effect in the 2-0 band emission spectrum.

Noll et al. [455] compared the observed airglow intensities for many bands with the Brooke et al. Einstein-*A* values and found generally good agreement for the P- and R-branches, but the Q-branches showed discrepancies. These discrepancies vary considerably depending on the band; a recent check using the 2–0 band in the laboratory spectrum shows satisfactory agreement with the Brooke et al. values for the P-, Q-, and R-branches. The discrepancies reported in Ref. [455] are attributed to interactions with the $A^2\Sigma^+$ state that are not included in the intensity calculation. Work is continuing in order to improve the line strength values.

The line strengths for $A^2\Sigma^+$–$X^2\Pi$ bands are from the calculations of Ref. [463]. This work uses the same methodology [467] as described above for the Meinel bands. A new *ab initio* transition dipole function was calculated and RKR potentials were used in LEVEL to compute *N*-dependent transition dipole matrix elements. The Herman-Wallis effect was included in the PGOPHER intensity calculations but, in contrast to the Meinel bands, was relatively small. The intensities in the line list were compared with a laboratory emission spectrum and with astronomical spectra: satisfactory agreement was obtained.

All line positions and intensities (of ^{16}OH) for the Meinel bands and $A^2\Sigma^+$–$X^2\Pi$ band have been updated for HITRAN2020, except for hyperfine transitions of the pure rational transitions. The ^{18}OH and ^{16}OD isotopologues remain unchanged.

The air-broadening coefficients applied to all additional OH Meinel band transitions follow the linearly dependent values (from $N = 1$ to 4) described in HITRAN1996 [11], with a constant value of $\gamma_{air} = 0.040$ cm^{-1}/atm for $N \geq 5$. For *A*–*X* transitions, the *N*-dependant values from Gillis et al. [468] are used (introduced

as part of HITRAN2000 [12]), with a constant value of $\gamma_{air} = 0.0526$ cm^{-1}/atm for $N \geq 4$. For typical atmospheric modeling applications, the self-broadening contribution of OH is expected to be negligible; however a default estimated value of $\gamma_{self} = 0.30$ cm^{-1}/atm has been applied for all transitions to avoid null values. A value of $n_{air} = 0.66$ is applied for the temperature dependence of the air-broadened half-widths of all additional lines [11].

H_2- and He-broadening coefficients (and their temperature dependencies) for OH have also been estimated and introduced to HITRAN and are described in detail by Tan et al. [266].

The line list of OH described above was also used to update the HITEMP database [53]. An intensity threshold of $S = 1.0 \times 10^{-99}$ cm/molecule has been applied to the HITRAN2020 update, but all lines have been added to HITEMP.

2.14. HF: *hydrogen fluoride (molecule 14)*

Unchanged.

2.15. HCl: *hydrogen chloride (molecule 15)*

Unchanged.

2.16. HBr: *hydrogen bromide (molecule 16)*

Unchanged.

2.17. HI: *hydrogen iodide (molecule 17)*

Unchanged.

2.18. ClO: *chlorine monoxide (molecule 18)*

Unchanged.

2.19. OCS: *carbonyl sulfide (molecule 19)*

Carbonyl sulfide (OCS) is the most abundant sulfur-containing gas in the terrestrial atmosphere, with a tropospheric mixing ratio of about 500 ppt [469]. It makes a significant contribution to the formation of stratospheric sulfate aerosols and influences the radiative properties of the Earth's atmosphere, climate change, and stratospheric ozone concentration [470–474]. Carbonyl sulfide is released to the atmosphere by biomass burning, oceans, the oxidation of dimethyl sulfide and carbon disulfide (CS_2), and several anthropogenic sources (coal combustion, aluminum production, and sulfur recovery) [475,476]. OCS is also present in the atmosphere of Venus [477].

When retrieving OCS abundances from infrared atmospheric spectra measured by the JPL MkIV Fourier transform infrared (FTIR) spectrometer, Toon et al. [478] have identified that several bands of observable intensity were missing from the HITRAN database in the region of the strong ν_3 fundamental. To mitigate this deficiency, Toon et al. [478] used 709 unassigned lines, spectral parameters of which were inferred empirically from available laboratory data.

In the course of preparing the HITRAN2020 edition, it was recognized (based on the line positions) that many of these "missing" lines were present in the original unpublished line list from Brown and Fayt [479] (briefly explained in Ref. [12]) which formed a substantial bulk of the HITRAN2000 [12] data for the OCS molecule. These particular lines from Brown and Fayt [479] were, however, omitted from HITRAN because of some concerns regarding the accuracy of their intensities. They were included in the GEISA database [418] and given vibrational assignments. For HITRAN2020 these new bands for the $^{16}O^{12}C^{32}S$, $^{16}O^{12}C^{34}S$, $^{16}O^{13}C^{32}S$ isotopologues were therefore based on simultaneous analyses of the lines from Toon et al. [478] and previously unused data from Brown and Fayt [479]. Effectively, the line intensities from Ref. [12] were scaled to the experimental data [478] by factors of 1.1579 and 2.2592 for the 1111–1110 and 0331–0330 bands of the $^{16}O^{12}C^{32}S$ isotopologue, respectively. Moreover, in the course of analyzing lines from Toon et al. [478], 91 lines of the ν_3 band of the $^{16}O^{13}C^{34}S$ isotopologue (band center 2008.46 cm^{-1}) were identified, which were not present in Ref. [12], HITRAN, nor GEISA. Therefore, line positions and intensities of these lines have been fit to obtain spectroscopic parameters for this isotopologue. These parameters were used to compute the line positions and intensities of 221 lines up to $J = 110$. As a result of this analysis, the lines of the $^{16}O^{13}C^{34}S$ isotopologue now make their debut in HITRAN. The abundance of 4.675×10^{-4} is calculated for this isotopologue with $Q(296K) = 2546.53$ [417]. Uncertainty codes 3 for the line positions and 3 for the line intensities (see Table 2) were used in the case of the new added bands. Fig. 26 gives an overview comparison between HITRAN2016 and the new added bands in HITRAN2020 in the 0–8000 cm^{-1} spectral range.

2.19.1. He-, H_2-, *and* CO_2*-broadening parameters*

The He-broadened and H_2-broadened half-widths of OCS were added to the HITRAN2016 database using the semi-empirical models by Wilzewski et al. [393]. The recent experimental data by Hays et al. [480] (using an E-band chirped pulse spectrometer) showed that the previous values of γ_{He} in HITRAN were approximately half the values obtained in these experiments. A new semi-empirical model, based on a Padé approximant (Eq. (1)), has been used to update the He-line broadening parameters for $J'' \leq 64$. The new fit (which ignored the vibrational dependence) incorporated the early experimental results from Refs. [481–484] as well as the recent measurements by Hays et al. [480]. The H_2-broadened half-widths were also updated using a Padé approximant fitted to the data from Broquier et al. [483]. These H_2- and He-broadening for OCS will be described in detail in Ref. [266].

The CO_2-broadened half-widths of the OCS lines were also updated based on semi-empirical calculations from Ref. [485]. Their temperature dependencies were also updated based on the same work, introducing rotational dependence, while previously only a constant value was used.

2.20. H_2CO: *formaldehyde (molecule 20)*

2.20.1. He-, H_2-, *and* CO_2*-broadening parameters*

The He-broadening of formaldehyde (H_2CO) lines has been measured in the millimeter-wave spectral region in the early work of Nerf [486], and more recently, in the $2\nu_5$ band by cavity-enhanced absorption spectroscopy [487], as well as two strongest transitions in the ν_6 band by direct absorption spectroscopy [488]. A Padé approximant (Eq. (1)) has been applied to fit the ratio of all collected experimental data to HITRAN air-broadening values as a function of the index $J + 0.2K_a$. It was then used to generate γ_{He} for all H_2CO lines in the database from the available air-broadened values.

As for H_2-broadening of H_2CO lines, experiments were carried out in both the millimeter-wave region [486] and the 9–11 μm region [489]. A good agreement was claimed in comparison with these two experiments indicating no vibrational dependence in these data. A similar approach has been carried out to obtain γ_{H_2} using the Padé approximant with additional fitting to an extra constrained point at a higher $J + 0.2K_a$ value.

The CO_2-broadening of two strongest transitions of H_2CO in the ν_6 band been measured by Wang et al. [488]. These measurements were used to scale the air-broadening parameters in the line list to

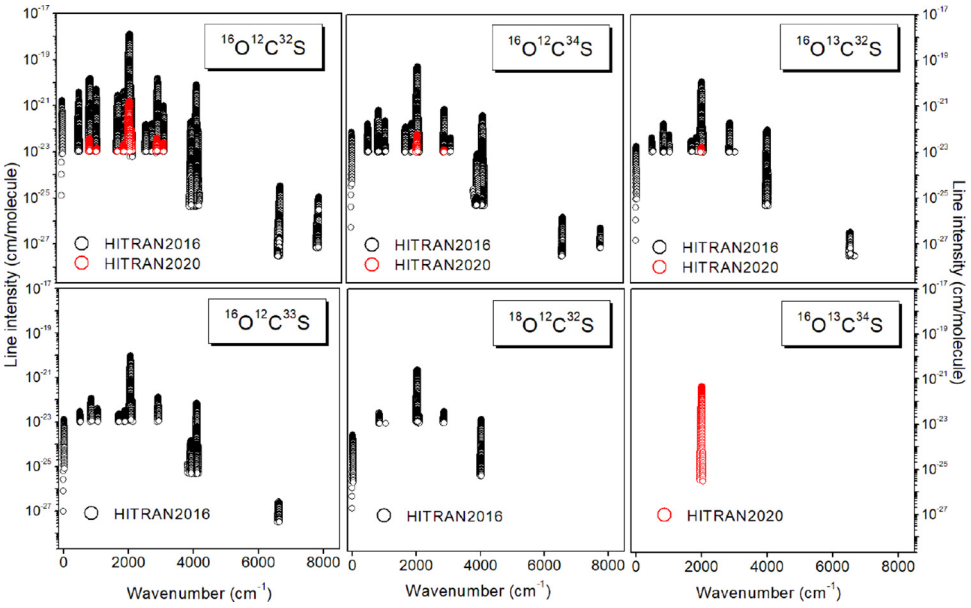

Fig. 26. Overview of the line lists of $^{16}O^{12}C^{32}S$, $^{16}O^{12}C^{34}S$, $^{16}O^{13}C^{32}S$, $^{16}O^{12}C^{33}S$, $^{18}O^{12}C^{32}S$, and $^{16}O^{13}C^{34}S$ isotopologues in HITRAN2016 and the new added bands in HITRAN2020 in the 0–8000 cm^{-1} range.

obtain the estimates for CO_2-broadened half-widths. For the lack of measurements, the same temperature dependence as for air-broadening was used.

2.20.2. Future work

Formaldehyde has been the subject of a recent MARVEL study (see paper published as part of this special issue [490]). This study assembled and validated 16,596 non-redundant transitions from the literature, with a few newly measured as part of the study, giving 5029 empirical energy levels determined to high-resolution accuracy. These empirical levels were then used to replace the computed energy levels in the ExoMol AYTY line list [491] giving 367 779 transitions with empirically-determined wavenumbers of which 183,673 are more intense than the HITRAN cutoff at 296 K. This updated line list will be considered for a future HITRAN upgrade for formaldehyde.

2.21. HOCl*: hypochlorous acid (molecule 21)*

For typical atmospheric modeling applications, the self-broadening contribution of HOCl is expected to be negligible; however a default estimated value of $\gamma_{self} = 0.15$ cm^{-1}/atm has been applied for all transitions to avoid null values.

2.22. N_2*: molecular nitrogen (molecule 22)*

Unchanged.

2.23. HCN*: hydrogen cyanide (molecule 23)*

2.23.1. $H^{12}CN$

HCN is a product of biomass burning in the Earth's atmosphere [492] and it is studied as a possible indicator for bacterial lung infection [493]. HCN, and its isomer HNC which is not included in HITRAN, are important astrophysical species. HCN has recently been detected in Pluto's atmosphere [494] and the atmosphere of exoplanet 55 Cancri e [495]. Isotopologue ratios such as $H^{12}CN/H^{13}CN$ encode information on the thermal and chemical histories of a variety of solar system materials and provide insights into their origins [496].

For the main isotopologue $H^{12}C^{14}N$, the HITRAN entry has been expanded using data from the ExoMol [342] line list due to Barber et al. [497]. This line list is based on the *ab initio* transition intensities of Harris et al. [498] with empirical energy levels from the experiments of Mellau [499]. All lines stronger than 10^{-30} cm/molecule at 296 K and wavenumbers up to 4001 cm^{-1} not in HITRAN2016 were added. HITRAN2016 contained 58,109 lines; the new release more than doubles this number to 131,031 lines.

A new, significantly improved line list for $H^{12}C^{14}N$ called "MOMeNT-90" is published as part of this special issue [500]. A unique feature of this polyatomic line list comes from the fact that all the line positions, even for the very weak lines that are hardly observable experimentally, were derived from experimental energy levels obtained from the corresponding high-temperature studies [499]. At the same time, this large set of empirical vibrational-rotational energy levels made it possible to improve the fitting procedure used to determine the PES and the nonadiabatic correction used in the variational calculations. The new intensities show many differences from the intensities given in HITRAN2016. The accuracy of the calculated line intensities were demonstrated using a variety of absorption and emission spectra. This line list will form the basis for a future update and is highly recommended for practical usage

2.23.2. $H^{13}CN$

The spectrum of $H^{13}C^{14}N$ at wavenumbers below 3405 cm^{-1} was included in HITRAN2004 based on the experiments of Maki et al. [501] and Maiwald et al. [502]. Similar to the subsequent updates in HITRAN for the parent isotopologue, we add many new hot and combinationa bands for $H^{13}C^{14}N$ effectively extending the data to higher wavenumbers based on the use of empirically corrected variational line lists. A new line list was computed using the semi-empirical potential energy surface (PES) and *ab initio* dipole moment surface (DMS) by Makhnev et al. [503]. The update considered wavenumbers up to 8000 cm^{-1} and, limited to transitions which have intensity greater than 10^{-29} cm/molecule at 296 K (at natural abundance). Wavenumbers for the majority of these lines were generated using the empirical energy levels of Ref. [504] but the transition intensities are the *ab initio* ones. These intensities can be considered fairly reliable based on comparisons with the

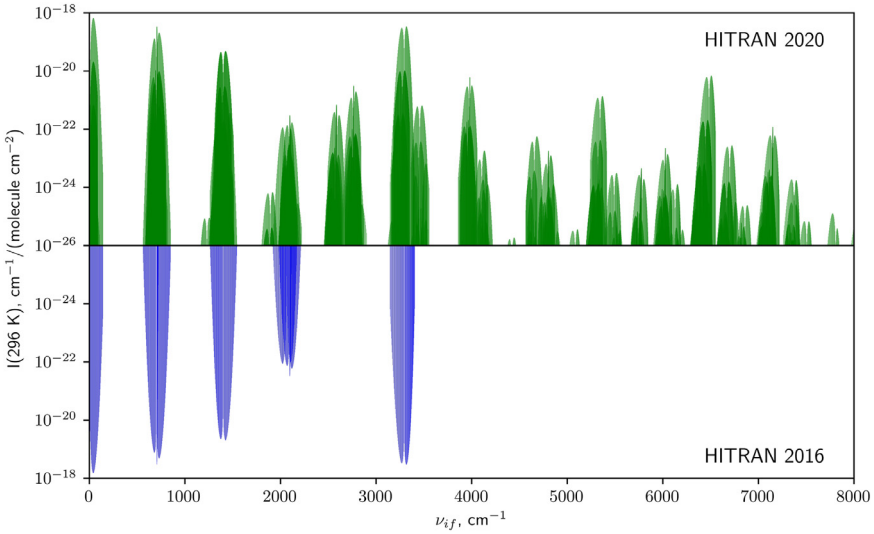

Fig. 27. Comparison of thenew line list for $H^{13}CN$ and that from the HITRAN2016 edition[−1].

recent experimental study by Guay et al. [505] which used a free-running, all-fiber dual electro-optic frequency comb system. An overview of the $H^{13}C^{14}N$ line list in HITRAN2020 is given in Fig. 27.

2.23.3. H_2- *and* He-*broadening parameters*

There are a number of experimental measurements regarding He-broadening in early works [506–510]; however there is generally poor agreement between studies. A critical evaluation has been made to filter selected data, and the rotational distribution of the He-broadening line width (γ_{He}) is described using a Padé approximant (Eq. (1)) with $J'' \leq 16$.

The microwave transient emission technique has been used to study the *l*-doublet transitions of HCN with H_2-broadening [507,510]. Later, frequency-stabilized tunable diode laser spectrometers have been used to study the H_2-broadening line width in the ν_2 band [508,511]. More recently, new experimental measurements of H_2-broadening in the millimeter-wave region have been reported [512]. Comprehensive comparisons with all experimental results exhibit a strong rotational dependence, while they appear to be vibrationally independent. A similar procedure has been used to derive the semi-empirical H_2-broadening line width (γ_{H_2}) based on the Padé approximant for transitions with $J'' \leq 31$.

2.24. CH_3Cl*: methyl chloride (molecule 24)*

Unchanged.

2.25. H_2O_2*: hydrogen peroxide (molecule 25)*

For the self-broadening half-width (which previously had values of zero), a default estimate value of 0.3 cm^{-1}/atm has now been assigned to all transitions for this molecule.

2.26. C_2H_2*: acetylene (molecule 26)*

Acetylene is a minor trace gas in the terrestrial atmosphere, primarily originating from combustion sources, and therefore its concentration is highly correlated with carbon monoxide [513]. It is also present in the atmospheres of solar system gas giants and their satellites [514–516]. The acetylene (C_2H_2) molecule is a prototype system for molecular dynamics with a very rich IR spectra as a consequence of strong couplings between vibrational modes. However, the NIR spectral region in HITRAN had been missing many spectral details.

The global modeling of the C_2H_2 spectrum in the frame of the polyad model has been developed at ULB-Brussels [517], and IAO-Tomsk [518,519]. The approximate relations of the vibrational modes give rise to polyads such that $P = 5V_1 + 3V_2 + 5V_3 + V_4 + V_5$ (where V_i are the vibrational normal mode quantum numbers, with $i = 1 - 5$). The vibrational assignments used for C_2H_2 in previous editions of HITRAN only indicated the total bending angular momentum, $|l_4 + l_5|$. However, as many more bands have been added to HITRAN in recent additions, it has become necessary to separate the bending angular momentum quantum numbers to avoid degeneracy and allow unique identification. For HITRAN2020, the vibrational assignment has been updated for all acetylene transitions of the three isotopologues so that $V_1, V_2, V_3, V_4, V_5, l_4, l_5$,+/-, *u*/*g* quantum numbers are now used to identify each vibrational state (see the Supplementary Material of this paper for a description of the upper- and lower-state quanta in the ".par" format).

For HITRAN2016, numerous bands were added in the 13–248 cm^{-1} and 390–634 cm^{-1} spectral regions. The last region was supplemented and extended (in the 390–893 cm^{-1} region) based on the recent $\Delta P = 1$ work of Jacquemart et al. [520]. This work used a multi-spectrum analysis of FTS measurements, and line intensities were measured for 18 bands (only four of them previously reported). The very good predictability of the theoretical model developed in IAO-Tomsk has been used to include new hot bands in this region as well as to improve line positions and/or intensities of the existing HITRAN2016 bands.

Comparisons to N_2-broadened (1 atm) PNNL spectra [244] of C_2H_2 for the beginning of the $\Delta P = 6$ region indicated absorption features of some bands not present in HITRAN. Based on the global model developed in IAO-Tomsk [519], 8 hot bands have been added to HITRAN between 3738 and 3996 cm^{-1} (see Table 9). Note that under atmospheric pressures, Q-branches of acetylene are affected by line-mixing. This line-mixing is especially the case for the intense Q-branches of $^{12}C_2H_2$ located at 730, 3881, 3896 and 4090 cm^{-1}. Using a Voigt line profile for these Q-branches in atmospheric retrievals will lead to systematic residuals due to line-mixing. Studies are in progress to model line-mixing effects for Q-branches of acetylene under atmospheric conditions and will be considered for updates to HITRAN.

Lyulin and Campargue [521] collected together the recent experimental studies covering the 5850–6341 cm^{-1} and 7000–9415 cm^{-1} spectral regions that used FTS measurements for the stronger

Table 9
Hot bands of acetylene included in HITRAN between 3738 and 3996 cm^{-1}. N is the number of transitions per band, ν_{min} and ν_{max} are the minimum and maximum wavenumbers (in cm^{-1}), and S_{sum} is the sum of line intensities (in 10^{-20} cm/molecule).

Upper state[a]	Lower state[a]	N	ν_{min}	ν_{max}	S_{sum}
01031 3 −1 u	00010 1 0 g	263	3744	3969	0.58
00120 2 0 u	00010 1 0 g	250	3770	3984	0.58
01031 1 −1 $\pm u$	00010 1 0 g	205	3794	3977	0.36
00120 0 0 $+u$	00010 1 0 g	101	3817	3975	0.24
00111 1 1 g	00001 0 1 u	240	3772	3980	0.20
00111 1 −1 $\pm g$	00001 0 1 u	233	3780	3975	0.16
01022 2 0 g	00001 0 1 u	220	3756	3963	0.13
01022 2 −2 $\pm g$	00001 0 1 u	251	3749	3959	0.12

[a]The upper and lower vibrational states have the format V_1, V_2, V_3, V_4, V_5, l_4, l_5, $\pm$, u/g. The full FORTRAN descriptors for the global and local quanta are provided in the Supplementary Material.

bands [522–524] and Cavity Ring Down Spectroscopy (CRDS) for the weaker absorption windows between bands [525–527]. Additional CRDS [528] and FTS [529,530] studies covered the 5693–5882 cm^{-1} and 9280–10,740 cm^{-1} spectral ranges, respectively. Following Ref. [521], these studies have been compiled into an empirical line list for HITRAN. The line list includes numerous $^{12}C_2H_2$ and $^{12}C^{13}CH_2$ bands that have not previously been included in HITRAN. Fig. 28 displays the significant number of additional bands that have been included in the NIR for HITRAN2020.

As part of the ExoMol project [531], the "aCeTY" line list has been built for $^{12}C_2H_2$ [532] using the MARVEL acetylene database wherever possible [533]. Comparisons of the aCeTY line list and global model developed in IAO-Tomsk with measurements in the $\Delta P = 1$ region are presented in Jacquemart et al. [520]. The line lists from aCeTY and the ASD-1000 database [518] are intended for use at high temperature, therefore further comparisons between models and measurements will be investigated for updates to HITEMP [53].

In addition, H_2-, He- and CO_2-broadening coefficients that were introduced to HITRAN by Wilzewski et al. [393] have been extended to the new transitions for C_2H_2.

A small number of Einstein-A coefficients and statistical weights have also been corrected for some of the bands of C_2H_2.

2.27. C_2H_6: ethane (molecule 27)

Ethane (C_2H_6) is the most abundant non-methane hydrocarbon (NMHC) in the atmosphere of the outer planets [534] and Titan [535], playing an important role as a tracer of atmospheric chemistry and dynamics. Ethane is also an important constituent of comets and their gaseous envelopes [536]. The relative abundance of isotopic species of ethane, such as D/H ratio from C_2H_5D/C_2H_6, can carry valuable information about the atmospheric formation and chemical evolution. In this work, we have expanded the ethane line list in HITRAN to include the ν_5, ν_7 and underlying combination bands of $^{12}C_2H_6$ and the ν_4, ν_{12}, and $2\nu_6$ bands of $^{12}C_2H_5D$ from recent model predictions validated through a laboratory study.

2.27.1. Region of ν_5 and ν_7 fundamentals (2800–3071 cm^{-1})

Until this present edition, HITRAN contained only strong Q-branch lines of the ν_7 band in the spectral region around 3.3 μm. Nevertheless, these lines alone are insufficient to correctly interpret atmospheric and planetary spectra and a better high-resolution spectroscopic model was needed. This spectral range is dominated by the C-H stretching fundamental of ν_5 (parallel band) and ν_7 (degenerate perpendicular band), and the $\nu_8 + \nu_{11}$ combination band (ν_8 and ν_{11} are the degenerate antisymmetric and symmetric deformations of the two methyl groups, respectively). The characterization of rotational structure in this complex molecule is non-trivial because the ν_7 band is severely perturbed by overtones and combination states (with a low-frequency torsional mode, ν_4 at 289 cm^{-1}) that are in Fermi or Coriolis resonance with ν_7 [537].

For the HITRAN2020 edition, we expand and advance the ν_7 band at 3.3 μm based on Refs. [536,538], add a linelist for the ν_5 band of ethane at 3.4 μm based on Radeva et al. [539], and add combination bands that include the strong $\nu_8 + \nu_{11}$ band based on Lattanzi et al. [538]. These references, and a summary of how their data were adapted to HITRAN, are described below.

2.27.2. Line list from Ref. [538]

Relying on a high-resolution FTS spectrum recorded at 229 K in Brussels and line positions measured in a Doppler-limited spectrum recorded at 119 K using a tunable difference-frequency laser spectrometer [538,540] , the 2860–3060 cm^{-1} region of ethane was re-investigated.

This work led to some progress in the understanding of the complex network of interacting vibrational levels occurring in this

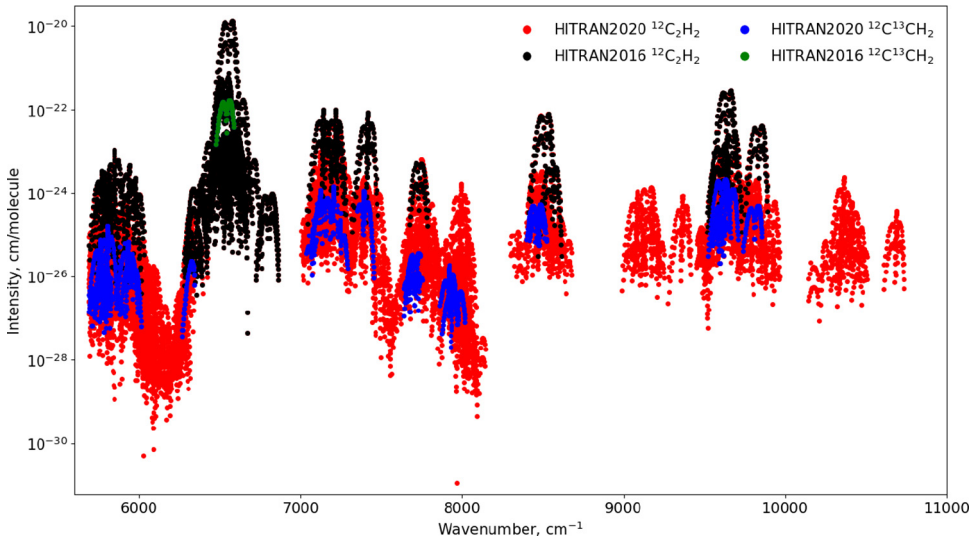

Fig. 28. An overview of the NIR bands of C_2H_2 that have been added to HITRAN based on FTS and CRDS measurements [521–530].

energy range (see Fig. 2 of Lattanzi et al. [538]). In particular, 572 line positions belonging to ^{p}P and ^{r}R transitions in the ν_7 band (maximum $J = 30$), $^{r}Q_0$, $^{p}P_1$ and $^{r}R_1$ transitions in the $\nu_8 + \nu_{11}$ band, and $^{p}P_6$ transitions in the $\nu_3 + 2\nu_4 + \nu_8$ band were least-squares fit to a Hamiltonian. The model involved the ν_7 degenerate vibrational level and four degenerate perturbers, i.e., the $\nu_8 + \nu_{11}$, $\nu_3 + 2\nu_4 + \nu_8$, $\nu_4 + \nu_{11} + \nu_{12}$ and $\nu_3 + 3\nu_4 + \nu_{12}$ vibrational levels. Although RMS deviations as large as 0.018 cm^{-1} were obtained, indicating that the analysis is far from complete, a line list was generated because it still provided a much improved description of the 3.3 μm region of the ethane spectrum. Positions, relative intensities, and lower-state energies of 4969 lines associated with transitions belonging to five perpendicular bands ($\nu_8 + \nu_{11}$, $\nu_4 + \nu_{11} + \nu_{12}$, $\nu_3 + 3\nu_4 + \nu_{12}$, $\nu_8 + \nu_{11}$ and $\nu_3 + 2\nu_4 + \nu_8$) were calculated between 2900 and 3071 cm^{-1}, relying on the model and parameters involved therein and resulting from the least squares analysis. The content of the line list is summarized in Table 8 of Ref. [538]. As detailed in Ref. [538], incorrectly predicted line positions were recomputed using empirical upper-state energies. These altered positions are indicated by the HITRAN error code of 4 (see Table 2), while a conservative error code of 2 was assigned to the remaining predicted positions. The predicted relative line intensities were normalized by inspection of observed and calculated spectra (HITRAN error code = 2). The Lattanzi et al. [538] line list covers the 2900–3071 cm^{-1} region.

2.27.3. Line lists from Refs. [536,539]

These models of ν_5 and ν_7 were generated by characterizing the upper ro-vibrational states using linear progressions of J and K. For the ground vibrational state, spectroscopic constants from Pine and Lafferty [537] were used, with specific corrections for some J/K ladders (see details in Villanueva et al. [536]). For the ν_5 model, as explained in Radeva et al. [539], the upper-state rotational constants were not present in the literature. Therefore they were obtained by fitting experimental data given in Ref. [541] for each K ladder. For the band intensity of the ν_5 band, parameters reported in Ref. [542] were employed.

The ν_7 upper-state ro-vibrational structure was derived by fitting to experimental data as presented in Ref. [543], in which cross-sections for ethane in the 3-μm region at temperatures between 194 and 297 K and total pressures from 0.0689 Torr to 763.48 Torr were reported. Using this dataset, we identified 466 lines, which were consolidated with 122 lines reported in Ref. [542] and 66 reported in Ref. [541], ultimately deriving rotational constants for 30 K-ladders of the ν_7 band of ethane. Our model does provide good results for the selected lines (standard deviation of 0.005 cm^{-1} for the 654 lines), but because of the numerous perturbations, their validity is relatively uncertain.

Determining accurate band intensities from experimental data in this highly active spectral region can be complex, in particular for ethane at 3.3 μm, since multiple fundamental (e.g., ν_7 and ν_5), combination (e.g., $\nu_8 + \nu_{11}$), and hot-bands (e.g., $\nu_7 + \nu_4$–ν_4) overlap at these wavelengths. As reported in Ref. [543], accurate absorption cross sections for ethane at these wavelengths were determined, with an overall uncertainty of 4%. Their cross-sections were calibrated against PNNL spectra [244]. Considering these new absorption cross-sections and taking into account the first torsional hot-band, we derived a band intensity of 301 cm^{-2}atm^{-1} for the ν_7 band [536].

2.27.4. Combining the line lists based on validations against laboratory data

The three line lists described above were cross-evaluated against each other, HITRAN2016 data, and the experimental cross-sections from Refs. [543,544]. To that end, HAPI [52] was used to generate cross-sections under the same thermodynamic conditions and resolution as experimental data and the synthetic cross-sections were compared with the experimental ones. It was found that data from Refs. [536,538] both agree quite well with the experimental data near the ν_7 band center, with both line lists being superior to the HITRAN2016 data except for the region around the $^{p}Q_7$ manifold near 2976 cm^{-1} where HITRAN was based on purely empirical data from Pine and Lafferty [537]. As rotational quanta increase, Ref. [538] produced much better agreement with the experimental data. At around 3070 cm^{-1}, the deviations of the Ref. [536] line list from experimental data becomes so significant (up to 0.5 cm^{-1}) that it was decided to not use this list in the 3071-3100 cm^{-1} interval, which is not available in Ref. [538]. In summary, the ν_7 band and combination bands were taken from Ref. [538]. However in selected spectral windows where the residuals based on the Ref. [536] data were better, the latter line list was employed. In the small spectral window around 2976 cm,$^{-1}$ HITRAN2016 data were retained (although several lines had to be reassigned to the $\nu_8 + \nu_{11}$ band).

Only the Ref. [539] line list is available for the ν_5 band. Validations have shown substantially larger disagreements than those observed with either of the line lists in the ν_7 band. Some notable modifications were therefore applied to the line list from Ref. [539]. First, intensities for all the lines have been reduced by 20% to better agree with both sets of experimental cross-sections. The line positions for many lines with $K > 1$ appeared to strongly deviate from their observed values. For instance, the deviations from experimental values for lines with K=2 ranged from 0.004 cm^{-1} (for J=2) up to 0.17 cm^{-1} (for J=21). We therefore applied a third order polynomial correction in J to adjust the line positions of transitions with $K = 2$ and 3, but further refinements are needed in the future. Considering the rapidly growing deviations (with rotational quanta), the Ref. [539] line list was also truncated by applying an intensity cutoff of 10^{-24} cm/molecule (as opposed to 10^{-33} cm/molecule used in the original line list). After these modifications the resulting line list produced satisfactory agreement with laboratory cross-sections. However, further improvements in this region, including addition of the hot bands, would clearly be beneficial.

Fig. 29 provides an overview of the ethane spectra in the 3.3-μm spectral region, showing experimental cross-sections from Ref. [544] in the lower panel, and those generated with HAPI using HITRAN2016 and HITRAN2020.

2.27.5. $^{12}CH_3{}^{12}CH_2D$

Mono-deuterated ethane is the third most abundant isotope of ethane, with a HITRAN abundance of 9.131×10^{-4} [57]. The deuterium substitution reduces the symmetry, which results in significantly more transitions being visible in the mid-infrared. It also slightly offsets the bright series of Q-branches around 2980 cm^{-1}, which are characteristic for C_2H_6, allowing the possibility of remote observations of the D/H ratio in this spectral range. Doney et al. [545] determined line positions and relative intensities of transitions in the C-D (centered around 2170 cm^{-1}) and C-H (2850–3030 cm^{-1}) stretches, capturing the ν_4 band (2170 cm^{-1}), the $2\nu_7$ band (2770 cm^{-1}), as well as a series of bands between 2850 and 3030 cm^{-1} ($2\nu_{14}$, $2\nu_6$, $2\nu_5$, ν_1, ν_2 and ν_{12}). The assignments were made by employing *ab initio* CCSD(T)/ANO1 calculations. The study was based on spectra recorded at high resolution using a Bruker IFS-125HR spectrometer equipped with a cryogenic Herriott cell at JPL [546,547]. For the assignments in Ref. [545], spectra were recorded at 85 K, at very low pressures below 0.0022 Torr with a pathlength of 20.941 m. The model includes transitions up to $J'' \leq 22$, $K_a'' \leq 10$ and $K_c'' \leq 18$, with uncertainties of the order of ~0.05 cm^{-1}. Although the model captures most of the strong transitions, further work is needed to refine the description

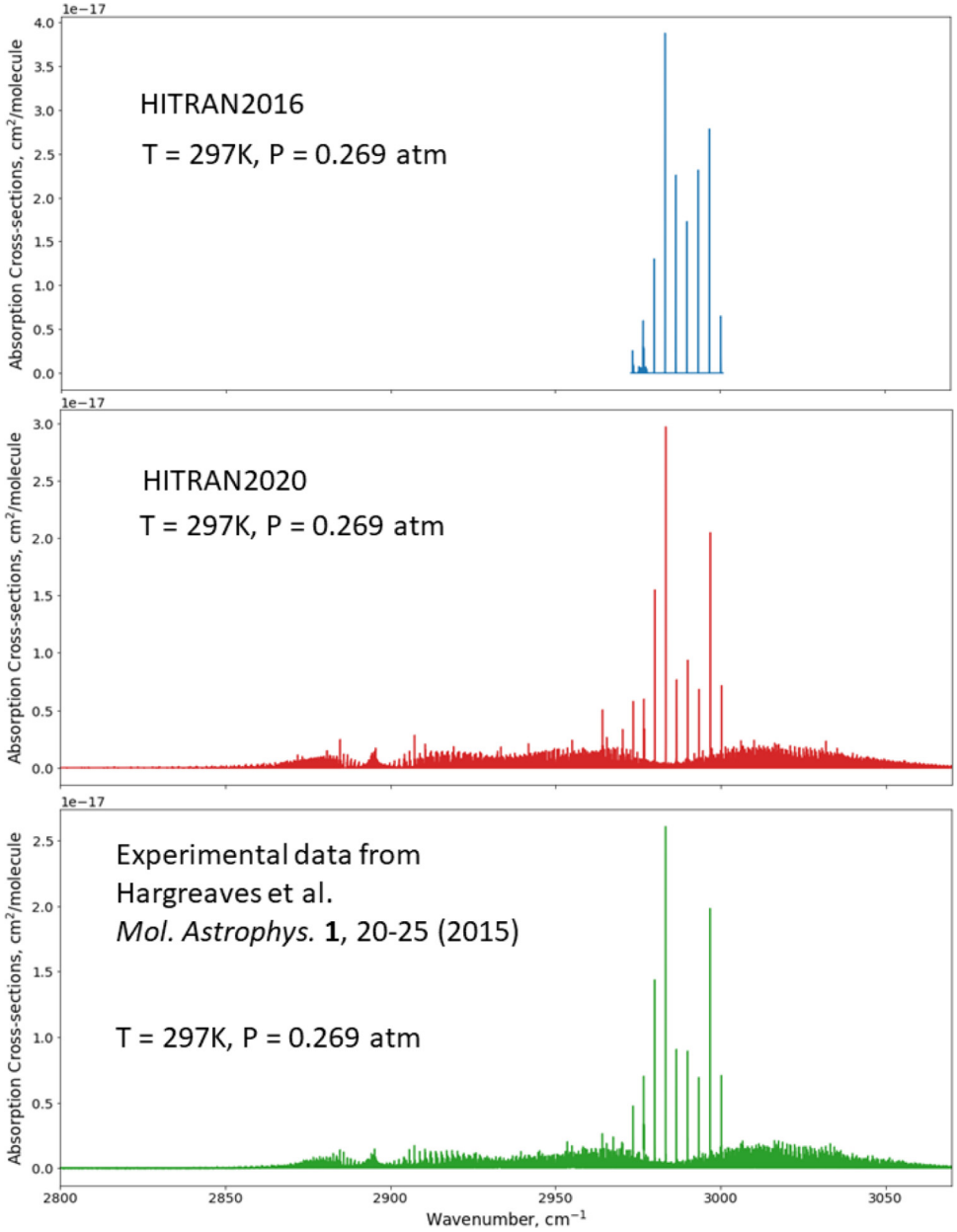

Fig. 29. The ethane spectra in the 3.3-μm spectral region, showing experimental cross-sections from Ref. [544] in the lower panel, and those generated with HAPI (under the same thermodynamic conditions) using HITRAN2016 and HITRAN2020 in the top and middle panels, respectively.

of weak transitions in the 2850–3030 cm^{-1} region. No hot bands are included in this line list.

For inclusion into HITRAN, the intensities of the C_2H_5D transitions have been calibrated against additional experimental spectra recorded using the same setup, but at higher pressures (2.023 and 0.1367 Torr), shorter path lengths (0.2038 and 0.1526 m), but at intermediate cold and room temperatures (130 and 298 K). This line list will be provided as one of the immediate updates to the official release of HITRAN2020.

2.27.6. Line-shape parameters

For all of the new bands of ethane (including the deuterated isotopologue) self- and air-broadening half-widths, and their temperature dependencees, were estimated using the expressions reported by Devi et al. [548,549] from measurements in the Q-branch of the ν_9 band near 822 cm^{-1}. The parameters involved in these expressions were applied from $K'' = 0$ to $K_{max} = 3$ for the broadening coefficients and $K'' = 0$ to $K_{max} = 7$ for their temperature dependence, while those provided for K_{max} were used for transitions with $K'' > K_{max}$. The uncertainties for these pressure-induced coefficients are conservatively set (error code = 2, see Table 2) with the warning that the uncertainty is unknown for $J'' > 31$. Finally, a constant value of -0.004 cm^{-1}atm^{-1} (error code = 1) was estimated for air pressure induced shifts, from the average of two air-broadening measurements at 296 K for $^rQ_0$ and $^pQ_3$ of the ν_7 band [541]. For pressure-shifts, we considered the N_2-broadened pressure-induced shifts of -0.004 cm^{-1}atm^{-1} reported in Ref. [541] from $^rQ_0$ and $^pQ_3$.

For the ν_4 torsional band at 35 μm region [550], the temperature dependence exponent of the air-broadened line half-widths, n_{N_2}, listed in HITRAN2016 [16] had a truncation error which removed the integer part when the exponent is greater than 1. This issue has been fixed for HITRAN2020. In addition, the self-broadening values in that band were previously given as a con-

stant, while in HITRAN2020 they correspond to those in Ref. [548] as was originally intended.

2.28. PH_3: *phosphine (molecule 28)*

On Earth, phosphine (PH_3) is a trace constituent of the lower troposphere with very low, but highly variable, atmospheric concentrations [551]. PH_3 has also long been observed in the atmospheres of Jupiter and Saturn due to prominent spectral IR features [552] and is used as a tracer for tropospheric dynamics in gas giant planets [553]. While PH_3 is associated with anaerobic ecosystems of Earth, and notoriously toxic for humans [554], it has also been proposed as a potential biosignature gas in anoxic exoplanets [555].

Recently, a tentative detection of the $R(0)$ rotational transition in the atmosphere of Venus using mm-wave observations [556] has prompted significant discussion relating to the chemical (and suggested biological) production pathways that can account for the observed concentration. However, a number of followup studies [557–560] have cast substantial doubt on the original detection and conclusions. Nevertheless, these recent works have contributed to a surge of interest in accurate PH_3 spectroscopic parameters.

The IR spectrum of PH_3 forms distinct polyad bands due to the approximate relationship of the vibrational modes: $\nu_1 \approx 2\nu_2 \approx \nu_3 \approx 2\nu_4 \approx \nu_2 + \nu_4$. For HITRAN2020, the line positions and intensities in the dyad (750–1500 cm^{-1}), pentad (1750–2600 cm^{-1}) and octad (2750–3650 cm^{-1}) spectral regions have been extended or updated, while pure rotational transitions remain unchanged from HITRAN2016 [16].

Kleiner and Devi [561] produced an extensive line list covering the pentad region, based upon the experimental measurements of Refs. [562,563] that were described in HITRAN2016. The Ref. [561] line list consists of 9894 transitions of the $2\nu_2$, $2\nu_4$, $\nu_2 + \nu_4$, ν_1, ν_3 bands. Line positions were obtained by fitting 3403 experimental measurements with a Hamiltonian including the interactions within the $V_2 = 2$, $V_4 = 2$, $V_2 = V_4 = 1$, $V_1 = 1$ and $V_3 = 1$ upper states (up to $J = 14$) [563], which were combined with empirically-determined transition frequencies calculated from accurate ground-state energy levels [564]. Line intensities were based on a fit to 1579 selected transitions [563] with RMS deviations of 7.7%. The methods used for both energy level and intensity fittings are described in Ref. [565].

The octad region has been analysed by Nikitin et al. [566] between 2733–3660 cm^{-1} using a global approach. This analysis builds on a previous model for the lower three polyads [567], which was noted to have poor simulation of spectra above 3100 cm^{-1}. The new model extended the assignments in Ref. [568] for the octad region and has been validated against FTS spectra [244,568,569] with a quoted RMS deviation of 0.0018 cm^{-1} and 11% for the positions and intensities, respectively.

Recently, Rey et al. [570] have produced an updated vibration-rotation line list of PH_3 in several steps. As PH_3 is a semi-rigid molecule without large amplitude vibrations, the normal mode representation provides an adequate description of the nuclear motions. At the first step, the full nuclear motion Hamiltonian was built in the Eckart-Watson form [571] from the PES reported by Nikitin et al. [572] using the reduction techniques described in Ref. [573]. For a full account of symmetry, the energy levels and transitions were computed by the variational method using the irreducible tensor operators following the technique of Refs. [574,575]. At the second step, the *ab initio* PES was empirically optimized to match precisely the four observed fundamental band origins. The line intensities were computed from the *ab initio* DMS of Nikiin et al. [576]. The RMS deviations for energy levels up to $J = 20$ between the variational calculations and the empirically-fitted effective Hamiltonian were 0.04, 0.05 and 0.07 cm^{-1} for the dyad, pentad and octad, respectively. Additionally, to improve the accuracy of the line positions, we have followed the strategy successfully applied for methane line lists [309], which consists of making empirical corrections using a set of experimental vibration-rotation energy levels. Finally, a data set composed of 14,400 energy levels up to the octad ($J_{max} = 25$) and obtained from previous analyses [566–568] was used to provide empirical corrections for more than 100,000 line positions. The corresponding line list is available via the TheoReTS web site [310]. To determine the preferred line intensities and positions for each spectral region, comparisons have been made to high-resolution FTS spectra recorded at PNNL covering the dyad [577] and pentad [562] regions (resolutions of 0.0020 cm^{-1} and 0.0115 cm^{-1}, respectively), along with those obtained from the McMath-Pierce FTS at Kitt Peak [568] for the octad region (0.0115 cm^{-1} resolution). Further FTS measurements from PNNL [244], which include all three polyads at lower resolution (0.112 cm^{-1}), have also been used.

For the dyad region, the ν_2, ν_4 and $2\nu_2$–ν_2 bands from HITRAN2016 have been supplemented with the $\nu_2 + \nu_4$–ν_4, $\nu_2 + \nu_4$–ν_2 and $2\nu_4$–ν_4 hot bands from Rey et al. [570].

The line list of Kleiner and Devi [561] was intended to be used for updating the pentad region in HITRAN2016. However, the recent theoretical work of Ref. [570] was shown to provide a significant improvement toward the edges of the pentad region as higher rotational levels (i.e., $J'' > 14$, $K'' > 12$) were not included in the analysis of Ref. [561]. Fig. 30 demonstrates the significant improvement when compared to PNNL spectra at 25°C [244]. The positions and intensities of Ref. [570] have therefore been adopted for all pentad transitions in HITRAN2020.

In HITRAN2016, the octad region primarily constituted unassigned empirical lines, which restricts the applicable temperature range. The line lists provided by Nikitin et al. [566,570] are fully assigned and compared to HITRAN2016 in their ability to reproduce observations. It should be noted that comparisons for the $3\nu_2$ band are hindered by low signal to noise in the PNNL spectra. High-resolution comparisons demonstrated that the Ref. [566] list yields the best performance with smallest RMS residuals across the octad region and has been used to update HITRAN. The $4\nu_2$–ν_2 hot band from HITRAN2016 has been retained as these lines were observed in the spectra of Ref. [568]. The octad region of the PH_3 now includes quantum assignments for all transitions.

Sousa-Silva et al. [578] refined an earlier PES [579] to produce the "SAlTY" line list covering the spectral range up 10 000 cm^{-1} and temperatures up to 1500 K. A calculated spectrum for the pentad region is included in the comparisons of Fig. 30. While SAlTY is primarily intended for high-temperature simulations, these line predictions can be used to advance the assignment of experimental spectra. Furthermore, a MARVEL project is in progress which will allow many of the lines in SAlTY to reach experimental accuracy.

There is potential for further empirical improvements to line positions in the dyad, pentad and octad regions. This analysis will be considered for future updates for PH_3.

2.28.1. *Line-shape parameters of* PH_3

The air-broadening half-widths introduced in HITRAN2008 [14] have been extended to all new transitions and are based on scaled N_2-broadening measurements [568,580–582]. The linear relationship for the temperature dependence exponents of the air-broadening coefficients $n_{air} = 0.702 - 0.01J''$ [582,583] has also been extended to all new transitions. For HITRAN2020, all self-broadening half-widths have been updated with the method described in Ref. [566] for the octad region, using an empirical function developed for the ν_3 band [562]. The self-broadening coefficients are given by

$$\gamma_{self} = 0.1172 - 9.257 \times 10^{-5}[J_m(J_m + 1) + K_m^2] \quad (3)$$

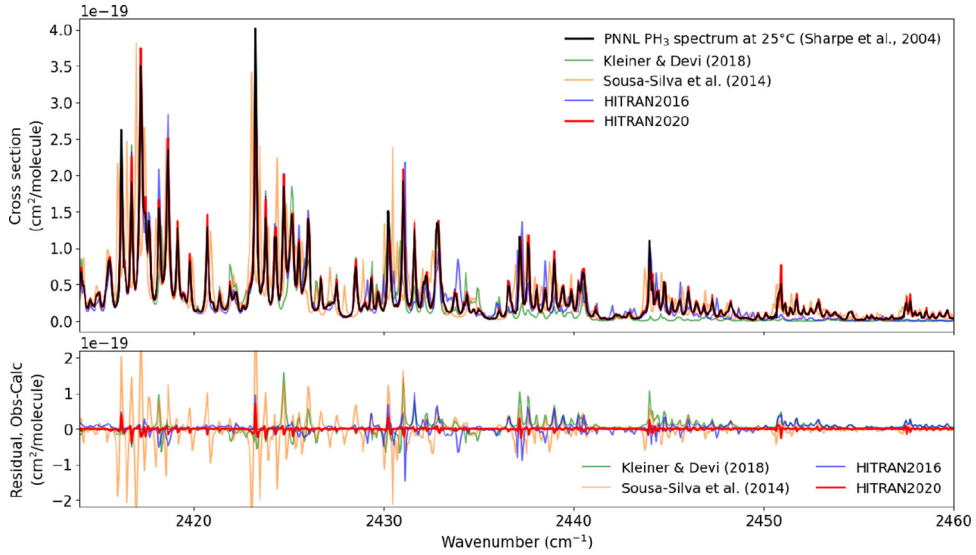

Fig. 30. Spectra for the pentad region of PH_3 compared to the PNNL absorption cross sections at 25°C [244]. The upper panel displays calculated spectra using the HITRAN2020 (see text for details), HITRAN2016 [16], Kleiner and Devi [561] and Sousa-Silva et al. [578] line lists. The lower panel displays the obs-calc residuals, where the observation corresponds to the PNNL spectrum and calculated spectra are identified by the legend (all are shown in the upper panel).

where J_m and K_m refer to the maximum values of J and K, respectively, for each transition. A minimum value of $\gamma_{self} = 0.05$ cm^{-1}/atm is applied when the predicted values become too small.

Due to the presence of PH_3 in the atmospheres of Jupiter and Saturn, there have been numerous studies aimed at measuring the H_2- and He-broadening half-widths as well as their temperature dependencies [562,568,580,582–591]. For HITRAN, H_2- and He-broadening coefficients and temperature dependencies have been introduced for PH_3, which will be described in detail in Ref. [266].

While updating HITRAN, the Einstein-*A* coefficients for all *E* symmetry transitions have been corrected.

Line-mixing coefficients for phosphine have not been introduced to HITRAN yet, although values are available from experimental [562,589] and theoretical [591] studies. This will be considered for the future.

2.29. COF_2: *carbonyl fluoride (molecule 29)*

Unchanged.

2.30. SF_6: *sulfur hexafluoride (molecule 30)*

Sulfur hexafluoride (SF_6) line lists in the ν_3 (stretching) and ν_4 (bending) regions have been largely updated recently thanks to new global analyses of high-resolution infrared spectra [592,593]. For the main isotopologue, $^{32}SF_6$, these lists now contain some hot bands. This amounts to more than 350,000 calculated lines in the SHeCaSDa database (Sulfur Hexafluoride Calculated Spectroscopic Database) [594] which are included in the present HITRAN2020 edition.

Interestingly, the amount of lines for this molecule reduce by about a factor of eight. The reason is a substantially smaller cutoff in rotational quanta. Indeed, as it is demonstrated in the *ab initio* work [595] from the TheoReTs group [310], one needs to include a large amount of hot-bands in order to model even room temperature absorption accurately. Ref. [595] demonstrated that their *ab initio* calculations are able to model the PNNL spectra [244] accurately. The corresponding line list by Rey et al. [596] will be considered for future updates, although it contains billions of lines. Even with the use of "effective" lines proposed in Ref. [56], it will likely contain tens of millions of transitions and therefore SF_6 line list will continue to reside in the supplementary folder of static files. It is worth reminding the HITRAN users that there is a comprehensive set of experimental cross-sections, which are provided in HITRAN for this molecule (see Section 3.1 for details).

For the $^{33}SF_6$, $^{34}SF_6$ and $^{36}SF_6$ minor isotopologues, only the ν_3 fundamental band are present [597] in the SHeCaSDa database, but it will be considered to include those data [596] in the future.

2.31. H_2S: *hydrogen sulfide (molecule 31)*

There are no changes to the line positions or intensities of this molecule. However, some recent works offer promising potential for updates in the near future. Recent semi-empirical NIR line lists from Ulenikov et al. [598,599] could be a potential source for improvements to the intensities of relevant bands in future updates.

The line positions throughout the database can be further revised with some recent data including that from the MARVEL analyses [600]. A total of 44,325 measured and assigned transitions were collected in the MARVEL database [600] and a careful analysis of these transitions resulted in 7436 empirical ro-vibrational energy levels up to 16,890 cm^{-1}; these empirical energy levels have already been used to improve the ExoMol line list for H_2S [601]. Self-broadening parameters from Ref. [602] could also be used as a source for future updates.

2.31.1. He-, H_2-, *and* CO_2*-broadening parameters*

The rotational dependence of He-broadening for H_2S lines was studied in the ν_2 band [603,604], and in the ν_1 and ν_3 band [605]. An optimal set of parameters for a model inter-molecular potential that provides the best reproduction of noble gas broadening coefficients for H_2S lines was reported by Starikov et al. [606]. However, significant discrepancies take place for almost all transitions in the ν_2 band for H_2S-He, and in some cases can reach 100%. We excluded the early work of Ref. [603] because of large discrepancies, and utilized experimental results from Kissel et al. [604,605]. The broadening coefficients for γ_{He} decrease rapidly with increasing rotational quantum numbers. A Padé approximant (Eq. (1)) has been applied to fit all collected experimental data, and a semi-empirical model has been used to generate γ_{He} for H_2S lines in the database versus the index $J + 0.2K_a$.

The H_2-broadening for H_2S lines has been measured from a pulse-driven diode laser spectrometer [607] in the ν_2 band, and also calculated based on experimental results [608]. For HITRAN, the H_2-broadening is fit using a similar procedure to that of He-broadening, with a Padé approximant (Eq. (1)) being applied to the experimental results covering J'' up to 12.

Experimentally determined CO_2-broadening parameters for 39 transitions of H_2S in the ν_2 band were presented in Ref. [607] with uncertainties about 2%. Just as in the case of H_2- and He-broadening, a semi-empirical method was used to model these parameters.

These H_2-, He-, and CO_2-broadening for H_2S will be described in detail in Ref. [266].

2.32. HCOOH: *formic acid (molecule 32)*

Formic acid is one of the most abundant organic acids in the terrestrial atmosphere and is being monitored by different remote sensing instruments, including IASI [609] and ACE [610]. In this edition, a line list for the ν_7 and ν_9 fundamentals of HCOOH at 16 μm has been included. All simulations and fits described in this section were performed using PGOPHER [460]. Line positions were computed using the spectroscopic constants previously reported for the ground vibrational state and the strongly interacting 7^1 and 9^1 vibrational states of the normal isotopologue of formic acid [611]. This corresponds to the inclusion of 53 diagonal parameters and 12 off-diagonal parameters. The 7^1–0 and 9^1–0 bands are hybrid *a*/*b*-type and *c*-type, respectively. Their relative transition moments were determined by performing a fit to the intensities of 2239 isolated peaks (using 3125 transitions) identified in a high resolution (0.00096 cm^{-1}) experimental spectrum of HCOOH (similar to that reported in Ref. [612]) with absorbances (base-10) ranging from 0.1 to 1; they are $\mu_a/\mu_b/\mu_c$ = 1/-1.62/3.45. The experimental spectrum, which covered 400-1250 cm^{-1} (8-25 μm) allowed scaling the calculated relative line intensities within the 16 μm bands to the known spectral line intensities, within the 9 μm bands (already in HITRAN) [613]. The intensities included in the 16-μm line list cover seven orders of magnitude (2.24×10^{-27} to 2.24×10^{-20} cm/molecule). Fig. 31 provides a comparison of the experimental and simulated spectra in arbitrarily chosen regions.

One should take note, as pointed out by Kochanov et al. [614], that infrared spectra calculated using HITRAN HCOOH data underestimates cross-sections when compared to the PNNL spectra [244] by about 40%. Not surprisingly, the new FIR bands introduced here exhibit the same trend because they were scaled based on the HITRAN data for the ν_6 band. The source of this discrepancy remains unclear. One of the possible explanations could be the lack of hot bands in HITRAN, but it would unlikely to be responsible for a uniform 40% difference across all spectral regions. Further investigations are needed to understand the source of the discrepancy of the HITRAN and PNNL intensities.

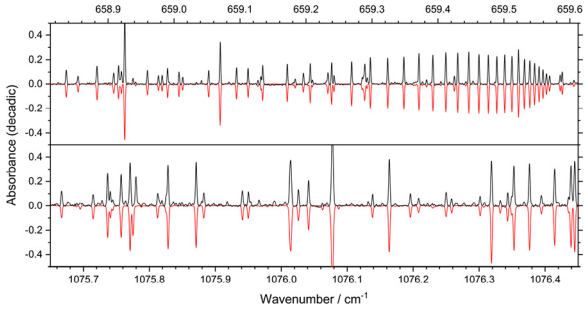

Fig. 31. Top panel: Experimental (upward) and simulated (downward) spectra of HCOOH within the ν_9 fundamental using a Gaussian FWHM of 0.00171 cm^{-1}. Bottom panel: Experimental (upward) and simulated (downward) spectra spectra within the ν_6 fundamental using a Gaussian FWHM of 0.00245 cm^{-1}.

2.33. HO_2: *hydroperoxyl radical (molecule 33)*

Unchanged.

2.34. O: *atomic oxygen ("molecule" 34)*

Unchanged.

2.35. $ClONO_2$: *chlorine nitrate (molecule 35)*

Unchanged.

2.36. NO^+: *nitric oxide cation (molecule 36)*

For typical atmospheric modeling applications, the self-broadening contribution of NO^+ is expected to be negligible; however the previous default value of $\gamma_{self} = 0.05$ cm^{-1}/atm (as used for pure rotational lines) has been extended for all transitions to avoid null values.

2.37. HOBr: *hypobromous acid (molecule 37)*

For typical atmospheric modeling applications the self-broadening of HOBr is expected to be negligible, however a default estimated value of $\gamma_{self} = 0.15$ cm^{-1}/atm has been applied for all transitions to avoid null values.

2.38. C_2H_4: *ethylene (molecule 38)*

Unchanged.

The 3 μm region (C-H stretch) is presently under reinvestigation for both line positions and line intensities thanks to new experimental spectra and to the tensorial formalism developed in Dijon [615]. This line-by-line analysis will be considered for a future HITRAN update for this molecule. A complete analysis of the 10-μm region for the $^{13}C_2H_4$ isotopologue is also planned. Finally, the *ab initio* line lists for different isotopologues [616–618] from the TheoReTs database [310] will also be evaluated for future updates.

2.39. CH_3OH: *methanol (molecule 39)*

Unchanged.

2.40. CH_3Br: *methyl bromide (molecule 40)*

Unchanged.

2.41. CH_3CN: *methyl cyanide (molecule 41)*

Unchanged.

The ν_4 band of methyl cyanide was introduced into HITRAN2008 [14]. The data were based on a multispectrum analysis of this band and a preliminary model of the positions and intensities [619]. A complex model of low-lying vibrational states was recently expanded to include extensive $\Delta\nu_4 = 1$ data [620]. These are ν_4 transition frequencies up to $J = 61$ and $K = 13$ along with rotational data up to $J = 79$ and $K = 16$. These new data will allow for a substantial improvement to the database in this spectral region.

For bands involving ν_8 at longer wavelengths, a case study describing the $\Delta\nu_8 = 0$, 1, and 2 states that employed IR and very extensive rotational data was presented by Müller et al. [621]. We expect to include these line lists as forthcoming updates to HITRAN2020.

2.42. CF_4: *carbon tetrafluoride (molecule 42)*

The line list is unchanged, but the quantum number format has been made consistent with similar species. See the Supplementary Material of this paper for a description of the upper- and lower-state quanta in the ".par" format.

Recent and ongoing global analyses of carbon tetrafluoride (CF_4) [622] already partly included in the TFMeCaSDa database (TetraFluoro-Methane Calculated Spectroscopic Database) [594] should lead, in the near future, to further improvements for this molecule (especially concerning hot bands) that will be considered for the next HITRAN update.

Another alternative source of data is the TheoReTs [310] line list calculated with help of *ab initio* methods. Completeness of line lists is essential for appropriate atmospheric retrievals. CF_4 is heavier than methane and has two low-lying bending frequencies at 440 and 640 cm^{-1} leading to a huge number of IR-active transitions belonging to the hot bands. A major challenge concerns the modeling of these hot bands that strongly contribute to the absorption, even at room temperature. It has recently been shown [573] that converged opacity calculations for CF_4 in the IR using global variational methods requires the same amount of computational effort at room temperature as lighter systems (such as methane) for very elevated temperatures of about 1000 K. The corresponding CF_4 line list in the 0–4000 cm^{-1} region, generated from potential energy and *ab initio* dipole moment surfaces by Rey et al. [573], contained about 2 billion transitions at room temperature. These data are currently too big for the standard HITRAN format but are accessible via the TheoReTs [310] information system in a hybrid compressed form. The initially computed full line-by-line lists were partitioned into two sets to accelerate modeling of spectral functions as described in Refs. [310,573] which also demonstrate very good agreement with the PNNL database [244]. In the future, this list could be accommodated into HITRAN with the use of "effective" lines, as proposed in Ref. [56] for methane.

2.43. C_4H_2: *diacetylene (molecule 43)*

Unchanged.

2.44. HC_3N: *cyanoacetylene (molecule 44)*

Cyanoacetylene is a molecule of notable astrochemical importance. It has been detected in a large number of astronomical environments (see Ref. and references therein), including planetary atmospheres [624], comets [625], and nearby galaxies [626]. Several laboratory works have been carried out that have mainly explored the rotational and ro-vibrational spectra of HC_3N. In 2017, a detailed global analysis of this molecule was published [623], which included pure rotational transitions in the ground and some excited vibrational states and ro-vibrational transitions in the 450–1350 cm range^{-1}, involving all the energy levels lower than 1000 cm^{-1}. Such analysis has been extended to the far-infrared region below 450 cm^{-1} and to the stretching region between 2034 and 3360 cm^{-1}. The newly recorded spectra and the related new global fit carried out in Bologna will be a subject for an upcoming publication [627]. All the experimental and theoretical details and the treatment of the data will be reported in Ref. [627]. From this analysis, a new line list of rotational and ro-vibrational transitions has been compiled and introduced in the HITRAN2020 database. The line list reports transition wavenumbers calculated with the best spectroscopic parameters obtained from a global fit. The main advantage of the new line list is the completeness of the data and their consistency, confirmed by the quality of the global fit. For the first time, the line list includes ro-vibrational transitions relative to all seven vibrational modes of HC_3N up to 3400 cm^{-1} (fundamentals, combinations, overtones, and their associated hot-bands) and rotational data in the ground and many vibrational states of all normal modes. The fundamental band ν_7, the lowest bending mode at 221.8 cm^{-1}, has been detected directly in the far infrared region for the first time. This is important for an accurate derivation of its vibrational energy and therefore for the analysis of many hot bands which originate from it. The global fit also accounts for two anharmonic resonance networks, and their upscale by one quantum of ν_7.

It is important to point out that the accuracy of the line positions for the ν_5 and ν_6 band systems is at least one order of magnitude better than that reported in the previous line list (although the differences do not exceed 0.001 cm^{-1} and in fact is much better than that for most of the lines). Very limited extrapolations to J values higher than the observed ones have been made. With that being said, the intensities of lines in these fundamentals in the new list exceed the intensities in HITRAN2016 (which originate from Ref. [628]). The origins of this discrepancy remain to be determined. Considering that the line list from Ref. [628] is used in Titan studies and no issues were reported in the literature, we retain HITRAN2016 parameters in the corresponding spectral regions (460–560 cm^{-1} and 620–750 cm^{-1}). This will be a subject of further investigation.

The intensities of the ν_1 fundamental reported in Ref. [625] are a factor of 3 stronger than those in the new line list adapted for HITRAN2020. This also will be a subject of further investigation.

2.45. H_2: *molecular hydrogen (molecule 45)*

The ro-vibrational spectra of molecular hydrogen are relevant for the atmospheres of the giant planets in the solar system and some types of super-Earth exoplanets [629]. Molecular hydrogen was first introduced in HITRAN2012 for the electric quadrupole and dipole lines in H_2 and HD isotopologues, respectively [15]. Default broadening values were used for all the lines. In HITRAN2016 [16], the electric quadrupole lines for HD were added and the line-shape parameters for the HT profile (based on experimental spectra) were added for self-perturbed H_2 [165].

In HITRAN2020, a comprehensive dataset of beyond-Voigt line-shape parameters for He-perturbed H_2 lines was added [630]. The dataset is based on *ab initio* quantum-scattering calculations and was validated on highly-accurate CRDS spectra to sub-percent levels [630]. It covers a wide temperature range from 20 to 1000 K; the temperature dependencies of all the six line-shape parameters (broadening and shift, γ_0 and δ_0, speed dependence of broadening and shift, γ_2 and δ_2, real and imaginary parts of the Dicke parameter, $\tilde{\nu}^r_{opt}$ and $\tilde{\nu}^i_{opt}$) are represented with the double-power-law (DPL) approximation [119,120] that recently was adopted in HITRAN [120] but will be made available after the official release of HITRAN2020. To make the self-perturbed H_2 line-shape parameter datasets [165] consistent with the He-perturbed H_2 dataset [630] and with the DPL format [120], the self-perturbed H_2 dataset, introduced into HITRAN in 2016 [165], was transformed into the DPL format [120].

Recently, it was demonstrated that for high-J levels of H_2 the intensities of the Q-branch lines are considerably influenced by the magnetic dipole contribution [631]. The H_2 line list will be updated in the near future to account for this effect.

The hydrogen-rich atmospheres are dominated by H_2 and He, but also contain the HD isotopologue whose low abundance is compensated by much larger intensities of dipole lines (compared to quadrupole lines in H_2). Therefore a complete dataset for planetary applications should include four systems: He-perturbed H_2, He-perturbed HD, H_2-perturbed HD and self-perturbed H_2. In the

near future, we plan to add a comprehensive dataset for the He-perturbed HD lines (both dipole and quadrupole).

Unlike the principal isotopologue, HD transitions in HITRAN have only Voigt values which are known to be not efficient for this molecule and were rather arbitrarily assigned 0.05 cm^{-1}/atm for self- and air-width by default. However, this value seems to be overestimated approximately by a factor of five when they are compared to laboratory measurements [632]. Recently, a new laboratory study of pure rotational transitions has reported the line-shape parameters of HD [633], confirming that the HITRAN default values are indeed overestimated. Thus, an update is planned for the near future based on the new experimental values, which will include the broadening and frequency shifts of HD by self and H_2 and their temperature dependences for R(0)-R(3) transitions [634].

2.46. CS: *carbon monosulfide (molecule 46)*

Unchanged.

2.46.1. *Future work*

The CS line list in HITRAN includes the four most abundant isotopologues ($^{12}C^{32}S$, $^{12}C^{34}S$, $^{13}C^{32}S$, $^{12}C^{33}S$) with line positions based on lower-state energies provided by CDMS [635] and intensities calculated from Einstein-*A* coefficients of Ref. [636]. In the time since these data were added to HITRAN, empirically-corrected *ab initio* line lists for the $X^1\Sigma^+$ electronic ground state of CS has been calculated by Paulose et al. [637] as part of the ExoMol project [342]. Eight isotopologues of CS ($^{12}C^{32}S$, $^{12}C^{33}S$, $^{12}C^{34}S$, $^{12}C^{36}S$, $^{13}C^{32}S$, $^{13}C^{33}S$, $^{13}C^{34}S$, and $^{13}C^{36}S$) were included and cover frequencies up to 11 000 cm^{-1}. More recently, Hou and Wei [638] have calculated comprehensive empirically-based line positions with *ab initio* intensities for the same eight isotopologues as Ref. [637] with frequencies extending up to 15 000 cm^{-1}.

The $^{12}C^{32}S$ intensities from CDMS [635], Exomol [637], and Ref. [638] have been compared to bands available in HITRAN [15]. Generally, there is good agreement between all sources for the $\Delta v = 0$ bands. For the 1–0 band, the intensities of Hou and Wei [638] appear ∼5% weaker than the other studies, whereas for the 2–0 band the intensities of Ref. [638] are ∼50% stronger than HITRAN (the weakest). The differences exhibited for the 2–0 transitions indicate that further validation of the line lists from Refs. [637,638] are required. Therefore these works will be considered for inclusion into future editions of HITRAN.

2.47. SO_3: *sulfur trrioxide (molecule 47)*

Unchanged.

2.48. C_2N_2: *cyanogen (molecule 48)*

Unchanged.

2.49. $COCl_2$: *phosgene (molecule 49)*

Unchanged.

2.50. SO: *sulfur monoxide (molecule 50)*

Sulfur monoxide is among the sulfur-containing compounds detected on Venus (see for instance Ref. [639]). This molecule has also been detected in the atmospheres of Jupiter's moon Io [640] and comets [641]. To aid interpretation of the spectra of planetary atmospheres a line list for this molecule was added to HITRAN.

The line positions, lower-state energies, and intensities for the three most abundant isotopologues of sulfur monoxide ($^{32}S^{16}O$, $^{34}S^{16}O$, and $^{32}S^{18}O$) were calculated using the SPCAT program [642]. For the principal isotopologue, 0-0, 1-1 and 2-2 bands were calculated, using constants provided by M.-A. Martin-Drumel (Paris) based on the fit of measurements from Ref. [643], and other available data. Note that these constants differ slightly from the ones reported in Ref. [643]. The value of the dipole moment is adapted from the CDMS database [635] which is in turn based on the values reported in Refs. [644,645]. There is a notable difference in the line positions for transitions with higher rotational quanta when compared with the CDMS catalogue (containing 0-0 and 1-1 bands) and especially the JPL catalogue [227], which is based on less recent results than CDMS. The intensities agree well with the CDMS catalogue for the 0-0 band but differ noticeably (about 14%) for the 1-1 band. This is due to a systematic difference of almost 30 cm^{-1} in the lowerstate energies. The lower-state energies calculated for HITRAN agree very well with literature values. For the $^{34}S^{16}O$ and $^{32}S^{18}O$ isotopologues, the 0-0 band was calculated based on constants from Martin-Drumel et al. [643] and the same dipole moment that was used for the principal isotopologue. There is a good agreement for intensities with the CDMS catalogue, but line positions deviate noticeably, especially with the increase of rotational quanta. It should be noted that the wavenumber format for SO in the traditional ".par" output is set to F12.9 for transitions below 1.0 cm^{-1}, F12.8 for transitions 1.0 to 10.0 cm^{-1}, and F12.7 for transitions 10.0 to 100.0 cm^{-1}.

The $a^1\Delta$–$X^3\Sigma^-$ and $b^1\Sigma^+$–$X^3\Sigma^-$ electronic transitions of $^{32}S^{16}O$ have been added to HITRAN based on the work of Ref. [646]. Fits to spectroscopic data in the literature (including Ref. [643] and references therein) were performed using PGOPHER [460]. The SO line list includes the transitions involving vibrational levels v=0-6 for the $X^3\Sigma^-$ state, v=0-5 for the $a^1\Delta$ state, and v=0-2 for the $b^1\Sigma^+$ state. For electric dipole transitions, the transition dipole moment matrix elements were obtained from *ab initio* calculations, but for magnetic dipole transitions, the transition dipole moment matrix elements were scaled to experimental values [647]. These matrix elements were used in PGOPHER to provide Einstein-*A* coefficients that were then converted to line intensities for inclusion to HITRAN. All lower-state energies have been adjusted by 5.5913 cm^{-1} to shift the zero energy to the lowest-lying energy level (to be consistent with the database formalism and the MW line list described above). The magnetic dipole transitions have been indicated by "d" in the lower-state quanta (see the Supplementary Material of this paper for a description of the upper- and lower-state quanta in the ".par" format).

No broadening parameters for SO are available in the literature. For that reason they have been estimated from those of the isoelectronic oxygen molecule. For air- and self-broadening, the functions used for the oxygen A-band have been applied from Robichaud et al. [325], with a default value for temperature dependence. It is worth pointing out that because SO has been observed on planets with a history of volcanic activity, measurements and broadening by pressure of CO_2 would be very welcomed.

2.51. CH_3F: *methyl fluoride (molecule 51)*

A line list for methyl fluoride (CH_3F) has been introduced to HITRAN for the first time. This tetrahedral molecule is present in traces in the terrestrial atmosphere and participates in global warming [648]. A line list for the intense ν_6 band around 1200 cm^{-1} has now been included in HITRAN, based on the work of Ref. [649] for line positions, on Ref. [650] for line intensities and self-broadening coefficients, and on Ref. [651] for air-broadening coefficients. For some of the lines, the quantum assignment is incomplete in the sense that A1 and A2 symmetry components are not distinguished. In the future a more detailed quantum assignment will be provided.

2.52. GeH_4: Germane (molecule 52)

Germane (GeH_4) is a tetrahedral molecule of interest for the study of the atmospheres of giant planets Jupiter and Saturn. The need for accurate line lists for this molecule has been especially renewed recently by the availability of spectroscopic measurements from the JIRAM (Jovian InfraRed Auroral Mapper) infrared spectrometer aboard NASA's Juno spacecraft [652]. Germane abundance retrieval in the Jovian atmosphere allows one to probe the planet's troposphere below the ammonia cloud level.

During the past few years, a new experimental and modeling study on this molecule has been undertaken by French (LISA in Créteil, ICB in Dijon) and Belgian (at ULB in Brussels) groups to remeasure high-resolution infrared spectra of the fundamental bands of germane in order to obtain accurate line positions and line intensities. The molecule was studied in natural abundance and effective Hamiltonian and dipole moment parameters were retrieved using the Dijon tensorial formalism and programs [653] for the five main isotopologues: $^{74}GeH_4$ (36.52 %), $^{72}GeH_4$ (27.41 %), $^{70}GeH_4$ (20.51 %), $^{73}GeH_4$ (7.76 %), and $^{76}GeH_4$ (7.46 %). Deuterated species have not been considered in these studies. A first paper was dedicated to the stretching dyad ν_1/ν_3 around 2100 cm^{-1} [654] and a second one to the bending dyad ν_2/ν_4 around 900 cm^{-1} [655].

The retrieved molecular parameters allowed the production of calculated germane line lists for both regions. These data were first used to setup GeCaSDa (Germane Calculated Spectroscopic Database) [594], which can be accessed either directly (http://vamdc.icb.cnrs.fr) or through the VAMDC (Virtual Atomic and Molecular Data Centre) portal [656].

The germane line list for HITRAN contains line positions and absolute line intensities for approximately 12,200 lines for each of the five isotopologues (with 60,878 lines in total). These lines pertain to the ν_1, ν_2, ν_3 and ν_4 fundamental bands only, in the 648–2271 cm^{-1} wavenumber range [654,655]. The lower intensity threshold for calculations is set to 10^{-23} cm^{-1}/(molecule cm^{-2}), which is sufficiently strong to avoid including exaggerated extrapolations from assigned experimental lines. The Einstein-*A* coefficients in HITRAN have been recalculated to enable consistency with the total internal partition sums of Ref. [417] described in Section 6.4.

For completeness, we also mention the work on germane by O. Ulenikov's group in Tomsk, Russia (see for instance Ref. [657] and references therein), where similar results have been obtained. More recently, a comprehensive study of the 1400–1950 cm^{-1} spectral region includes analysis of the $2\nu_2$, $2\nu_4$, and $\nu_2+\nu_4$ bands [658]. This line list has not been included into HITRAN, but the broadening measurements have been used to estimate self-broadening coefficients for HITRAN. A linear fit to the self-broadening coefficients of Ref. [658] yields $\gamma_{self} = 0.07615 - 0.00040J''$. This has been used to calculate the self-broadening for all bands (of all germane isotopologues) in the HITRAN line list. There are no known measurements of air-broadening therefore an average value of $\gamma_{air} = 0.06$ cm^{-1}/atm and $n_{air} = 0.75$ have been used based on comparisons to the methane parameters in HITRAN.

2.53. CS_2: carbon disulfide (molecule 53)

Carbon disulfide (CS_2) has been introduced in the line-by-line part of HITRAN for the first time. CS_2 is a molecule of interest in atmospheric environmental chemistry, medical diagnostics, and studies of planetary atmospheres. It has a significant effect on the global atmospheric sulfur budget and the oxidation of carbon disulfide in the atmosphere is a major source of OCS [470–473]. The CS_2 molecule has been detected in comets [659,660] and in Jupiter's atmosphere after the collision of the Shoemaker-Levy 9 comet [661]. The principal sources of CS_2 are industrial and natural processes (volcanic eruptions, evaporation from the oceans, soils, biomass burning, and petroleum refining) [662,663]. In addition, exposure to CS_2 can cause accelerated atherosclerosis and coronary artery disease [664,665], and therefore it is essential to monitor its concentrations in relevant production sites.

The HITRAN2020 carbon disulfide line list contains 83,420 transitions of the $^{12}C^{32}S_2$, $^{32}S^{12}C^{34}S$, $^{32}S^{12}C^{33}S$, and $^{13}C^{32}S_2$ isotopologues in the 1.2–6466.4 cm^{-1} spectral range. The line list is described in detail in Ref. [666]; therefore here we only briefly summarize the main characteristics. In the HITRAN2020 edition, the CS_2 molecule was given number "53" to be consistent with the Total Internal Partition Sums (TIPS2017) program [178] (isotopologue ID: $^{12}C^{32}S_2$: 1, $^{32}S^{12}C^{34}S$: 2, $^{32}S^{12}C^{33}S$: 3, and $^{13}C^{32}S_2$: 4). Although CS_2 has the same symmetry as CO_2, the quantum notation that was chosen for this molecule is more in line with that used for other linear molecules, including OCS. In particular, the labeling $\nu_1\nu_2l_2\nu_3$ of the vibrational states was used (see the Supplementary Material of this paper for a description of the upper- and lower-state quanta in the ".par" format). The calculations of the line positions and intensities were performed by applying the PGOPHER program [460] using a large set of measured line positions available in the literature, including the most recent high-precision dual-comb laser spectroscopy measurements [667] and transition dipole moments for each measured band. A global least-squares fit of measured line positions to the corresponding spectroscopic parameters for the $^{12}C^{32}S_2$, $^{32}S^{12}C^{34}S$, $^{32}S^{12}C^{33}S$, and $^{13}C^{32}S_2$ isotopologues was carried out. A unique set of parameters for each lower and upper state was obtained. The maximum rotational angular momentum in the line list was set to $J = 150$. In addition, the perturbed line positions of the $3\nu_3$, $\nu_1+3\nu_3$, and $3\nu_1+3\nu_3$ bands of the $^{12}C^{32}S_2$ isotopologue and the $3\nu_3$ band of the $^{32}S^{12}C^{34}S$ isotopologue were replaced by their experimental values from Refs. [668–670]. The calculations of line intensities for 423 bands of the $^{12}C^{32}S_2$, $^{32}S^{12}C^{34}S$, $^{32}S^{12}C^{33}S$, and $^{13}C^{32}S_2$ isotopologues have been carried out. For vibrational CS_2 bands known experimentally from the literature, the corresponding transitions of the dipole moments were fit to the measured line intensities. Different scaling factors were used to correct the line intensities for the carbon disulfide bands not having dedicated intensity measurements. In this case, validation and correction of the calculated line intensities have been performed using the PNNL [244] spectrum which covers the 600–6500 cm^{-1} spectral range. The comparison between the CS_2 line list (i.e., HITRAN line list) and experimental PNNL spectrum can be found in Figs. 9 and 10 of Ref. [666]. The overall agreement of the line positions and intensities is fairly good except for the spectral region around of 1535 cm^{-1}, where there is not enough data to calculate the line parameters for all the hot bands. More dedicated experimental and theoretical studies of the intensities in multiple bands are needed. Also, in the course of recalculation of the partition sums (TIPS-2021) for HITRAN2020 [417], it was found that the values at 296 K for $^{12}CS_2$ and $^{13}CS_2$ differed to their previous values (TIPS-2017) [178] by around 30%. It is important to note that the intensity cutoff 10^{-30} cm/molecule at 296 K, was applied when adapting the line list from Karlovets et al. [666] to HITRAN.

The HITRAN line list allowed one to extend the knowledge about the CS_2 line parameters in the 1–600 cm^{-1} spectral region dominated by the ν_2 band of $^{12}C^{32}S_2$. The line intensities of this band were calculated using data from Ref. [671] which may be considered to be imprecise; therefore, new experiments for this band are welcomed. Uncertainty codes for the line positions and the line intensities used in the CS_2 line list are described in Ref. [666].

Fig. 32 shows an overview of the line lists for the $^{12}C^{32}S_2$, $^{32}S^{12}C^{34}S$, $^{32}S^{12}C^{33}S$, and $^{13}C^{32}S_2$ isotopologues in the 0–7000 cm^{-1} region.

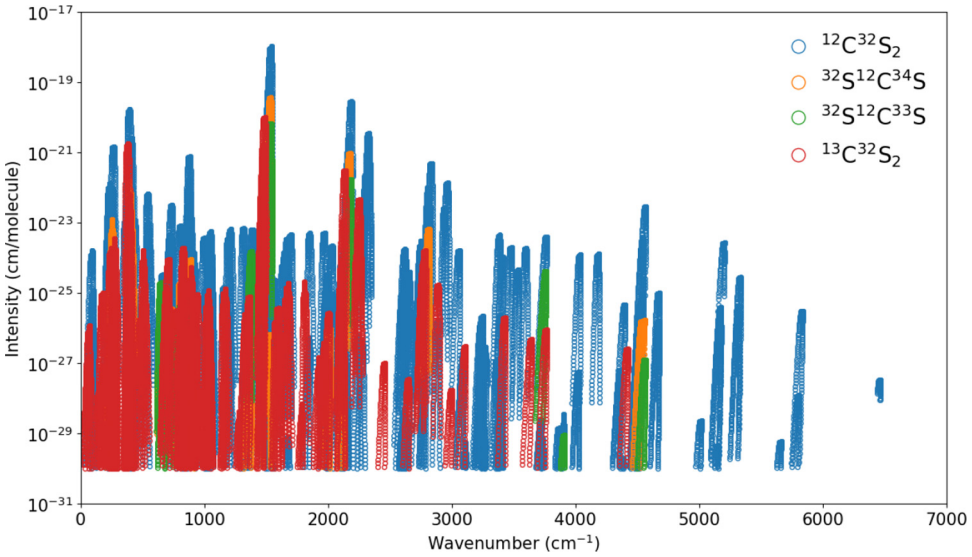

Fig. 32. Overview of the line lists of the $^{12}C^{32}S_2$, $^{32}S^{12}C^{34}S$, $^{32}S^{12}C^{33}S$, and $^{13}C^{32}S_2$ isotopologues in HITRAN.

We obtained the air- and self-broadening parameters of CS_2 and the temperature dependence exponents of the half-widths based on the measured or theoretically calculated data in the literature. To populate these parameters for all the lines of CS_2, the available results were fit using the Padé approximants (Eq. (1)) and these parameters (γ_{air}, γ_{self}, and n_{air}) were predicted for all the lines including the transitions with higher quantum numbers. The pressure shifts of CS_2 were not yet added to the database because of the lack of measured data for this parameter.

2.54. CH_3I: *methyl iodide (molecule 54)*

Methyl iodide (CH_3I), a naturally occurring halogenated volatile organic compound, is an important carrier of iodine from the ocean to the atmosphere and plays a crucial role in the chemistry of the atmosphere [672,673]. In addition, it is used in several industrial and agricultural applications. Examples include use as a methylation reagent in organic synthesis, a fumigant in buildings and soils, and as a pesticide. In nuclear power plants [674], methyl iodide is mainly produced in the containment by the reaction of iodine with organic coatings of the enclosure under ionizing radiation. In the case of a severe nuclear accident, iodine fission products represent a major part of the released radioactivity and are of deep concern due to the affinity of iodine with the thyroid. Therefore, it is crucial to monitor the release of iodine compounds into the atmosphere as part of nuclear safety and radio-protection. Relevant to all these applications is the capability to install leak detectors as well as to monitor personal exposure limits. Implementation of optical detection schemes is hindered by the lack of accurate spectroscopic models based on high-precision laboratory measurements.

2.54.1. ν_6 *band at 11.2* μm

A relatively strong ν_6 band of CH_3I is located around 893 cm^{-1}, coinciding with the 11-μm transparency window in the atmosphere [21,186], could be a good candidate for detection of this molecule in atmospheric spectra. Detailed studies concerning the line positions and intensities of the ν_6 fundamental and interacting $2\nu_3$ bands were recently carried out [675,676]. For the computation of the line positions and intensities, the hyperfine structure due to the iodine nuclear quadrupole moment was accounted for explicitly (Fig. 33), together with the vibration-rotation resonances

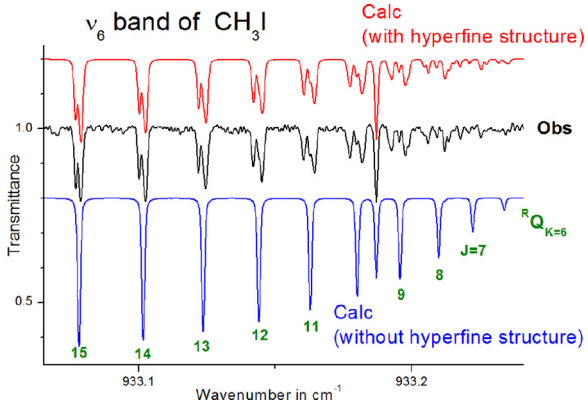

Fig. 33. Example of a calculation of methyl iodide transitions with and without accounting for the hyperfine structure.

which perturb them. Transitions from both the ν_6 and $2\nu_3$ bands have been included for HITRAN2020.

2.54.2. ν_4 *band at 3* μm

The reported line positions and intensities of the ν_4 band and nearby $\nu_3 + \nu_4 - \nu_3$ hot band are based on a high-precision measurement using optical frequency comb Fourier transform spectroscopy [677]. The details of the mid-IR frequency comb source [678], the home-built fast-scanning FTS [679], as well as the auto-balancing detection scheme in the FTS [680] and a Herriot cell are presented elsewhere. The high-resolution spectra were recorded in the region from 2800 to 3160 cm^{-1} with sampling point spacing of 11 MHz, utilizing the sub-nominal resolution interleaving scheme [681,682]. The measured spectrum, shown in Fig. 34(a), contains three main ro-vibrational features: the parallel vibrational overtone and combination bands centered around 2850 cm^{-1}, the strong symmetric stretch ν_1 band centered at 2971 cm^{-1}, and the asymmetric stretch ν_4 band centered at 3060 cm^{-1}. Based on the analysis of these spectra, the ν_4 band and the nearby $\nu_3 + \nu_4 - \nu_3$ hot band are included in the HITRAN2020 database.

Fig. 34 (b) shows the measured (black) spectrum of 0.11 mbar of pure CH_3I at 296 K together with the simulations of the ν_4 band (red) and the $\nu_3 + \nu_4 - \nu_3$ hot band (blue). Fig. 34(c) shows a further enlarged section of Fig. 34(b) around a $Q_K(J)$ sub-branch.

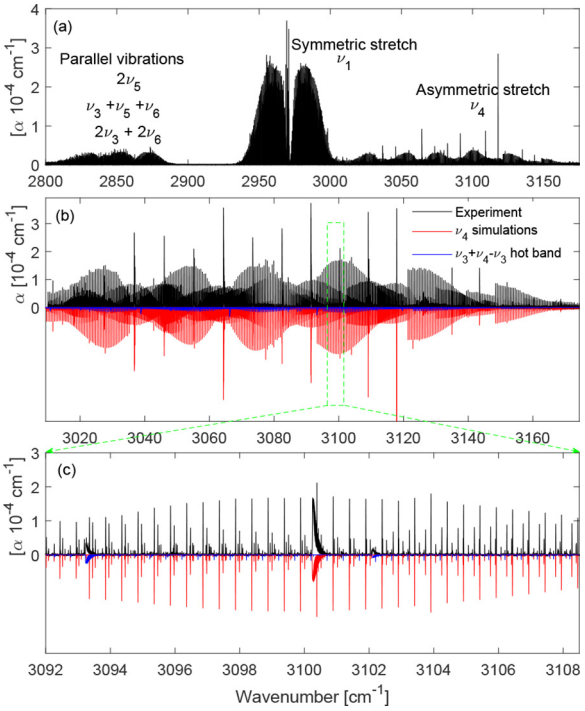

Fig. 34. (a) The broadband high-resolution spectrum of pure CH_3I measured at 0.03 mbar in the range from 2800–3160 cm^{-1} using comb-based FTS [677]. (b) The absorption coefficient, ,α of the ν_4 band measured at 0.11 mbar of pure CH_3I (black) together with the simulations of the ν_4 band (red) and the $\nu_3+\nu_4-\nu_3$ hot band (blue) obtained using PGOPHER. (c) Zoom in region around one of the $Q_K(J)$ subbranches of the ν_4 band.

The spectra of these two bands were simulated and assigned using PGOPHER [460]. The overall band structure, as well as the relative intensities of the individual lines in the simulations, agree very well with the experimental data. A least-square fit of the assigned transitions to the measured spectrum provided accurate upper-state rotational constants of both bands. The hyperfine splittings due to the ^{127}I iodine nuclear quadrupole moment are observed for transitions with $J \leq 2K$. Future work will involve further analysis of the hyperfine splittings and the analysis of the measured ν_1 band and the parallel vibration bands.

For inclusion to HITRAN, transitions with $J < 25$ contain hyperfine splitting. All CH_3I lower-state energies (including transitions for the ν_6 region) have been adjusted by 1.0×10^{-4} cm^{-1} to account for the lowest allowed energy level. Sadiek et al. [677] provided line intensities for 207 transitions obtained using a multi-spectrum fitting procedure and these intensities were adapted for HITRAN. Line intensities for the remaining transitions of the ν_4 band and $\nu_3+\nu_4-\nu_3$ hot band have been estimated by scaling the relative PGOPHER intensities. A single scale factor was determined by taking an average ratio of the empirical intensities from Sadiek et al. [677] to their corresponding PGOPHER relative intensities. A dependence on the rotational quanta was observed in this comparison. It has been shown [683] that Herman-Wallis coefficients are necessary for determining accurate line intensities for CH_3I and will therefore be considered for future intensity analyses.

The self-and air-broadening parameters for all CH_3I transitions are based on recent studies by Raddaoui et al. [648,684]. The values are based on FTS analysis of the ν_6 band, which proposed a set of smoothed empirical parameters to calculate widths up to $J = 80$. Empirical parameters are fitted through the K-rotational dependencies observed for transitions having the same lower J value. The rotational J- and K-dependencies calculated by this model reproduced the measurements (around 1000) with a sub-percent average discrepancy and one standard deviation of around 7% both for self- and air-broadening coefficients. The smoothed parameters of Table 4 from Ref. [648] and Table 5 from Ref. [684] for self- and air-broadening coefficients, respectively, have been used to generate broadening coefficients at 296 K for all CH_3I transitions. To avoid extrapolating the self-broadening coefficients to J'' and K'' pairs far beyond observation, a minimum value of 0.10 cm^{-1}/atm has been used. An error code of 5 (see Table 2) has been used for both self- and air-broadening coefficients.

There are no line shifts and temperature dependence parameters for this molecule available in the literature. Default values for temperature dependence (fixed to 0.75) of air-broadening coefficients have been used for all CH_3I transitions. For atmospheric applications, a study of the temperature dependence of the lineshape parameters of CH_3I (190–300 K) will be required.

2.55. NF_3: *nitrogen trifluoride (molecule 55)*

The nitrogen trifluoride (NF_3) line list is presented in the HITRAN database for the first time. This line list includes more than 40 cold and 680 hot sub-bands and covers the spectral range up to 2200 cm^{-1}. NF_3 is known as an anthropogenic greenhouse gas with a high global warming potential of about 17 000 [685–687]. The concentration of NF_3 has been increasing in the Earth's atmosphere during the past decade [688,689] because this gas is widely used in the semiconductor industry. The NF_3 molecule is semi-rigid, belonging to the C_{3v} point group; the symmetry properties and selection rules are quite similar to those of other symmetric tops included in the previous HITRAN2016 release like PH_3 or CH_3D, for which the reader can find detailed discussions in Ref. [690] (and references therein). However, nitrogen trifluoride has lower vibrational modes and smaller rotational constants resulting in a much more congested infrared spectra, which leads to complicated line-by-line analyses using a purely empirical approach. This is particularly true for line intensity determination because of numerous overlapping hot bands, even at room temperature. The HITRAN2020 version includes the global *combined* line list of Egorov et al. [691], which was based on large-scale variational calculations with *ab initio* PES and DMS constructed at the CCSD(T)/CVQZ and CCSD(T)/AVQZ levels of theory. The effective Hamiltonian of NF_3 was then obtained by the six-order contact transformation approach using the MOL_CT computational code [214,692] from the *ab initio* PES. The effective polyad model included six groups of vibrational states: from ground up to icosad. The *ab initio* parameters of the effective model were refined using the MIRS computational code [693,694] and experimental transitions of NF_3 existing in the literature. In particular, the experimental line positions from the following works were used for the fine tuning of the energy levels: ν_4(E) [695]; ν_2(A_1), $\nu_2+\nu_4$(E), and $2\nu_2$(A_1) [696]; $2\nu_4$(A_1, E) [697]; ν_1(E) [698]; ν_3(E) [699]; $\nu_1+\nu_4$(E) [700,701]; $2\nu_3$(A_1, E) and $\nu_1+\nu_3$(E) [702]; $\nu_2+\nu_3$(E), $2\nu_1$(A_1) and $\nu_1+\nu_2+\nu_4$(E) [703]. The empirical parameters of the ground state were taken from Ref. [697] where the "loop-method" was applied to determine the K-dependent parameters (C_0, D_K, H_K etc.) by combining the experimental pure rotational transitions with those from the ground state combination differences. All NF_3 line intensities were calculated variationally from the pure *ab initio* DMS and are available in the TheoReTS web site (http://theorets.univ-reims.fr ; http://theorets.tsu.ru). The first experimental studies of NF_3 integrated cross sections with medium spectral resolution were conducted in Ref. [704] and then revisited in Ref. [685]. The present NF_3 line list has been validated in detail in the work of Egorov et al. [691] by comparison with the PNNL absorption coefficients [244] above 600 cm^{-1}. The line positions and intensities in the region of the $2\nu_3$(A_1, E) and $\nu_1+\nu_3$(E) bands were additionally validated using low-temperature (196 K) FTS spectra [705]. The

Table 10
Absorption cross sections added to HITRAN2020 for remote sensing of the terrestrial atmosphere.

Molecule	Temperature range (K)	Pressure range (Torr)	Number of P,T sets	Spectral range (cm^{-1})
CCl_3F (CFC-11)	192 – 293	7.5 – 760	30	710 – 1290
CH_3CCl_2F (HCFC-141b)	188 – 295	7.5 – 761	30	705 – 1280
SF_6	189 – 294	7.5 – 751	37	780 – 1100
CF_4 (CFC-14)	190 – 296	7.5 – 760	34	1190 – 1336

NF_3 line list is now provided in the HITRAN database with averaged values for air- and self-broadened half-widths (γ_{air} = 0.1 $cm^{-1}atm^{-1}$, γ_{self} = 0.5 $cm^{-1}atm^{-1}$) as well as the temperature dependence exponent (n_{air} = 0.55). It is worth mentioning that only the principal isotopologue ($^{14}NF_3$) is included at this time with the abundance of 0.9964. The error codes (explained in Table 2) for all *ab initio* line intensities were set to 4, and set to 3 for the line positions of the ones corrected to the experiment bands, and to 2 for the *ab initio* line positions of all other bands. Due to a very large size of the file and the fact that ab initio line positions in some of the bands may deviate from the observed values, the line list for NF_3 have been placed in the folder with the other static line lists, e.g. SF_6, $ClONO_2$ and CF_4.

3. Absorption cross-sections

3.1. IR cross-sections

The comprehensive update of the infrared absorption cross-sections carried out for HITRAN2016 [706] dramatically extended the number of compounds represented in this section to almost 300. For HITRAN2020, some additional updates were introduced and are described below.

3.1.1. Halogenated species of atmospheric interest

Four high-spectral-resolution absorption cross-section datasets of the halogenated species trichlorofluoromethane (CCl_3F a.k.a. CFC-11), 1,1-dichloro-1-fluoroethane (CH_3CCl_2F a.k.a. HCFC-141b), sulfur hexafluoride (SF_6), and carbon tetrafluoride (CF_4 a.k.a. CFC-14) have been added to HITRAN2020 (see Table 10). Covering a wide range of atmospherically relevant pressures and temperatures, these datasets are intended for use by the atmospheric remote-sensing community, particularly for the interpretation of measurements by atmospheric infrared limb sounders such as the ACE-FTS [707]. CFC-11 was one of the first chlorofluorocarbons (CFCs) developed in the 1930s as inexpensive, reliable, safe and non-toxic refrigerants for domestic use. Its applications ranged from refrigerators and air conditioners to propellants in spray cans and blowing agents in foam production. As the use of CFCs became widespread, their atmospheric concentrations steadily rose. However, the discovery that they were destroying stratospheric ozone led to the signing of the 1987 Montreal Protocol. Designed to protect the Earth's ozone layer, the Protocol mandated the phasing out of CFC production. Although phased out, CFC-11 is still emitted into the atmosphere from existing "banks" (e.g., old refrigerators and air conditioners containing CFCs), but overall its atmospheric abundance is now decreasing. Despite the general success of the Montreal protocol, it was recently discovered that some countries have been emitting CFC-11 from around 2013 [708,709], although these emissions had largely been curbed by 2019 [710,711]. Hydrochlorofluorocarbons (HCFCs) were initially adopted as 'transitional' CFC replacements because of their shorter atmospheric lifetimes on account of their more efficient reaction with OH in the troposphere, and their reduced stratospheric ozone depletion potentials. With the worldwide CFC phase out achieved under the terms of the Montreal Protocol, the focus has now shifted to HCFCs themselves, with a final phase out currently scheduled for 2030 for developed countries and 2040 in the developing world. HCFC-141b is primarily used as a foam blowing agent, a solvent in electronics, and for precision cleaning applications. Like other HCFCs, its atmospheric abundance continues to increase. Both CF_4 and SF_6 belong to the class of source gases known as F-gases, with fluorine as the only halogen attached to either carbon, sulfur, or nitrogen. These gases are not ozone-depleting and are not regulated by the Montreal Protocol. They both have small natural sources: degassing of the Earth's crust sustains an atmospheric background of 34.7 ppt for CF_4 [712] and up to 0.01 ppt for SF_6 [713]. However, anthropogenic emissions of these species now dominate. As these species are potent greenhouse gases with very long atmospheric lifetimes, they fall within the remit of the Kyoto Protocol. CF_4 and SF_6 have leaked into the atmosphere from a number of industrial applications: CF_4 from the production of aluminium and the manufacture of microchips in the semiconductor industry, and SF_6 as an insulating medium in high-voltage electrical equipment, in particular in electricity distribution systems, magnesium production, and semiconductor manufacturing. Due to their very long atmospheric lifetimes, SF_6 and CF_4 in the stratosphere are useful tracers for age of air. Remote-sensing measurements of both species have the potential to investigate changes in the Brewer-Dobson circulation due to climate change.

3.1.1.1. Trichlorofluoromethane (CCl_3F, CFC-11). The CFC-11 cross section dataset in previous HITRAN compilations was provided by Varanasi et al. [12,714] and has been used extensively for remote-sensing applications. For HITRAN2020, this has been replaced by a new dataset from Harrison [715], determined from spectra recorded using a high-resolution FTS (Bruker IFS 125HR) and a 26-cm-pathlength cell at spectral resolutions between 0.01 and 0.03 cm^{-1} (see Table 10). This new dataset resolves a number of issues with the Varanasi et al. data, namely a more accurately calibrated wavenumber scale, more consistent integrated band intensities, improved signal-to-noise, no channel fringing, and a wider range of pressures and temperatures. The Varanasi et al. dataset is now available in the HITRAN alternate folder.

3.1.1.2. 1,1-Dichloro-1-fluoroethane (CH_3CCl_2F, HCFC-141b). The HITRAN2016 compilation included three 760-Torr-N_2-broadened HCFC-141b cross sections (278, 298, and 323 K) at 0.112 cm^{-1} spectral resolution, and seven cross sections (223, 233, 243, 253, 263, 273, and 283 K) for pure HCFC-141b at 0.02 cm^{-1} resolution [716]. However, these do not account for air-broadening below 760 Torr, so are not the most appropriate for use in remote sensing of the Earth's atmosphere. HITRAN2020 now includes air-broadened HCFC-141b cross sections [717] over a range of pressures and temperatures appropriate for atmospheric conditions (Table 10); these are derived from spectra recorded at spectral resolutions between 0.01 and 0.03 cm^{-1} using a high-resolution FTS (Bruker IFS 125HR) and a 26-cm-pathlength cell.

3.1.1.3. Sulfur hexafluoride (SF_6). As was discussed in Section 2.30, the extent of the line list for sulfur hexafluoride does not allow

modeling of complete spectral regions under atmospheric conditions, because of lack of hot bands. Therefore, it has always been recommended that HITRAN users make use of absorption cross sections of SF_6 for remote sensing purposes; in previous compilations this has meant using the dataset derived from measurements by Varanasi et al. [12,718]. For HITRAN2020, this dataset has been replaced by a new one from Harrison [719], which covers a wider range of pressures and temperatures, notably at the low-pressure end, has a more accurately calibrated wavenumber scale, with improved signal-to-noise, more consistent integrated band intensities, and no channel fringes. This new dataset has been determined from spectra of pure and air-broadened SF_6 recorded at spectral resolutions between 0.002 and 0.03 cm^{-1} using a high-resolution FTS (Bruker IFS 125HR) and a 26-cm-pathlength cell. The previous dataset is now available in the HITRAN alternate folder.

3.1.1.4. Carbon tetrafluoride (CF_4, CFC-14). In previous compilations, the IR absorption cross sections of CF_4 available for remote sensing were derived from measurements in the Varanasi group [12,720]. For HITRAN2020, this cross-section dataset has been replaced by a new one from Harrison [721], determined from spectra of pure and air-broadened CF_4 recorded at spectral resolutions between 0.0018 and 0.03 cm^{-1} using a high-resolution FTS (Bruker IFS 125HR) and 5 cm- and 26 cm-pathlength sample cells. The new dataset covers a wider range of pressures and temperatures, notably at the low-pressure end, and corrects problems with the under-resolved low-pressure measurements. Furthermore, it has a more accurately calibrated wavenumber scale, more consistent integrated band intensities, and improved signal-to-noise. The previous Varanasi et al. dataset is now available in the HITRAN alternate folder.

3.1.1.5. Dinitrogen pentoxide (N_2O_5). Cross-sections of dinitrogen pentoxide covering the spectral range of 555–1765 cm^{-1} were originally added to HITRAN in the 1992 edition [10] based on Ref. [722]. For the 2004 edition [13], these cross-sections were replaced by those from Ref. [723]. However, only 540–1380 cm^{-1} was covered by the 2004 update, while there is still a clear need for having the data in the higher wavenumber region. Therefore, cross-sections from Ref. [722] in the 1680–1765 cm^{-1} window previously available in HITRAN, but omitted in the 2004 edition, have made their way back to HITRAN. However, they have been modified in the following way. The overlapping regions of Refs. [722,723] were compared, and it became apparent that in order to make them consistent, a factor of 1.13 had to be applied to the Ref. [722] cross-sections. Hence, in the 1680-1765 cm^{-1} window, cross-sections from Cantrell et al. [722] have been multiplied by 1.13 and added to the database for HITRAN2020.

3.1.2. Planetary-relevant broadening and high temperatures

The vast majority of absorption cross-sections in HITRAN2016 were measurements of pure gases (or samples broadened by air or N_2). To extend the applicability of the HITRAN database to planetary environments, many line-by-line molecules in HITRAN now contain collisional broadening parameters for H_2, He, CO_2 and H_2O (see Section 2). This allows the HITRAN line lists to be applied in radiative-transfer calculations of planetary atmospheres. Similarly, absorption cross-sections broadened by planetary-relevant species (H_2, He, CO_2, N_2) and covering appropriate temperatures (including higher temperatures applicable to exoplanets) are also being added to HITRAN. In HITRAN2020 some of the first "planetary" cross-sections have been included, but a larger update of relevant cross-sections is planned in the near future.

The lower atmosphere of Titan predominantly consists of N_2 (~94.2%) and CH_4 (~5.6%) with a small H_2 contribution (0.1%) and other carbon-rich compounds [724]. Therefore, the N_2-broadened absorption cross-sections already contained in HITRAN can be applied to the study of Titan. These will be supplemented with N_2-broadened absorption cross-sections of many hydrocarbon compounds recorded with experimental conditions (pressure, composition and temperature) chosen to represent those found in Titan's atmosphere. N_2-broadened absorption cross-sections for the following molecules have been added to the database for HITRAN2020: propylene [725], propane [726], n-butane [727], isobutane [728], and benzene [729,730]. Further N_2-broadened absorption cross-sections will be included as an update to HITRAN2020 and include Refs. [731–734] and additional works.

For the atmospheres of outer planets and many exoplanets, the dominant constituents are typically H_2 and He. Again, many measurements have been recorded with experimental conditions (pressure, composition and temperature) with broadening applicable to the outer planets. For HITRAN2020, H_2-broadened absorption cross-sections for propane [735] and isobutane [728] have been added to the database, with He-broadened absorption cross-sections also included for propane [735]. Further absorption cross-sections broadened by H_2 and He will be included as an update to HITRAN2020 and include Refs. [728–733,735–739] and additional works.

The absorption cross-sections in HITRAN are typically recorded at room temperatures (and below) as appropriate for the terrestrial atmosphere. Absorption cross-sections of spectroscopically-challenging compounds are predicted to be abundant (with respect to the terrestrial atmosphere) in planetary atmospheres at elevated temperatures. A series of absorption cross-sections based on FTIR measurements at high-temperatures (up to 700 K) have been added to HITRAN2020 for ethane [544], propane [740], and propylene [741]. Further high-temperature (up to 1600 K) absorption cross sections have been measured for hydrocarbons [742–747], alcohols [748] and aldehydes [749] using either an FTS and a tube furnace setup or a rapid-tuning broad scan external cavity quantum cascade laser in conjunction with shock tube facilities. Therefore, to increase the applicability of the HITRAN data to planetary environments, these high-temperature absorption cross-sections (among other works) will be considered for future updates to HITRAN.

3.2. UV cross-sections

3.2.1. O_3

A new UV cross-section database for ozone (referred to as DLR-O3-2020), which straddles the peak of the Hartley band and covers the spectral range 28,000–42,000 cm^{-1} (357–238 nm) and temperature range 193–293 K was generated within the framework of the ESA project SEOM-IAS, ESA/AO/1-7566/13/I-BG [750]. The database was tested for analysis of OMI observations and found to be satisfactory [751].

FTS transmittance measurements were performed using a Bruker IFS 125 HR spectrometer in combination with a coolable 22.15-cm-long single-pass cell. Measurements of absorption spectra were performed under "sealed-off" conditions. Ozone was prepared from O_2 in a silent discharge and purified and handled applying procedures similar to those given in Ref. [219]. Because decomposition of ozone was negligible at low temperatures, number densities could be derived from absolute pressure measurements. Absorption cross-sections span a large dynamic range from 3×10^{-22} to 1.0×10^{-17} cm^2/molecule, requiring pressure measurements over the range 0.1 to 30 mbar. In total, 191 spectra were measured. The transmittance spectra are provided with an uncalibrated wavenumber scale, which is justified by the low-resolution nature of the O_3 spectra. It was confirmed that, due to this smooth spectral dependence, the cross-sections do not depend markedly

on the air pressure. Consequently, the total pressure dependence of the cross-sections was neglected.

A multi-spectrum fitting approach as described in Ref. [218] was applied for each of the 6 temperatures in the range 193–293 K. Above 35 000 cm^{-1} the original spectral resolution of 3.3 cm^{-1} was decreased to ~7.7 cm^{-1} by Gaussian smoothing. Uncertainties for each spectral point were propagated from the noise in the transmittance spectra.

Polynomials of first- (>37 000 cm^{-1}) and second-order (<37 000 cm^{-1}) in temperature (in K) were then fitted to the absorption cross sections for each spectral point. This fit reveals systematic errors and reduces the statistical uncertainty. Absorption cross-sections were calculated from the polynomials at temperatures (193, 213, 233, 253, 273, 293 K) near the measurement conditions and are given in the database. The relative systematic uncertainties in the DLR-O3-2020 absorption cross-sections are 0.3%.

This is the first work where a large wavelength range relevant for ozone remote sensing was measured entirely with the FTS technique and a single spectrometer. We find differences of relative absorption cross-sections between the DLR-O3-2020 data with those from older references and inconsistencies among previous data on the order of few percent, which can be attributed to radiometric problems in the grating instruments. This result is supported by the good agreement of relative absorption cross sections with UV FTS measurements in the range 310-350 nm by the Bremen spectroscopy group [752]. The high quality of the DLR-03-2020 data can be seen by the good agreement with recent high-accuracy, room temperature ozone cross-sections, which include the 254 nm value recommended by Hodges et al. [753] $u_r = 0.31\%$ (DLR-03-2020 data 0.64(35)% below) and the laser-based measurement at 325.126 nm of Janssen et al. [754] $u_r = 0.09\%$ (DLR-O3-2020 data 0.94(31)% below). We note that as described in Ref. [753], the choice of the cross-section at 254 nm constitutes the spectroscopic anchor point for SI-traceable measurements of ozone mole fraction in the lower atmosphere. These observations are ubiquitous and are based on an international network of ground-level standard reference photometers (SRPs) operating at 254 nm that are dedicated to environmental monitoring. Currently, these instruments use the outdated cross-section value reported by Hearn et al. [755], which has a value that is about 1.2% greater and sixfold more uncertain than that recommended by Hodges et al. [753]. We note that there will be a globally coordinated change to the new cross-section value lasting 3 to 5 years, with a target change date of January 1, 2024. For physically consistent comparisons with ozone mixing ratios provided by ground-based SRPs to be based on the updated cross-section at 254 nm, future satellite retrievals of ozone abundance that use the DLR-03-2020 data may be multiplied by 1.0064. Nevertheless, there remains some debate whether this scaling factor can be uniformly applied to the DLR-O3-2020 cross-section data at all wavelengths. At the moment, a broadband correction of this form will be left to the discretion of the user.

The measurement database, calculated absorption cross sections with statistical uncertainties, and polynomials can be downloaded from Ref. [750].

3.2.2. SO_2

Starting with the HITRAN2008 edition [14], UV cross-sections of SO_2 from Refs. [756,757] were used in the HITRAN database. While being of excellent quality, they only cover a relatively high (by terrestrial atmosphere standards) temperature range of 298–358 K. A new UV database in the spectral range 23,000–36,000 cm^{-1} (435–278 nm) and temperature range 193–293 K was generated within the framework of the ESA project SEOM-IAS, ESA/AO/1-7566/13/I-BG. A detailed publication is in preparation [758].

FTS transmittance measurements were performed using a Bruker IFS 125 HR spectrometer in combination with a 22.15 cm coolable single pass cell with a maximum optical path difference of 0.3 cm. Measurements of absorption spectra were performed under sealed-off conditions. SO_2 was supplied by Linde with a specified purity of 99.98%.

Since SO_2 is stable, number densities could be derived from absolute pressure measurements. The absorption cross sections have a large dynamic range from 10^{-24} to 10^{-18} cm^2/molecule, requiring a pressure range from 1.0 to 1000 mbar. In total, 87 spectra were measured. A calibration factor of 1.000003905 was applied, deduced from the calibration factor of a CH_4 measurement around 6000 cm^{-1} with a correction accounting for the different input aperture diameter.

A multi-spectrum fitting approach as described in Ref. [218] was applied for each of the 6 temperatures in the range 193 to 293 K. Uncertainties in the baseline were reduced by fixing the absorption cross sections in the ranges <23,500 cm^{-1} and 24,00024,400 cm^{-1} to zero. Uncertainties for each spectral point were propagated from the noise in the transmittance spectra.

In contrast to ozone, SO_2 showed high resolution features with widths down to the Doppler limit. An error-free absorption cross sections database would require air-broadened measurements with sub-Doppler instrumental resolution. To avoid self-broadening, SO_2 pressures must be below 10 mbar, which in turn requires multi-reflection cell measurements. In principle this could have been carried out, but is impractical due to resource limitations. Thus, it was decided to measure pure SO_2 up to 1000 mbar with a moderate resolution of 1.7 cm^{-1}. In order to assess the systematic errors associated with this approach, Doppler-limited measurements have been carried out as well as self-broadened measurements with sufficient instrumental resolution to have monochromatic spectra (not provided here). The impact under conditions relevant to the TROPOMI instrument was found to be small within the requirements. The total column error was <2% for all atmospheric scenarios with SO_2 columns up to 2000 DU.

Polynomials of second-order in temperature (in K) were then fitted to the absorption cross sections for each spectral point in the range 25,000–36,000 cm^{-1} (400–278 nm). This fit reveals systematic errors and improves the statistical uncertainty. Indeed, a fourth-order offset polynomial had to be fitted for the 213 K absorption cross sections in the range 25,000–30,900 cm^{-1} to reduce the residuals of the temperature dependence fit. The statistical errors of the absorption cross sections were propagated into the polynomial coefficients errors and are used together with the χ^2 of the polynomial fit to calculate absorption cross sections at about measurement temperatures.

The new data overcome some problems with the data sets used so far. The data from Hermans and Vandaele [756,757] are applied for high atmospheric SO_2 load in the spectral region 360–390 nm (27800–25640 cm^{-1}) and are extrapolated to lower temperature since measurements covered only 298–358 K. In the regions for lower volcanic (325–335 nm, 30,770–29,850 cm^{-1}) and background (312–326 nm, 32,050–30,675 cm^{-1}) $SO_{,2}$ the data from Bogumil et al. [759] are used for atmospheric retrieval. These data have an inconsistency between 203 and 223 K in the temperature dependence of the absorption cross sections. Applying the new absorption cross section data would yield maximum SO_2 column changes of 5% with respect to the Hermans and Vandaele data and 16% with respect to the Bogumil et al. data.

The measurement database, calculated (semi-empirical) absorption cross sections with statistical uncertainties and polynomials can be downloaded from Ref. [760]. The cross-sections from this work have been added to the HITRAN2020 database.

4. Collision-induced absorption

4.1. Description of 2019 update

Collision-induced absorption (CIA) is the process of absorption of light by pairs of colliding molecules, due to the dipole moment induced by interactions between the colliding molecules. That is, CIA is an additional source of absorption, not just broadening of the existing monomer absorption lines. However, often CIA will lead to absorption in the same spectral regions as monomer absorption, leading to a broad feature underneath sharp absorption lines. The contribution of this continuum absorption is especially important for forbidden transitions, where monomer transitions are weak, or conversely if the absorption lines are saturated, such that it becomes difficult to extract information from their intensity. In the far infrared, CIA contributes appreciably to the heat balance of planetary atmospheres due to absorption of outgoing blackbody radiation. In the terrestrial atmosphere, CIA by N_2 and O_2 molecules is important for the remote sensing applications [311,761–766], and in exoplanetary atmospheres O_2-O_2 collision absorption is an important target as a possible biomarker [767]. Collision-induced absorption involving N_2 and CO_2 molecules is important in the atmospheres of Titan and Venus, respectively, whereas collision partners such as He, H_2 and CH_4 are important in gas giants and brown dwarfs [768]. Collision-induced absorption by CH_4, CO_2, and H_2 was suggested to affect the modeling of Venusian and Martian atmospheres in the early stages of geological history [769,770].

HITRAN has a section devoted to collision-induced absorption, which was introduced in 2012 [771]. This section has recently been updated [772]. The temperature and spectral ranges for the bands included for each collisional pair can be found in Table 11. The main updates involved the rototranslational (RT) and vibrational bands of N_2-N_2, CO_2-CO_2, the RT band of CO_2-H_2 and CO_2-CH_4, collisions involving different molecules and helium atoms, H_2-H_2 at low temperatures, and electronic transitions in O_2-O_2 and O_2-N_2. The database now contains CIA for N_2-N_2, N_2-H_2, N_2-CH_4, N_2-H_2O, N_2-O_2, O_2-O_2, O_2-CO_2, CO_2-CO_2, H_2-H_2, H_2-He, H_2-CH_4, H_2-H, H-He, CH_4-CH_4, CH_4-CO_2, CH_4-He, and CH_4-Ar collision pairs. Instructions for accessing the CIA section of the HITRAN database can be found on the HITRAN website (www.hitran.org/cia). A set of supplementary files is available in the “Alternate folder” which contain data that are not recommended in general but do have a clear advantage over the recommended data, such as extended temperature ranges, accounting for spin statistics, or are constructed to be consistent with a particular line list. Further updates of the CIA data are forthcoming, as described below.

4.2. Post-2019 updates and prospects for the future

4.2.1. N_2-N_2 *rototranslational band*

In the Karman et al. [772] effort, the Main folder RT spectra for N_2-N_2 were updated with the results of quantum mechanical line-shape calculations from Karman et al. [806]. Also, the results of experimental measurements from Sung et al. [792] were provided in the Alternate folder. In the current edition, we have updated the Main folder N_2-N_2 CIA spectra with the slightly refined results of the semi-classical trajectory-based simulation performed by Chistikov et al. [789] at 34 temperatures between 70 and 400 K.

The trajectory-based approach developed in Ref. [789] relies on the assumption that the collisional dynamics, as well as the interaction with the electromagnetic field, can be considered within the classical framework. On the one hand, the use of a classical approximation allows the extension of this approach to the molecular systems, for which quantum consideration is presently unfeasible. On the other hand, immediately produced classical spectral profiles do not conform to the detailed balance principle [807], which is responsible for the striking asymmetry of the experimentally observed profiles. It is widely believed that this major defect of the classical approach can be approximately corrected through the use of the so-called desymmetrization procedure [807,808]. The latter, however, is not unambiguously defined (e.g., discussion in Ref. [808]). The use of a semi-empirically scaled variant of Egelstaff's procedure described by Frommhold [807] instead of the Schofield's procedure [809] adopted in Ref. [789] improved the agreement with the low-temperature measurements reported by Sung et al. [792].

Fig. 35 shows the results of the theoretical calculations for the N_2-N_2 RT band and experimental measurements [792] at two representative temperatures. It is seen that, at least in the vicinity of the absorption peak, the trajectory-based results [789] refined with the use of Egelstaff's procedure demonstrate an improvement compared to the previous results of Karman et al. [806]. For the temperatures 78.3, 89.3, 109.6, and 129.0 K, the measured data at the peak exceed the Karman et al. [806] calculations by 18, 13, 12, and 10%, respectively. In contrast, the trajectory-based spectra underestimates absorption with respect to experimental data by 5, 3, 3, and 2%, respectively. Such a deviation, at least for temperatures in excess of 80 K, is not significant given a reported ±3% uncertainty in the measured absorption. The measurements at 78 K appear to be suffering from the systematic non-zero offset; therefore the discrepancy with theoretical results should be interpreted with caution. In the far wing, beyond 150 cm^{-1}, irrespective of the temperature, neither of the calculations demonstrate perfect overall agreement. We have to note, however, that at 109.6 and 129.0 K (not shown) the Karman et al. [806] calculations appear to agree better with the experimental measurements at the band wing.

For the millimeter wavelength range, Serov et al. [811] have recently shown that trajectory-based spectra issued from Chistikov et al. [789], as well as Borysow et al. model [810], are in good agreement with new resonator spectrometer measurements from 105 to 200 GHz and the results of previous experimental studies, e.g., Meshkov et al. [812]. The N_2-N_2 data provided in the previous effort [772] were found to significantly underestimate absorption in the 105-200 GHz range due to the choice of interpolating procedure, which is imperative to simulate continuous frequency dependence since the calculations in Karman et al. [806] were carried out on a rare frequency grid.

4.2.2. O_2 *fundamental in* O_2-N_2, O_2-O_2 *and* O_2-air

In the Richard et al. [771] effort, the O_2 fundamental band O_2-O_2 data were adopted from Baranov et al. [790]. These Main folder data remained unchanged in the 2019 update [772]. Here, we include the data for the O_2 fundamental in O_2-N_2 and O_2-air, which weren't previously provided, and extend the data in the O_2-O_2 Alternate folder as described below.

Laboratory measurements of the absorption by pure O_2 and O_2-N_2 mixtures most recently have been reported in Thibault et al. [800], Orlando et al. [801], and Mate et al. [813]. The data from Mate et al. [813] will be retrieved from the authors and considered for future inclusion in the database. Thibault et al. [800] and Orlando et al. [801] performed comprehensive FTIR studies at 193–293 K with 0.5 cm^{-1} resolution and at 225–356 K with 1.0 cm^{-1} resolution, respectively. Both sets of measurements for O_2-O_2 were validated against the Baranov et al. [790] data. As seen in Fig. 36, Orlando et al. [801] data contain the most noise but extend to higher temperatures than those reported in Thibault et al. [800]. The absorption data from Thibault et al. [800] at 193–293 K and Orlando et al. [801] at 356 K converted to the HITRAN format are available in Main folder O_2-N_2 and Alternate folder O_2-O_2. The Orlando et al. [801] data at 356 K was cast to the same

Table 11
Summary of the different bands available in the HITRAN CIA section, including Supplementary folders for all collisional systems.

System	Folder	Spectral range (cm^{-1})	T range (K)	# of sets	Ref.
H_2-H_2	Main	20–10 000	200–3000	113	[773]
	Alternate	0–2400	40–400	120	[774]
H_2-He	Main	20–20 000	200–9900	334	[775]
H_2-H	Main	100–10 000	1000–2500	4	[776]
He-H	Main	50–11 000	1500–10 000	10	[777]
H_2-CH_4	Main	0–1946	40–400	10	[778]
N_2-He	Main	1–1000	300	1	[779]
CO_2-He	Main	0–1000	300	1	[779]
CO_2-Ar	Main	0–300	200–400	21	[780]
CH_4–He	Main	1–1000	40–350	10	[781]
CH_4–Ar	Alternate	1–697	70–296	5	[782]
CH_4–CH_4	Alternate	0–990	200–800	7	[783]
CO_2-H_2	Main	0–2000	200–350	4	[770]
CO_2-CH_4	Main	1–2000	200–350	4	[770]
CO_2-CO_2	Main	1–750	200–800	10	[784]
		1000–1800	200–350	6	[785]
		1000–1800	200–350	6	[786]
		2510–2850	221–297	3	[787]
		2850–3250	298	1	[787]
N_2-H_2	Main	0–1886	40–400	10	[788]
N_2-N_2	Main	0–450	70–200	14	[789]
		0–550	210–300	10	[789]
		0–650	310–400	10	[789]
		1850–3000	301–363	5	[790]
		2000–2698	228–272	5	[791]
		4300–5000	200–330	14	[764]
	Alternate	30–300	78–129	4	[792]
O_2-O_2	Main	1150–1950	193–353	15	[793]
		7450–8491	296	1	[794]
		9091–9596	293	1	[795]
		10 512–11 228	293	1	[796]
		12 600–13 839	296	1	[797]
		14 206–14 898	293	1	[798]
		15 290–16 664	203–287	4	[799]
		16 700–29 800	203–293	5	[799]
	Alternate	1300–1850	193–356	7	[800,801]
		7583–8183	206–346	15	[795]
		9060–9960	206–346	15	[795]
		10 525–11 125	206–346	15	[795]
		12 804–13 402	206–346	15	[795]
		14 296–14 806	206–346	15	[795]
O_2-N_2	Main	1300–1850	193–356	7	[800,801]
		1850–3000	301–363	5	[790,802]
		2000–2698	228–272	5	[791,802]
		7450–8488	293	1	[794]
		12 600–13 840	296	1	[797]
	Alternate	7583–8183	206–346	15	[795]
		12 804–13 402	206–346	15	[795]
N_2-Air	Main	1850–3000	301–363	5	[790,802]
		2000–2698	228–272	5	[791,802]
		4300–5000	200–330	14	[764]
O_2-Air	Main	1300–1850	193–356	7	[800,801]
		7450–8480	250–296	3	[794]
		9091–9596	293	1	[795]
		10 512–11 228	293	1	[796]
		12 600–13 839	300	1	[797]
	Alternate	12 990–13 220	298	1	[327]
		7583–8183	206–346	15	[795]
		9060–9960	206–346	15	[795]
		10 525–11 125	206–346	15	[795]
		12 802–13 402	206–346	15	[795]
		14 206–14 806	206–346	15	[795]
N_2-H_2O	Main	1930–2830	250–350	11	[803]
N_2-CH_4	Alternate	0–1379	40–400	10	[804]
O_2-CO_2	Main	12 600–13 839	200–300	1	[805]

frequency grid as was used in Thibault et al. [800] through cubic spline interpolation.

Following the concept introduced in the HITRAN2016 update [16], we provided O_2–air data useful for applications for the Earth's atmosphere. The data for O_2–air was represented as a sum of O_2–O_2 and O_2–N_2 continua taken with 79% and 21% weights corresponding to the oxygen and nitrogen abundances in the atmosphere. For consistency, the O_2–air cross-sections for each temperature are calculated based on the O_2–O_2 and O_2–N_2 data from the same source. Thibault et al. [800] data at 193–293 K and Orlando et al. data at 356 K were taken to estimate the O_2–air cross-sections. In order to reduce the noise, the Orlando et al. [801] data

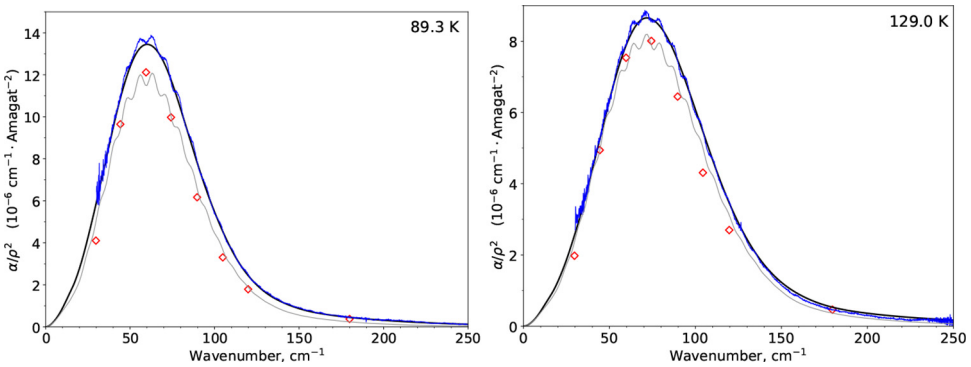

Fig. 35. N_2-N_2 collision-induced absorption spectra at two temperatures. The black curves indicate results from the trajectory-based calculation [789], the blue curves denote the experimental measurements [792], the red diamonds denote the results from the quantum-mechanical calculation [806], and the grey curves denote Borysow model spectra [810]. (For interpretation of the references to color in this figure legend, the reader is referred to the web version of this article.)

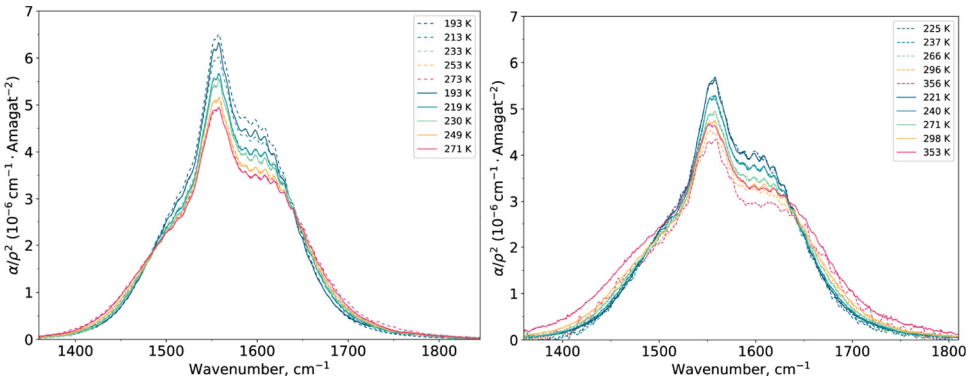

Fig. 36. Overview of O_2-O_2 data in the O_2 fundamental. Solid lines refer to the Baranov et al. [790] data, dashed lines refer to the Thibault et al. [800] data in the left panel and the Orlando et al. [801] data in the right panel, respectively.

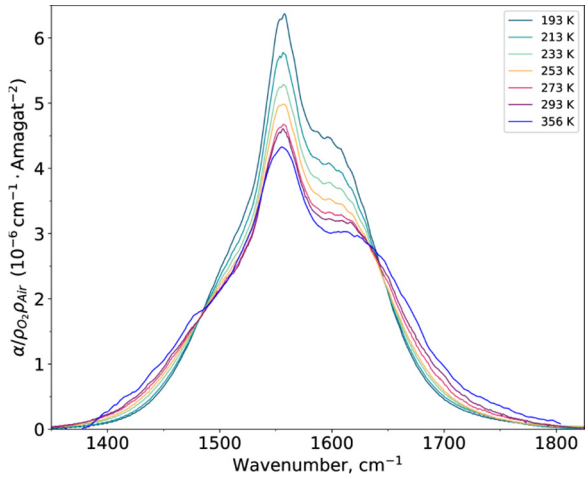

Fig. 37. Overview of O_2-air data. The data for 193-293K and 356K are derived from the Thibault et al. [800] and Orlando et al. [801] measurements, respectively.

were smoothed using a simple moving average routine with the window size of 15 cm^{-1}. Fig. 37 demonstrates that O_2–air absorption data, despite being compiled from two sources, exhibit consistent temperature dependence.

4.2.3. CO_2–*Ar rototranslational band*

Argon is known to be the third most abundant gas in the Earth's atmosphere, with a volume mixing ratio of 0.934%. It is more than twice as abundant as water vapor, and more than 20 times as abundant as carbon dioxide. Although largely inert in absorption, argon is capable of modifying radiative properties of other molecular species by virtue of weak intermolecular perturbation.

We include the CO_2–Ar RT spectra issued from the trajectory-based simulation carried out in Ref. [780]. In these calculations, an array of up to 20 million classical trajectories was rendered through the solution of dynamical equations in Hamilton form in the laboratory frame of reference. The ensemble-averaged autocorrelation function of the induced dipole moment is obtained from these simulations, and its Fourier transform yields the absorption spectrum. The contributions to CIA profile from the free/quasibound and true bound states were calculated separately using the same computational approach. The trajectory-based calculations were performed using *ab initio* potential energy and induced dipole surfaces obtained with the coupled-cluster (CCSD(T)) method.

The absorption spectra at millimeter wavelengths in the CO_2–Ar mixtures have been recorded with a resonator spectrometer as is described in detail in Odintsova et al. [780]. These spectra were measured in the 105-240 GHz range at 297.3 K. An excellent agreement between reported experimental data and calculated profiles was achieved. In an earlier study, Oparin et al. [814] examined the CO_2–Ar RT band using classical trajectories method and simplified potential energy and induced dipole surfaces. A thorough comparison of the data from Ref. [814] with the results of the recent trajectory-based simulation in Odintsova et al. [780] showed good agreement of both sets of calculated CIA spectra over the entire range of CO_2–Ar RT band including the millimeter wavelength range. However, we consider the data from Ref. [780], which are based on *ab initio* potential energy and induced dipole surfaces, to be somewhat more precise. Moreover, the

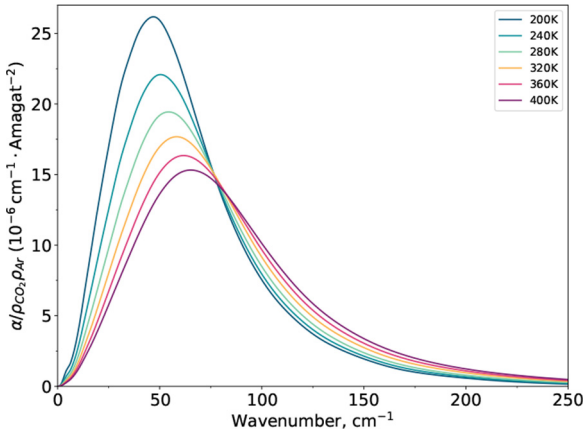

Fig. 38. The temperature variation of the CO_2-Ar CIA RT band-shape in the 200-400 K range.

Odintsova et al. [780] data cover a wider temperature range compared to the Oparin et al. data [814].

Overall, HITRAN CIA tabulates 21 spectra for the CO_2–Ar RT band from 200 K to 400 K with steps of 10 K. The temperature variation in the CO_2–Ar RT band-shape is shown in Fig. 38. The contribution from true bound states manifests itself as a secondary peak in the 3-7 cm^{-1} interval, which becomes more pronounced at lower temperatures.

4.2.4. Outlook for the future

The CIA section of the HITRAN database underwent a substantial update in 2019 [772] featuring improvements to the existing data, extension of temperature and spectral ranges, and addition of new collisional pairs. Nevertheless, there is a growing demand to further improve and extend CIA data in HITRAN. This update represents a small revision of the CIA section. For the next update of the CIA section, data from a number of recent papers will be evaluated, such as measurements and semi-empirical models of CO_2–H_2 within RT band [769,815,816] and (1-0) band of H_2 [817] and CH_4–CO_2 within RT band [769,815,816], results of trajectory-based simulation of CH_4–N_2 RT band [818], measurements of $a^1\Delta_g(v=1) \leftarrow X^3\Sigma_g^-(v=0)$ O_2–CO_2 [819] and $a^1\Delta_g \leftarrow X^3\Sigma_g^-$ O_2–O_2 [820] CIA bands.

5. Aerosol refractive indices

HITRAN2020 contains refractive indices in the visible, infrared, and millimeter spectral ranges of many types of materials which make up cloud, aerosol particles, and planetary surfaces. The indices apply to materials found in the Earth's atmosphere and surface, and candidate exoplanet atmospheres. Knowing the real and imaginary indices of particles, as a function of wavelength, and the particle size distribution of cloud or aerosol particles, one can calculate the extinction, scattering, and absorptive properties of the atmospheric particles [821]. These particle optical depths add to gas optical depths, which in combination, determine the wavelength dependent total optical depths of an atmosphere. The interpretation of remote-sensing retrievals of gaseous species is limited frequently by how well one can separate gaseous opacity from that of clouds and aerosols. Clouds and aerosols also take part in chemical reactions in both the liquid and solid phases, with heterogeneous chemistry on Polar Stratospheric Clouds (PSCs) being a particularly important example [822]. Table 12 lists the HITRAN2020 indices. The listing is comprised of main and supplementary data sets. Several of the supplementary datasets are older, correspond to a limited number of wavelengths, or are not complete, e.g., just the imaginary component is tabulated. Several of the supplementary datasets are for similar materials in the main set and can be used to compare indices from different laboratories. Table 12 begins with the venerable set of indices compiled at the Air Force Cambridge Research Laboratory in 1987 [823], which includes a wide variety of materials: Water, ice, sodium chloride, sea salt, water-soluble aerosol, ammonium sulfate, carbonaceous aerosol, volcanic dust, sulfuric acid, meteoric dust, quartz, hematite, and sand. Table 12 then lists indices of supercooled water, ice at various temperatures, materials which comprise PSC particles, Saharan dust, volcanic ash, secondary organic aerosol (SOA), brown carbon, biomass fire particles, flame particles, surface minerals, Titan tholins, and candidate exoplanet atmospheric particulates.

As discussed in the Bohren and Huffman [873] text on light scattering and Mie calculations, the complex refractive index m is a function of wavelength, with real m_{real} and imaginary m_{imag} components.

$$m = m_{real} + i m_{imag} \tag{4}$$

A plane light wave of wavelength λ is attenuated along the propagation x-axis according to

$$E = E_0 \exp(-2\pi m_{imag} x/\lambda)\exp(i2\pi m_{real} x/\lambda - i2\pi ct/\lambda) \tag{5}$$

with time t and the speed of light c. The imaginary refractive index m_{imag} therefore determines the amount of light absorption in a medium, attenuating the light intensity by $\exp(-4\pi m_{imag} x/\lambda)$ along a path of distance x.

Exoplanet atmosphere particles are produced at a variety of temperatures from 700 K (e.g., ZnS) to 1725 K (e.g., SiO_2). HITRAN2020 includes most of the condensates tabulated by Wakeford and Sing [874], who studied hot-Jupiter exoplanet atmospheres. Dr. Harrald Mutschke of the Friedrich Schiller University Jena kindly provided the exoplanet indices to HITRAN. Additional exoplanet material indices not listed in Table 12 are accessible from the extensive Jena website (http://www.astro.uni-jena.de/Laboratory/OCDB/index.html). New indices in HITRAN2020 include the secondary organic aerosol (SOA) indices of Liu et al. [837,838] and Dingle et al. [864], volcanic ash indices of Deguine [836], and additional indices of Titan tholins (Imanaka et al. [849]). While primary organic aerosols are emitted into the troposphere directly by the biosphere, SOA is produced by a series of gas-phase organic chemistry reactions. The Liu et al. [837,838] indices (from 0.23 to 1.2 μm) and the Dingle et al. [864] indices (at 532 and 1064 nm) correspond to several sets of indices, each of which corresponds to a specific set of hydrocarbon, hydroxyl radical sources, and NO initial laboratory conditions. SOA comprises an important fraction of tropospheric aerosols. An example of the new volcanic ash indices is presented in Fig. 39, which displays the volcanic ash

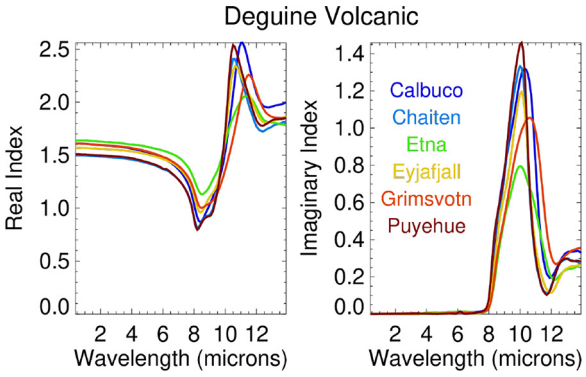

Fig. 39. Variations in the real and imaginary indices in volcanic samples from six volcanoes [836].

Table 12
Refractive indices included in HITRAN2020.

Compound	Measurement Specifics	Reference
Water, ice, sodium chloride, sea salt, water soluble aerosol, ammonium sulfate, carbonaceous aerosol, volcanic dust, sulfuric acid, meteoric dust, quartz, hematite, sand	Room temperature, 0.2-40 μm	[823]
Water	27°C, 10-5000 cm^{-1}	[824]
Supercooled water	238 - 269 K, 1100 - 4500 cm^{-1}	[825]
Ice	266 K, 0.04μm - 2 m	[826]
Ice	130 - 210 K, 800 - 4000 cm^{-1}	[827]
Sulfuric acid (H_2SO_4/H_2O)	215 K, 499-6996 cm^{-1}	[828]
Sulfuric acid (H_2SO_4/H_2O)	273 - 298 K, 400 - 7500 cm^{-1}	[829]
Nitric acid (HNO_3)	223 - 293 K, 450 - 6500 cm^{-1}	[830]
Ternary Solution ($H_2SO_4/H_2O/HNO_3$)	203 - 293 K, 450 - 6500 cm^{-1}	[830]
NAD (nitric acid dihydrate)	160-190 K, 700-4700 cm^{-1}	[831]
NAT (nitric acid trihydrate)	160 K, 711-4004 cm^{-1}	[832]
Amorphous nitric acid (aNAM, aNAD, aNAT)	153 K, 482-7000 cm^{-1}	[833]
NAM (nitric acid monohydrate)	179 K, 482-6002 cm^{-1}	[833]
NAD	184 K, 482-6981 cm^{-1}	[833]
αNAT	181 K, 482-6989 cm^{-1}	[833]
βNAT	196 K, 482-6364 cm^{-1}	[833]
Saharan dust	0.30 - 0.95 μm	[834]
Volcanic ash	0.45 - 25 μm	[835]
Volcanic ash	690 - 32500 cm^{-1}	[836]
SOA	0.23 - 1.2 μm	[837]
SOA	0.23 - 1.2 μm	[838]
Organic acids (Oxalic, malonic, succinic, pinonic, pyruvic, phthalic)	0.25 - 1.1 μm	[839]
Brown carbon	0.2 - 1.2 μm	[840]
Burning vegetation	525-5000 cm^{-1}	[841]
Burning vegetation	0.35 - 1.5 μm	[842]
Carbon flame	0.4 - 0.7 μm, 25 - 600°C	[843]
Flame soot	0.2 - 38 μm	[844]
Minerals (clay, illite, kaolin, montmorillonite)	2.5 - 200 μm	[845]
Minerals (granite, montmorillonite)	5 - 40 μm	[846]
Titan tholins	0.02 - 920 μm	[847]
Titan tholins	0.2 - 1 μm	[848]
Titan tholins	2.5 - 25 μm	[849]
KCl	0.22 - 166 μm	[845]
ZnS	0.22 - 166 μm	[845]
SiO_2 (amorphous)	6.6 - 487 μm, 10 - 300 K	[850]
SiO_2 (crystalline)	6.25 μm - 10 μm, 300 - 928 K	[851]
Al_2O_3	7.8 - 200 μm	[852]
FeO	0.2 - 500 μm	[853]
$CaTiO_3$ (Perovskite)	2.0 - 500 μm	[854]
Fe_2O_3	0.1 - 1000 μm	[855]
Fe_2SiO_4 (Fayalite)	0.4 - 10 μm	[856]
Fe_2SiO_4 (Fayalite)	2 μm- 10 μm	[857]
$MgAl_2O_4$ (annealed)	1.6 - 6825 μm	[858]
$MgAl_2O_4$ (natural)	2.0 μm - 10 μm	[858]
Mg_2SiO_4	0.19 - 948 μm	[859]
$MgSiO_3$	0.2 - 500 μm	[859]
TiO_2 (Rutile)	0.47 - 36.2 μm	[860]
TiO_2 (Anatase)	2.0 - 5843 μm	[860]
TiO_2 (Brookite)	2.0 - 5843 μm	[861]
Supplementary		
Water and Ice	0.67 - 2.5 μm, imaginary	[862]
Saharan Dust	0.35 -0.65 μm	[863]
SOA	0.375 and 0.632 μm, various radical sources	[864]
SOA	0.532 μm, various cases	[865]
Diesel Soot	0.45 - 10 μm	[845]
Sulfuric acid (H_2SO_4/H_2O)	200-300 K, 825-4700 cm^{-1}	[866]
Sulfuric acid (H_2SO_4/H_2O)	183- 293 K, 2 - 23 μm	[867]
Nitric acid (H_2SO_4/HNO_3)	213-293 K, 2 - 23 μm	[867]
Sulfuric acid (H_2SO_4/H_2O)	Room temperature, 75 and 90% H_2SO_4	[868]
Nitric acid (H_2SO_4/HNO_3)	220 K, 754-4700 cm^{-1}	[869]
Nitric acid (H_2SO_4/HNO_3)	Room temperature, 2 - 40 μm	[870]
Sulfuric and Nitric acids	Room temperature, 6 - 11 μm	[871]
Titan organic haze	0.532 μm (single wavelength)	[872]

indices of Deguine et al. [836]. Due to the impact upon civil aviation by the Icelandic Eyjafjallajökull eruption in 2010, there is interest in the optical properties of dust emissions from active volcanoes. Fig. 39 displays the indices for six volcanoes, including Eyjafjallajökull. There is a sizable difference (by a factor of 1.5) in the imaginary indices near 10.6 μm for the Etna (Italy) and Grímsvötn (Iceland) volcanoes, and thus for the same particle size distribution, a sizable difference in the extinction spectra (a factor of 1.6 at 10.6 μm).

HITRAN2020 extends the HITRAN-RI program [875] that resides on the HITRAN website, by including a version of the program written in Python. HITRAN-RI is also written in the IDL (Interactive Design Language) and FORTRAN 90 programming languages, and all three versions apply the Bohren-Huffman [873] Mie code. The FORTRAN 90 version has been changed to read in ASCII files for compilation ease purposes. All programs and subdirectories are bundled together in a single tar file. In all three versions of the program, the user edits the directory path names in the `directory.dat` ASCII file, specifying the subdirectories that have the input data sets and the output subdirectory to which files are written to. One then examines the `indices.dat` ASCII file to determine which material to work with. The editing of the `work.dat` file just requires simply replacing integers and floating-point numbers with new values. The wavelength range, and the particle size distribution, are also specified in the `work.dat` file. The use of the ".dat" files allows the user to specify the HITRAN-RI calculations without having to modify the source code. The HITRAN-RI program then calculates optical property spectra of extinction, scattering, absorption, single scattering albedo, and the asymmetry parameter. The IDL version of HITRAN-RI generates output postscript and NetCDF files of the input indices, particle size distribution, and wavelength dependent optical properties. As an instructional aid, test cases can be run. PDF versions of the original reference papers are contained in a subdirectory, while the refractive indices are stored in subdirectories in ASCII and NetCDF formats. The user can edit the `work.dat` file to instruct the program to read in user-specified refractive indices and/or the particle size distribution. Since all of the source code is fully accessible, HITRAN-RI can be modified as desired by the user.

6. Global data and software

6.1. Database structure and interface

HITRAN*online*, the software providing an online interface to the HITRAN database at https://hitran.org, has undergone a series of improvements and minor modifications since its release in 2015 [51]. In addition to bug-fixes and security patches, the entire code base was ported to Python 3 in 2019, using Django 2 as its web framework. At the same time the web server was configured to use the HTTPS protocol for secure communication with client computers. Errors in the HDF-5 output format were corrected and compatibility with the major web browsers on both Windows and Unix-like operating systems improved.

To access the database, HITRAN*online* requires users to register for an account by providing a name and using a valid email address. An ongoing inconvenience has been the large number of automated bots signing up fake accounts with the website that consequently required removal. This has been mitigated by the introduction of a question on the registration page which is found to be difficult to parse by a bot but intended to be easy for humans to answer correctly. The question is currently “1 + tωo”; for the avoidance of doubt, the correct answer to this question is “3” or “three”.

A number of video tutorials (https://hitran.org/videos/) have been created to guide users through the main aspects of the database and demonstrate how to navigate the website and make queries in different formats. These tutorials have proven to be very helpful to new users, and on aggregate they have been watched over 9500 times so far.

Recently, a new automated referencing system has been developed and implemented as part of the HITRAN project to provide consistent, accurate and detailed bibliographies for every source of data in the HITRAN database. Administrators using this system can obtain the complete bibliographic entry for the article they wish to cite by entering only its unique digital object identifier (DOI). The referencing program, which is available as open source software, is described by Skinner et al. [876]. It provides a convenient, customizable bibliographic system to allow database administrators to implement bibliographies in their database systems more efficiently and with fewer human errors.

6.2. HAPI2

The first generation of the HITRAN Application Programming Interface (HAPI) [52] has proven to be a convenient tool for acquiring and working with HITRAN data. The HAPI library provided a means of downloading and filtering the spectroscopic transitions for molecules provided by the HITRAN*online* [51] web server, using a range of partition sums and spectral line parameters. A significant feature of HAPI was the ability to calculate absorption coefficients based on the line-by-line spectroscopic parameters. For a more detailed description of this software library, we refer readers to the dedicated paper [52] and corresponding user manual available online (https://hitran.org/hapi).

Although the first generation of HAPI allows users to build new functions, it does not have the functionality to make use the whole range of spectroscopic data currently available in the HITRAN database. For instance, the first version of the REST-API used by HAPI only allowed line-by-line data to be downloaded. For this reason, an extended version of HAPI (with greater functionality) is provided as part of HITRAN2020. This extended version, named “HAPI2”, includes all the functionality of HAPI but with a new Python library and has been designed to be backward-compatible. To take advantage of the more advanced features in the “second generation” extension library, users will be required to upgrade to HAPI2.

One main feature of HAPI2 will be the ability to consider more objects available for downloading. This essentially means users will now be able to access the vast library of absorption cross-sections, CIA, and more. This was achieved by revisiting the HITRAN server’s REST API. A new version is able to access the information for a number of entities available in HITRAN. Among these entities are molecule information, reference sources, line-by-line transitions, monomer and collision-induced absorption cross-sections, and metadata on line parameters. An example of the REST API query for the water molecule and corresponding JSON response are shown in Fig. 40. Users should note that, in order to be able to query the new REST API, a valid API key is required in the request. An API key is a unique string identifier, which can be generated in the HITRAN*online* user profile by pressing the button “generate API key”, as shown in Fig. 41.

Secondly, for applications that require numerous transitions to be considered in absorption coefficient calculations (such as at high-temperatures), the speed of calculation is of paramount importance. Although the first generation of HAPI [52] contained some Numpy-based optimizations [877], it lacked the means for fast cross-section computation. In HAPI2, efficient coding for HT and SDV profiles [74,878,879] that makes use of the “Just-in-time” compilation approach, has provided a significant speed increase for computations.

Fig. 40. Sample JSON response for the REST API query requesting molecule information, with an additional restriction imposed on the HITRAN ID value. The JSON fields contain the information on the molecule entry with the id=1 (water vapor).

Fig. 41. An API key is required to make use of the full querying capabilities of HAPI2. Users can generate a personal API key from their HITRAN*online* user profile at www.hitran.org by clicking "Generate API key". The resulting API key will be be displayed in the location indicated in the screenshot.

In addition, among the prominent features of HAPI2 is the ability to account for the full line-mixing. Following the work of Hashemi et al. [161], the latest versions (starting from v1.1) of HAPI [52] can account for line-mixing effects through the implementation of the first-order Rosenkranz line-mixing parameters Y [232] into the Hartmann-Tran profile for the CO_2 molecule. Despite the advantages of the first-order approach (e.g., reduced number of collisional quantities and fast computations of the profiles), it fails to model the absorption for regions where lines are dense and strongly affected by line-mixing, such as Q-branches of CO_2. The HAPI2 extension includes the Python version of the line-mixing code by Lamouroux et al. [166] with account of the corrections made by Hashemi et al. [161]. Despite the structure of the Python version, it has essentially the same structure as the FORTRAN version [166] (and references therein), the major difference is that the database files are no longer provided. They will be constructed from the code locally by the users, as a preliminary step of the first CO_2 line-mixing calculation. If the files were already built, this step will not be executed by the code, except if it is explicitly asked by the user.

As was the case for HAPI [52], the HAPI2 extension stores the downloaded files locally. Thus, the final prominent feature of HAPI2 is the ability to make use of the fast and flexible relational database on these local files. This gives users the ability to perform data mining on the stored sets of molecules, references, line parameters, and cross-sections, including user-supplied data sets. The data scheme used in this relational engine is an extension of the relational scheme constructed by Hill et al. [50]. In the HAPI2 implementation, this scheme was created using the SQLAlchemy (https://www.sqlalchemy.org/) library which provides back-ends for many existing database management systems such as SQLite, MySQL, PostgreSQL, and more. HAPI2 uses SQLite as the default database back-end. The back-ends in HAPI2 use the Object Relational Mapping (ORM) technique to connect with the low-level database. Some of the data filtering is available through the REST API on the server side (e.g., setting the wavenumber range for transitions and specifying the set of isotopologues). Nevertheless, the full capability of the data filtering can be done locally by the means of the standard SQLAlchemy ORM methods.

The HAPI2 extension is currently available on the Github repository (https://github.com/hitranonline/hapi2) as well as in the Python Package Index. A more complete description of the HAPI2 extension library will be described in a separate paper.

6.3. *HAPIEST*

The HITRAN Application Programming Interface and Efficient Spectroscopic Tools (HAPIEST) is a joint project which started in the Fall of 2017 as a collaboration between the HITRAN team and the State University of New York at Oswego. The purpose of HAPIEST is to simplify usage of HAPI to work efficiently with HITRAN*online* and to allow users who are not familiar with Python to access the spectroscopic data offered by HITRAN.

HAPIEST provides a cross-platform graphical user interactive that gives access to the basic features of HAPI (such as data fetching and filtering), as well as calculating and plotting spectral functions (absorption coefficients, and transmittance, absorption, and radiance spectra). Moreover, HAPIEST provides access to most of the controls that are involved in spectral filtering and simulation, and is distributed both as binary and source code. The most recent version of the source code can be found on Github (https://github.com/hitranonline/hapiest), as well as the most recent binary versions (https://github.com/hitranonline/hapiest/releases).

Using the HAPI and HAPI2 libraries, HAPIEST can retrieve the spectroscopic line-by-line data for any molecule or isotopologue in HITRAN. There are currently three functionalities provided in HAPIEST for line-by-line data: viewing, graphing, and data selection. The "view" feature allows line-by-line data to be viewed in a spreadsheet-like widget. This feature automatically paginates tables to save on system resources, but this page-length can be changed in the user-configurable settings. One major feature of HAPIEST is the graphing capability. HAPIEST is able to display the line-by-line data in graphical form by calculating absorption coefficients, as well as absorption, transmittance, and radiance spectra, with a variety of instrumental functions and line profiles. As part of the HAPIEST functionality, users are able to filter (e.g., by vibrational band) and plot results separately. When bands are plotted, HAPIEST creates a legend for band graphs which will display upper- and lower-quanta of each band. In addition, the absorption cross-section data can also be downloaded from the HITRAN*online* web server and plotted by HAPIEST. Multiple absorp-

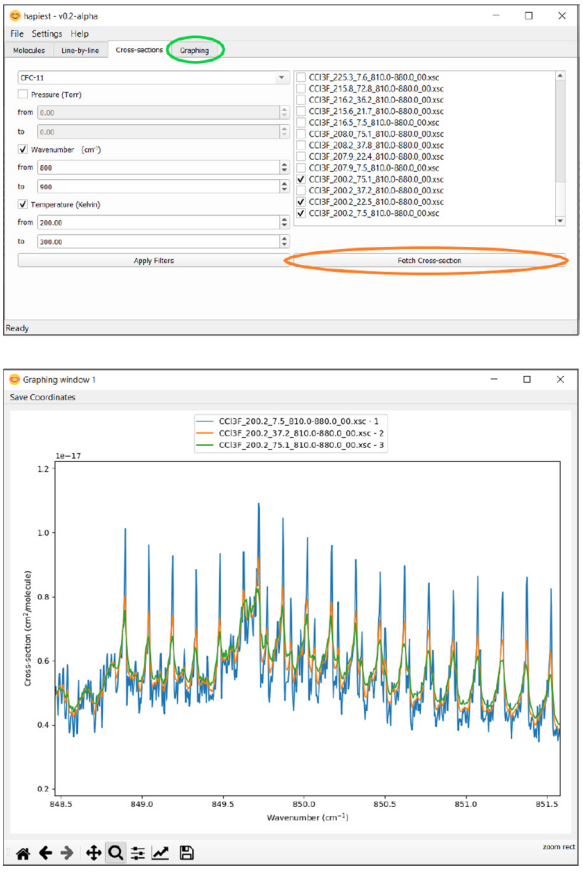

Fig. 42. Screenshots of the graphical user interface of HAPIEST. The upper window displays the tab where absorption cross-section spectra from HITRAN*online* can be queried and filtered, then downloaded using the "Fetch cross-section" button (circled orange). In this example, three absorption cross-sections of CFC-11 (CCl_3F) with different pressures have been selected by filtering the available CFC-11 absorption cross-sections between 800–900 cm^{-1} and 200–300 K. Clicking the "Graphing" tab (circled green) allows users to create a plot of their chosen cross-section spectra. The same three CFC-11 cross-sections have been plotted in the lower window using the graphing functionality of HAPIEST. Here, users are able to adjust their plot using the tools on the lower left of the window (such as by zooming to compare spectral regions) and the results can be saved.

tion cross-sections can be plotted on the same axes and compared, as shown in Fig. 42 for three different temperature-pressure sets of CFC-11.

6.4. Total internal partition sums (TIPS)

New total internal partition sums (TIPS) were calculated or re-calculated for many HITRAN molecules and their isotopologues [417]. Naturally, TIPS were calculated for all new isotopologues ($^{33}S^{16}O_2$, $^{16}O^{32}S^{18}O$, $^{15}N^{16}O_2$, $^{16}O^{13}C^{34}S$, $^{12}C_2H_5D$) and molecules (SO, CH_3F, GeH_4, CS_2, CH_3I, NF_3) that have been introduced to the database for HITRAN2020 and were not included as part of TIPS2017 [178]. Also, partition sums were revised for a number of molecules and isotopologues. In particular, TIPS of ozone have been recalculated to eliminate discrepancies noted in Ref. [200]. The TIPS are calculated in one-degree intervals from 1 K until the convergence of each partition sum (which is different for each molecule) and will be provided as an update to TIPS2017, which was used for all isotopologues in the previous edition of HITRAN [16]. The full TIPS for each new isotopologue and molecule will be made available through the HITRAN*online* website (https://hitran.org/docs/iso-meta/) where the corresponding partition sum, $Q(296\ K)$, is provided at 296 K.

Table 13
A list of the 24 coefficients that define the DPL parametrization for all the six line-shape parameters: pressure broadening and shift (γ_0 and δ_0), speed dependence of pressure broadening and shift (γ_2 and δ_2), real and imaginary parts of the complex Dicke parameter ($\tilde{\nu}^r_{opt}$ and $\tilde{\nu}^i_{opt}$).

	Coefficient 1	Coefficient 2	Exponent 1	Exponent 2
$\gamma_0(T)$	g_0	g'_0	n	n'
$\delta_0(T)$	d_0	d'_0	m	m'
$\gamma_2(T)$	g_2	g'_2	j	j'
$\delta_2(T)$	d_2	d'_2	k	k'
$\tilde{\nu}^r_{opt}(T)$	r	r'	p	p'
$\tilde{\nu}^i_{opt}(T)$	i	i'	q	q'

7. Conclusions and future work

This article introduces and details the improvements and expansion of the new HITRAN2020 database release with respect to its predecessor, HITRAN2016 [16]. These improvements include the increased quality of reference spectral parameters, expansions of spectral and dynamic ranges, and new parametrizations and capabilities. The addition of new molecules and isotopologues or new collisional complexes is justified and explained. Non-Voigt line shapes continue to be expanded in the database. In this edition, important atmospheric absorbers that include CO_2, N_2O and CO, now have, not only Voigt, but also speed-dependent Voigt parameters (for both air- and self-broadening) for every transition of these molecules in the database. In addition, many molecules now have line-shape parameters due to ambient water-vapor pressure provided for all transitions. There are also substantially more molecules with parameters associated with the pressure of "planetary" gases: H_2, He and CO_2. Experimental cross-sections, aerosols, and collision induced absorption datasets have also been revised and extended. The new data were validated against laboratory and atmospheric spectra whenever possible.

Furthermore, HITRAN continues to evolve in terms of structure and scope. This evolution includes expanded capabilities and documentation for the online server and restructuring and optimization of HAPI, which now also has a GUI.

In summary, the capabilities of HITRAN have been significantly enhanced compared to previous editions, in terms of quality, extent and accessibility of the data.

The HITRAN compilation is free to use and can be accessed through www.hitran.org.

7.1. Future plans for expansion of HITRAN

7.1.1. Double-power-law (DPL) representation of the temperature dependencies of the line-shape parameters

Recently, a new scheme of representing the temperature dependencies of the line-shape parameters was adopted in HITRAN [120]. The approach approximates the temperature dependencies with a double-power-law (DPL) function [119]. The scheme adopted in HITRAN [120] is very general and applicable also to beyond-Voigt cases. It should be noted, however, that for many molecular systems, not all the collisional effects are important at the considered accuracy level and, for a given experimental temperature range, a simple single-power law suffices. In such cases, either a single-power law and a smaller number of line-shape parameters will be stored in HITRAN, or the full DPL parametrization will be adopted but some of the coefficients will be set to zero.

In the most general case, the DPL parametrization involves 24 coefficients, i.e., four DPL coefficients per each of the six line-shape parameters, see Table 13. The explicit formulas for the DPL temperature dependencies are following [120]:

$$\gamma_0(T) = g_0(T_{\text{ref}}/T)^n + g'_0(T_{\text{ref}}/T)^{n'},$$

$$\begin{aligned}
\delta_0(T) &= d_0(T_{\text{ref}}/T)^m + d_0'(T_{\text{ref}}/T)^{m'},\\
\gamma_2(T) &= g_2(T_{\text{ref}}/T)^j + g_2'(T_{\text{ref}}/T)^{j'},\\
\delta_2(T) &= d_2(T_{\text{ref}}/T)^k + d_2'(T_{\text{ref}}/T)^{k'},\\
\tilde{\nu}^{\text{r}}_{\text{opt}}(T) &= r(T_{\text{ref}}/T)^p + r'(T_{\text{ref}}/T)^{p'},\\
\tilde{\nu}^{\text{i}}_{\text{opt}}(T) &= i(T_{\text{ref}}/T)^q + i'(T_{\text{ref}}/T)^{q'},
\end{aligned} \tag{6}$$

where $T_{\text{ref}} = 296$ K.

The DPL parametrization replaces the four temperature ranges (4TR) representation introduced in 2016 [165]. It was shown in Ref. [120] that the DPL parametrization requires fewer parameters, gives better accuracy and is more self-consistent than 4TR. In the immediate update to HITRAN2020, the full structure of the DPL parametrization will be provided for the cases of self- and He-perturbed H_2 lines.

7.1.2. Water-vapor continuum

In the last 50 years, HITRAN has made enormous progress toward being a complete source for all atmospheric absorption parameters. Nevertheless, it has not yet expanded to include continuum absorption by water vapor. This gap in the database will be filled in forthcoming updates to HITRAN2020.

Absorption and emission by the water-vapor continuum play an important role in radiative processes in the terrestrial atmosphere and have an appreciable impact on weather and the climate of the Earth [880–882]. There is still uncertainty with respect to the physical phenomena behind either the self (interactions of water vapor with other water vapor molecules) or the foreign (interaction of water vapor with dry air molecules) continuum, with bound dimers, quasi-stable dimers, and monomer far wings possibly contributing to the total absorption. Theoretical analysis has not yet been able to disentangle the relative contributions of these phenomena as a function of wavenumber and temperature. This is still the subject of an active debate (e.g., see reviews [883,884]).

The next version of HITRAN will include the updated and well-documented MT_CKD (Mlawer-Tobin_Clough-Kneizys-Davies) water-vapor continuum model [881], which is widely used in atmospheric radiative-transfer codes. The MT_CKD model is based on a combination of analyses of field measurements, laboratory measurements, and semi-empirical model calculations, and is a descendant of the CKD (Clough-Kneizys-Davies) continuum model [885] developed in the 1980s. The goal of these models is to provide a representation of smoothly varying water-vapor absorption that, once added to the absorption due to water vapor lines (cut-off at 25 cm^{-1} from line center), best agrees with high-quality observations and theoretical calculations of the total water-vapor absorption. In many spectral regions, observations from different studies provide conflicting information on the strength of the water-vapor continuum, and a judgment must be made as to which source should provide the basis for the coefficients in MT_CKD. The overall perspective in developing the MT_CKD water-vapor continuum is consistent with that of HITRAN – regular updates to the spectroscopic parameters in order to agree with studies considered to be most accurate.

The importance of the water-vapor continuum and aforementioned discrepancies have sparked a number of new laboratory measurements in different spectral regions [883,886–900]. While many of these experiments show a decent level of consistency with MT_CKD (see discussion in Ref. [893], for instance) they nevertheless have warranted revisions to the model. For example, MT_CKD recently incorporated the results of numerous lab measurements in near-infrared windows by the group of Campargue at Grenoble, which provided water-vapor continuum absorption coefficients with stated uncertainties lower than had previously been reported in these regions. In some window regions, these continuum values disagreed by more than an order of magnitude with previous measurements (see, for instance, the recent review [901]). These improvements to the MT_CKD self and foreign continua due to the measurements in Grenoble [893–898,900] have made a noticeable positive impact on the retrievals of carbon dioxide with the OCO-2 mission [323]. Uncertainties still remain, however. The water-vapor continuum model from Paynter and Ramaswamy [902], named “BPS” due to the articles describing the input measurements [886,903–905], has different absorption coefficients than MT_CKD in certain near-infrared windows and other regions, leading to different results in the atmosphere.

Other recent updates to MT_CKD include the far-infrared foreign continuum, which was modified based on an analysis of field campaign observations [122]. Subsequent studies [906,907] have provided validation for these far-infrared absorption coefficients. The most recent revision was MT_CKD_3.5, which improved the continuum in the microwave (self and foreign) and far-infrared (self) based on analyses of field and lab experiments (see, e.g., Ref. [908]). Ongoing analyses are expected to lead to improvements in the MT_CKD model in the infrared window (self and possibly foreign) and water vapor ν_2 band (foreign).

7.1.3. Pre-calculated absorption cross-sections

The complexity and the amount of the new parameters included in HITRAN is putting a lot of demand on the user community to know how to implement the new data in the radiative-transfer codes. While we provide tutorials and enable some of the tools through HAPI, it may still be challenging for some of the users. Therefore we plan to provide the pre-calculated sets of cross-sections to use for atmospheric research. There are some accepted format and parameter space used in many of the remote-sensing missions. For instance, OCO-2/3 [17,18] and TES [19] research teams employ the so-called ABSCO [323] format. We, therefore, plan to pre-calculate ABSCO-formatted cross-sections for selected molecules and spectral ranges, determined in consultation with the remote-sensing community. Other commonly used formats will also be explored.

8. Acknowledgements

The global COVID-19 pandemic has impacted the working conditions and lives of everyone involved in the production of HITRAN2020. In recognition of the difficult conditions of the previous year, we would like to extend our sincere gratitude to all researchers and collaborators who have been able to contribute to this edition. We also thank the anonymous reviewers for their very constructive criticism and suggestions.

Development of the HITRAN2020 database and associated tools was supported through the NASA grants NNX17AI78G, NNX16AG51G, 80NSSC20K0962, 80NSSC20K1059.

We gratefully acknowledge the many researchers who provided data, experimental and/or theoretical: Ad van der Avoird, Yury Baranov, Chris Benner, Yury Borkov, Christian Boulet, Daniil Chistikov, Malathy Devi, Randika Dodangodage, Samuel Gordon, Gerrit Groenenboom, Magnus Gustafsson, Adrian Hjältén, Shuiming Hu, Christof Janssen, Aleksandra Kyuberis, Julien Lamouroux, Daniel Lisak, Anwen Liu, Sergei Lokshtanov, Marie Aline Martin-Drumel, Andrey Muraviev, Harrald Mutschke, Laurence Régalia, Shanelle Samuels, Mary-Ann Smith, Alexander M. Solodov, Alexander A. Solodov, Ryan Thalman, Mikhail Tretyakov, Yixin Wang, Edward Wishnow, Wim van der Zande, Konstantin Vodopyanov, Rainer Volkamer, Shanshan Yu, Nikolai Zobov.

Those who provided independent validations are also acknowledged: Matthew Alvarado, Juyeson Bak, Natasha Batalha, Chris Boone, Ryan Cole, Sergio DeSouza-Machado, Richard Larsson, Xiong Liu, Emile Medvedev, Clayton Mulvihill, Fabiano Oyafuso, Erwan

Pannier, Vivienne Payne, Olivier Pirali, Greg Rieker, Keith Shine, Clara Sousa-Silva, Kang Sun, Boris Voronin.

Portions of the research described in this paper were performed at the Jet Propulsion Laboratory, California Institute of Technology, under contract with NASA. The research from the V.E. Zuev Institute of Atmospheric Optics of Siberian Branch of Russian Academy of Sciences were supported by the Ministry of Science and Higher Education of the Russian Federation. The work of the Tomsk group on ozone spectroscopy was supported by the Russian Science Foundation RNF grant no. 19-12-00171. GSMA Reims and LiPhy Grenoble acknowledge support from the French-Russian collaboration program LIA CNRS "SAMIA". AGC, TF, and RT received support from the ELTE Institutional Excellence Program (TKP2020-IKA-05) and from NKFIH (K119658). OLP and JT received support from the UK Natural Environment Research Council under grants NE/N001508/1 and the European Research Council under ERC Advanced Investigator grant 8838302

Declaration of Competing Interest

The authors declare that they have no known competing financial interests or personal relationships that could have appeared to influence the work reported in this paper.

Appendix A. Abbreviations

When describing the inclusion of data into HITRAN, the following abbreviations, acronyms, and initialisms have been used at various points throughout the article:

- 4TR – Four-temperature range
- ABSCO – Absorption coefficient [323]
- ACE – Atmospheric Chemistry Experiment [21]
- API – Application programming interface
- ARIEL – Atmospheric Remote-sensing Infrared Exoplanet Large-survey [47]
- ARTS – Atmospheric Radiative Transfer Simulator [31]
- ASCII – American standard code for information interchange
- CCSD(T) – Coupled-cluster singles, doubles, and perturbative triples
- CDMS – Cologne Database for Molecular Spectroscopy [344]
- CDSD – Carbon Dioxide Spectroscopic Database [135]
- CFC – Chlorofluorocarbon
- CIA – Collision-induced absorption
- CLS – Canadian Light Source
- CRDS – Cavity ring-down spectroscopy
- DLR – Deutsches Zentrum für Luft und Raumfahrt (German Aerospace Center)
- DMS – Dipole moment surface
- DOI – Digital object identifier
- DPL – Double-power law
- DU – Dobson unit
- EDTM – Effective dipole transition moment
- EH – Effective Hamiltonian
- EPG – Exponential power gap
- ESA – European Space Agency
- FIR – Far-infrared
- FORUM – Far-infrared Outgoing Radiation Understanding and Monitoring [24]
- FT – Fourier transform
- FTIR – Fourier transform infrared
- FTS – Fourier transform spectrometer
- GARLIC – Generic Atmospheric Radiation Line-by-line Infrared Code [32]
- GeCaSDa – Germane Calculated Spectroscopic Database [594]
- GEISA – Gestion et Etude des Informations Spectroscopiques Atmosphériques (Management and Study of Atmospheric Spectroscopic Information) [418]
- GEMS – Geostationary Environment Monitoring Spectrometer [23]
- GENLN – General Line-by-line Atmospheric Transmittance and Radiance Model [29]
- GOSAT – Greenhouse Gases Observing Satellite [20]
- HAPI – HITRAN Application Programming Interface [52]
- HAPIEST – HITRAN Application Programming Interface and Efficient Spectroscopic Tools
- HCFC – Hydrochlorofluorocarbon
- HDF-5 – Hierarchical Data Format version 5
- HITRAN – High-resolution transmission molecular absorption database [16]
- HITEMP – High-temperature molecular spectroscopic database [53]
- HR – High-resolution
- HT – Hartmann–Tran
- HTTPS – Hypertext transfer protocol secure
- IAO – Institute of Atmospheric Optics
- IASI – Infrared Atmospheric Sounding Interferometer [186]
- ICB – Laboratoire Interdisciplinaire Carnot de Bourgogne
- IDL – Interactive Design Language
- IR – Infrared
- JIRAM – Jovian Infrared Auroral Mapper [652]
- JPL – Jet Propulsion Laboratory
- JSON – JavaScript Object Notation
- JWST – James Webb Space Telescope [46]
- LBL – Line-by-line
- LBLRTM – Line-by-line Radiative Transfer Model [27]
- LERMA – Laboratoire d'étude du rayonnement et de la matière en astrophysique
- LIDAR – Light detection and ranging
- LISA – Laboratoire Interuniversitaire des Systèmes Atmosphériques
- MARVEL – Measured Active Rotational-Vibrational Energy Levels [58,59]
- MATS – Multi-spectrum analysis tool for spectroscopy [238]
- MCRB – Modified complex Robert-Bonamy
- MIR – Mid-infrared
- MODTRAN – Moderate resolution atmospheric transmission code [28]
- MT_CKD – Mlawer-Tobin Clough-Kneizys-Davies [881]
- MW – Microwave
- NASA – National Aeronautics and Space Administration
- NDSD-1000 – Nitrogen Dioxide Spectroscopic Data Bank at 1000 K [398,399]
- NEMESIS – Non-linear optimal estimator for multivariate spectral analysis [35]
- netCDF – Network common data form
- NIR – Near-infrared
- NIST – National Institute of Standards and Technology
- NMHC – Non-methane hydrocarbon
- NOSD-1000 – Nitrous Oxide Spectroscopic Data Bank at 1000 K [243]
- NSO – National Solar Observatory
- OCO – Orbiting Carbon Observatory [17,18]
- ODU – Old Dominion University
- ORM – Object-relational mapping
- PES – Potential energy surface
- PNNL – Pacific Northwest National Laboratory
- PSC – Polar stratospheric cloud
- PSG – Planetary Spectrum Generator [37]
- rCMDS – Requantized Classical Molecular Dynamics Simulation

- REST API – Representational state transfer application programming interface
- RFM – Reference Forward Model [30]
- RI – Refractive indices
- RKR – Rydberg-Klein-Rees
- RMS – Root mean square
- RT – Rototranslational
- S&MPO – Spectroscopy and Molecular Properties of Ozone [194]
- SB RAS - Siberian Branch, Russian Academy of Sciences
- SDV – Speed-dependent Voigt
- SEOM-IAS – Scientific Exploitation of Operational Missions - Improved Atmospheric Spectroscopy Databases
- SHeCaSDa – Sulfur Hexafluoride Calculated Spectroscopic Database [594]
- SI – Système International
- SISAM – Spectromètre Interférentiel à Sélection par l'Amplitude de la Modulation (Interferential Spectrometer by Selection of Amplitude Modulation)
- SNR – Signal to noise ratio
- SOA – Secondary organic aerosol
- SRP – Standard reference photometer
- TCCON – Total Carbon Column Observing Network [145,146]
- TEMPO – Tropospheric Emissions: Monitoring of Pollution [25]
- TES – Tropospheric Emission Spectrometer [19]
- TFMeCaSDa – TetraFluoro-Methane Calculated Spectroscopic Database [594]
- TheoReTS – Theoretical Reims-Tomsk Spectral data [310]
- TIPS – Total Internal Partition Sums
- TROPOMI – Tropospheric Monitoring Instrument [22]
- UCL – University College London
- ULB – Université Libre de Bruxelles
- UV – Ultraviolet
- UVES – Ultraviolet-Visual Echelle Spectrograph [909]
- VAMDC – Virtual Atomic and Molecular Data Centre [656]
- VLIDORT – Vector Linearized Discrete Ordinate Radiative Transfer [34]
- VP – Voigt profile

Supplementary material

Supplementary material associated with this article can be found, in the online version, at 10.1016/j.jqsrt.2021.107949

References

[1] Rothman LS. History of the HITRAN database. Nat Rev Phys 2021;0123456789. doi:10.1038/s42254-021-00309-2. http://www.nature.com/articles/s42254-021-00309-2

[2] McClatchey R, Benedict W, Clough S, Burch D, Calfee R, Fox K, et al. AFCRL atmospheric absorption line parameters compilation. Environ Res Pap 1973;434:1–86. https://lweb.cfa.harvard.edu/HITRAN/Download/AFCRL73.pdf

[3] Rothman LS, McClatchey RA. Updating of the AFCRL atmospheric absorption line parameters compilation. Appl Opt 1976;15(11):2616–17. doi:10.1364/AO.15.2616_1.

[4] Rothman LS. Update of the AFGL atmospheric absorption line parameters compilation. Appl Opt 1978;17(22):3517–18. doi:10.1364/AO.17.003517.

[5] Rothman LS, Clough SA, McClatchey RA, Young LG, Snider DE, Goldman A. AFGL trace gas compilation. Appl Opt 1978;17(4):507. doi:10.1364/AO.17.000507.

[6] Rothman LS, Goldman A, Gillis JR, Tipping RH, Brown LR, Margolis JS, et al. AFGL trace gas compilation: 1980 version. Appl Opt 1981;20(8):1323–8. doi:10.1364/AO.20.001323.

[7] Rothman LS, Gamache RR, Barbe A, Goldman A, Gillis JR, Brown LR, et al. AFGL atmospheric absorption line parameters compilation: 1982 edition. Appl Opt 1983;22(15):2247–56. doi:10.1364/ao.22.002247.

[8] Rothman LS, Goldman A, Gillis JR, Gamache RR, Pickett HM, Poynter RL, et al. AFGL trace gas compilation: 1982 version. Appl Opt 1983;22(11):1616–27. doi:10.1364/ao.22.001616.

[9] Rothman LS, Gamache RR, Goldman A, Brown LR, Toth RA, Pickett HM, et al. The HITRAN database: 1986 edition. Appl Opt 1987;26:4058–97. doi:10.1364/AO.26.004058.

[10] Rothman L, Gamache R, Tipping R, Rinsland C, Smith M, Benner D, et al. The HITRAN molecular database: editions of 1991 and 1992. J Quant Spectrosc Radiat Transf 1992;48(5-6):469–507. doi:10.1016/0022-4073(92)90115-K.

[11] Rothman LS, Rinsland CP, Goldman A, Massie ST, Edwards DP, Flaud J-M, et al. The HITRAN molecular spectroscopic database and HAWKS (HITRAN atmospheric workstation): 1996 edition. J Quant Spectrosc Radiat Transf 1998;60:665–710. doi:10.1016/S0022-4073(98)00078-8.

[12] Rothman LS, Barbe A, Benner DC, Brown LR, Camy-Peyret C, Carleer MR, et al. The HITRAN molecular spectroscopic database: edition of 2000 including updates through 2001. J Quant Spectrosc Radiat Transf 2003;82:5–44. doi:10.1016/S0022-4073(03)00146-8.

[13] Rothman LS, Jacquemart D, Barbe A, Chris Benner D, Birk M, Brown LR, et al. The HITRAN 2004 molecular spectroscopic database. J Quant Spectrosc Radiat Transf 2005;96:139–204. doi:10.1016/j.jqsrt.2004.10.008.

[14] Rothman LS, Gordon IE, Barbe A, Benner DC, Bernath PF, Birk M, et al. The HITRAN 2008 molecular spectroscopic database. J Quant Spectrosc Radiat Transf 2009;110:533–72. doi:10.1016/j.jqsrt.2009.02.013.

[15] Rothman L, Gordon I, Babikov Y, Barbe A, Chris Benner D, Bernath P, et al. The HITRAN2012 molecular spectroscopic database. J Quant Spectrosc Radiat Transf 2013;130:4–50. doi:10.1016/j.jqsrt.2013.07.002.

[16] Gordon IE, Rothman LS, Hill C, Kochanov RV, Tan Y, Bernath PF, et al. The HITRAN2016 molecular spectroscopic database. J Quant Spectrosc Radiat Transf 2017;203:3–69. doi:10.1016/j.jqsrt.2017.06.038.

[17] Crisp D, Atlas R, Breon F-M, Brown L, Burrows J, Ciais P, et al. The Orbiting Carbon Observatory (OCO) mission. Adv Space Res 2004;34(4):700–9. doi:10.1016/j.asr.2003.08.062.

[18] Eldering A, Taylor TE, O'Dell CW, Pavlick R. The OCO-3 mission: measurement objectives and expected performance based on 1 year of simulated data. Atmos Meas Tech 2019;12(4):2341–70. doi:10.5194/amt-12-2341-2019.

[19] Beer R. TES on the aura mission: scientific objectives, measurements, and analysis overview. IEEE Trans Geosci Remote Sens 2006;44(5):1102–5. doi:10.1109/TGRS.2005.863716.

[20] Kuze A, Suto H, Nakajima M, Hamazaki T. Thermal and near infrared sensor for carbon observation Fourier-transform spectrometer on the greenhouse gases observing satellite for greenhouse gases monitoring. Appl Opt 2009;48(35):6716. doi:10.1364/AO.48.006716.

[21] Bernath PF. Atmospheric Chemistry Experiment (ACE): mission overview. Geophys Res Lett 2005;32(15):L15S01. doi:10.1029/2005GL022386.

[22] Veefkind J, Aben I, McMullan K, Förster H, de Vries J, Otter G, et al. TROPOMI on the ESA sentinel-5 precursor: a GMES mission for global observations of the atmospheric composition for climate, air quality and ozone layer applications. Remote Sens Environ 2012;120:70–83. doi:10.1016/j.rse.2011.09.027.

[23] Kim J, Jeong U, Ahn M-H, Kim JH, Park RJ, Lee H, et al. New era of air quality monitoring from space: Geostationary Environment Monitoring Spectrometer (GEMS). Bull Am Meteorol Soc 2020;101(1):E1–E22. doi:10.1175/BAMS-D-18-0013.1.

[24] Palchetti L, Brindley H, Bantges R, Buehler SA, Camy-Peyret C, Carli B, et al. FORUM: unique far-infrared satellite observations to better understand how earth radiates energy to space. Bull Am Meteorol Soc 2020;101(12):E2030–46. doi:10.1175/bams-d-19-0322.1.

[25] Zoogman P, Liu X, Suleiman R, Pennington W, Flittner D, Al-Saadi J, et al. Tropospheric Emissions: Monitoring of Pollution (TEMPO). J Quant Spectrosc Radiat Transf 2017;186:17–39. doi:10.1016/j.jqsrt.2016.05.008.

[26] Wofsy SC, Hamburg S. MethaneSAT - a new observing platform for high resolution measurements of methane and carbon dioxide. In: Proceedings of the AGU fall meeting abstracts, 2019; 2019. A53F–02.

[27] Shephard MW, Clough SA, Payne VH, Smith WL, Kireev S, Cady-Pereira KE. Performance of the Line-by-Line Radiative Transfer Model (LBLRTM) for temperature and species retrievals: IASI case studies from JAIVEx. Atmos Chem Phys 2009;9(19):7397–417. doi:10.5194/acp-9-7397-2009.

[28] Berk A, Hawes F. Validation of MODTRAN®6 and its line-by-line algorithm. J Quant Spectrosc Radiat Transf 2017;203:542–56. doi:10.1016/J.JQSRT.2017.03.004.

[29] Edwards D. GENLN2: a general line-by-line atmospheric transmittance and radiance model. Version 3.0 description and users guide. NCAR technical note NCAR/TN-367+STR. Technical Report. National Center for Atmospheric Research; 1992. doi:105065/D6W37T86.

[30] Dudhia A. The Reference Forward Model (RFM). J Quant Spectrosc Radiat Transf 2017;186:243–53. doi:10.1016/j.jqsrt.2016.06.018.

[31] Buehler SA, Eriksson P, Kuhn T, von Engeln A, Verdes C. ARTS, the atmospheric radiative transfer simulator. J Quant Spectrosc Radiat Transf 2005;91(1):65–93. doi:10.1016/j.jqsrt.2004.05.051.

[32] Schreier F, Gimeno García S, Hedelt P, Hess M, Mendrok J, Vasquez M, et al. GARLIC — a general purpose atmospheric radiative transfer line-by-line infrared-microwave code: Implementation and evaluation. J Quant Spectrosc Radiat Transf 2014;137:29–50. doi:10.1016/J.JQSRT.2013.11.018.

[33] Desouza-Machado S, Larrabee Strow L, Motteler H, Hannon S. kCARTA: a fast pseudo line-by-line radiative transfer algorithm with analytic Jacobians, fluxes, nonlocal thermodynamic equilibrium, and scattering for the infrared. Atmos Meas Tech 2020;13:323–39. doi:10.5194/amt-13-323-2020.

[34] Spurr RJ. VLIDORT: a linearized pseudo-spherical vector discrete ordinate radiative transfer code for forward model and retrieval studies in multilayer multiple scattering media. J Quant Spectrosc Radiat Transf 2006;102(2):316–42. doi:10.1016/j.jqsrt.2006.05.005.

[35] Irwin PGJ, Teanby NA, de Kok R, Fletcher LN, Howett CJA, Tsang CCC, et al. The

NEMESIS planetary atmosphere radiative transfer and retrieval tool. J Quant Spectrosc Radiat Transf 2008;109:1136–50. doi:10.1016/j.jqsrt.2007.11.006.
[36] Mollière P, Wardenier JP, van Boekel R, Henning T, Molaverdikhani K, Snellen IAG. petitRADTRANS: a Python radiative transfer package for exoplanet characterization and retrieval. Astron Astrophys 2019;627. doi:10.1051/0004-6361/201935470.
[37] Villanueva GL, Smith MD, Protopapa S, Faggi S, Mandell AM. Planetary spectrum generator: an accurate online radiative transfer suite for atmospheres, comets, small bodies and exoplanets. J Quant Spectrosc Radiat Transf 2018;217:86–104. doi:10.1016/j.jqsrt.2018.05.023.
[38] Kempton EM, Lupu R, Owusu-Asare A, Slough P, Cale B. Exo-transmit: an open-source code for calculating transmission spectra for exoplanet atmospheres of varied composition. Publ Astron Soc Pac 2017;129(974):044402. doi:10.1088/1538-3873/aa61ef.
[39] Grimm SL, Malik M, Kitzmann D, Guzmán-Mesa A, Hoeijmakers HJ, Fisher C, et al. HELIOS-K 2.0 opacity calculator and open-source opacity database for exoplanetary atmospheres. Astrophys J Suppl 2021;253:30. doi:10.3847/1538-4365/abd773.
[40] Titov DV, Svedhem H, McCoy D, Lebreton JP, Barabash S, Bertaux JL, et al. Venus express: scientific goals, instrumentation, and scenario of the mission. Cosm Res 2006;44(4):334–48. doi:10.1134/S0010952506040071.
[41] Trompet L, Geunes Y, Ooms T, Mahieux A, Wilquet V, Chamberlain S, et al. Description, accessibility and usage of SOIR/Venus express atmospheric profiles of Venus distributed in VESPA (Virtual European Solar and Planetary Access). Planet Space Sci 2018;150:60–4. doi:10.1016/j.pss.2017.04.022.
[42] Korablev O, Montmessin F, Trokhimovskiy A, Fedorova AA, Shakun AV, Grigoriev AV, et al. The Atmospheric Chemistry Suite (ACS) of three spectrometers for the ExoMars 2016 trace gas orbiter. Space Sci Rev 2018;214(1):29. doi:10.1007/s11214-017-0437-6.
[43] Vandaele AC, Lopez-Moreno J-J, Patel MR, Bellucci G, Daerden F, Ristic B, et al. NOMAD, an integrated suite of three spectrometers for the ExoMars trace gas mission: technical description, science objectives and expected performance. Space Sci Rev 2018;214(5):80. doi:10.1007/s11214-018-0517-2.
[44] Jaffe LD, Herrell LM. Cassini/Huygens science instruments, spacecraft, and mission. J Spacec Rocket 1997;34(4):509–21. doi:10.2514/2.3241.
[45] Tsiaras A, Waldmann IP, Rocchetto M, Varley R, Morello G, Damiano M, et al. A new approach to analyzing HST spatial scans: the transmission spectrum of HD 209458 b. Astrophys J 2016;832(2). doi:10.3847/0004-637X/832/2/202.
[46] Baudino J-L, Mollière P, Venot O, Tremblin P, Bézard B, Lagage P-O. Toward the analysis of JWST exoplanet spectra: identifying troublesome model parameters. Astrophys J 2017;850(2). doi:10.3847/1538-4357/aa95be.
[47] Tinetti G, Drossart P, Eccleston P, Hartogh P, Heske A, Leconte J, et al. A chemical survey of exoplanets with ARIEL. Exp Astron 2018;46(1):135–209. doi:10.1007/s10686-018-9598-x.
[48] Bertaux JL, Lallement R, Ferron S, Boonne C, Bodichon R. TAPAS, a web-based service of atmospheric transmission computation for astronomy. Astron Astrophys 2014;564:46. doi:10.1051/0004-6361/201322383.
[49] Tan Y, Kochanov RV, Rothman LS, Gordon IE. Introduction of water-vapor broadening parameters and their temperature-dependent exponents into the HITRAN database: Part I—CO_2, N_2O, CO, CH_4, O_2, NH_3, and H_2S. J Geophys Res (Atmos) 2019;124(21) 580–11. doi:10.1029/2019JD030929.
[50] Hill C, Gordon IE, Rothman LS, Tennyson J. A new relational database structure and online interface for the HITRAN database. J Quant Spectrosc Radiat Transf 2013;130:51–61. doi:10.1016/j.jqsrt.2013.04.027.
[51] Hill C, Gordon IE, Kochanov RV, Barrett L, Wilzewski JS, Rothman LS. HITRANonline: an online interface and the flexible representation of spectroscopic data in the HITRAN database. J Quant Spectrosc Radiat Transf 2016;177:4–14. doi:10.1016/j.jqsrt.2015.12.012.
[52] Kochanov RV, Gordon IE, Rothman LS, Wcisło P, Hill C, Wilzewski JS. HITRAN Application Programming Interface (HAPI): a comprehensive approach to working with spectroscopic data. J Quant Spectrosc Radiat Transf 2016;177:15–30. doi:10.1016/j.jqsrt.2016.03.005.
[53] Rothman LS, Gordon IE, Barber RJ, Dothe H, Gamache RR, Goldman A, et al. HITEMP, the high-temperature molecular spectroscopic database. J Quant Spectrosc Radiat Transf 2010;111:2139–50. doi:10.1016/j.jqsrt.2010.05.001.
[54] Rothman LS, Wattson RB, Gamache R, Schroeder JW, McCann A. HITRAN HAWKS and HITEMP: high-temperature molecular database. In: Dainty JC, editor. Atmospheric propagation and remote sensing IV. Society of Photo-Optical Instrumentation Engineers (SPIE) Conference Series, 2471; 1995. p. 105–11. doi:10.1117/12.211919.
[55] Hargreaves RJ, Gordon IE, Rothman LS, Tashkun SA, Perevalov VI, Lukashevskaya AA, et al. Spectroscopic line parameters of NO, NO_2, and N_2O for the HITEMP database. J Quant Spectrosc Radiat Transf 2019;232:35–53. doi:10.1016/j.jqsrt.2019.04.040.
[56] Hargreaves RJ, Gordon IE, Rey M, Nikitin AV, Tyuterev VG, Kochanov RV, et al. An accurate, extensive, and practical line list of methane for the HITEMP database. Astrophys J Suppl Ser 2020;247(2). doi:10.3847/1538-4365/ab7a1a.
[57] De Biévre P, Gallet M, Holden NE, Barnes IL. Isotopic abundances and atomic weights of the elements. J Phys Chem Ref Data 1984;13(3):809–91. doi:10.1063/1.555720.
[58] Furtenbacher T, Császár AG, Tennyson J. MARVEL: measured active rotational-vibrational energy levels. J Mol Spectrosc 2007;245:115–25. doi:10.1016/j.jms.2007.07.005.
[59] Furtenbacher T, Császár AG. MARVEL: measured active rotational-vibrational energy levels. II. Algorithmic improvements. J Quant Spectrosc Radiat Transf 2012;113:929–35. doi:10.1016/j.jqsrt.2012.01.005.
[60] Tennyson J, Bernath PF, Brown LR, Campargue A, Császár AG, Daumont L, et al. A database of water transitions from experiment and theory (IUPAC technical report). Pure Appl Chem 2014;86:71–83. doi:10.1515/pac-2014-5012.
[61] Toth RA. Linelist of water vapor parameters from 500 to 8000 cm^{-1}; 2009. https://mark4sun.jpl.nasa.gov/h2o.html
[62] Brown L, Toth R, Dulick M. Empirical line parameters of $H_2^{16}O$ near 0.94 μm: positions, intensities and air-broadening coefficients. J Mol Spectrosc 2002;212:57–82. doi:10.1006/jmsp.2002.8515.
[63] Tolchenov R, Tennyson J. Water Line Parameters from Refitted Spectra constrained by empirical upper state levels: study of the 9500 – 14500 cm^{-1} region. J Quant Spectrosc Radiat Transf 2008;109:559–68. doi:10.1016/j.jqsrt.2007.08.001.
[64] Tolchenov RN, Naumenko O, Zobov NF, Shirin SV, Polyansky OL, Tennyson J, et al. Water vapour line assignments in the 9250 – 26 000 cm^{-1} frequency range. J Mol Spectrosc 2005;233:68–76. doi:10.1016/j.jms.2005.05.015.
[65] Wagner G, Birk M. Water line intensities in the 1 μm region; 2013.
[66] Loos J, Birk M, Wagner G. Measurement of positions, intensities and self-broadening line shape parameters of H_2O lines in the spectral ranges 1850–2280 cm^{-1} and 2390–4000 cm^{-1}. J Quant Spectrosc Radiat Transf 2017;203:119–32. doi:10.1016/j.jqsrt.2017.02.013. HITRAN2016 Special Issue
[67] Lisak D, Havey D, Hodges JT. Spectroscopic line parameters of water vapor for rotation-vibration transitions near 7180 cm^{-1}. Phys Rev A 2009;79:52507. doi:10.1103/PhysRevA.79.052507.
[68] Mikhailenko S, Kassi S, Wang L, Campargue A. The absorption spectrum of water in the 1.25 μm transparency window (7408-7920 cm^{-1}). J Mol Spectrosc 2011;269:92–103. doi:10.1016/j.jms.2011.05.005.
[69] Leshchishina O, Mikhailenko S, Mondelain D, Kassi S, Campargue A. CRDS of water vapor at 0.1 Torr between 6886 and 7406 cm^{-1}. J Quant Spectrosc Radiat Transf 2012;113:2155–66. doi:10.1016/j.jqsrt.2012.06.026.
[70] Regalia L, Oudot C, Mikhailenko S, Wang L, Thomas X, Jenouvrier A, et al. Water vapor line parameters from 6450 to 9400 cm^{-1}. J Quant Spectrosc Radiat Transf 2014;136:119–36. doi:10.1016/j.jqsrt.2013.11.019.
[71] Campargue A, Mikhailenko S, Lohan B, Karlovets E, Mondelain D, Kassi S. The absorption spectrum of water vapor in the 1.25 μm atmospheric window (7911-8337 cm^{-1}). J Quant Spectrosc Radiat Transf 2015;157:135–52. doi:10.1016/j.jqsrt.2015.02.011.
[72] Sironneau V, Hodges J. Line shapes, positions and intensities of water transitions near 1.28 μm. J Quant Spectrosc Radiat Transf 2015;152:1–15. doi:10.1016/j.jqsrt.2014.10.020.
[73] Gordon IE, Rothman LS, Gamache RR, Jacquemart D, Boone C, Bernath PF, et al. Current updates of the water-vapor line list in HITRAN: a new "Diet" for air-broadened half-widths. J Quant Spectrosc Radiat Transf 2007;108(3):389–402. doi:10.1016/j.jqsrt.2007.06.009.
[74] N. H. Ngo, D. Lisak, H. Tran, J. -M. Hartmann. An isolated line-shape model to go beyond the Voigt profile in spectroscopic databases and radiative transfer codes. J Quant Spectrosc Radiat Transf 2013;129:89–100. doi:10.1016/j.jqsrt.2013.05.034.
[75] Tennyson J, Bernath PF, Campargue A, Császár AG, Daumont L, Gamache RR, et al. Recommended isolated-line profile for representing high-resolution spectroscopic transitions (IUPAC technical report). Pure Appl Chem 2014;86(12):1931–43. doi:10.1515/pac-2014-0208.
[76] Olsen K, Boone C, Toon G, Montmessin F, Fedorova A, Korablev O, et al. Validation of the HITRAN 2016 and GEISA 2015 line lists using ACE-FTS solar occultation observations. J Quant Spectrosc Radiat Transf 2019;236:106590. doi:10.1016/J.JQSRT.2019.106590.
[77] Baker AD, Blake CH, Reiners A. The IAG solar flux atlas: telluric correction with a semiempirical model. Astrophys J Suppl Ser 2020;247(1):24. doi:10.3847/1538-4365/ab6a1c.
[78] Conway EK, Kyuberis AA, Polyansky OL, Tennyson J, Zobov N. A highly accurate *ab initio* dipole moment surface for the ground electronic state of water vapour for spectra extending into the ultraviolet. J Chem Phys 2018;149:084307. doi:10.1063/1.5043545.
[79] Gonzalo GA, et al. Five decades observing Earth's atmospheric trace gases using ultraviolet and visible backscatter solar radiation from space. J Quant Spectrosc Radiat Transf 2019;238:106478. doi:10.1016/j.jqsrt.2019.04.030.
[80] Wang H, Souri AH, González Abad G, Liu X, Chance K. Ozone Monitoring Instrument (OMI) total column water vapor version 4 validation and applications. Atmos Meas Tech 2019;12(9):5183–99. doi:10.5194/amt-12-5183-2019.
[81] Wang H, Liu X, Chance K, Abad GG, Miller CC. Water vapor retrieval from OMI visible spectra. Atmos Meas Tech 2014;7:1901–13. doi:10.5194/amt-7-1901-2014.
[82] Lampel J, Pöhler D, Polyansky OL, Kyuberis AA, Zobov NF, Tennyson J, et al. Detection of water vapour absorption around 363 nm in measured atmospheric absorption spectra and its effect on DOAS evaluations. Atmos Chem Phys 2017;17:1271–95. doi:10.5194/acp-2016-388.
[83] Polyansky OL, Kyuberis AA, Zobov NF, Tennyson J, Yurchenko SN, Lodi L. ExoMol molecular line lists XXX: a complete high-accuracy line list for water. Mon Not R Astron Soc 2018;480:2597–608. doi:10.1093/mnras/sty1877.
[84] Lodi L, Tennyson J, Polyansky OL. A global, high accuracy ab initio dipole moment surface for the electronic ground state of the water molecule. J Chem Phys 2011;135:034113. doi:10.1063/1.3604934.
[85] Conway EK, Gordon IE, Kyuberis AA, Polyansky OL, Tennyson J, Zobov NF. Calculated line lists for $H_2{}^{16}O$ and $H_2{}^{18}O$ with extensive comparisons to theoretical and experimental sources including the HITRAN2016 database. J Quant Spectrosc Radiat Transf 2020;241:106711. doi:10.1016/j.jqsrt.2019.106711.

[86] Conway EK, Gordon IE, Tennyson J, Polyansky OL, Yurchenko SN, Chance K. A semi-empirical potential energy surface and line list for $H_2{}^{16}O$ extending into the near-ultraviolet. Atmos Chem Phys 2020;20(16):10015–27. doi:10.5194/acp-20-10015-2020.

[87] Lampel J, Pöhler D, Tschritter J, Frieß U, Platt U. On the relative absorption strengths of water vapour in the blue wavelength range. Atmos Meas Tech 2015;8:4329–46. doi:10.5194/amt-8-4329-2015.

[88] Wilson EM, Wenger JC, Venables DS. Upper limits for absorption by water vapor in the near-UV. J Quant Spectrosc Radiat Transf 2016;170:194–9. doi:10.1016/j.jqsrt.2015.11.015.

[89] Du J, Huang L, Min Q, Zhu L. The influence of water vapor absorption in the 290-350 nm region on solar radiance: laboratory studies and model simulation. Geophys Res Lett 2013;40:4788-4792. doi:10.1002/grl.50935.

[90] Pei L, Min Q, Du Y, Wang Z, Yin B, Yang K, et al. Water vapor near-UV absorption: laboratory spectrum, field evidence, and atmospheric impacts. J Geophys Res (Atmos) 2019;124:14310–24. doi:10.1029/2019JD030724.

[91] Mikhailenko S, Kassi S, Mondelain D, Campargue A. Water vapor absorption between 5690 and 8340 cm^{-1}: accurate empirical line centers and validation tests of calculated line intensities. J Quant Spectrosc Radiat Transf 2020;245:106840. doi:10.1016/j.jqsrt.2020.106840.

[92] Bubukina II, Polyansky OL, Zobov NF, Yurchenko SN. Optimized semiempirical potential energy surface for $H_2^{16}O$ up to 26 000 cm^{-1}. Opt Spectrosc 2011;110:160–6. doi:10.1134/S0030400X11020032.

[93] Mizus II, Kyuberis AA, Zobov NF, Makhnev VY, Polyansky OL, Tennyson J. High accuracy water potential energy surface for the calculation of infrared spectra. Philos Trans R Soc Lond A 2018;376:20170149. doi:10.1098/rsta.2017.0149.

[94] Császár AG, Furtenbacher T. Spectroscopic networks. J Mol Spectrosc 2011;266:99–103. doi:10.1016/j.jms.2011.03.031.

[95] Tóbiás R, Furtenbacher T, Simkó I, Császár AG, Diouf ML, Cozijn FMJ, et al. Spectroscopic-network-assisted precision spectroscopy and its application to water. Nat Commun 2020;11(1):1708. doi:10.1038/s41467-020-15430-6.

[96] Furtenbacher T, Tóbiás R, Tennyson J, Polyansky OL, Császár AG. W2020: a database of validated rovibrational experimental transitions and empirical energy levels of $H_2{}^{16}O$. J Phys Chem Ref Data 2020;49(3):033101. doi:10.1063/5.0008253.

[97] Furtenbacher T, Tóbiás R, Tennyson J, Polyansky OL, Kyuberis AA, Ovsyannikov RI, et al. The W2020 database of validated rovibrational experimental transitions and empirical energy levels of water isotopologues. II. $H_2{}^{17}O$ and $H_2{}^{18}O$ with an update to $H_2{}^{16}O$. J Phys Chem Ref Data 2020;49(4):043103. doi:10.1063/5.0030680.

[98] Conway EK, Gordon IE, Polyansky OL, Tennyson J. Determination of quantum labels based on projections of the total angular momentum on the molecule-fixed axis. J Quant Spectrosc Radiat Transf 2021;270:107716. doi:10.1016/j.jqsrt.2021.107716.

[99] Hose G, Taylor HS. Quantum Kolmogorov-arnol'd-moser-like theorem: fundamentals of localization in quantum theory. Phys Rev Lett 1983;51:947–50. doi:10.1103/PhysRevLett.51.947.

[100] Tennyson J, Kostin MA, Barletta P, Harris GJ, Polyansky OL, Ramanlal J, et al. DVR3D: a program suite for the calculation of rotation-vibration spectra of triatomic molecules. Comput Phys Commun 2004;163:85–116. doi:10.1016/j.cpc.2003.10.003.

[101] Harder JW, Brault JW. Atmospheric measurements of water vapor in the 442-nm region. J Geophys Res Atmos 1997;102(D5):6245–52. doi:10.1029/96JD01730.

[102] Loos J, Birk M, Wagner G. Measurement of air-broadening line shape parameters and temperature dependence parameters of H_2O lines in the spectral ranges 1850–2280 cm^{-1} and 239–4000 cm^{-1}. J Quant Spectrosc Radiat Transf 2017;203:103–18. doi:10.1016/j.jqsrt.2017.03.033. HITRAN2016 Special Issue

[103] Birk M, Wagner G, Loos J, Mondelain D, Campargue A. ESA SEOM-IAS - spectroscopic parameters database 2.3 μm region. Technical Report. Scientific Exploitation of Operational Missions - Improved Atmospheric Spectroscopy Databases; 2017. doi:105281/zenodo1009126.

[104] Birk M, Wagner G, Loos J, Lodi L, Polyansky OL, Kyuberis AA, et al. Accurate line intensities for water transitions in the infrared: comparison of theory and experiment. J Quant Spectrosc Radiat Transf 2017;203:88–102. doi:10.1016/j.jqsrt.2017.03.040. HITRAN2016 Special Issue

[105] Conway EK, Gordon IE, Polyansky OL, Tennyson J. Use of the complete basis set limit for computing highly accurate ab initio dipole moments. J Chem Phys 2020;152(2):024105. doi:10.1063/1.5135931.

[106] Toth RA, Sung K, Brown LR. $H_2{}^{16}O$ line strengths revisited: ν_2 and $2\nu_2$-ν_2 at 6 μm. J Mol Spectrosc 2011;265(2):59–68. doi:10.1016/j.jms.2010.10.009.

[107] Campargue A, Kassi S, Yachmenev A, Kyuberis AA, Küpper J, Yurchenko SN. Observation of electric-quadrupole infrared transitions in water vapor. Phys Rev Res 2020;2:023091. doi:10.1103/PhysRevResearch.2.023091.

[108] Campargue A, Solodov AM, Solodov AA, Yachmenev A, Yurchenko SN. Detection of electric-quadrupole transitions in water vapour near 5.4 and 2.5 μm. Phys Chem Chem Phys 2020;22(22):12476–81. doi:10.1039/d0cp01667e.

[109] Yurchenko SN, Thiel W, Jensen P. Theoretical ROVibrational Energies (TROVE): a robust numerical approach to the calculation of rovibrational energies for polyatomic molecules. J Mol Spectrosc 2007;245:126–40. doi:10.1016/j.jms.2007.07.009.

[110] Owens A, Yachmenev A. Richmol: a general variational approach for rovibrational molecular dynamics in external electric fields. J Chem Phys 2018;148(12):124102. doi:10.1063/1.5023874.

[111] Borger C, Beirle S, Dörner S, Sihler H, Wagner T. Total column water vapour retrieval from S-5P/TROPOMI in the visible blue spectral range. Atmos Meas Tech 2020;13(5):2751–83. doi:10.5194/amt-13-2751-2020.

[112] Wallace L, Livingston W. An atlas of the solar spectrum in the infrared from 1850 to 9000 cm^{-1} (1.1 to 5.4 micrometer); 2003.

[113] Tanaka M, Naumenko O, Brault JW, Tennyson J. Fourier transform absorption spectra of $H_2{}^{18}O$ and $H_2{}^{17}O$ in the 3ν+δ and 4ν polyad region. J Mol Spectrosc 2005;234(1):1–9. doi:10.1016/j.jms.2005.07.007.

[114] Mikhailenko S, Serdyukov V, Sinitsa L. Study of $H_2{}^{16}O$ and $H_2{}^{18}O$ absorption in the 16 460-17 200 cm^{-1} range using LED-based Fourier transform spectroscopy. J Quant Spectrosc Radiat Transf 2018;217:170–7. doi:10.1016/j.jqsrt.2018.05.032.

[115] Lodi L, Tennyson J. Line lists for $H_2{}^{18}O$ and $H_2{}^{17}O$ based on empirically-adjusted line positions and *ab initio* intensities. J Quant Spectrosc Radiat Transf 2012;113:850–8. doi:10.1016/j.jqsrt.2012.02.023.

[116] Polyansky OL, Kyuberis AA, Lodi L, Tennyson J, Ovsyannikov RI, Zobov N. ExoMol molecular line lists XIX: high accuracy computed line lists for $H_2{}^{17}O$ and $H_2{}^{18}O$. Mon Not R Astron Soc 2017;466:1363–71. doi:10.1093/mnras/stw3125.

[117] Mikhailenko S, Serdyukov V, Sinitsa L. LED-based Fourier transform spectroscopy of $H_2{}^{18}O$ in the 15 000–16 000 cm^{-1} range. J Quant Spectrosc Radiat Transf 2015;156:36–46. doi:10.1016/j.jqsrt.2015.02.001.

[118] Kyuberis AA, Zobov NF, Naumenko OV, Voronin BA, Polyansky OL, Lodi L, et al. Room temperature line lists for deuterated water. J Quant Spectrosc Radiat Transf 2017;203:175–85. doi:10.1016/j.jqsrt.2017.06.026.

[119] Gamache RR, Vispoel B. On the temperature dependence of half-widths and line shifts for molecular transitions in the microwave and infrared regions. J Quant Spectrosc Radiat Transf 2018;217:440–52. doi:10.1016/j.jqsrt.2018.05.019.

[120] N. Stolarczyk, F. Thibault, H. Cybulski, H. Jóźwiak, G. Kowzan, B. Vispoel, I.E. Gordon, L.S. Rothman, R.R. Gamache, P. Wcisło. Evaluation of different parameterizations of temperature dependences of the line-shape parameters based on *ab initio* calculations: case study for the HITRAN database. J Quant Spectrosc Radiat Transf 2020;240:106676. doi:10.1016/j.jqsrt.2019.106676.

[121] Gamache RR, Hartmann J-M. An intercomparison of measured pressure-broadening and pressure-shifting parameters of water vapor. Can J Chem 2004;82(6):1013–27. doi:10.1139/v04-069.

[122] Mlawer EJ, Turner DD, Paine SN, Palchetti L, Bianchini G, Payne VH, et al. Analysis of water vapor absorption in the far-infrared and submillimeter regions using surface radiometric measurements from extremely dry locations. J Geophys Res Atmos 2019;124(14):8134–60. doi:10.1029/2018JD029508.

[123] Vispoel B, Cavalcanti JH, Gamache RR. Modified complex Robert-Bonamy calculations of line shape parameters and their temperature dependence for water vapor in collision with N_2. J Quant Spectrosc Radiat Transf 2019;228:79–89. doi:10.1016/j.jqsrt.2019.02.023.

[124] Gamache RR, Farese M, Renaud CL. A spectral line list for water isotopologues in the 1100-4100 cm^{-1} region for application to CO_2-rich planetary atmospheres. J Mol Spectrosc 2016;326:144–50. doi:10.1016/j.jms.2015.09.001.

[125] Malathy Devi V, Benner DC, Sung K, Crawford TJ, Gamache RR, Renaud CL, et al. Line parameters for CO_2- and self-broadening in the ν_1 band of $HD^{16}O$. J Quant Spectrosc Radiat Transf 2017;203:133–57. doi:10.1016/j.jqsrt.2017.01.032.

[126] Malathy Devi V, Benner DC, Sung K, Crawford TJ, Gamache RR, Renaud CL, et al. Line parameters for CO_2- and self-broadening in the ν_3 band of $HD^{16}O$. J Quant Spectrosc Radiat Transf 2017;203:158–74. doi:10.1016/j.jqsrt.2017.02.020.

[127] Gamache RR, Hartmann J-M. Collisional parameters of H_2O lines: effects of vibration. J Quant Spectrosc Radiat Transf 2004;83(2):119–47. doi:10.1016/S0022-4073(02)00296-0.

[128] Jacquemart D, Gamache RR, Rothman LS. Semi-empirical calculation of air-broadened half-widths and air pressure-induced frequency shifts of water-vapor absorption lines. J Quant Spectrosc Radiat Transf 2005;96(2):205–39. doi:10.1016/j.jqsrt.2004.11.018.

[129] Gamache RR, Lamouroux J. Predicting accurate line-shape parameters for CO_2 transitions. J Quant Spectrosc Radiat Transf 2013;130:158–71. doi:10.1016/j.jqsrt.2013.05.021. HITRAN2012 special issue

[130] Gamache RR, Vispoel B, Renaud CL, Cleghorn K, Hartmann L. Vibrational dependence, temperature dependence, and prediction of line shape parameters for the H_2O-H_2 collision system. Icarus 2019;326:186–96. doi:10.1016/j.icarus.2019.02.011.

[131] Vispoel B, Cavalcanti JH, Paige ET, Gamache RR. Vibrational dependence, temperature dependence, and prediction of line shape parameters for the H_2O-N_2 collision system. J Quant Spectrosc Radiat Transf 2020;253:107030. doi:10.1016/j.jqsrt.2020.107030.

[132] Birk M, Wagner G, Loos J, Mondelain D, A Campargue. ESA SEOM-IAS - Measurement database 2.3 μm region. Zenodo 2017. doi:10.5281/zenodo.1009121.

[133] C. E. Miller, L. R. Brown, R. A. Toth, D. C. Benner, V. M. Devi. Spectroscopic challenges for high accuracy retrievals of atmospheric CO_2 and the Orbiting Carbon Observatory (OCO) experiment. C R Phys 2005;6(8):876–87. doi:10.1016/j.crhy.2005.09.005.

[134] Karlovets E, Gordon I, Rothman L, Hashemi R, Hargreaves R, Toon G, et al. The update of the line positions and intensities in the line list of carbon dioxide for the HITRAN2020 spectroscopic database. J Quant Spectrosc Radiat Transf 2021:107896. doi:10.1016/j.jqsrt.2021.107896.

[135] Tashkun SA, Perevalov VI, Gamache RR, Lamouroux J. CDSD-296, high resolution carbon dioxide spectroscopic databank: version for atmospheric appli-

cations. J Quant Spectrosc Radiat Transf 2015;152:45–73. doi:10.1016/j.jqsrt.2014.10.017.
[136] Polyansky OL, Bielska K, Ghysels M, Lodi L, Zobov NF, Hodges JT, et al. High accuracy CO_2 line intensities determined from theory and experiment. Phys Rev Lett 2015;114:243001. doi:10.1103/PhysRevLett.114.243001.
[137] Zak EJ, Polyansky OL, Lodi L, Zobov NF, Tashkun SA, Perevalov VI. A room temperature CO_2 line list with ab initio computed intensities. J Quant Spectrosc Radiat Transf 2016;177:31–42. doi:10.1016/j.jqsrt.2015.12.022.
[138] Zak EJ, Tennyson J, Polyansky OL, Lodi L, Zobov NF, Tashkun SA, et al. Room temperature line lists for CO_2 symmetric isotopologues with ab initio computed intensities. J Quant Spectrosc Radiat Transf 2017;189:267–80. doi:10.1016/j.jqsrt.2016.11.022.
[139] Zak EJ, Tennyson J, Polyansky OL, Lodi L, Zobov NF, Tashkun SA, et al. Room temperature linelists for CO_2 asymmetric isotopologues with ab initio computed intensities. J Quant Spectrosc Radiat Transf 2017;203:265–81. doi:10.1016/j.jqsrt.2017.01.037.
[140] Tashkun SA, Perevalov VI, Gamache RR, Lamouroux J. CDSD-296, high-resolution carbon dioxide spectroscopic databank: an update. J Quant Spectrosc Radiat Transf 2019;228:124–31. doi:10.1016/j.jqsrt.2019.03.001.
[141] Yurchenko SN, Mellor TM, Freedman RS, Tennyson J. ExoMol line lists - XXXIX. Ro-vibrational molecular line list for CO_2. Mon Not R Astron Soc 2020;496(4):5282–91. doi:10.1093/mnras/staa1874.
[142] Huang X, Schwenke DW, Freedman RS, Lee TJ. Ames-2016 line lists for 13 isotopologues of CO_2: updates, consistency, and remaining issues. J Quant Spectrosc Radiat Transf 2017;203:224–41. doi:10.1016/j.jqsrt.2017.04.026.
[143] Karlovets EV, Kassi S, Campargue A. High sensitivity CRDS of CO_2 in the 1.18 μm transparency window. Validation tests of current spectroscopic databases. J Quant Spectrosc Radiat Transf 2020;247. doi:10.1016/j.jqsrt.2020.106942.
[144] Perevalov VI, Tashkun SA. CDSD-296 (Carbon Dioxide Spectroscopic Databank): updated and enlarged version for atmospheric applications. In: Proceedings of the 10th biennial HITRAN conference; 2008. p. 7. doi:10.5281/zenodo.17520.
[145] G. C. Toon. CO_2 spectroscopy evaluation: 670 to 7000 cm^{-1}; 2020. https://mark4sun.jpl.nasa.gov/presentation.html. Reports and Presentations for the HITRAN meeting, Jun 2020, Jet Propulsion Laboratory, California Institute of Technology
[146] G. C. Toon. CO_2 spectroscopy evaluation: 670 to 7000 cm^{-1}; 2018. https://mark4sun.jpl.nasa.gov/presentation.html. Reports and Presentations for the ACE STM, Oct 2018, Jet Propulsion Laboratory, California Institute of Technology
[147] Butler JJ, Xiong XJ, Gu X. Measuring atmospheric carbon dioxide from space with the Orbiting Carbon Observatory-2 (OCO-2). In: Butler JJ, Xiong XJ, Gu X, editors. Earth observing systems XX. Society of Photo-Optical Instrumentation Engineers (SPIE) Conference Series, 9607; 2015. p. E2. doi:10.1117/12.2187291.
[148] Čermák P, Karlovets EV, Mondelain D, Kassi S, Perevalov VI, Campargue A. High sensitivity CRDS of CO_2 in the 1.74 μm transparency window. A validation test for the spectroscopic databases. J Quant Spectrosc Radiat Transf 2018;207:95–103. doi:10.1016/j.jqsrt.2017.12.018.
[149] Karlovets EV, Čermák P, Mondelain D, Kassi S, Campargue A, Tashkun SA, et al. Analysis and theoretical modeling of the ^{18}O enriched carbon dioxide spectrum by CRDS near 1.74 μm. J Quant Spectrosc Radiat Transf 2018;217:73–85. doi:10.1016/j.jqsrt.2018.05.017.
[150] Karlovets EV, Sidorenko AD, Čermák P, Mondelain D, Kassi S, Perevalov VI, et al. The $^{13}CO_2$ absorption spectrum by CRDS near 1.74 μm. J Mol Spectrosc 2018;354:54–9. doi:10.1016/j.jms.2018.10.003.
[151] Fleurbaey H, Yi H, Adkins EM, Fleisher AJ, Hodges JT. Cavity ring-down spectroscopy of CO_2 near $\lambda = 2.06$ μm: accurate transition intensities for the Orbiting Carbon Observatory-2 (OCO-2) “strong band”. J Quant Spectrosc Radiat Transf 2020;252. doi:10.1016/j.jqsrt.2020.107104.
[152] Long DA, Reed ZD, Fleisher AJ, Mendonca J, Roche S, Hodges JT. High-accuracy near-infrared carbon dioxide intensity measurements to support remote sensing. Geophys Res Lett 2020;47. doi:10.1029/2019GL086344.
[153] Birk M, Röske C, Wagner G. High accuracy CO_2 Fourier transform measurements in the range 6000-7000 cm^{-1}. J Quant Spectrosc Radiat Transf 2021:107791. doi:10.1016/j.jqsrt.2021.107791.
[154] Birk M, Röske C, Wagner G. Measurement and line parameter database CO_2 6000-7000 cm^{-1}. Zenodo 2021. doi:10.5281/zenodo.4525272.
[155] Campbell JF, Lin B, Dobler J, Pal S, Davis K, Obland MD, et al. Field evaluation of column CO_2 retrievals from intensity-modulated continuous-wave differential absorption lidar measurements during the act-america campaign. Earth Space Sci 2020;7(12). doi:10.1029/2019EA000847.
[156] Trokhimovskiy A, Perevalov V, Korablev O, Fedorova AA, Olsen KS, Bertaux JL, et al. First observation of the magnetic dipole CO_2 absorption band at 3.3 μm in the atmosphere of Mars by the ExoMars Trace Gas Orbiter ACS instrument. Astron Astrophys 2020;639. doi:10.1051/0004-6361/202038134.
[157] Perevalov VI, Trokhimovskiy AY, Lukashevskaya AA, Korablev OI, Fedorova A, Montmessin F. Magnetic dipole and electric quadrupole absorption in carbon dioxide. J Quant Spectrosc Radiat Transf 2021;259. doi:10.1016/j.jqsrt.2020.107408.
[158] Y. G. Borkov, A. M. Solodov, A. A. Solodov, V. I. Perevalov. Line intensities of the 01111-00001 magnetic dipole absorption band of $^{12}C^{16}O_2$: laboratory measurements. J Mol Spectrosc 2021;376:111418. doi:10.1016/j.jms.2021.111418.
[159] Majcherova Z, Macko P, Romanini D, Perevalov VI, Tashkun SA, Teffo JL, et al. High-sensitivity CW-cavity ringdown spectroscopy of $^{12}CO_2$ near 1.5 μm. J Mol Spectrosc 2005;230(1):1–21. doi:10.1016/j.jms.2004.09.011.
[160] Fleurbaey H, Grilli R, Mondelain D, Kassi S, Yachmenev A, Yurchenko SN, et al. Electric-quadrupole and magnetic-dipole contributions to the $\nu_2 + \nu_3$ band of carbon dioxide near 3.3 μm. J Quant Spectrosc Radiat Transf 2021. doi:10.1016/j.jqsrt.2021.107558.
[161] Hashemi R, Gordon IE, Tran H, Kochanov RV, Karlovets EV, Tan Y, et al. Revising the line-shape parameters for air- and self-broadened CO_2 lines toward a sub-percent accuracy level. J Quant Spectrosc Radiat Transf 2020;256:107283. doi:10.1016/j.jqsrt.2020.107283.
[162] Voigt W. Über das gesetz intensitätsverteilung innerhalb der linien eines gas spektrams. Sitzber Bayr Akad München Ber 1912;603:18.
[163] A. S. Pine. Line shape asymmetries in Ar-broadened HF (ν = 1–0) in the Dicke-narrowing regime. J Chem Phys 1994;101(5):3444–52. doi:10.1063/1.467529.
[164] H. M. Pickett. Effects of velocity averaging on the shapes of absorption lines. J Chem Phys 1980;73(12):6090–4. doi:10.1063/1.440145.
[165] P. Wcisło, I.E. Gordon, H. Tran, Y. Tan, S.-M. Hu, A. Campargue, S. Kassi, D. Romanini, C. Hill, R.V. Kochanov, L.S. Rothman. The implementation of non-Voigt line profiles in the HITRAN database: H_2 case study. J Quant Spectrosc Radiat Transf 2016;177:75–91. doi:10.1016/j.jqsrt.2016.01.024.
[166] Lamouroux J, Régalia L, Thomas X, Vander Auwera J, Gamache RR, Hartmann JM. CO_2 line-mixing database and software update and its tests in the 2.1 μm and 4.3 μm regions. J Quant Spectrosc Radiat Transf 2015;151:88–96. doi:10.1016/j.jqsrt.2014.09.017.
[167] Long D, Wójtewicz S, Miller C, Hodges J. Frequency-agile, rapid scanning cavity ring-down spectroscopy (FARS-CRDS) measurements of the 30012–00001 near-infrared carbon dioxide band. J Quant Spectrosc Radiat Transf 2015;161:35–40. doi:10.1016/j.jqsrt.2015.03.031.
[168] D. A. Long, K. Bielska, D. Lisak, D. K. Havey, M. Okumura, C. E. Miller, J. T. Hodges. The air-broadened, near-infrared CO_2 line-shape in the spectrally isolated regime: Evidence of simultaneous Dicke narrowing and speed dependence. J Chem Phys 2011;135(6):064308. doi:10.1063/1.3624527.
[169] T. Q. Bui, D. A. Long, A. Cygan, V. T. Sironneau, D. W. Hogan, P. M. Rupasinghe, R. Ciuryło, D. Lisak, M. Okumura. Observations of Dicke narrowing and speed dependence in air-broadened CO_2 line-shapes near 2.06 μm. J Chem Phys 2014;141(17):174301. doi:10.1063/1.4900502.
[170] M. V. Devi, D. C. Benner, K. Sung, L. R. Brown, T. J. Crawford, C. E. Miller, B. J. Drouin, V. H. Payne, S. Yu, M. A. H. Smith, A. W. Mantz, R. R. Gamache. Line parameters including temperature dependences of self- and air-broadened line-shapes of $^{12}C^{16}O_2$: 1.6 μm region. J Quant Spectrosc Radiat Transf 2016;177:117–44. doi:10.1016/j.jqsrt.2015.12.020.
[171] Hashemi R, Rozario H, Ibrahim A, Predoi-Cross A. line-shape study of the carbon dioxide laser band I. Can J Phys 2013;91(11):924–36. doi:10.1139/cjp-2013-0051.
[172] Predoi-Cross A, Liu W, Holladay C, Unni A, Schofield I, McKellar A, et al. Line profile study of transitions in the 30012–00001 and 30013–00001 bands of carbon dioxide perturbed by air. J Mol Spectrosc 2007;246(1):98–112. doi:10.1016/j.jms.2007.08.008.
[173] Hartmann J-M. A simple empirical model for the collisional spectral shift of air-broadened CO_2 lines. J Quant Spectrosc Radiat Transf 2009;110(18):2019–26. doi:10.1016/j.jqsrt.2009.05.016.
[174] Nguyen H, Ngo N, Tran H. Line-shape parameters and their temperature dependence predicted from molecular dynamics simulations for O_2- and air-broadened CO_2 lines. J Quant Spectrosc Radiat Transf 2020;242:106729. doi:10.1016/j.jqsrt.2019.106729.
[175] Adkins EM, Long DA, Hodges JT. Air-broadening in near-infrared carbon dioxide line shapes: quantifying contributions from O2, N2, and Ar. J Quant Spectrosc Radiat Transf 2021;270:107669. doi:10.1016/j.jqsrt.2021.107669.
[176] Predoi-Cross A, Unni A, Liu W, Schofield I, Holladay C, McKellar A, et al. Line-shape parameters measurement and computations for self-broadened carbon dioxide transitions in the 30012–00001 and 30013–00001 bands, line mixing, and speed dependence. J Mol Spectrosc 2007;245(1):34–51. doi:10.1016/j.jms.2007.07.004.
[177] L. Daneshvar, T. Földes, J. Buldyreva and J. Vander Auwera. Infrared absorption by pure CO_2 near 3340 cm^{-1}: measurements and analysis of collisional coefficients and line mixing effects at subatmospheric pressures. J Quant Spectrosc Radiat Transf 2014;149:258–74. doi:10.1016/j.jqsrt.2014.08.007.
[178] Gamache RR, Roller C, Lopes E, Gordon IE, Rothman LS, Polyansky OL, et al. Total internal partition sums for 166 isotopologues of 51 molecules important in planetary atmospheres: Application to HITRAN2016 and beyond. J Quant Spectrosc Radiat Transf 2017;203:70–87. doi:10.1016/j.jqsrt.2017.03.045.
[179] Hashemi R. CO_2 absorption coefficients (ABSCO) tables for the 4700 to 5100 cm^{-1} region using Voigt profile accounting for the line mixing; 2020. doi:105281/zenodo4126999.
[180] Hashemi R, Gordon I, Tran H, Kochanov RV, Karlovets E, Tan Y, et al. Evaluating the line-shape parameters of air- and self- broadened CO_2 lines toward a sub-percent accuracy level in atmospheric retrievals. In: Proceedings of the AGU fall meeting abstracts, 2020; 2020. p. A221–0012.
[181] Rosenmann L, Hartmann J-M, Perrin M-Y, Taine J. Accurate calculated tabulations of IR and Raman CO_2 line broadening by CO_2, H_2O, N_2, O_2 in the 300-2400 K temperature range. Appl Opt 1988;27(18):3902–7. doi:10.1364/AO.27.003902.
[182] Rosenmann L, Perrin MY, Hartmann JM, Taine J. Diode-laser measurements and calculations of CO_2-line-broadening by H_2O from 416 to 805 K and by N_2

from 296 to 803 K. J Quant Spectrosc Radiat Transf 1988;40:569–76. doi:10.1016/0022-4073(88)90137-9.
[183] Sung K, Brown LR, Toth RA, Crawford TJ. Fourier transform infrared spectroscopy measurements of H_2O-broadened half-widths of CO_2 at 4.3 μm. Can J Phys 2009;87(5):469–84. doi:10.1139/P08-130.
[184] Wallace CJ, Jeon C, Anderson CN, Havey DK. H_2O broadening of a CO_2 line and its nearest neighbors near 6360 cm^{-1}. J Phys Chem A 2011;115(47):13804–10. doi:10.1021/jp208800s.
[185] Delahaye T, Landsheere X, Pangui E, Huet F, Hartmann JM, Tran H. Broadening of CO_2 lines in the 4.3 μm region by H_2O. J Mol Spectrosc 2016;326:17–20. doi:10.1016/j.jms.2016.02.007.
[186] Clerbaux C, Boynard A, Clarisse L, George M, Hadji-Lazaro J, Herbin H, et al. Monitoring of atmospheric composition using the thermal infrared IASI/MetOp sounder. Atmos Chem Phys 2009;9(16):6041–54. doi:10.5194/acp-9-6041-2009.
[187] Hilsenrath E, Attmannspacher W, Bass A, Evans W, Hagemeyer R, Barnes RA, et al. Results from the balloon ozone intercomparison campaign (BOIC). J Geophys Res 1986;91(D12):13137. doi:10.1029/JD091iD12p13137.
[188] Murata I, Sato K, Okano S, Tomikawa Y. Measurements of stratospheric ozone with a balloon-borne optical ozone sensor. Int J Remote Sens 2009;30(15-16):3961–6. doi:10.1080/01431160902822823.
[189] Hubert D, Lambert JC, Verhoelst T, Granville J, Keppens A, Baray JL, et al. Ground-based assessment of the bias and long-term stability of 14 limb and occultation ozone profile data records. Atmos Meas Tech 2016;9(6):2497–534. doi:10.5194/amt-9-2497-2016.
[190] Barbe A, Mikhailenko S, Starikova E, De Backer MR, Tyuterev VG, Mondelain D, et al. Ozone spectroscopy in the electronic ground state: High-resolution spectra analyses and update of line parameters since 2003. J Quant Spectrosc Radiat Transf 2013;130:172–90. doi:10.1016/j.jqsrt.2013.06.007.
[191] Toon G. Evaluation of HITRAN 2016 O_3 linelist, (private communication); 2017. https://mark4sun.jpl.nasa.gov/report/o3_spectroscopy_evaluation_20170930.compressed.pdf
[192] Glatthor N, von Clarmann T, Stiller GP, Kiefer M, Laeng A, Dinelli BM, et al. Differences in ozone retrieval in MIPAS channels A and AB: a spectroscopic issue. Atmos Meas Tech 2018;11(8):4707–23. doi:10.5194/amt-11-4707-2018.
[193] Birk M, Wagner G, Flaud JM. Experimental linestrengths of far-infrared pure rotational transitions of ozone. J Mol Spectrosc 1994;163(1):245–61. doi:10.1006/jmsp.1994.1021.
[194] Babikov YL, Mikhailenko SN, Barbe A, Tyuterev VG. S&MPO - an information system for ozone spectroscopy on the WEB. J Quant Spectrosc Radiat Transf 2014;145:169–96. doi:10.1016/j.jqsrt.2014.04.024.
[195] Drouin BJ, Crawford TJ, Yu S. Validation of ozone intensities at 10 μm with THz spectrometry. J Quant Spectrosc Radiat Transf 2017;203:282–92. doi:10.1016/j.jqsrt.2017.06.035.
[196] Janssen C, Boursier C, Elandaloussi H, Jeseck P, Koshelev D, Marie-Jeanne P, Rouillé C, et al. Multi-spectral investigation of ozone: Part I. Setup & uncertainty budget. J Quant Spectrosc Radiat Transf 2021. Submitted.
[197] Jacquemart D, Boursier C, Elandaloussi H, Jeseck P, Té Y, Janssen C. Multi--spectral investigation of ozone: Part II. Line intensities at 5 μm and 10 μm at one percent accuracy. J Quant Spectrosc Radiat Transf 2021. Submitted.
[198] Wagner G, Birk M, Flaud J-M. In preparation; 2021.
[199] Flaud JM, Bacis R. The ozone molecule: infrared and microwave spectroscopy. Spectrochim Acta Part A Mol Spectrosc 1998;54(1):3–16. doi:10.1016/S1386-1425(97)00214-X.
[200] Birk M, Wagner G, Gordon IE, Drouin BJ. Ozone intensities in the rotational bands. J Quant Spectrosc Radiat Transf 2019;226:60–5. doi:10.1016/J.JQSRT.2019.01.004.
[201] Tyuterev VG, Barbe A, Jacquemart D, Janssen C, Mikhailenko SN, Starikova EN. *Ab initio* predictions and laboratory validation for consistent ozone intensities in the MW, 10 and 5 μm ranges. J Chem Phys 2019;150(18). doi:10.1063/1.5089134.
[202] Tyuterev V, Barbe A, Mikhailenko S, Starikova E, Babikov Y. Towards the intensity consistency of the ozone bands in the infrared range: ab initio corrections to the S&MPO database. J Quant Spectrosc Radiat Transf 2021;272:107801. doi:10.1016/j.jqsrt.2021.107801.
[203] Barbe A, Mikhailenko S, Starikova E, Tyuterev V. Infrared spectra of $^{16}O_3$ in 900-5600 cm^{-1} range revisited: empirical corrections to S&MPO and HITRAN2020 line lists. J Quant Spectrosc Radiat Transf 2021:107936. doi:10.1016/J.JQSRT.2021.107936.
[204] Barbe A, Starikova E, De Backer M-R. High resolution infrared spectra of the $^{16}O^{16}O^{17}O$ and the $^{16}O^{17}O^{16}O$ ozone isotopic species. The 5 and 10 micron spectral ranges revisited. J Quant Spectrosc Radiat Transf 2017;203:293–9. doi:10.1016/j.jqsrt.2017.03.034.
[205] Barbe A, Starikova E, De Backer MR, Tyuterev VG. Analyses of infrared FT spectra of asymmetric ozone isotopologue $^{16}O^{16}O^{18}O$ in the range 950-3850 cm^{-1}. J Quant Spectrosc Radiat Transf 2018;218:231–47. doi:10.1016/j.jqsrt.2018.06.022.
[206] Guillon G, Honvault P, Kochanov R, Tyuterev V. First-principles computed rate constant for the O+O_2 isotopic exchange reaction now matches experiment. J Phys Chem Lett 2018;9(8):1931–6. doi:10.1021/acs.jpclett.8b00661.
[207] Yuen CH, Lapierre D, Gatti F, Kokoouline V, Tyuterev VG. The role of ozone vibrational resonances in the isotope exchange reaction $^{16}O^{16}O + {}^{18}O \rightarrow {}^{18}O^{16}O + {}^{16}O$: The Time-Dependent Picture. J Phys Chem A 2019;123(36):7733–43. doi:10.1021/acs.jpca.9b06139.
[208] Kokoouline V, Lapierre D, Alijah A, Tyuterev V. Localized and delocalized bound states of the main isotopologue $^{48}O_3$ and of ^{18}O-enriched $^{50}O_3$ isotopomers of the ozone molecule near the dissociation threshold. Phys Chem Chem Phys (Inc Faraday Trans) 2020;22(28):15885–99. doi:10.1039/D0CP02177F.
[209] Vasilchenko S, Barbe A, Starikova E, Kassi S, Mondelain D, Campargue A, et al. Detection and assignment of ozone bands near 95% of the dissociation threshold: Ultrasensitive experiments for probing potential energy function and vibrational dynamics. Phys Rev A 2020;102(5). doi:10.1103/PhysRevA.102.052804.
[210] Tyuterev VG, Kochanov RV, Tashkun SA, Holka F, Szalay PG. New analytical model for the ozone electronic ground state potential surface and accurate ab initio vibrational predictions at high energy range. J Chem Phys 2013;139(13):134307. doi:10.1063/1.4821638.
[211] Tyuterev VG, Kochanov RV, Tashkun SA. Accurate ab initio dipole moment surfaces of ozone: first principle intensity predictions for rotationally resolved spectra in a large range of overtone and combination bands. J Chem Phys 2017;146(6). doi:10.1063/1.4973977.
[212] Mack KM, Muenter JS. Stark and Zeeman properties of ozone from molecular beam spectroscopy. J Chem Phys 1977;66(12):5278–83. doi:10.1063/1.433909.
[213] Mikhailenko S, Barbe A. High resolution infrared spectrum of $^{16}O_3$: The 3600–4300 cm^{-1} range reinvestigated. J Quant Spectrosc Radiat Transf 2020;244. doi:10.1016/j.jqsrt.2019.106823.
[214] Tyuterev VG, Tashkun SA, Seghir H. High-order contact transformations: general algorithm, computer implementation, and triatomic tests. In: Sinitsa LN, Mikhailenko SN, editors. Proceedings of the 14th symposium on high-resolution molecular spectroscopy. Society of Photo-Optical Instrumentation Engineers (SPIE) Conference Series, 5311; 2004. p. 164–75. doi:10.1117/12.545641.
[215] Mikhailenko SN, Tyuterev VG, Starikov VI, Albert KK, Winnewisser BP, Winnewisser M, et al. Water spectra in the region 4200-6250 cm $^{-1}$, extended analysis of $\nu_1+\nu_2$, $\nu_2+\nu_3$, and $3\nu_2$ Bands and Confirmation of Highly Excited States from Flame Spectra and from Atmospheric Long-Path Observations. J Mol Spectrosc 2002;213(2):91–121. doi:10.1006/jmsp.2002.8558.
[216] Heyart M, Perrin A, Flaud J-M, Camy-Peyret C, Rinsland C, Smith M, et al. The ν_1 and ν_3 bands of $^{16}O^{17}O^{16}O$ line positions and intensities. J Mol Spectrosc 1992;156(1):210–16. doi:10.1016/0022-2852(92)90104-V.
[217] Perrin A, Flaud JM, Keller F, Smith MAH, Rinsland CP, Devi VM, et al. The $\nu_1+\nu_3$ bands of the ^{16}O ^{17}O ^{16}O and ^{16}O ^{16}O ^{17}O isotopomers of ozone. J Mol Spectrosc 2001;207(1):54–9. doi:10.1006/jmsp.2001.8320.
[218] Wagner G, Birk M. New infrared spectroscopic database for bromine nitrate. J Mol Spectrosc 2016;326:95–105. doi:10.1016/j.jms.2016.03.007.
[219] Wagner G, Birk M, Schreier F, Flaud JM. Spectroscopic database for ozone in the fundamental spectral regions. J Geophys Res (Atmos) 2002;107(D22). doi:10.1029/2001JD000818.
[220] Birk M, Wagner G, Barbe A, De Backer M-R, Rotger M, Flaud J-M. ESA SEOM-IAS - measurement and line parameter database O_3 MIR region. Zenodo 2021. doi:10.5281/zenodo.1492542.
[221] Minissale M, Zanon-Willette T, Jeseck P, Boursier C, Janssen C. First pressure shift measurement of ozone molecular lines at 9.54 μm using a tunable quantum cascade laser. J Mol Spectrosc 2018;348:103–13. doi:10.1016/j.jms.2017.12.009.
[222] Jacquemart D, Polyansky OL, Maknev V, Tennyson J. Synthesis of *ab initio* and effective Hamiltonian line lists for ozone. J Quant Spectrosc Radiat Transf 2021;269:107651. doi:10.1016/j.jqsrt.2021.10765.
[223] Polyansky OL, Zobov NF, Mizus II, Kyuberis AA, Lodi L, Tennyson J. Potential energy surface, dipole moment surface and the intensity calculations for the 10 μm, 5 μm and 3 μm bands of ozone. J Quant Spectrosc Radiat Transf 2018;210:127–35. doi:10.1016/j.jqsrt.2018.02.018.
[224] Flaud JM, Wagner G, Birk M, Camy-Peyret C, Claveau C, de Backer-Barilly MR, et al. Ozone absorption around 10 μm. J Geophys Res (Atmos) 2003;108(D9). doi:10.1029/2002JD002755.
[225] Flaud JM. Effective Hamiltonian calculation at 10 μm; 2019. Private communication
[226] Toon G. Ozone spectroscopy evaluation; 2020. https://mark4sun.jpl.nasa.gov/report/O3_Spectroscopy_Eval_2021_07_14.pdf. Report, Jet Propulsion Laboratory,California Institute of Technology
[227] Pickett HM, Poynter RL, Cohen EA, Delitsky ML, Pearson JC, Müller HSP. Submillimeter, millimeter and microwave spectral line catalog. J Quant Spectrosc Radiat Transf 1998;60:883–90. doi:10.1016/S0022-4073(98)00091-0.
[228] Adkins EM, Long DA, Fleisher AJ, Hodges JT. Near-infrared cavity ring-down spectroscopy measurements of nitrous oxide in the (4200)←(0000) and (5000)←(0000) bands. J Quant Spectrosc Radiat Transf 2021;262:107527. doi:10.1016/j.jqsrt.2021.107527.
[229] Toth RA. Linelist of N_2O parameters from 500 to 7500 cm^{-1}. JPL online 2004 https://mark4sunjplnasagov/n2ohtml.
[230] Daumont L, Vander Auwera J, Teffo J-L, Perevalov VI, Tashkun SA. Line intensity measurements in $^{14}N_2{}^{16}O$ and their treatment using the effective dipole moment approach II. The 5400–11 000 cm^{-1} region. J Quant Spectrosc Radiat Transf 2007;104:342–56 http://www.elsevier.com/locate/jqsrt. doi:10.1016/j.jqsrt.2006.09.004.
[231] Boone CD, Bernath PF, Cok D, Jones SC, Steffen J. Version 4 retrievals for the atmospheric chemistry experiment Fourier transform spectrometer (ACE-FTS) and imagers. J Quant Spectrosc Radiat Transf 2020;247:106939. doi:10.1016/j.jqsrt.2020.106939.
[232] Rosenkranz P. Shape of the 5 mm oxygen band in the atmosphere. IEEE Trans Antennas Propag 1975;23(4):498–506. doi:10.1109/TAP.1975.1141119.
[233] Hashemi R, Gordon IE, Adkins EM, Hodges JT, Long DA, Birk M, et al. Improve-

ment of the spectroscopic parameters of the air- and self-broadened N_2O and CO lines for the HITRAN2020 database applications. J Quant Spectrosc Radiat Transf 2021:107735. doi:10.1016/j.jqsrt.2021.107735.
[234] Lacome N, Levy A, Guelachvili G. Fourier transform measurement of self-, N_2-, and O_2-broadening of N_2O lines: temperature dependence of linewidths. Appl Opt 1984;23(3):425–35. doi:10.1364/AO.23.000425.
[235] Toth RA. Line strengths (900–3600 cm^{-1}), self-broadened linewidths, and frequency shifts (1800–2360 cm^{-1}) of N_2O. Appl Opt 1993;32(36):7326–65. doi:10.1364/AO.32.007326.
[236] Nemtchinov V, Sun C, Prasad Varanasi. Measurements of line intensities and line widths in the ν_3-fundamental band of nitrous oxide at atmospheric temperatures. J Quant Spectrosc Radiat Transf 2004;83(3):267–84. doi:10.1016/S0022-4073(02)00355-2.
[237] Toth RA. N_2- and air-broadened linewidths and frequency-shifts of N_2O. J Quant Spectrosc Radiat Transf 2000;66(3):285–304. doi:10.1016/S0022-4073(99)00167-3.
[238] Adkins EM. MATS: multi-spectrum analysis tool for spectroscopy. NIST online 2020. doi:10.18434/M32200.
[239] Werwein V, Brunzendorf J, Serdyukov A, Werhahn O, Ebert V. First measurements of nitrous oxide self-broadening and self-shift coefficients in the 0002-0000 band at 2.26 μm using high resolution Fourier transform spectroscopy. J Mol Spectrosc 2016;323:28–42. doi:10.1016/j.jms.2016.01.010. Atmospheric Spectroscopy
[240] Loos J, Birk M, Wagner G. Pressure broadening, -shift, speed dependence and line mixing in the ν_3 rovibrational band of N_2O. J Quant Spectrosc Radiat Transf 2015;151:300–9. doi:10.1016/j.jqsrt.2014.10.008.
[241] Odintsova T, Fasci E, Gravina S, Gianfrani L, Castrillo A. Optical feedback laser absorption spectroscopy of N_2O at 2 μm. J Quant Spectrosc Radiat Transf 2020;254:107190. doi:10.1016/j.jqsrt.2020.107190.
[242] Gentry B, Strow LL. Line mixing in a N_2-broadened CO_2 Q branch observed with a tunable diode laser. J Chem Phys 1987;86(10):5722–30. doi:10.1063/1.452770.
[243] Tashkun SA, Perevalov VI, Lavrentieva NN. NOSD-1000, the high-temperature nitrous oxide spectroscopic databank. J Quant Spectrosc Radiat Transf 2016;177:43–8. doi:10.1016/j.jqsrt.2015.11.014.
[244] Sharpe SW, Johnson TJ, Sams RL, Chu PM, Rhoderick GC, Johnson PA. Gas-phase databases for quantitative infrared spectroscopy. Appl Spectrosc 2004;58:1452–61. doi:10.1366/0003702042641281.
[245] Tashkun SA, Perevalov VI, Karlovets EV, Kassi S, Campargue A. High sensitivity cavity ring down spectroscopy of N_2O near 1.22 μm: (II) $^{14}N_2{}^{16}O$ line intensity modeling and global fit of $^{14}N_2{}^{18}O$ line positions. J Quant Spectrosc Radiat Transf 2016;176:62–9. doi:10.1016/j.jqsrt.2016.02.020.
[246] Toth RA. Line positions and strengths of N_2O between 3515 and 7800 cm^{-1}. J Mol Spectrosc 1999;197(2):158–87. doi:10.1006/jmsp.1999.7907.
[247] Karlovets E, Kassi S, Tashkun S, Campargue A. The absorption spectrum of nitrous oxide between 8325 and 8622 cm^{-1}. J Quant Spectrosc Radiat Transf 2021;262:107508. doi:10.1016/j.jqsrt.2021.107508.
[248] Liu AW, Kassi S, Malara P, Romanini D, Perevalov VI, Tashkun SA, et al. High sensitivity CW-cavity ring down spectroscopy of N_2O near 1.5 μm (I). J Mol Spectrosc 2007;244(1):33–47. doi:10.1016/j.jms.2007.01.007.
[249] Liu AW, Kassi S, Perevalov VI, Tashkun SA, Campargue A. High sensitivity CW-cavity ring down spectroscopy of N_2O near 1.5 μm (II). J Mol Spectrosc 2007;244(1):48–62. doi:10.1016/j.jms.2007.05.010.
[250] Lu Y, Mondelain D, Liu AW, Perevalov VI, Kassi S, Campargue A. High sensitivity CW-cavity ring down spectroscopy of N_2O between 6950 and 7653 cm^{-1} (1.44-1.31 μm): I. Line positions. J Quant Spectrosc Radiat Transf 2012;113(10):749–62. doi:10.1016/j.jqsrt.2012.03.005.
[251] Karlovets EV, Lu Y, Mondelain D, Kassi S, Campargue A, Tashkun SA, et al. High sensitivity CW-cavity ring down spectroscopy of N_2O between 6950 and 7653 cm^{-1} (1.44-1.31 μm): II. Line intensities. J Quant Spectrosc Radiat Transf 2013;117:81–7. doi:10.1016/j.jqsrt.2012.11.003.
[252] Karlovets EV, Campargue A, Kassi S, Perevalov VI, Tashkun SA. High sensitivity cavity ring down spectroscopy of N_2O near 1.22 μm: (I) rovibrational assignments and band-by-band analysis. J Quant Spectrosc Radiat Transf 2016;169:36–48. doi:10.1016/j.jqsrt.2015.09.012.
[253] Bertin T, Mondelain D, Karlovets E, Kassi S, Perevalov V, Campargue A. High sensitivity cavity ring down spectroscopy of N_2O near 1.74 μm. J Quant Spectrosc Radiat Transf 2019;229:40–9. doi:10.1016/j.jqsrt.2019.02.011.
[254] Liu AW, Kassi S, Perevalov VI, Tashkun SA, Campargue A. High sensitivity CW-cavity ring down spectroscopy of N_2O near 1.28 μm. J Mol Spectrosc 2011;267(1-2):191–9. doi:10.1016/j.jms.2011.03.025.
[255] Liu AW, Kassi S, Perevalov VI, Hu SM, Campargue A. High sensitivity CW-cavity ring down spectroscopy of N_2O near 1.5 μm (III). J Mol Spectrosc 2009;254(1):20–7. doi:10.1016/j.jms.2008.12.006.
[256] Liu AW, Hu CL, Wang J, Perevalov VI, Hu SM. Cavity ring-down spectroscopy of ^{15}N enriched N_2O near 1.56 μm. J Quant Spectrosc Radiat Transf 2019;232:1–9. doi:10.1016/j.jqsrt.2019.04.035.
[257] Li G, Gordon IE, Rothman LS, Tan Y, Hu S-M, Kassi S, et al. Rovibrational line lists for nine isotopologues of the CO molecule in the $X^1\Sigma^+$ ground electronic state. Astrophys J Suppl Ser 2015;216. doi:10.1088/0067-0049/216/1/15.
[258] Devi VM, Benner DC, Sung K, Crawford TJ, Li G, Gamache RR, et al. Positions, intensities and line shape parameters for the 1←0 bands of CO isotopologues. J Quant Spectrosc Radiat Transf 2018;218:203–30. doi:10.1016/J.JQSRT.2018.06.007.
[259] Wójtewicz S, Stec K, Masłowski P, Cygan A, Lisak D, Trawiński R, et al. Low pressure line-shape study of self-broadened CO transitions in the (3←0) band. J Quant Spectrosc Radiat Transf 2013;130:191–200. doi:10.1016/j.jqsrt.2013.06.005.
[260] Cygan A, Wcisło P, Wójtewicz S, Kowzan G, Zaborowski M, Charczun D, et al. High-accuracy and wide dynamic range frequency-based dispersion spectroscopy in an optical cavity. Opt Express 2019;27(15):21810. doi:10.1364/OE.27.021810.
[261] Borkov YG, Solodov AM, Solodov AA, Petrova TM, Karlovets EV, Perevalov VI. Fourier transform CO spectra near 1.6 μm. J Quant Spectrosc Radiat Transf 2020;253:107064. doi:10.1016/j.jqsrt.2020.107064.
[262] Borkov YG, Solodov AM, Petrova TM, Solodo AA, Karlovets EV, Perevalov VI. Fourier transforms CO spectra near 1.19 μm. J Quant Spectrosc Radiat Transf 2020;242:106790. doi:10.1016/j.jqsrt.2019.106790.
[263] Bordet B, Kassi S, Campargue A. Line parameters of the 4–0 band of carbon monoxide by high sensitivity cavity ring down spectroscopy near 1.2 μm. J Quant Spectrosc Radiat Transf 2021;260:107453. doi:10.1016/j.jqsrt.2020.107453.
[264] Hochstaffl P, Schreier F, Birk M, Wagner G, G Feist D, Notholt J, et al. Impact of molecular spectroscopy on carbon monoxide abundances from TROPOMI. Remote Sens 2020;12(21):3486. doi:10.3390/rs12213486.
[265] Hochstaffl P, Schreier F. Impact of molecular spectroscopy on carbon monoxide abundances from SCIAMACHY. Remote Sens 2020;12(7):1084. doi:10.3390/rs12071084.
[266] Tan Y, Samuels S, Hargreaves RJ, Hashemi R, Skinner FM, Gordon IE. H_2, He, and CO_2 line-broadening coefficients, and temperature-dependence exponents for the HITRAN database. Part II: CO_2, N_2O, CO, OH, OCS, H_2CO, HCN, PH_3, H_2S and GeH_4. Astrophys J Suppl Ser 2021;In Preparation.
[267] Régalia-Jarlot L, Thomas X, von der Heyden P, Barbe A. Pressure-broadened line widths and pressure-induced line shifts coefficients of the (1–0) and (2–0) bands of $^{12}C^{16}O$. J Quant Spectrosc Radiat Transf 2005;91(2):121–31. doi:10.1016/j.jqsrt.2004.05.042.
[268] Varanasi P. Measurement of line widths of CO of planetary interest at low temperatures. J Quant Spectrosc Radiat Transf 1975;15(2):191–6. doi:10.1016/0022-4073(75)90017-5.
[269] Sung K, Varanasi P. Intensities, collision-broadened half-widths, and collision-induced line shifts in the second overtone band of $^{12}C^{16}O$. J Quant Spectrosc Radiat Transf 2004;83(3):445–58. doi:10.1016/S0022-4073(03)00015-3.
[270] Malathy Devi V, Chris Benner D, Smith MAH, Mantz AW, Sung K, Brown LR, et al. Spectral line parameters including temperature dependences of self- and air-broadening in the 2←0 band of CO at 2.3 μm. J Quant Spectrosc Radiat Transf 2012;113(11):1013–33. doi:10.1016/j.jqsrt.2012.02.010.
[271] Malathy Devi V, Chris Benner D, Smith MAH, Mantz AW, Sung K, Brown LR. Spectral line parameters including temperature dependences of air-broadening for the 2 ← 0 bands of $^{13}C^{16}O$ and $^{12}C^{18}O$ at 2.3 μm. J Mol Spectrosc 2012;276:33–48. doi:10.1016/j.jms.2012.05.005.
[272] Ngo N, Landsheere X, Pangui E, Morales S, Tran H, Hartmann J-M. Self-broadening and -shifting of very intense lines of the 1←0 band of $^{12}C^{16}O$. J Quant Spectrosc Radiat Transf 2014;149:285–90. doi:10.1016/j.jqsrt.2014.08.021.
[273] Malathy Devi V, Predoi-Cross A, Chris Benner D, Smith MAH, Rinsland CP, Mantz AW. Self- and H_2-broadened width and shift coefficients in the 2←0 band of $^{12}C^{16}O$: revisited. J Mol Spectrosc 2004;228(2):580–92. doi:10.1016/j.jms.2004.05.006.
[274] Esteki K, Predoi-Cross A, Povey C, Ivanov S, Ghoufi A, Thibault F, et al. Room temperature self- and H_2-broadened line parameters of carbon monoxide in the first overtone band: Theoretical and revised experimental results. J Quant Spectrosc Radiat Transf 2017;203:309–24. doi:10.1016/j.jqsrt.2017.04.008.
[275] Predoi-Cross A, Bouanich JP, Benner DC, May AD, Drummond JR. Broadening, shifting, and line asymmetries in the 2← band of CO and CO-N_2: experimental results and theoretical calculations. J Chem Phys 2000;113(1):158–68. doi:10.1063/1.481783.
[276] Predoi-Cross A, Hnatovsky C, Strong K, Drummond JR, Chris Benner D. Temperature dependence of self- and N_2-broadening and pressure-induced shifts in the 3←0 band of CO. J Mol Struct 2004;695-696:269–86. doi:10.1016/j.molstruc.2003.12.043.
[277] Sung K, Varanasi P. Hydrogen-broadened half-widths and hydrogen-induced line shifts of $^{12}C^{16}O$ relevant to the Jovian atmospheric spectra. J Quant Spectrosc Radiat Transf 2004;85:165–82. doi:10.1016/S0022-4073(03)00202-4.
[278] Sinclair PM, Duggan P, Berman R, Drummond JR, May AD. Line broadening in the fundamental band of CO in CO-He and CO-Ar mixtures. J Mol Spectrosc 1998;191:258–64. doi:10.1006/jmsp.1998.7628.
[279] Mantz AW, Malathy Devi V, Chris Benner D, Smith MAH, Predoi-Cross A, Dulick M. A multispectrum analysis of widths and shifts in the 2010–2260 cm^{-1} region of $^{12}C^{16}O$ broadened by Helium at temperatures between 80 and 297 K. J Mol Struct 2005;742(1-3):99–110. doi:10.1016/j.molstruc.2004.11.094.
[280] Predoi-Cross A, Esteki K, Rozario H, Naseri H, Latif S, Thibault F, et al. Theoretical and revisited experimentally retrieved He-broadened line parameters of carbon monoxide in the fundamental band. J Quant Spectrosc Radiat Transf 2016;184:322–40. doi:10.1016/j.jqsrt.2016.08.007.
[281] C. Luo, R. Wehr, J. R. Drummond, A. D. May, F. Thibault, J. Boissoles, J. M. Launay, C. Boulet, J.-P. Bouanich, and J.-M. Hartmann. Shifting and broadening in the fundamental band of CO highly diluted in He and Ar: a comparison with theory. J Chem Phys 2001;115(5):2198–206. doi:10.1063/1.1383049.
[282] Thibault F, Boissoles J, Doucen RL, Farrenq R, Morillon-Chapey M, Boulet C. Line-by-line measurements of interference parameters for the 0–1 and 0–2 bands of CO in He, and comparison with coupled-states calculations. J Chem Phys 1992;97(7):4623–32. doi:10.1063/1.463865.

[283] Hashemi R, Predoi-Cross A, Dudaryonok A, Lavrentieva N, Vandaele A, Vander Auwera J. CO_2 pressure broadening and shift coefficients for the 2–0 band of $^{12}C^{16}O$. J Mol Spectrosc 2016;326:60–72. doi:10.1016/j.jms.2016.02.014. New Visions of Spectroscopic Databases, Volume I

[284] Chesnokova TY, Makarova MV, Chentsov AV, Kostsov VS, Poberovskii AV, Zakharov VI, et al. Estimation of the impact of differences in the CH_4 absorption line parameters on the accuracy of methane atmospheric total column retrievals from ground-based FTIR spectra. J Quant Spectrosc Radiat Transf 2020;254:107187. doi:10.1016/j.jqsrt.2020.107187.

[285] Rodina A, Nikitin A, Thomas X, Manceron L, Daumont L, Rey M, et al. Improved line list of $^{12}CH_4$ in the 3760-4100 cm^{-1} region. J Quant Spectrosc Radiat Transf 2019;225:351–62. doi:10.1016/J.JQSRT.2018.12.034.

[286] Lorente A, Borsdorff T, Butz A, Hasekamp O, aan de Brugh J, Schneider A, et al. Methane retrieved from TROPOMI: improvement of the data product and validation of the first 2 years of measurements. Atmos Meas Tech 2021;14(1):665–84. doi:10.5194/amt-14-665-2021.

[287] Nikitin A, Rodina A, Thomas X, Manceron L, Daumont L, Rey M, et al. Line list of $^{12}CH_4$ in the 4300-4600 cm^{-1} region. J Quant Spectrosc Radiat Transf 2020;253:107061. doi:10.1016/j.jqsrt.2020.107061.

[288] Wagner G, Birk M. Spectroscopy of methane in the Octad region. In preparation; 2021.

[289] Predoi-Cross A, Brawley-Tremblay M, Brown LR, Devi VM, Benner DC. Multispectrum analysis of $^{12}CH_4$ from 4100 to 4635 cm^{-1}: II. Air-broadening coefficients (widths and shifts). J Mol Spectrosc 2006;236(2):201–15. doi:10.1016/j.jms.2006.01.013.

[290] Nikitin A, Protasevich A, Rey M, Serdyukov V, Sinitsa L, Lugovskoy A, et al. Improved line list of $^{12}CH_4$ in the 8850–9180 cm^{-1} region. J Quant Spectrosc Radiat Transf 2019;239:106646. doi:10.1016/J.JQSRT.2019.106646.

[291] Devi VM, Benner DC, Sung K, Crawford TJ, Yu S, Brown LR, et al. Self- and air-broadened line shapes in the $2\nu_3$ P- and R-branches of $^{12}CH_4$. J Mol Spectrosc 2015;315:114–36. doi:10.1016/j.jms.2015.05.003. Spectroscopy with Synchrotron Radiation

[292] Devi V, Benner DC, Sung K, Brown LR, Crawford TJ, Yu S, et al. Spectral line parameters including line shapes in the $2\nu_3$ Q branch of $^{12}CH_4$. J Quant Spectrosc Radiat Transf 2016;177:152–69. doi:10.1016/j.jqsrt.2015.12.009. XVIIIth Symposium on High Resolution Molecular Spectroscopy (HighRus-2015), Tomsk, Russia

[293] Nikitin A, Lyulin O, Mikhailenko S, Perevalov V, Filippov N, Grigoriev I, et al. Gosat-2014 methane spectral line list. J Quant Spectrosc Radiat Transf 2015;154:63–71. doi:10.1016/j.jqsrt.2014.12.003.

[294] Kocheril PA, Markus CR, Esposito AM, Schrader AW, Dieter TS, McCall BJ. Extended sub-Doppler resolution spectroscopy of the ν_3 band of methane. J Quant Spectrosc Radiat Transf 2018;215:9–12. doi:10.1016/J.JQSRT.2018.04.033.

[295] Gotti R, Prevedelli M, Kassi S, Marangoni M, Romanini D. Feed-forward coherent link from a comb to a diode laser: application to widely tunable cavity ring-down spectroscopy. J Chem Phys 2018;148(5):054202. doi:10.1063/1.5018611.

[296] Kiseleva M, Mandon J, Persijn S, Harren F. Accurate measurements of line strengths and air-broadening coefficients in methane around 1.66 μm using cavity ring down spectroscopy. J Quant Spectrosc Radiat Transf 2019;224:9–17. doi:10.1016/J.JQSRT.2018.10.040.

[297] Yang L, Lin H, Plimmer M, Feng X, Zhang J. Lineshape test on overlapped transitions (R9F1, R9F2) of the $2\nu_3$ band of $^{12}CH_4$ by frequency-stabilized cavity ring-down spectroscopy. J Quant Spectrosc Radiat Transf 2018;210:82–90. doi:10.1016/J.JQSRT.2018.02.019.

[298] Ghysels M, Mondelain D, Kassi S, Nikitin A, Rey M, Campargue A. The methane absorption spectrum near 1.73 μm (5695-5850 cm^{-1}): empirical line lists at 80 K and 296 K and rovibrational assignments. J Quant Spectrosc Radiat Transf 2018;213:169–77. doi:10.1016/J.JQSRT.2018.04.007.

[299] Starikova E, Sung K, Nikitin AV, Rey M. Assignment and modeling of the $^{13}CH_4$ cold absorption spectrum in the 5471–5852 cm^{-1} spectral range. J Quant Spectrosc Radiat Transf 2019;235:278–86. doi:10.1016/J.JQSRT.2019.06.002.

[300] Panda B, Maithani S, Pradhan M. High-resolution investigation of temperature and pressure-induced spectroscopic parameters of ^{13}C-isotopomer of CH_4 in the ν_4 band using cavity ring-down spectroscopy. Chem Phys 2020;535:110769. doi:10.1016/j.chemphys.2020.110769.

[301] Campargue A, Karlovets E, Starikova E, Sidorenko A, Mondelain D. The absorption spectrum of $^{13}CH_4$ in the 1.58 μm transparency window (6147–6653 cm^{-1}). J Quant Spectrosc Radiat Transf 2020;244:106842. doi:10.1016/j.jqsrt.2020.106842.

[302] Yang L, Lin H, Plimmer M, Feng X-J, Ma Y-J, Luo J-T, et al. Measurement of the spectral line positions in the $2\nu_3$ R(6) manifold of methane. J Quant Spectrosc Radiat Transf 2020;245:106888. doi:10.1016/j.jqsrt.2020.106888.

[303] Foltynowicz A, Rutkowski L, Silander I, Johansson AC, Silva de Oliveira V, Axner O, et al. Measurement and assignment of double-resonance transitions to the 8900-9100- cm^{-1} levels of methane. Phys Rev A 2021;103(2):022810. doi:10.1103/PhysRevA.103.022810.

[304] Konefał M, Ghysels M, Mondelain D, Kassi S, Campargue A. The absorption spectrum of $^{13}CH_4$ at 80 K and 296 K near 1.73 μm. J Mol Spectrosc 2018;351:14–20. doi:10.1016/j.jms.2018.06.003.

[305] Nikitin A, Thomas X, Daumont L, Rey M, Sung K, Toon G, et al. Assignment and modelling of $^{12}CH_4$ spectra in the 5550-5695, 5718-5725 and 5792–5814 cm^{-1} regions. J Quant Spectrosc Radiat Transf 2018;219:323–32. doi:10.1016/J.JQSRT.2018.08.006.

[306] Koshelev M, Vilkov I, Egorov O, Nikitin A, Rey M. High-sensitivity measurements of $^{12}CH_3D$ pure rotational lines in ground and excited vibrational states in the subTHz region. J Quant Spectrosc Radiat Transf 2020;242:106781. doi:10.1016/j.jqsrt.2019.106781.

[307] Bray C, Cuisset A, Hindle F, Bocquet R, Mouret G, Drouin BJ. $^{12}CH_3D$ photomixing spectroscopy up to 2.5 THz: new set of rotational and dipole parameters, first THz self-broadening measurements. J Quant Spectrosc Radiat Transf 2017;189:198–205. doi:10.1016/j.jqsrt.2016.11.011.

[308] Bray C, Cuisset A, Hindle F, Bocquet R, Mouret G, Drouin BJ. Corrigendum to "$^{12}CH_3D$ photomixing spectroscopy up to 2.5 THz: new set of rotational and dipole parameters, first THz self-broadening measurements" [Journal of Quantitative Spectroscopy and Radiative Transfer 189 (2017) 198-205]. J Quant Spectrosc Radiat Transf 2020;241:106758. doi:10.1016/j.jqsrt.2019.106758.

[309] Rey M, Nikitin AV, Tyuterev VG. Accurate theoretical methane line lists in the infrared up to 3000 K and Quasi-continuum absorption/emission modeling for astrophysical applications. Astrophys J 2017;847(2). doi:10.3847/1538-4357/aa8909.

[310] Rey M, Nikitin AV, Babikov YL, Tyuterev VG. TheoReTS - an information system for theoretical spectra based on variational predictions from molecular potential energy and dipole moment surfaces. J Mol Spectrosc 2016;327:138–58. doi:10.1016/j.jms.2016.04.006.

[311] Gordon IE, Kassi S, Campargue A, Toon GC. First identification of the $a^1\Delta_g$–$X^3\Sigma_g^-$ electric quadrupole transitions of oxygen in solar and laboratory spectra. J Quant Spectrosc Radiat Transf 2010;111(9):1174–83. doi:10.1016/j.jqsrt.2010.01.008.

[312] Wunch D, Toon GC, Blavier J-FL, Washenfelder RA, Notholt J, Connor BJ, et al. The total carbon column observing network. Philos Trans R Soc A Math Phys Eng Sci 2011;369(1943):2087–112. doi:10.1098/rsta.2010.0240.

[313] Sun K, Gordon IE, Sioris CE, Liu X, Chance K, Wofsy SC. Reevaluating the use of O_2 $a^1\Delta_g$ band in spaceborne remote sensing of greenhouse gases. Geophys Res Lett 2018;45(11):5779–87. doi:10.1029/2018GL077823.

[314] Pasternak F, Georges L, Pascal V, Bernard P. The microcarb instrument. In: Karafolas N, Cugny B, Sodnik Z, editors. Proceedings of the international conference on space optics ' ICSO 2016, 10562. SPIE; 2017. p. 258. ISBN 9781510616134. doi:10.1117/12.2296225.

[315] Gordon IE, Kassi S, Mondelain D, Campargue A, Fleurbaey H, Hodges JT. Generalized model for magnetic dipole and electric quadrupole transitions of molecular oxygen at 1.27 μm. J Quant Spectrosc Radiat Transf 2021;In Preparation.

[316] Mishra A, Balasubramanian T, Shetty B. Generalized electric quadrupole branch linestrengths for the infrared atmospheric oxygen bands. J Quant Spectrosc Radiat Transf 2011;112(14):2303–9. doi:10.1016/j.jqsrt.2011.05.013.

[317] Konefał M, Kassi S, Mondelain D, Campargue A. High sensitivity spectroscopy of the O_2 band at 1.27 μm: (I) pure O_2 line parameters above 7920 cm^{-1}. J Quant Spectrosc Radiat Transf 2020;241:106653. doi:10.1016/j.jqsrt.2019.106653.

[318] Tran DD, Tran H, Vasilchenko S, Kassi S, Campargue A, Mondelain D. High sensitivity spectroscopy of the O_2 band at 1.27 μm: (II) air-broadened line profile parameters. J Quant Spectrosc Radiat 2020;240:106673. doi:10.1016/j.jqsrt.2019.106673.

[319] Mendonca J, Strong K, Wunch D, Toon GC, Long DA, Hodges JT, et al. Using a speed-dependent Voigt line shape to retrieve O_2; from total carbon column observing network solar spectra to improve measurements of XCO_2. Atmos Meas Tech 2019;12(1):35–50. doi:10.5194/amt-12-35-2019.

[320] Balasubramanian TK, Bellary VP. Intensity distribution in the rotational structure of $^1\Delta - ^3\Sigma$ and $^1\Pi - ^3\Sigma$ transitions in diatomic molecules. Acta Phys Hung 1988;63(3):249. doi:10.1007/BF03156015.

[321] Yu S, Drouin BJ, Miller CE. High resolution spectral analysis of oxygen. IV. Energy levels, partition sums, band constants, RKR potentials, Franck-Condon factors involving the $X^3\Sigma^-_g$, $a^1\Delta_g$ and $b^1\Sigma^+_g$ states. J Chem Phys 2014;141(17). doi:10.1063/1.4900510.

[322] Hobbs JM, Drouin BJ, Oyafuso F, Payne VH, Gunson MR, McDuffie J, et al. Spectroscopic uncertainty impacts on OCO-2/3 retrievals of XCO_2. J Quant Spectrosc Radiat Transf 2020;257. doi:10.1016/j.jqsrt.2020.107360.

[323] Payne VH, Drouin BJ, Oyafuso F, Kuai L, Fisher BM, Sung K, et al. Absorption coefficient (ABSCO) tables for the orbiting carbon observatories: version 5.1. J Quant Spectrosc Radiat Transf 2020;255. doi:10.1016/j.jqsrt.2020.107217.

[324] Lunny EM. High-resolution photoacoustic spectroscopy of the oxygen a-band. California Institute of Technology; 2020. Ph.D. thesis. https://resolver.caltech.edu/CaltechTHESIS:06082020-132244698

[325] Robichaud DJ, Hodges JT, Brown LR, Lisak D, Maslowski P, Yeung LY, et al. Experimental intensity and lineshape parameters of the oxygen A-band using frequency-stabilized cavity ring-down spectroscopy. J Mol Spectrosc 2008;248(1):1–13. doi:10.1016/j.jms.2007.10.010.

[326] Long DA, Havey DK, Okumura M, Miller CE, Hodges JT. O_2 A-band line parameters to support atmospheric remote sensing. J Quant Spectrosc Radiat Transf 2010;111(14):2021–36. doi:10.1016/j.jqsrt.2010.05.011.

[327] Drouin BJ, Benner DC, Brown LR, Cich MJ, Crawford TJ, Devi VM, et al. Multispectrum analysis of the oxygen A-band. J Quant Spectrosc Radiat Transf 2017;186(SI):118–38. doi:10.1016/j.jqsrt.2016.03.037.

[328] Payne VH, Drouin BJ, Oyafuso F, Kuai L, Fisher BM, Sung K, et al. Corrigendum to "Absorption coefficient (ABSCO) tables for the orbiting carbon observatories: version 5.1" [J. Quant. Spectrosc. Radiat. Transf. 255 (2020) 107217]. J Quant Spectrosc Radiat Transf 2020;257. doi:10.1016/j.jqsrt.2020.107333.

[329] Domysławska J, Wójtewicz S, Masłowski P, Cygan A, Bielska K, Trawiński RS,

et al. Spectral line shapes and frequencies of the molecular oxygen B-band R-branch transitions. J Quant Spectrosc Radiat Transf 2015;155:22–31. doi:10.1016/j.jqsrt.2014.12.015.
[330] Domysławska J, Wójtewicz S, Masłowski P, Cygan A, Bielska K, Trawiński RS, et al. A new approach to spectral line shapes of the weak oxygen transitions for atmospheric applications. J Quant Spectrosc Radiat Transf 2016;169:111–21. doi:10.1016/j.jqsrt.2015.10.019.
[331] Sung K, Wishnow EH, Crawford TJ, Nemchick D, Drouin BJ, Toon GC, et al. FTS measurements of O_2 collision-induced absorption in the 565-700 nm region using a high pressure gas absorption cell. J Quant Spectrosc Radiat Transf 2019;235:232–43. doi:10.1016/j.jqsrt.2019.06.016.
[332] Fanjoux G, Millot G, Saint-Loup R, Chaux R, Rosenmann L. Coherent anti-Stokes Raman spectroscopy study of collisional broadening in the O_2-H_2O Q-branch. J Chem Phys 1994;101(2):1061–71. doi:10.1063/1.467803.
[333] Vess EM, Wallace CJ, Campbell HM, Awadalla VE, Hodges JT, Long DA, et al. Measurement of H_2O Broadening of O_2 A-band transitions and implications for atmospheric remote sensing. J Phys Chem A 2012;116(16):4069–73. doi:10.1021/jp301194j.
[334] Drouin BJ, Payne V, Oyafuso F, Sung K, Mlawer E. Pressure broadening of oxygen by water. J Quant Spectrosc Radiat Transf 2014;133:190–8. doi:10.1016/j.jqsrt.2013.08.001.
[335] Koshelev MA, Vilkov IN, Tretyakov MY. Pressure broadening of oxygen fine structure lines by water. J Quant Spectrosc Radiat Transf 2015;154:24–7. doi:10.1016/j.jqsrt.2014.11.019.
[336] Delahaye T, Landsheere X, Pangui E, Huet F, Hartmann JM, Tran H. Measurements of H_2O-broadening coefficients of O_2 A-band lines. J Quant Spectrosc Radiat Transf 2016;184:316–21. doi:10.1016/j.jqsrt.2016.07.019.
[337] Koshelev M, Vilkov I, Makarov D, Tretyakov M, Rosenkranz P. Speed-dependent broadening of the O_2 fine-structure lines. J Quant Spectrosc Radiat Transf 2021;264:107546. doi:10.1016/j.jqsrt.2021.107546.
[338] Crutzen PJ. The role of NO and NO_2 in the chemistry of the troposphere and stratosphere. Ann Rev Earth Planet Sci 1979;7:443. doi:10.1146/annurev.ea.07.050179.002303.
[339] Logan JA. Nitrogen oxides in the troposphere: global and regional budgets. J Geophys Res 1983;88(C15) 10,785–10,807. doi:10.1029/JC088iC15p10785.
[340] Gardner JL, Funke B, Mlynczak MG, López-Puertas M, Martin-Torres FJ, Russell JM, et al. Comparison of nighttime nitric oxide 5.3 μm emissions in the thermosphere measured by MIPAS and SABER. J Geophys Res (Space Phys) 2007;112(A10). doi:10.1029/2006JA011984.
[341] Wong A, Yurchenko SN, Bernath P, Müller HSP, McConkey S, Tennyson J. ExoMol line list - XXI. Nitric oxide (NO). Mon Not R Astron Soc 2017;470:882–97. doi:10.1093/mnras/stx1211.
[342] Tennyson J, Yurchenko SN. ExoMol: molecular line lists for exoplanet and other atmospheres. Mon Not R Astron Soc 2012;425:21–33. doi:10.1111/j.1365-2966.2012.21440.x.
[343] Yurchenko SN, Lodi L, Tennyson J, Stolyarov AV. DUO: a general program for calculating spectra of diatomic molecules. Comput Phys Commun 2016;202:262–75. doi:10.1016/j.cpc.2015.12.021.
[344] Müller HSP, Kobayashi K, Takahashi K, Tomaru K, Matsushima F. Terahertz spectroscopy of $N^{18}O$ and isotopic invariant fit of several nitric oxide isotopologs. J Mol Spectrosc 2015;310:92–8. doi:10.1016/j.jms.2014.12.002.
[345] Spencer MN, Chackerian C, Giver LP, Brown LR. The nitric oxide fundamental band: frequency and shape parameters for rovibrational lines. J Mol Spectrosc 1994;165(2):506–24. doi:10.1006/jmsp.1994.1154.
[346] Hartmann JM, Boulet C. Line shape parameters for HF in a bath of argon as a test of classical path models. J Chem Phys 2000;113:9000–10. doi:10.1063/1.1319346.
[347] Heinrich K, Fritsch T, Hering P, Mürtz M. Infrared laser-spectroscopic analysis of ^{14}NO and ^{15}NO in human breath. Appl Phys B Lasers Opt 2009;95(2):281–6. doi:10.1007/s00340-009-3423-1.
[348] Qu Q, Cooper B, Yurchenko SN, Tennyson J. A spectroscopic model for the low-lying electronic states of NO. J Chem Phys 2021;154(7):074112. doi:10.1063/5.0038527.
[349] Qu Q, Yurchenko SN, Tennyson J. ExoMol molecular line lists – XLII: rovibronic molecular line list for the low-lying states of NO. Mon Not R Astron Soc 2021;504:5768–77. doi:10.1093/mnras/stab1154.
[350] Carn SA, Fioletov VE, Mclinden CA, Li C, Krotkov NA. A decade of global volcanic SO_2 emissions measured from space. Sci Rep 2017;7(1):1–12. doi:10.1038/srep44095.
[351] Lin CK, Lin RT, Chen PC, Wang P, De Marcellis-Warin N, Zigler C, et al. A global perspective on sulfur oxide controls in coal-fired power plants and cardiovascular disease. Sci Rep 2018;8(1):2611. doi:10.1038/s41598-018-20404-2.
[352] Vandaele AC, Korablev O, Belyaev D, Chamberlain S, Evdokimova D, Encrenaz T, et al. Sulfur dioxide in the venus atmosphere: I. Vertical distribution and variability. Icarus 2017;295:16–33. doi:10.1016/j.icarus.2017.05.003.
[353] Encrenaz T, Greathouse TK, Richter MJ, Lacy JH, Fouchet T, Bézard B, et al. A stringent upper limit to SO_2 in the Martian atmosphere. Astron Astrophys 2011;530:37. doi:10.1051/0004-6361/201116820.
[354] Krasnopolsky VA. Search for methane and upper limits to ethane and SO_2 on Mars. Icarus 2012;217(1):144–52. doi:10.1016/j.icarus.2011.10.019.
[355] Loftus K, Wordsworth RD, Morley CV. Sulfate aerosol hazes and SO_2 gas as constraints on rocky exoplanets' surface liquid water. Astrophys J 2019;887(2):231. doi:10.3847/1538-4357/ab58cc.
[356] Webster CR, Blacksberg J, Christensen LE, Flesch GJ, Forouhar S, Briggs R, et al. Digital tunable laser spectrometer for venus atmospheric isotope ratios. In: Venus science priorities for laboratory measurements, 1838; 2015. p. 4012.
[357] Huang X, Schwenke DW, Lee TJ. Quantitative validation of Ames IR intensity and new line lists for $^{32/33/34}S^{16}O_2$, $^{32}S^{18}O_2$ and $^{16}O^{32}S^{18}O$. J Quant Spectrosc Radiat Transf 2019;225:327–36. doi:10.1016/j.jqsrt.2018.11.039.
[358] Naumenko OV, Horneman V-M. $^{32}S^{16}O_2$ line list; 2019. Private communication
[359] Tóbiás R, Furtenbacher T, Császár AG, Naumenko OV, Tennyson J, Flaud J-M, et al. Critical evaluation of measured rotational-vibrational transitions of four sulphur isotopologues of $S^{16}O_2$. J Quant Spectrosc Radiat Transf 2018;208:152–63. doi:10.1016/j.jqsrt.2018.01.006.
[360] Huang X, Schwenke DW, Lee TJ. Highly accurate potential energy surface, dipole moment surface, rovibrational energy levels, and infrared line list for $^{32}S^{16}O_2$ up to 8000 cm^{-1}. J Chem Phys 2014;140(11). doi:10.1063/1.4868327.
[361] Huang X, Schwenke DW, Lee TJ. Empirical infrared line lists for five SO_2 isotopologues: $^{32/33/34/36}S^{16}O_2$ and $^{32}S^{18}O_2$. J Mol Spectrosc 2015;311:19–24. doi:10.1016/j.jms.2015.01.010.
[362] Huang X, Schwenke DW, Lee TJ. Ames $^{32}S^{16}O^{18}O$ line list for high-resolution experimental IR analysis. J Mol Spectrosc 2016;330:101–11. doi:10.1016/j.jms.2016.08.013.
[363] Huang X, Schwenke DW, Lee TJ. Isotopologue consistency of semi-empirically computed infrared line lists and further improvement for rare isotopologues: CO_2 and SO_2 case studies. J Quant Spectrosc Radiat Transf 2019;230:222–46. doi:10.1016/j.jqsrt.2019.03.002.
[364] Huang X, Schwenke DW, Lee TJ. Exploring the limits of the data-model-theory synergy: "Hot" MW transitions for rovibrational IR studies. J Mol Struct 2020;1217:128260. doi:10.1016/j.molstruc.2020.128260.
[365] Underwood DS, Tennyson J, Yurchenko SN, Huang X, Schwenke DW, Lee TJ, et al. ExoMol molecular line lists - XIV. The rotation-vibration spectrum of hot SO_2. Mon Not R Astron Soc 2016;459(4):3890–9. doi:10.1093/mnras/stw849.
[366] Ulenikov O, Bekhtereva E, Horneman V-M, Alanko S, Gromova O. High resolution study of the $3\nu_1$ band of SO_2. J Mol Spectrosc 2009;255(2):111–21. doi:10.1016/j.jms.2009.03.009.
[367] Ulenikov O, Bekhtereva E, Alanko S, Horneman V, Gromova O, Leroy C. On the high resolution spectroscopy and intramolecular potential function of SO_2. J Mol Spectrosc 2009;257(2):137–56. doi:10.1016/j.jms.2009.07.005.
[368] Ulenikov O, Bekhtereva E, Gromova O, Alanko S, Horneman V-M, Leroy C. Analysis of highly excited 'hot' bands in the SO_2 molecule: $\nu_2 + 3\nu_3 - \nu_2$ and $2\nu_1 + \nu_2 + \nu_3 - \nu_2$. Mol Phys 2010;108(10):1253–61. doi:10.1080/00268970903468297.
[369] Ulenikov O, Gromova O, Bekhtereva E, Bolotova I, Leroy C, Horneman V-M, et al. High resolution study of the $\nu_1+2\nu_2-\nu_2$ and $2\nu_2+\nu_3-\nu_2$ "hot" bands and ro-vibrational re-analysis of the $\nu_1+\nu_2/\nu_2+\nu_3/3\nu_2$ polyad of the $^{32}SO_2$ molecule. J Quant Spectrosc Radiat Transf 2011;112(3):486–512. doi:10.1016/j.jqsrt.2010.09.013.
[370] Ulenikov O, Gromova O, Bekhtereva E, Bolotova I, Konov I, Horneman V-M, et al. High resolution analysis of the SO_2 spectrum in the 2600-2900 cm^{-1} region: $2\nu_3$, $\nu_2+2\nu_3-\nu_2$ and $2\nu_1+\nu_2$ bands. J Quant Spectrosc Radiat Transf 2012;113(7):500–17. doi:10.1016/j.jqsrt.2012.01.006.
[371] Ulenikov O, Onopenko G, Gromova O, Bekhtereva E, Horneman V-M. Re-analysis of the (100), (001), and (020) rotational structure of SO_2 on the basis of high resolution FTIR spectra. J Quant Spectrosc Radiat Transf 2013;130:220–32. doi:10.1016/j.jqsrt.2013.04.011.
[372] Ulenikov O, Gromova O, Bekhtereva E, Belova A, Bauerecker S, Maul C, et al. High resolution analysis of the (111) vibrational state of SO_2. J Quant Spectrosc Radiat Transf 2014;144:1–10. doi:10.1016/j.jqsrt.2014.03.027.
[373] Ulenikov O, Bekhtereva E, Gromova O, Berezkin K, Horneman V, Sydow C, et al. First high resolution analysis of the $3\nu_2$ and $3\nu_2 - \nu_2$ bands of $^{32}S^{16}O_2$. J Quant Spectrosc Radiat Transf 2017;202:1–5. doi:10.1016/j.jqsrt.2017.07.012.
[374] Blake T, Flaud J-M, Lafferty W. First analysis of the rotationally-resolved ν_2 and $2\nu_2-\nu_2$ bands of sulfur dioxide, $^{33}S^{16}O_2$. J Mol Spectrosc 2017;333:19–22. doi:10.1016/j.jms.2016.12.011.
[375] Flaud J-M, Blake T, Lafferty W. First high-resolution analysis of the ν_1, ν_3 and $\nu_1 + \nu_3$ bands of sulphur dioxide $^{33}S^{16}O_2$. Mol Phys 2017;115(4):447–53. doi:10.1080/00268976.2016.1269966.
[376] Ulenikov O, Gromova O, Bekhtereva E, Fomchenko A, Sydow C, Bauerecker S. First high resolution analysis of the $3\nu_1$ band of $^{34}S^{16}O_2$. J Mol Spectrosc 2016;319:50–4. doi:10.1016/j.jms.2015.11.002.
[377] Ulenikov O, Bekhtereva E, Gromova O, Buttersack T, Sydow C, Bauerecker S. High resolution FTIR study of $^{34}S^{16}O_2$: The bands $2\nu_1$, $\nu_1 +\nu_3$, $\nu_1 +\nu_2 +\nu_3 -\nu_2$ and $\nu_1 +\nu_2 +\nu_3$. J Quant Spectrosc Radiat Transf 2016;169:49–57. doi:10.1016/j.jqsrt.2015.09.015.
[378] Ulenikov O, Gromova O, Bekhtereva E, Krivchikova Y, Sklyarova E, Buttersack T, et al. High resolution FTIR study of $^{34}S^{16}O_2$: the bands $2\nu_3$, $2\nu_1 +\nu_2$ and $2\nu_1 +\nu_2 -\nu_2$. J Mol Spectrosc 2015;318:26–33. doi:10.1016/j.jms.2015.09.009.
[379] Ulenikov O, Bekhtereva E, Gromova O, Buttersack T, Sydow C, Bauerecker S. High resolution FTIR study of $^{34}S^{16}O_2$: re-analysis of the bands $\nu_1 +\nu_2$, $\nu_2 +\nu_3$, and first analysis of the hot band $2\nu_2 +\nu_3 -\nu_2$. J Mol Spectrosc 2016;319:17–25. doi:10.1016/j.jms.2015.11.003.
[380] Ulenikov O, Bekhtereva E, Krivchikova Y, Zamotaeva V, Buttersack T, Sydow C, et al. Study of the high resolution spectrum of $^{32}S^{16}O^{18}O$: The ν_1 and ν_3 bands. J Quant Spectrosc Radiat Transf 2016;168:29–39. doi:10.1016/j.jqsrt.2015.08.010.
[381] Ulenikov O, Bekhtereva E, Gromova O, Zamotaeva V, Kuznetsov S, Sydow C,

et al. High resolution study of the rotational structure of doubly excited vibrational states of $^{32}S^{16}O^{18}O$: The first analysis of the $2\nu_1$, $\nu_1+\nu_3$, and $2\nu_3$ bands. J Quant Spectrosc Radiat Transf 2017;189:344–50. doi:10.1016/j.jqsrt.2016.12.019.

[382] O. N. Ulenikov, O. V. Gromova, E. S. Bekhtereva, A. G. Ziatkova, E. A. Sklyarova, S. I. Kuznetsov, C. Sydow and S. Bauerecker. First rotational analysis of the (111) and (021) vibrational state of $S^{16}O^{18}O$ from the "hot" $\nu_1+\nu_2+\nu_3-\nu_2$ and $2\nu_2+\nu_3-\nu_2$ bands. J Quant Spectrosc Radiat Transf 2017;202:98–103. doi:10.1016/j.jqsrt.2017.07.029.

[383] Ulenikov ON, Bekhtereva ES, Gromova OV, Horneman VM, Sydow C, Bauerecker S. High resolution FTIR spectroscopy of sulfur dioxide in the 1550-1950 cm^{-1} region: First analysis of the $\nu_1+\nu_2/\nu_2+\nu_3$ bands of $^{32}S^{16}O^{18}O$ and experimental line intensities of ro-vibrational transitions in the $\nu_1+\nu_2/\nu_2+\nu_3$ bands of $^{32}S^{16}O_2$, $^{34}S^{16}O_2$, $^{32}S^{18}O_2$ and $^{32}S^{16}O^{18}O$. J Quant Spectrosc Radiat Transf 2017;203:377–91. doi:10.1016/j.jqsrt.2017.02.005.

[384] Gueye F, Manceron L, Perrin A, Tchana FK, Demaison J. First far-infrared high-resolution analysis of the ν_2 band of sulphur dioxide $^{32}S^{16}O^{18}O$ and $^{32}S^{18}O_2$. Mol Phys 2016;114(19):2769–76. doi:10.1080/00268976.2016.1154619.

[385] Müller HS. Online EH(CDMS) model data for the $^{34}S^{16}O_2$ isotopologue; 2008. https://cdms.astro.uni-koeln.de/classic/predictions/daten/SO2/34SO2/s34.par

[386] Flaud J-M. Private email communications; 2018.

[387] Lafferty W, Flaud J-M, Ngom EHA, Sams R. $^{34}S^{16}O_2$: high-resolution analysis of the (030), (101), (111), (002) and (201) vibrational states; determination of equilibrium rotational constants for sulfur dioxide and anharmonic vibrational constants. J Mol Spectrosc 2009;253(1):51–4. doi:10.1016/j.jms.2008.09.006.

[388] Vasilenko IA, Naumenko OV, Horneman V-M. Expert list of absorption lines of the SO_2 molecule in the 2000-3000 cm^{-1} spectral region, 33; 2020. p. 443–8. doi:10.1134/S1024856020050188.

[389] Naumenko OV, Vasilenko IA, Horneman V-M. High-resolution FTIR spectrum of SO_2 molecule in the region of the $2\nu_1+\nu_3$ band 2019;Book of abstracts:74.

[390] Borkov YG, Lyulin OM, Petrova TM, Solodov AM, Solodov AA, Deichuli VM, et al. CO_2-broadening and shift coefficients of sulfur dioxide near 4 μm. J Quant Spectrosc Radiat Transf 2019;225:119–24. doi:10.1016/j.jqsrt.2018.12.030.

[391] Tan Y, Kochanov RV, Rothman LS, Gordon IE. The broadening coefficients of SO_2. In: Proceedings of the towards HITRAN 2016; 2016. p. 2. doi:10.5281/zenodo.163447.

[392] Hargreaves RJ, Bernath PF, Bailey J, Dulick M. Empirical line lists and absorption cross sections for methane at high temperatures. Astrophys J 2015;813(1). doi:10.1088/0004-637X/813/1/12.

[393] Wilzewski JS, Gordon IE, Kochanov RV, Hill C, Rothman LS. H_2, He, and CO_2 line-broadening coefficients, pressure shifts and temperature-dependence exponents for the HITRAN database. Part 1: SO_2, NH_3, HF, HCl, OCS and C_2H_2. J Quant Spectrosc Radiat Transf 2016;168:193–206. doi:10.1016/j.jqsrt.2015.09.003.

[394] Dudaryonok A, Lavrentieva N. Theoretical estimation of SO_2 line broadening coefficients induced by carbon dioxide in the 150–300 K temperature range. J Quant Spectrosc Radiat Transf 2018;219:360–5. doi:10.1016/J.JQSRT.2018.08.022.

[395] Vinken GCM, Boersma KF, Maasakkers JD, Adon M, Martin RV. Worldwide biogenic soil NO_x emissions inferred from OMI NO_2 observations. Atmos Chem Phys 2014;14(18):10363–81. doi:10.5194/acp-14-10363-2014.

[396] Anenberg SC, Henze DK, Tinney V, Kinney PL, Raich W, Fann N, et al. Estimates of the global burden of ambient $PM_{2.5}$, ozone, and NO_2 on asthma incidence and emergency room visits. Environ Health Perspect 2018;126(10):107004. doi:10.1289/EHP3766.

[397] Misra P, Takigawa M, Khatri P, Dhaka SK, Dimri AP, Yamaji K, et al. Nitrogen oxides concentration and emission change detection during COVID-19 restrictions in North India. Sci Rep 2021;11. doi:10.1038/s41598-021-87673-2.

[398] Lukashevskaya AA, Lavrentieva NN, Dudaryonok AC, Perevalov VI. NDSD-1000: high-resolution, high-temperature nitrogen dioxide spectroscopic databank. J Quant Spectrosc Radiat Transf 2016;184:205–17. doi:10.1016/j.jqsrt.2016.07.014.

[399] Lukashevskaya AA, Lavrentieva NN, Dudaryonok AS, Perevalov VI. Corrected version of the NDSD-1000 databank. J Quant Spectrosc Radiat Transf 2017;202:37. doi:10.1016/j.jqsrt.2017.07.011.

[400] Perrin A, Kassi S, Campargue A. First high-resolution analysis of the $4\nu_1+\nu_3$ band of nitrogen dioxide near 1.5 μm. J Quant Spectrosc Radiat Transf 2010;111:2246–55. doi:10.1016/j.jqsrt.2010.03.004.

[401] Naumenko OV, Lukashevskaya AA, Kassi S, Béguier S, Campargue A. The $\nu_1+3\nu_3$ absorption band of nitrogen dioxide ($^{14}N^{16}O_2$) by CRDS near 6000 cm^{-1}. J Quant Spectrosc Radiat Transf 2019;232:146–51. doi:10.1016/j.jqsrt.2019.04.029.

[402] Lukashevskaya AA, Naumenko OV, Mondelain D, Kassi S, Campargue A. High sensitivity cavity ring down spectroscopy of the $3\nu_1+3\nu_2+\nu_3$ band of NO_2 near 7587 cm^{-1}. J Quant Spectrosc Radiat Transf 2016;177:225–33. doi:10.1016/j.jqsrt.2015.12.017.

[403] Lukashevskaya AA, Naumenko OV, Kassi S, Campargue A. First detection and analysis of the $3\nu_1+\nu_2+\nu_3$ band of NO_2 by CRDS near 6156 cm^{-1}. J Mol Spectrosc 2017;338:91–6. doi:10.1016/j.jms.2017.06.005.

[404] Lukashevskaya AA, Kassi S, Campargue A, Perevalov VI. High sensitivity cavity ring down spectroscopy of the $4\nu_3$ band of NO_2 near 1.59 μm. J Quant Spectrosc Radiat Transf 2017;202:302–7. doi:10.1016/j.jqsrt.2017.07.024.

[405] Lukashevskaya AA, Kassi S, Campargue A, Perevalov VI. High sensitivity cavity ring down spectroscopy of the $2\nu_1+3\nu_2+\nu_3$ band of NO_2 near 1.57 μm. J Quant Spectrosc Radiat Transf 2017;200:17–24. doi:10.1016/j.jqsrt.2017.05.017.

[406] Lukashevskaya AA, Mondelain D, Campargue A, Perevalov VI. High sensitivity cavity ring down spectroscopy of the $\nu_1+4\nu_3$ band of NO_2 near 1.34 μm. J Quant Spectrosc Radiat Transf 2018;219:393–8. doi:10.1016/j.jqsrt.2018.07.021.

[407] Lukashevskaya AA, Naumenko OV, Perrin A, Mondelain D, Kassi S, Campargue A. High sensitivity cavity ring down spectroscopy of NO_2 between 7760 and 7917 cm^{-1}. J Quant Spectrosc Radiat Transf 2013;130:249–59. doi:10.1016/j.jqsrt.2013.06.026.

[408] Mondelain D, Perrin A, Kassi S, Campargue A. First high-resolution analysis of the $5\nu_3$ band of nitrogen dioxide near 1.3 μm. J Quant Spectrosc Radiat Transf 2012;113(11):1058–65. doi:10.1016/j.jqsrt.2011.10.005.

[409] Bykov AD, Lavrentieva NN, Sinitsa LN. Semi-empiric approach to the calculation of H_2O and CO_2 line broadening and shifting. Mol Phys 2004;102(14):1653–8. doi:10.1080/00268970410001725765.

[410] Dudaryonok AS, Lavrentieva NN, Q M. The average energy difference method for calculation of line broadening of asymmetric tops. Atmos Ocean Opt 2015;28:503–9. doi:10.1134/S1024856015060056.

[411] Dana V, Mandin JY, Allout MY, Perrin A, Régalia L, Barbe A, et al. Broadening parameters of NO_2 lines in the 3.4 μm spectral region. J Quant Spectrosc Radiat Transf 1997;57(4):445–57. doi:10.1016/S0022-4073(96)00161-6.

[412] Benner DC, Blake TA, Brown LR, Malathy Devi V, Smith MAH, Toth RA. Air-broadening parameters in the ν_3 band of $^{14}N^{16}O_2$ using a multispectrum fitting technique. J Mol Spectrosc 2004;228(2):593–619. doi:10.1016/j.jms.2004.07.006.

[413] Perrin A, Manceron L, Flaud J-M, Kwabia-Tchana F, Armante R, Roy P, et al. The new nitrogen dioxide (NO_2) linelist in the GEISA database and first identification of the $\nu_1+2\nu_3-\nu_3$ band of $^{14}N^{16}O_2$. J Mol Spectrosc 2021;376:111394. doi:10.1016/j.jms.2020.111394.

[414] Orphal J, Perrin A, Flaud JM, Smirnov M, Himmelmann S, Voigt S, et al. New high-resolution analysis of the ν_3 band of the $^{15}N^{16}O_2$ isotopomer of nitrogen dioxide by fourier transform spectroscopy. J Mol Spectrosc 2000;204(1):72–9. doi:10.1006/jmsp.2000.8190.

[415] Perrin A, Toon G, Orphal J. Detection of atmospheric $^{15}NO_2$ in the ν_3 spectral region (6.3 μm). J Quant Spectrosc Radiat Transf 2015;154:91–7. doi:10.1016/j.jqsrt.2014.12.006.

[416] Perrin A, Flaud JM, Camy-Peyret C, Vasserot AM, Guelachvili G, Goldman A, et al. The ν_1, $2\nu_2$, and ν_3 interacting bands of $^{14}N^{16}O_2$: line positions and intensities. J Mol Spectrosc 1992;154(2):391–406. doi:10.1016/0022-2852(92)90217-C.

[417] Gamache RR, Vispoel B, Rey M, Nikitin A, Tyuterev V, Egorov O, et al. Total internal partition sums for the HITRAN2020 database. J Quant Spectrosc Radiat Transf 2021:107713. doi:10.1016/j.jqsrt.2021.107713.

[418] Jacquinet-Husson N, Armante R, Scott NA, Chédin A, Crépeau L, Boutammine C, et al. The 2015 edition of the GEISA spectroscopic database. J Mol Spectrosc 2016;327:31–72. doi:10.1016/j.jms.2016.06.007.

[419] Erisman JW, Sutton MA, Galloway J, Klimont Z, Winiwarter W. How a century of ammonia synthesis changed the world. Nat Geosci 2008;1(10):636–9. doi:10.1038/ngeo325.

[420] Aneja VP, Schlesinger WH, Li Q, Nahas A, Battye WH. Characterization of the global sources of atmospheric ammonia from agricultural soils. J Geophys Res Atmos 2020;125(3). doi:10.1029/2019JD031684.

[421] Lutsch E, Strong K, Jones DBA, Ortega I, Hannigan JW, Dammers E, et al. Unprecedented atmospheric ammonia concentrations detected in the high arctic from the 2017 Canadian wildfires. J Geophys Res Atmos 2019;124(14):8178–202. doi:10.1029/2019JD030419.

[422] Van Damme M, Clarisse L, Whitburn S, Hadji-Lazaro J, Hurtmans D, Clerbaux C, et al. Industrial and agricultural ammonia point sources exposed. Nature 2018;564(7734):99–103. doi:10.1038/s41586-018-0747-1.

[423] Tournadre B, Chelin P, Ray M, Cuesta J, Kutzner RD, Landsheere X, et al. Atmospheric ammonia (NH_3) over the Paris megacity: 9 years of total column observations from ground-based infrared remote sensing. Atmos Meas Tech 2020;13(7):3923–37. doi:10.5194/amt-13-3923-2020.

[424] Dammers E, McLinden CA, Griffin D, Shephard MW, Van Der Graaf S, Lutsch E, et al. NH_3 emissions from large point sources derived from CrIS and IASI satellite observations. Atmos Chem Phys 2019;19(19) 12 261–12 293. doi:10.5194/acp-19-12261-2019.

[425] Clarisse L, Van Damme M, Gardner W, Coheur PF, Clerbaux C, Whitburn S, et al. Atmospheric ammonia (NH_3) emanations from lake Natron's saline mudflats. Sci Rep 2019;9. doi:10.1038/s41598-019-39935-3.

[426] Guillot T, Stevenson DJ, Atreya SK, Bolton SJ, Becker HN. Storms and the depletion of ammonia in Jupiter: I. Microphysics of "Mushballs". J Geophys Res Planets 2020;125(8). doi:10.1029/2020JE006403.

[427] Guillot T, Li C, Bolton SJ, Brown ST, Ingersoll AP, Janssen MA, et al. Storms and the depletion of ammonia in Jupiter: II. Explaining the juno observations. J Geophys Res Planets 2020;125(8). doi:10.1029/2020JE006404.

[428] Canty JI, Lucas PW, Yurchenko SN, Tennyson J, Leggett SK, Tinney CG, et al. Methane and ammonia in the near-infrared spectra of late-T dwarfs. Mon Not R Astron Soc 2015;450(1):454–80. doi:10.1093/mnras/stv586.

[429] MacDonald RJ, Madhusudhan N. HD 209458b in new light: evidence of nitrogen chemistry, patchy clouds and sub-solar water. Mon Not R Astron Soc 2017;469(2):1979–96. doi:10.1093/mnras/stx804.

[430] Coles PA, Ovsyannikov RI, Polyansky OL, Yurchenko SN, Tennyson J. Improved potential energy surface and spectral assignments for ammonia in

the near-infrared region. J Quant Spectrosc Radiat Transf 2018;219:199–212. doi:10.1016/j.jqsrt.2018.07.022.
[431] Coles PA, Yurchenko SN, Tennyson J. ExoMol molecular line lists - XXXV. A rotation-vibration line list for hot ammonia. Mon Not R Astron Soc 2019;490(4):4638–47. doi:10.1093/mnras/stz2778.
[432] Yurchenko SN, Barber RJ, Tennyson J. A variationally computed hot line list for NH_3. Mon Not R Astron Soc 2011;413:1828–34. doi:10.1111/j.1365-2966.2011.18261.x.
[433] Furtenbacher T, Coles PA, Tennyson J, Yurchenko SN, Yu S, Drouin B, et al. Empirical rovibrational energy levels of ammonia up to 7500 cm^{-1}. J Quant Spectrosc Radiat Transf 2020;251. doi:10.1016/j.jqsrt.2020.107027.
[434] Beale CA, Hargreaves RJ, Coles P, Tennyson J, Bernath PF. Infrared absorption spectra of hot ammonia. J Quant Spectrosc Radiat Transf 2017;203:410–16. doi:10.1016/j.jqsrt.2017.02.012.
[435] Beale CA, Hargreaves RJ, Coles P, Tennyson J, Bernath PF. Erratum to "Infrared absorption spectra of hot ammonia" [J Quant Spectrosc Radiat Transf 203 (2017) 410-416]. J Quant Spectrosc Radiat Transf 2020;245. doi:10.1016/j.jqsrt.2020.106870.
[436] Beale CA, Wong A, Bernath P. Infrared transmission spectra of hot ammonia in the 4800-9000 cm^{-1} region. J Quant Spectrosc Radiat Transf 2020;246. doi:10.1016/j.jqsrt.2020.106911.
[437] Cacciani P, Čermák P, Béguier S, Campargue A. The absorption spectrum of ammonia between 5650 and 6350 cm^{-1}. J Quant Spectrosc Radiat Transf 2021;258. doi:10.1016/j.jqsrt.2020.107334.
[438] Vander Auwera J, Vanfleteren T. Line positions and intensities in the 7400–8600 cm^{-1} region of the ammonia spectrum. J Quant Spectrosc Radiat Transf 2018;116:3621–30. doi:10.1080/00268976.2018.1467054.
[439] Sung K, Yu S, Pearson J, Pirali O, Kwabia Tchana F, Manceron L. Far-infrared $^{14}NH_3$ line positions and intensities measured with a FT-IR and AILES beamline, synchrotron SOLEIL. J Mol Spectrosc 2016;327:1–20. doi:10.1016/j.jms.2016.06.011.
[440] Sung K, Brown LR, Huang X, Schwenke DW, Lee TJ, Coy SL, et al. Extended line positions, intensities, empirical lower state energies and quantum assignments of NH_3 from 6300 to 7000 cm^{-1}. J Quant Spectrosc Radiat Transf 2012;113(11):1066–83. doi:10.1016/j.jqsrt.2012.02.037.
[441] Barton EJ, Yurchenko SN, Tennyson J, Béguier S, Campargue A. A near infrared line list for NH_3: analysis of a Kitt Peak spectrum after 35 years. J Mol Spectrosc 2016;325:7–12. doi:10.1016/j.jms.2016.05.001.
[442] Yurchenko SN. A theoretical room-temperature line list for $^{15}NH_3$. J Quant Spectrosc Radiat Transf 2015;152:28–36. doi:10.1016/j.jqsrt.2014.10.023.
[443] Nemtchinov V. Measurements of line intensities and half-widths in the 10-μm bands of $^{14}NH_3$. J Quant Spectrosc Radiat Transf 2004;83(3-4):243–65. doi:10.1016/S0022-4073(02)00354-0.
[444] Skinner FM, Hargreaves RJ, Gordon IE. Modeling planetary opacities with HITRAN and HAPI: test case of ammonia microwave absorption spectra under jovian condition. In: Proceedings of the AGU fall meeting abstracts; 2020. p. A076–08.
[445] Mills E, Corby J, Clements A, Butterfield N, Jones P, Cunningham M, et al. A centimeter-wave study of methanol and ammonia isotopologues in Sgr B2 (N): physical and chemical differentiation between two hot cores. Astrophys J 2018;869(2):121. doi:10.3847/1538-4357/aaed3f.
[446] Canè E, Di Lonardo G, Fusina L, Tamassia F, Predoi-Cross A. The $\nu_2 = 1, 2$ and $\nu_4 = 1$ bending states of $^{15}NH_3$ and their analysis at experimental accuracy. J Chem Phys 2019;150(19). doi:10.1063/1.5088751.
[447] Canè E, Lonardo GD, Fusina L, Tamassia F, Predoi-Cross A. Spectroscopic characterization of the $\nu_2 = 3$ and $\nu_2 = \nu_4 = 1$ states for $^{15}NH_3$ from high resolution infrared spectra. J Quant Spectrosc Radiat Transf 2020;250. doi:10.1016/j.jqsrt.2020.106987.
[448] Pearson JC, Yu S, Pirali O. Modeling the spectrum of the $2\nu_2$ and ν_4 states of ammonia to experimental accuracy. J Chem Phys 2016;145(12):124301. doi:10.1063/1.4961656.
[449] Pearson J, Yu S, Pearson J, Sung K, Drouin B, Pirali O. Extended measurements and an experimental accuracy effective hamiltonian model for the $3\nu_2$ and $\nu_4 + \nu_2$ states of ammonia. J Mol Spectrosc 2018;353:60–6. doi:10.1016/j.jms.2018.09.004.
[450] Zobov NF, Bertin T, Vander Auwera J, Civis S, Knizek A, Ferus M, et al. The spectrum of ammonia near 0.793 μm. J Quant Spectrosc Radiat Transf 2021. This issue
[451] Zobov NF, Coles PA, Ovsyannikov RI, Kyuberis AA, Hargreaves RJ, Bernath PF, et al. Analysis of the red and green optical absorption spectrum of gas phase ammonia. J Quant Spectrosc Radiat Transf 2018;209:224–31. doi:10.1016/j.jqsrt.2018.02.001.
[452] Irwin PGJ, Bowles N, Braude AS, Garland R, Calcutt S, Coles PA, et al. Analysis of gaseous ammonia (NH_3) absorption in the visible spectrum of Jupiter - update. Icarus 2019;321:572–82. doi:10.1016/j.icarus.2018.12.008.
[453] Pickett HM, Drouin BJ, Canty T, Salawitch RJ, Fuller RA, Perun VS, et al. Validation of aura microwave limb sounder OH and HO_2 measurements. J Geophys Res Atmos 2008;113(D16). doi:10.1029/2007JD008775.
[454] Carlotti M, Ade PAR, Carli B, Chipperfield M, Hamilton PA, Mencaraglia F, et al. Diurnal variability and night detection of stratospheric hydroxyl radical from far infrared emission measurements. J Atmos Sol Terr Phys 2001;63(14):1509–18. doi:10.1016/S1364-6826(01)00030-X.
[455] Noll S, Winkler H, Goussev O, Proxauf B. OH level populations and accuracies of Einstein-A coefficients from hundreds of measured lines. Atmos Chem Phys 2020;20(9):5269–92. doi:10.5194/acp-20-5269-2020.
[456] Cheung R, Fai Li K, Wang S, Pongetti TJ, Cageao RP, Sander SP, et al. Atmospheric hydroxyl radical (OH) abundances from ground-based ultraviolet solar spectra: an improved retrieval method. Appl Opt 2008;47(33):6277. doi:10.1364/AO.47.006277.
[457] Asplund M, Grevesse N, Sauval AJ, Allende Prieto C, Kiselman D. Line formation in solar granulation. IV. [O I], O I and OH lines and the photospheric O abundance. Astron Astrophys 2004;417:751–68. doi:10.1051/0004-6361:20034328.
[458] Goicoechea JR, Joblin C, Contursi A, Berné O, Cernicharo J, Gerin M, et al. OH emission from warm and dense gas in the Orion Bar PDR. Astron Astrophys 2011;530. doi:10.1051/0004-6361/201116977.
[459] Maillard JP, Chauville J, Mantz AW. High-resolution emission spectrum of OH in an oxyacetylene flame from 3.7 to 0.9 μm. J Mol Spectrosc 1976;63(1):120–41. doi:10.1016/0022-2852(67)90139-7.
[460] Western CM. PGOPHER: a program for simulating rotational, vibrational and electronic spectra. J Quant Spectrosc Radiat Transf 2017;186:221–42. doi:10.1016/j.jqsrt.2016.04.010.
[461] Brooke JSA, Bernath PF, Western CM, Sneden C, Afşar M, Li G, et al. Line strengths of rovibrational and rotational transitions in the $X^2\Pi$ ground state of OH. J Quant Spectrosc Radiat Transf 2016;168:142–57. doi:10.1016/j.jqsrt.2015.07.021.
[462] Bernath PF, Colin R. Revised molecular constants and term values for the $X^2\Pi$ and $B^2\Sigma^+$ states of OH. J Mol Spectrosc 2009;257(1):20–3. doi:10.1016/j.jms.2009.06.003.
[463] Yousefi M, Bernath PF, Hodges J, Masseron T. A new line list for the $A^2\Sigma^+$–$X^2\Pi$ electronic transition of OH. J Quant Spectrosc Radiat Transf 2018;217:416–24. doi:10.1016/j.jqsrt.2018.06.016.
[464] Stark G, Brault JW, Abrams MC. Fourier-transform spectra of the $A^2\Sigma^+$–$X^2\Pi\Delta v = 0$ bands of OH and OD. J Opt Soc Am B Opt Phys 1994;11(1):3–32. doi:10.1364/JOSAB.11.000003.
[465] Fast A, Furneaux JE, Meek SA. Precision spectra of $A^2\Sigma^+$, $v' = 0 \leftarrow X^2\Pi_{3/2}$, $v'' = 0$, $J'' = 3/2$ transitions in ^{16}OH and ^{16}OD. Phys Rev A 2018;98(5). doi:10.1103/PhysRevA.98.052511.
[466] Le Roy RJ. LEVEL: a computer program for solving the radial Schrödinger equation for bound and quasibound levels. J Quant Spectrosc Radiat Transf 2017;186:167–78. doi:10.1016/j.jqsrt.2016.05.028.
[467] Bernath PF. MoLLIST: molecular line lists, intensities and spectra. J Quant Spectrosc Radiat Transf 2020;240. doi:10.1016/j.jqsrt.2019.106687.
[468] Gillis JR, Goldman A, Stark G, Rinsland CP. Line parameters for the $A^2\Sigma^+$–$X^2\Pi$ bands of OH. J Quant Spectrosc Radiat Transf 2001;68:225–30. doi:10.1016/S0022-4073(00)00011-X.
[469] Kremser S, Thomason LW, von Hobe M, Hermann M, Deshler T, Timmreck C, et al. Stratospheric aerosol—observations, processes, and impact on climate. Rev Geophys 2016;54(2):278–335. doi:10.1002/2015RG000511.
[470] Hofmann DJ. Increase in the stratospheric background sulfuric acid aerosol mass in the past 10 years. Science 1990;248:996–1000. doi:10.1126/science.248.4958.996.
[471] Chin M, Davis DD. A reanalysis of carbonyl sulfide as a source of stratospheric background sulfur aerosol. J Geophys Res Atmos 1995;100(D5):8993–9005. doi:10.1029/95JD00275.
[472] Taubman SJ, Kasting JF. Carbonyl sulfide: no remedy for global warming. Geophys Res Lett 1995;22(7):803–5. doi:10.1029/95GL00636.
[473] Bandy AR, Thornton DC, Johnson JE. Carbon disulfide measurements in the atmosphere of the western North Atlantic and the northwestern South Atlantic Oceans. J Geophys Res Atmos 1993;98(D12) 23 449–23 457. doi:10.1029/93JD02411.
[474] Brühl C, Lelieveld J, Crutzen PJ, Tost H. The role of carbonyl sulphide as a source of stratospheric sulphate aerosol and its impact on climate. Atmos Chem Phys 2012;12(3):1239–53. doi:10.5194/acp-12-1239-2012.
[475] Campbell JE, Whelan ME, Seibt U, Smith SJ, Berry JA, Hilton TW. Atmospheric carbonyl sulfide sources from anthropogenic activity: implications for carbon cycle constraints. Geophys Res Lett 2015;42(8):3004–10. doi:10.1002/2015GL063445.
[476] Kettle AJ, Kuhn U, von Hobe M, Kesselmeier J, Andreae MO. Global budget of atmospheric carbonyl sulfide: temporal and spatial variations of the dominant sources and sinks. J Geophys Res Atmos 2002;107(D22). doi:10.1029/2002JD002187.
[477] Krasnopolsky VA. High-resolution spectroscopy of Venus: detection of OCS, upper limit to H_2S, and latitudinal variations of CO and HF in the upper cloud layer. Icarus 2008;197(2):377–85. doi:10.1016/j.icarus.2008.05.020.
[478] Toon GC, Blavier J-FL, Sung K. Atmospheric carbonyl sulfide (OCS) measured remotely by FTIR solar absorption spectrometry. Atmos Chem Phys 2018;18(3):1923–44. doi:10.5194/acp-18-1923-2018.
[479] Brown L, Fayt A; 1997. Private Communication
[480] Hays BM, Guillaume T, Hearne TS, Cooke IR, Gupta D, Abdelkader Khedaoui O, et al. Design and performance of an E-band chirped pulse spectrometer for kinetics applications: OCS - He pressure broadening. J Quant Spectrosc Radiat Transf 2020;250. doi:10.1016/j.jqsrt.2020.107001.
[481] Mäder H, Ekkers J, Hoke W, Flygare WH. A π, τ, $\pi/2$ type pulse sequence method for the determination of T_1 in rotational transitions. J Chem Phys 1975;62(11):4380–7. doi:10.1063/1.430338.
[482] Story IC, Metchnik VI, Parsons RW. The measurement of the widths and pressure-induced shifts of microwave spectra lines. J Phys B Atom Mol Phys 1971;4(4):593–608. doi:10.1088/0022-3700/4/4/023.
[483] Broquier M, Picard-Bersellini A, Whitaker BJ, Green S. Rotational inelastic cross sections for OCS-Ar, OCS-He, OCS-H_2 collisions - a comparison between theory and experiment. J Chem Phys 1986;84:2104–7. doi:10.1063/1.450421.

[484] Jellali C, Dridi N, Maaroufi N, Kwabia Tchana F, Landsheere X, Aroui H. He-broadening coefficients and line intensities in the $2\nu_1$ band of carbonyl sulfide (OCS). J Mol Struct 2019;1180:747–53. doi:10.1016/j.molstruc.2018.12.028.
[485] Lavrentieva N, Dudaryonok A. OCS-CO2 line broadening coefficients and their temperature dependences for the Earth and Venus atmospheres. Icarus 2020;336:113452. doi:10.1016/J.ICARUS.2019.113452.
[486] Nerf RB. Pressure broadening and shift in the millimeter-wave spectrum of formaldehyde. J Mol Spectrosc 1975;58(3):451–73. doi:10.1016/0022-2852(75)90225-8.
[487] Barry HR, Corner L, Hancock G, Peverall R, Ranson TL, Ritchie GAD. Measurements of pressure broadening coefficients of selected transitions in the $2\nu_5$ band of formaldehyde. Phys Chem Chem Phys (Inc Faraday Trans) 2003;5(15):3106. doi:10.1039/B304139P.
[488] Wang L, Sharples TR. Intrapulse quantum cascade laser spectroscopy: pressure induced line broadening and shifting in the ν_6 band of formaldehyde. Appl Phys B Lasers Opt 2012;108(2):427–35. doi:10.1007/s00340-012-5085-7.
[489] Nadler S, Reuter DC, Daunt SJ. Tunable diode laser measurements of formaldehyde foreign-gas broadening parameters and line strengths in the 9-11 μm region. Appl Opt 1987;26(9):1641–6. doi:10.1364/AO.26.001641.
[490] Al-Derzi AR, Yurchenko SN, Tennyson J, Melosso M, Jiang N, Puzzarini C, et al. MARVEL analysis of the measured high-resolution spectra of formaldehyde. J Quant Spectrosc Radiat Transf 2021;266:107563. doi:10.1016/j.jqsrt.2021.107563.
[491] Al-Refaie AF, Yurchenko SN, Yachmenev A, Tennyson J. ExoMol line lists - VIII: a variationally computed line list for hot formaldehyde. Mon Not R Astron Soc 2015;448:1704–14. doi:10.1093/mnras/stv091.
[492] Hot D, Pedersen RL, Weng W, Zhang Y, Alden M, Li Z. Spatially and temporally resolved IR-DFWM measurement of HCN released from gasification of biomass pellets. Proc Combust Inst 2019;37:1337–44. doi:10.1016/j.proci.2018.07.105.
[493] Azhar M, Mandon J, Neerincx A, Liu Z, Mink J, Merkus P, et al. A widely tunable, near-infrared laser-based trace gas sensor for hydrogen cyanide (HCN) detection in exhaled breath. Appl Phys B 2017;123(11):1–7. doi:10.1007/s00340-017-6842-4.
[494] Lellouch E, Gurwell M, Butler B, Fouchet T, Lavvas P, Strobel D, et al. Detection of CO and HCN in Pluto's atmosphere with ALMA. Icarus 2017;286:289–307. doi:10.1016/j.icarus.2016.10.013.
[495] Tsiaras A, Rocchetto M, Waldmann IP, Venot O, Varley R, Morello G, et al. Detection of an atmosphere around the super-earth 55 Cancri e. Astrophys J 2016;820(2). doi:10.3847/0004-637X/820/2/99.
[496] Cordiner M, Palmer M, de Val-Borro M, Charnley S, Paganini L, Villanueva G, et al. ALMA autocorrelation spectroscopy of comets: the $HCN/H^{13}CN$ ratio in C/2012 S1 (ISON). Astrophys J Lett 2019;870(2):L26. doi:10.3847/2041-8213/aafb05.
[497] Barber RJ, Strange JK, Hill C, Polyansky OL, Mellau GC, Yurchenko SN, et al. ExoMol line lists – III. An improved hot rotation-vibration line list for HCN and HNC. Mon Not R Astron Soc 2014;437:1828–35. doi:10.1093/mnras/stt2011.
[498] Harris GJ, Polyansky OL, Tennyson J. Opacity data for HCN and HNC from a new*ab initio* linelist. Astrophys J 2002;578:657–63. doi:10.1086/342318.
[499] Mellau GC. Complete experimental rovibrational eigenenergies of HCN up to 6880 cm^{-1} above the ground state. J Chem Phys 2011;134:234303. doi:10.1063/1.3598942.
[500] Mellau GC, Makhnev VY, Gordon IE, Zobov NF, Tennyson J, Polyansky OL. An experimentally-accurate and complete room-temperature infrared HCN line-list for the HITRAN database. J Quant Spectrosc Radiat Transf 2021;270:107666. doi:10.1016/j.jqsrt.2021.107666.
[501] Maki A, Mellau GC, Klee S, Winnewisser M, Quapp W. High-temperature infrared measurements in the region of the bending fundamental of $H^{12}C^{14}N$, $H^{12}C^{15}N$, and $H^{13}C^{14}N$. J Mol Spectrosc 2000;202(1):67–82. doi:10.1006/jmsp.2000.8113.
[502] Maiwald F, Lewen F, Ahrens V, Beaky M, Gendriesch R, Koroliev A, et al. Pure rotational spectrum of HCN in the Terahertz region: use of a new planar Schottky diode multiplier. J Mol Spectrosc 2000;1(202):166–8. doi:10.1006/jmsp.2000.8118.
[503] Makhnev VY, Kyuberis AA, Polyansky OL, Mizus II, Tennyson J, Zobov NF. A new spectroscopically-determined potential energy surface and ab initio dipole moment surface for high accuracy HCN intensity calculations. J Mol Spectrosc 2018;353:40–53. doi:10.1016/j.jms.2018.09.002.
[504] Hofmann JP, Eifert B, Mellau GC. Near infrared emission spectrum of $H^{13}CN$. J Mol Spectrosc 2010;262(2):75–81. doi:10.1016/j.jms.2010.05.005.
[505] Guay P, Genest J, Fleisher AJ. Precision spectroscopy of $H^{13}CN$ using a free-running, all-fiber dual electro-optic frequency comb system. Opt Lett 2018;43(6):1407–10. doi:10.1364/OL.43.001407.
[506] Cohen JB, Wilson EB. Rotational energy transfer in pure HCN and in HCN-rare gas mixtures by microwave double resonance and pressure broadening. J Chem Phys 1973;58(2):442–55. doi:10.1063/1.1679224.
[507] Mehrotra SC, Mäder H, de Vreede JPM, Dijkerman HA. J-dependence of self-, H_2- and He-broadened linewidth parameters for l-type doublet transitions in the bending vibrational state (01^10) of HCN. Chem Phys 1985;93(1):115–25. doi:10.1016/0301-0104(85)85053-9.
[508] Lemaire V, Babay A, Lemoine B, Rohart F, Bouanich JP. Self- and foreign-gas-broadening and shifting of lines in the ν_2 band of HCN. J Mol Spectrosc 1996;177(1):40–5. doi:10.1006/jmsp.1996.0115.
[509] D'Eu JF, Lemoine B, Rohart F. Infrared HCN lineshapes as a test of Galatry and speed-dependent Voigt profiles. J Mol Spectrosc 2002;212(1):96–110. doi:10.1006/jmsp.2002.8520.
[510] Charròn M, Anderson TG, Steinfeld JI. Measurements of T_2 in excited vibrational states of HCN. J Chem Phys 1980;73(4):1494–7. doi:10.1063/1.440354.
[511] Landrain V, Blanquet G, Lepère M, Walrand J, Bouanich J-P. Diode-laser measurements of H_2-broadening coefficients in the ν_2 band of HCN. J Mol Spectrosc 1997;182(1):184–8. doi:10.1006/jmsp.1996.7223.
[512] Rohart F, Nguyen L, Buldyreva J, Colmont JM, Wlodarczak G. Lineshapes of the 172 and 602 GHz rotational transitions of $HC^{15}N$. J Mol Spectrosc 2007;246(2):213–27. doi:10.1016/j.jms.2007.09.009.
[513] Xiao Y, Jacob DJ, Turquety S. Atmospheric acetylene and its relationship with CO as an indicator of air mass age. J Geophys Res 2007;112(D12):D12305. doi:10.1029/2006JD008268.
[514] Nixon CA, Achterberg RK, Romani PN, Allen M, Zhang X, Teanby NA, et al. Abundances of Jupiter's trace hydrocarbons from Voyager and Cassini. Planet Space Sci 2010;58(13):1667–80. doi:10.1016/j.pss.2010.05.008.
[515] Orton GS, Aitken DK, Smith C, Roche PF, Caldwell J, Snyder R. The spectra of uranus and neptune at 8-14 and 17-23 μm. Icarus 1987;70(1):1–12. doi:10.1016/0019-1035(87)90070-4.
[516] Dinelli BM, López Puertas M, Fabiano F, Adriani A, Moriconi ML, Funke B, et al. Climatology of CH_4, HCN and C_2H_2 in Titan's upper atmosphere from Cassini/VIMS observations. Icarus 2019;331:83–97. doi:10.1016/j.icarus.2019.04.026.
[517] Amyay B, Fayt A, Herman M, Vander Auwera J. Vibration-rotation spectroscopic database on acetylene, $\tilde{X}^1\Sigma_g^+$ ($^{12}C_2H_2$). J Phys Chem Ref Data 2016;45(2). doi:10.1063/1.4947297.
[518] Lyulin OM, Perevalov VI. ASD-1000: High-resolution, high-temperature acetylene spectroscopic databank. J Quant Spectrosc Radiat Transf 2017;201:94–103. doi:10.1016/j.jqsrt.2017.06.032.
[519] Lyulin OM, Perevalov VI. Global modeling of vibration-rotation spectra of the acetylene molecule. J Quant Spectrosc Radiat Transf 2016;177:59–74. doi:10.1016/j.jqsrt.2015.12.021.
[520] Jacquemart D, Soulard P, Lyulin OM. Recommended acetylene $^{12}C_2H_2$ line list in 13.6 μm spectral region: new measurements and global modeling. J Quant Spectrosc Radiat Transf 2021;258. doi:10.1016/j.jqsrt.2020.107200.
[521] Lyulin OM, Campargue A. An empirical spectroscopic database for acetylene in the regions of 5850–6341 cm^{-1} and 7000–9415 cm^{-1}. J Quant Spectrosc Radiat Transf 2017;203:461–71. doi:10.1016/j.jqsrt.2017.01.036.
[522] Lyulin OM, Vander Auwera J, Campargue A. The Fourier transform absorption spectrum of acetylene between 7000 and 7500 cm^{-1}. J Quant Spectrosc Radiat Transf 2015;160:85–93. doi:10.1016/j.jqsrt.2015.03.018.
[523] Lyulin OM, Vander Auwera J, Campargue A. The Fourier transform absorption spectrum of acetylene between 8280 and 8700 cm^{-1}. J Quant Spectrosc Radiat Transf 2016;177:234–40. doi:10.1016/j.jqsrt.2015.11.026.
[524] Béguier S, Lyulin OM, Hu SM, Campargue A. Line intensity measurements for acetylene between 8980 and 9420 cm^{-1}. J Quant Spectrosc Radiat Transf 2017;189:417–20. doi:10.1016/j.jqsrt.2016.12.020.
[525] Lyulin OM, Campargue A, Mondelain D, Kassi S. The absorption spectrum of acetylene by CRDS between 7244 and 7918 cm^{-1}. J Quant Spectrosc Radiat Transf 2013;130:327–34. doi:10.1016/j.jqsrt.2013.04.028.
[526] Lyulin OM, Mondelain D, Béguier S, Kassi S, Vander Auwera J, Campargue A. High-sensitivity CRDS absorption spectroscopy of acetylene between 5851 and 6341 cm^{-1}. Mol Phys 2014;112(18):2433–44. doi:10.1080/00268976.2014.906677.
[527] Kassi S, Lyulin OM, Béguier S, Campargue A. New assignments and a rare peculiarity in the high sensitivity CRDS spectrum of acetylene near 8000 cm^{-1}. J Mol Spectrosc 2016;326:106–14. doi:10.1016/j.jms.2016.02.013.
[528] Lyulin O, Vasilchenko S, Mondelain D, Campargue A. The CRDS spectrum of acetylene near 1.73 μm. J Quant Spectrosc Radiat Transf 2019;234:147–58. doi:10.1016/j.jqsrt.2019.04.006.
[529] Lyulin OM, Campargue A. The absorption spectrum of acetylene near 1 μm (9280–10 740 cm^{-1}) (II): Line intensities. J Quant Spectrosc Radiat Transf 2018;215:51–8. doi:10.1016/j.jqsrt.2018.04.025.
[530] Lyulin OM, Béguier S, Hu SM, Campargue A. The absorption spectrum of acetylene near 1 μm (9280-10740 cm^{-1}) (I): line positions. J Quant Spectrosc Radiat Transf 2018;208:179–87. doi:10.1016/j.jqsrt.2018.01.007.
[531] Tennyson J, Yurchenko SN, Al-Refaie AF, Barton EJ, Chubb KL, Coles PA, et al. The ExoMol database: Molecular line lists for exoplanet and other hot atmospheres. J Mol Spectrosc 2016;327:73–94. doi:10.1016/j.jms.2016.05.002.
[532] Chubb KL, Tennyson J, Yurchenko SN. ExoMol molecular line lists - XXXVII. Spectra of acetylene. Mon Not R Astron Soc 2020;493(2):1531–45. doi:10.1093/mnras/staa229.
[533] Chubb KL, Joseph M, Franklin J, Choudhury N, Furtenbacher T, Császár AG, et al. MARVEL analysis of the measured high-resolution rovibrational spectra of C_2H_2. J Quant Spectrosc Radiat Transf 2018;204:42–55. doi:10.1016/j.jqsrt.2017.08.018.
[534] Sada PV, Mccabe GH, Bjoraker GL, Jennings DE, Reuter DC. ^{13}C-Ethane in the atmospheres of Jupiter and Saturn. Astrophys J 1996;472(2):903–7. doi:10.1086/178120.
[535] Flasar FM, Achterberg RK, Conrath BJ, Gierasch PJ, Kunde VG, Nixon CA, et al. Titan's atmospheric temperatures, winds, and composition. Science 2005;308(5724):975–8. doi:10.1126/science.1111150.
[536] Villanueva GL, Mumma MJ, Magee-Sauer K. Ethane in planetary and cometary atmospheres: transmittance and fluorescence models of the ν_7 band at 3.3 μm. J Geophys Res 2011;116(E08012):1–23. doi:10.1029/2010JE003794.

http://adsabs.harvard.edu/cgi-bin/nph-data_query?bibcode=2011JGRE..11608012V&link_type=ABSTRACT
[537] Pine AS, Lafferty WJ. Torsional splittings and assignments of the Doppler-limited spectrum of ethane in the C-H stretching region. J Res Natl Bureau Stand 1982;83(3):1–20.
[538] Lattanzi F, Di Lauro C, Vander Auwera J. Toward the understanding of the high resolution infrared spectrum of C_2H_6 near 3.3 μm. J Mol Spectrosc 2011;267:71–9. doi:10.1016/j.jms.2011.02.003.
[539] Radeva YL, Mumma MJ, Villanueva GL, A'Hearn MF. A newly developed fluorescence model for $C_2H_6\nu_5$ and application to cometary spectra acquired with NIRSPEC at Keck II. Astrophys J 2011;729(2):135. doi:10.1088/0004-637X/729/2/135. http://adsabs.harvard.edu/cgi-bin/nph-data_query?bibcode=2011ApJ...729..135R&link_type=ABSTRACT
[540] Pine AS, Lafferty WJ. Torsional splittings and assignments of the Doppler-limited spectrum of ethane in the C–H stretching region. J Res Natl Bureau Stand 1982;87:237–56. doi:10.6028/jres.087.017.
[541] Pine AS, Stone SC. Torsional tunneling and A_1–A_2 splittings and air broadening of the $^rQ_0$ and $^pQ_3$ subbranches of the ν_7 band of ethane. J Mol Spectrosc 1995;175:21–30. doi:10.1006/jmsp.1996.0004.
[542] Dang-Nhu M, Pine AS, Lafferty WJ. Intensities in the ν_5, ν_7, and $\nu_8 + \nu_{11}$ bands of ethane $^{12}C_2H_6$. Can J Phys 1984;62:512. doi:10.1139/p84-069. http://adsabs.harvard.edu/cgi-bin/nph-data_query?bibcode=1984CaJPh..62..512D&link_type=REFERENCES
[543] Harrison JJ, Allen NDC, Bernath PF. Infrared absorption cross sections for ethane (C_2H_6) in the 3 μm region. J Quant Spectrosc Radiat Transf 2010;111:357. doi:10.1016/j.jqsrt.2009.09.010. http://adsabs.harvard.edu/cgi-bin/nph-data_query?bibcode=2010JQSRT.111..357H&link_type=EJOURNAL
[544] Hargreaves RJ, Buzan E, Dulick M, Bernath PF. High-resolution absorption cross sections of C_2H_6 at elevated temperatures. Mol Astrophys 2015;1:20–5. doi:10.1016/j.molap.2015.09.001.
[545] Doney KD, Kofman V, Villanueva G, Sung K. A new model of monodeuterated ethane (C_2H_5D) spectrum: enabling sensitive constraints on the D/H in ethane emission in comets. J Quant Spectrosc Radiat Transf 2020;255. doi:10.1016/j.jqsrt.2020.107225.
[546] Sung K, Mantz AW, Smith MAH, Brown LR, Crawford TJ, Devi VM, et al. Cryogenic absorption cells operating inside a Bruker IFS-125HR: first results for $^{13}CH_4$ at 7 μm. J Mol Spectrosc 2010;262(2):122–34. doi:10.1016/j.jms.2010.05.004.
[547] Mantz AW, Sung K, Brown LR, Crawford TJ, Smith MAH, Malathy Devi V, et al. A cryogenic Herriott cell vacuum-coupled to a Bruker IFS-125HR. J Mol Spectrosc 2014;304:12–24. doi:10.1016/j.jms.2014.07.006.
[548] Devi VM, Rinsland CP, Benner DC, Sams RL, Blake TA. Multispectrum analysis of the ν_9 band of $^{12}C_2H_6$: Positions, intensities, self- and N_2-broadened half-width coefficients. J Quant Spectrosc Radiat Transf 2010;111:1234–51. doi:10.1016/j.jqsrt.2009.10.017.
[549] Malathy Devi V, Chris Benner D, Rinsland C, Smith M, Sams R, Blake T, et al. Multispectrum measurements of spectral line parameters including temperature dependences of N_2- and self-broadened half-width coefficients in the region of the ν_9 band of $^{12}C_2H_6$. J Quant Spectrosc Radiat Transf 2010;111(17):2481–504. doi:10.1016/j.jqsrt.2010.07.010.
[550] Moazzen-Ahmadi N, Norooz Oliaee J, Ozier I, Wishnow EH, Sung K, Crawford TJ, et al. An intensity study of the torsional bands of ethane at 35 μm. J Quant Spectrosc Radiat Transf 2015;151:123–32. doi:10.1016/j.jqsrt.2014.09.016.
[551] Pasek MA, Sampson JM, Atlas Z. Redox chemistry in the phosphorus biogeochemical cycle. Proc Natl Acad Sci 2014;111(43):15468–73. doi:10.1073/pnas.1408134111.
[552] Larson HP, Treffers RR, Fink U. Phosphine in Jupiter's atmosphere: the evidence from high-altitude observations at 5 micrometers. Astrophys J 1977;211:972–9. doi:10.1086/155009.
[553] Fletcher LN, Orton GS, Teanby NA, Irwin PGJ. Phosphine on Jupiter and Saturn from Cassini/CIRS. Icarus 2009;202(2):543–64. doi:10.1016/j.icarus.2009.03.023.
[554] Burgess JL, Burgess DJ. Phosphine exposure from a methamphetamine laboratory investigation. J Toxicol Clin Toxicol 2001;39(2):165–8. doi:10.1081/CLT-100103833.
[555] Sousa-Silva C, Seager S, Ranjan S, Petkowski JJ, Zhan Z, Hu R, et al. Phosphine as a biosignature gas in exoplanet atmospheres. Astrobiology 2020;20(2):235–68. doi:10.1089/ast.2018.1954.
[556] Greaves JS, Richards AMS, Bains W, Rimmer PB, Sagawa H, Clements DL, et al. Phosphine gas in the cloud decks of Venus. Nat Astron 2021;5:655–64. doi:10.1038/s41550-020-1174-4.
[557] Villanueva G., Cordiner M., Irwin P., de Pater I., Butler B., Gurwell M., et al. No phosphine in the atmosphere of Venus, *Nat Astron* **5**, 2021, 631–635, doi:10.1038/s41550-021-01422-z.
[558] Encrenaz T, Greathouse TK, Marcq E, Widemann T, Bézard B, Fouchet T, et al. A stringent upper limit of the PH_3 abundance at the cloud top of Venus. Astron Astrophys 2020;643. doi:10.1051/0004-6361/202039559.
[559] Snellen IAG, Guzman-Ramirez L, Hogerheijde MR, Hygate APS, van der Tak FFS. Re-analysis of the 267 GHz ALMA observations of Venus, no statistically significant detection of phosphine. Astron Astrophys 2020;644. doi:10.1051/0004-6361/202039717.
[560] Trompet L, Robert S, Mahieux A, Schmidt F, Erwin J, Vandaele AC. Phosphine in Venus' atmosphere: detection attempts and upper limits above the cloud top assessed from the SOIR/VEx spectra. Astron Astrophys 2021;645. doi:10.1051/0004-6361/202039932.
[561] Kleiner I, Devi VM. PH_3 line list; Private communication. 2018.
[562] Devi VM, Benner DC, Kleiner I, Sams RL, Fletcher LN. Line shape parameters of PH_3 transitions in the Pentad near 4-5 μm: self-broadened widths, shifts, line mixing and speed dependence. J Mol Spectrosc 2014;302:17–33. doi:10.1016/j.jms.2014.06.003.
[563] Devi VM, Kleiner I, Sams RL, Brown LR, Benner DC, Fletcher LN. Line positions and intensities of the phosphine (PH_3) pentad near 4.5 μm. J Mol Spectrosc 2014;298:11–23. doi:10.1016/j.jms.2014.01.013.
[564] Fusina L, Carlotti M. The far-infrared spectrum and spectroscopic parameters of PH_3 in the ground state. J Mol Spectrosc 1988;130(2):371–81. doi:10.1016/0022-2852(88)90083-5.
[565] Tarrago G, Lacome N, Lévy A, Guelachvili G, Bézard B, Drossart P. Phosphine spectrum at 4-5 μm: analysis and line-by-line simulation of $2\nu_2$, $\nu_2 + \nu_4$, $2\nu_4$, ν_1, and ν_3 bands. J Mol Spectrosc 1992;154(1):30–42. doi:10.1016/0022-2852(92)90026-K.
[566] Nikitin AV, Ivanova YA, Rey M, Tashkun SA, Toon GC, Sung K, et al. Analysis of PH_3 spectra in the Octad range 2733–3660 cm^{-1}. J Quant Spectrosc Radiat Transf 2017;203:472–9. doi:10.1016/j.jqsrt.2017.04.032.
[567] Nikitin AV, Champion JP, Butler RAH, Brown LR, Kleiner I. Global modeling of the lower three polyads of PH_3: preliminary results. J Mol Spectrosc 2009;256(1):4–16. doi:10.1016/j.jms.2009.01.008.
[568] Butler RAH, Sagui L, Kleiner I, Brown LR. The absorption spectrum of phosphine (PH_3) between 2.8 and 3.7 μm: Line positions, intensities, and assignments. J Mol Spectrosc 2006;238(2):178–92. doi:10.1016/j.jms.2006.04.021.
[569] Wang L, Chen P, Cheng G-S, Ding Y, Hu S-M. Absorption line intensities of phosphine in the regions 1950–2480 cm^{-1} and 3280–3580 cm^{-1} studied by Fourier-transform spectroscopy. Spectrosc Spectr Anal 2005;25(8):1221–6. http://europepmc.org/abstract/MED/16329485
[570] Rey M, Nikitin AV, Tyuterev VG. TheoReTS line list of PH_3; 2020.
[571] Watson JKG. Simplification of the molecular vibration-rotation Hamiltonian. Mol Phys 1968;15(5):479–90. doi:10.1080/00268976800101381.
[572] Nikitin AV, Holka F, Tyuterev VG, Fremont J. Vibration energy levels of the PH_3, PH_2D, and PHD_2 molecules calculated from high order potential energy surface. J Chem Phys 2009;130(24):244312. doi:10.1063/1.3156311.
[573] Rey M, Chizhmakova IS, Nikitin AV, Tyuterev VG. Understanding global infrared opacity and hot bands of greenhouse molecules with low vibrational modes from first-principles calculations: the case of CF_4. Phys Chem Chem Phys (Inc Faraday Trans) 2018;20(32):21008–33. doi:10.1039/C8CP03252A.
[574] Rey M, Nikitin AV, Tyuterev VG. Ab initio ro-vibrational Hamiltonian in irreducible tensor formalism: a method for computing energy levels from potential energy surfaces for symmetric-top molecules. Molecular Physics 2010;108(16):2121–35. doi:10.1080/00268976.2010.506892.
[575] Rey M, Nikitin AV, Tyuterev VG. Accurate first-principles calculations for $^{12}CH_3D$ infrared spectra from isotopic and symmetry transformations. J Chem Phys 2014;141(4). doi:10.1063/1.4890956.
[576] Nikitin AV, Rey M, Tyuterev VG. High order dipole moment surfaces of PH_3 and ab initio intensity predictions in the Octad range. J Mol Spectrosc 2014;305:40–7. doi:10.1016/j.jms.2014.09.010.
[577] Brown LR, Sams RL, Kleiner I, Cottaz C, Sagui L. Line intensities of the phosphine Dyad at 10 μm. J Mol Spectrosc 2002;215(2):178–203. doi:10.1006/jmsp.2002.8638.
[578] Sousa-Silva C, Al-Refaie AF, Tennyson J, Yurchenko SN. ExoMol line lists - VII. The rotation-vibration spectrum of phosphine up to 1500 K. Mon Not R Astron Soc 2015;446(3):2337–47. doi:10.1093/mnras/stu2246.
[579] Sousa-Silva C, Yurchenko SN, Tennyson J. A computed room temperature line list for phosphine. J Mol Spectrosc 2013;288:28–37. doi:10.1016/j.jms.2013.04.002.
[580] Bouanich J-P, Walrand J, Blanquet G. N_2-broadening coefficients in the ν_2 and ν_4 bands of PH_3. J Mol Spectrosc 2005;232(1):40–6. doi:10.1016/j.jms.2005.02.005.
[581] Bouanich J-P, Blanquet G. N_2-broadening coefficients in the ν_2 and ν_4 bands of PH_3 at low temperature. J Mol Spectrosc 2007;241(2):186–91. doi:10.1016/j.jms.2006.12.006.
[582] J.-P. Bouanich, J. Salem, H. Aroui, J. Walrand,G. Blanquet. H_2-broadening coefficients in the ν_2 and ν_4 bands of PH_3. J Quant Spectrosc Radiat Transf 2004;84:195–205. doi:10.1016/S0022-4073(03)00143-2.
[583] Salem J, Bouanich J-P, Walrand J, Aroui H, Blanquet G. Hydrogen line broadening in the ν_2 and ν_4 bands of phosphine at low temperature. J Mol Spectrosc 2004;228(1):23–30. doi:10.1016/j.jms.2004.06.015.
[584] Pickett HM, Poynter RL, Cohen EA. Pressure broadening of phosphine by hydrogen and helium. J Quant Spectrosc Radiat Transf 1981;26:197. doi:10.1016/0022-4073(81)90113-8.
[585] Sergent-Rozey M, Nguyen-van-Thanh, Rossi I, Lacome N, Levy A. Collisional broadening and line intensities in the pure rotational spectrum of PH_3. J Mol Spectrosc 1988;131(1):66–76. doi:10.1016/0022-2852(88)90107-5.
[586] Levy A, Lacome N, Tarrago G. Hydrogen- and Helium-broadening of phosphine lines. J Mol Spectrosc 1993;157(1):172–81. doi:10.1006/jmsp.1993.1014.
[587] Levy A, Lacome N, Tarrago G. Temperature dependence of collision-broadened lines of phosphine. J Mol Spectrosc 1994;166(1):20–31. doi:10.1006/jmsp.1994.1168.
[588] Salem J, Bouanich J-P, Walrand J, Aroui H, Blanquet G. Helium- and argon-broadening coefficients of phosphine lines in the ν_2 and ν_4 bands. J Mol Spectrosc 2005;232(2):247–54. doi:10.1016/j.jms.2005.04.014.
[589] Salem J, Blanquet G, Lepère M, Aroui H. H_2 line mixing coefficients in the ν_2 and ν_4 bands of PH_3. J Mol Spectrosc 2014;297:58–61. doi:10.1016/j.jms.2014.01.003.

[590] Barton EJ, Hill C, Czurylo M, Li HY, Hyslop A, Yurchenko SN, et al. The ExoMol pressure broadening diet: H_2 and He line-broadening parameters. J Quant Spectrosc Radiat Transf 2017;203:490–5. doi:10.1016/j.jqsrt.2017.01.028.

[591] Boulet C, Ma Q. Line shape parameters of PH_3 transitions: Theoretical studies of self-broadened widths and line mixing effects. J Chem Phys 2020;152(21):214305. doi:10.1063/5.0008535.

[592] Faye M, Boudon V, Loëte M, Roy P, Manceron L. The high overtone and combination levels of SF_6 revisited at Doppler-limited resolution: a global effective rovibrational model for highly excited vibrational states. J Quant Spectrosc Radiat Transf 2017;190:38–47. doi:10.1016/j.jqsrt.2017.01.006.

[593] Ke H, Boudon V, Richard C, Madhur V, Faye M, Manceron L. Analysis and modeling of combination bands of sulfur hexafluoride $^{32}SF_6$ based on global fits. Update of the SHeCaSDa database. J Mol Spectrosc 2020;368:111251. doi:10.1016/j.jms.2020.111251.

[594] Richard C, Boudon V, Rotger M. Calculated spectroscopic databases for the VAMDC portal: new molecules and improvements. J Quant Spectrosc Radiat Transf 2020;251:107096. doi:10.1016/j.jqsrt.2020.107096.

[595] Nikitin AV, Rey M, Chizhmakova IS, Tyuterev VG. First full-dimensional potential energy and dipole moment surfaces of SF 6. J Phys Chem A 2020;2020:7023. doi:10.1021/acs.jpca.0c02733.

[596] Rey M, Chizhmakova IS, Nikitin AV, Tyuterev VG. Towards a complete elucidation of the ro-vibrational band structure in the sf_6 infrared spectrum from full quantum-mechanical calculations. Phys Chem Chem Phys 2021;23(21):12115–26. doi:10.1039/d0cp05727d.

[597] Faye M, Manceron L, Roy P, Boudon V, Loëte M. First high resolution analysis of the ν_3 band of the $^{36}SF_6$ isotopologue. J Mol Spectrosc 2018;346:23–6. doi:10.1016/j.jms.2018.01.002.

[598] O. N. Ulenikov, E. S. Bekhtereva, O. V. Gromova, N. I. Raspopova, A. S. Belova, C. Maul, C. Sydow and S. Bauerecker. Experimental line strengths of the $5\nu_2$ band of $H_2^{32}S$ in comparison with the results of "variational" calculation and HITRAN database. J Quant Spectrosc Radiat Transf 2020;243:106812. doi:10.1016/j.jqsrt.2019.106812.

[599] Ulenikov ON, Bekhtereva ES, Gromova OV, Zhang F, Raspopova NI, Sydow C, et al. Ro-vibrational analysis of the first hexad of hydrogen sulfide: Line position and strength analysis of the $4\nu_2$ band of $H_2{}^{32}S$ and $H_2{}^{34}S$ for HITRAN applications. J Quant Spectrosc Radiat Transf 2020;255:107236. doi:10.1016/j.jqsrt.2020.107236.

[600] Chubb KL, Naumenko O, Keely S, Bartolotto S, MacDonald S, Mukhtar M, et al. MARVEL analysis of the measured high-resolution rovibrational spectra of H_2S. J Quant Spectrosc Radiat Transf 2018;218:178–86. doi:10.1016/j.jqsrt.2018.07.012.

[601] Azzam AAA, Yurchenko SN, Tennyson J, Naumenko OV. ExoMol line lists XVI: A Hot Line List for H_2S. Mon Not R Astron Soc 2016;460:4063–74. doi:10.1093/mnras/stw1133.

[602] Mouelhi M, Cuisset A, Hindle F, Jellali C, Galalou S, Aroui H, et al. Self and N_2 broadening coefficients of H_2S probed by submillimeter spectroscopy: comparison with IR measurements and semi-classical calculations. J Quant Spectrosc Radiat Transf 2020;247:106955. doi:10.1016/j.jqsrt.2020.106955.

[603] Waschull J, Kuhnemann F, Sumpf B. Self-, Air-, and Helium-Broadening in the ν_2 Band of H_2S. J Mol Spectrosc 1994;165(1):150–8. doi:10.1006/jmsp.1994.1117.

[604] Kissel A, Sumpf B, Kronfeldt HD, Tikhomirov BA, Ponomarev YN. Noble gas induced line-shift and line-broadening in the ν_2 band of H_2S. J Mol Struct 2000;517-518(1-3):477–92. doi:10.1016/S0022-2860(99)00270-7.

[605] Sumpf B, Meusel I, Kronfeldt HD. Noble gas broadening in fundamental bands of H_2S. J Mol Spectrosc 1997;184(1):51–5. doi:10.1006/jmsp.1997.7290.

[606] Starikov VI. Broadening of vibrational-rotational lines of the H_2S molecule by pressure of monatomic gases. Opt Spectrosc 2013;115(1):18–27. doi:10.1134/S0030400X13070187.

[607] Kissel A, Sumpf B, Kronfeldt HD, Tikhomirov BA, Ponomarev YN. Molecular-gas-pressure-induced line-shift and line-broadening in the ν_2 band of H_2S. J Mol Spectrosc 2002;216(2):345–54. doi:10.1006/jmsp.2002.8630.

[608] Starikov VI, Protasevich AE. Broadening of absorption lines of the ν_2 band of the H_2S molecule by the pressure of atmospheric gases. Opt Spectrosc 2006;101(4):523–31. doi:10.1134/S0030400X06100043.

[609] Franco B, Clarisse L, Stavrakou T, Müller J, Taraborrelli D, Hadji-Lazaro J, et al. Spaceborne measurements of formic and acetic acids: a global view of the regional sources. Geophys Res Lett 2020;47(4). doi:10.1029/2019GL086239.

[610] González Abad G, Bernath PF, Boone CD, McLeod SD, Manney GL, Toon GC. Global distribution of upper tropospheric formic acid from the ACE-FTS. Atmos Chem Phys 2009;9(20):8039–47. doi:10.5194/acp-9-8039-2009.

[611] Baskakov OI, Alekseev EA, Motiyenko RA, Lohilahti J, Horneman V-M, Alanko S, et al. FTIR and millimeter wave investigation of the 7^1 and 9^1 states of formic acid HCOOH and $H^{13}COOH$. J Mol Spectrosc 2006;240(2):188–201. doi:10.1016/j.jms.2006.09.001.

[612] Hull K, Wells T, Billinghurst BE, Bunn H, Raston PL. Synchrotron-based infrared spectroscopy of formic acid: confirmation of the reassignment of Fermi-coupled 8 μm states. AIP Adv 2019;9(1):015021. doi:10.1063/1.5063010.

[613] Perrin A, Vander Auwera J. An improved database for the 9 μ m region of the formic acid spectrum. J Quant Spectrosc Radiat Transf 2007;108(3):363–70. doi:10.1016/j.jqsrt.2007.05.002.

[614] Kochanov RV, Gordon IE, Rothman LS, Sharpe SW, Johnson TJ, Sams RL. Comment on "Radiative forcings for 28 potential Archean greenhouse gases" by Byrne and Goldblatt (2014). Clim Past Discuss 2015;11(3):1985–2007. doi:10.5194/cpd-11-1985-2015.

[615] Raballand W, Rotger M, Boudon V, Loëte M. Spectroscopy of $X_2Y_4(D_{2h})$ molecules : tensorial formalism adapted to the $O(3) \supset D_{2h}$ chain, Hamiltonian and transition moment operators. J Mol Spectrosc 2003;217(2):239–48. doi:10.1016/S0022-2852(02)00038-3.

[616] Rey M, Delahaye T, Nikitin AV, Tyuterev VG. First theoretical global line lists of ethylene ($^{12}C_2H_4$) spectra for the temperature range 50–700 K in the far-infrared for quantification of absorption and emission in planetary atmospheres. Astron Astrophys 2016;594:A47. doi:10.1051/0004-6361/201629004.

[617] Viglaska D, Rey M, Delahaye T, Nikitin AV. First-principles calculations of infrared spectra for three ethylene isotopologues: $^{13}C_2H_4$, $^{13}C^{12}CH_4$ and $^{12}C_2H_3D$. J Quant Spectrosc Radiat Transf 2019;230:142–54. doi:10.1016/J.JQSRT.2019.04.011.

[618] Viglaska D, Rey M, Nikitin AV, Tyuterev VG. Symmetry effects in rotationally resolved spectra of bi-deuterated ethylene: theoretical line intensities of cis, trans, and as-$C_2H_2D_2$ isotopomers. J Chem Phys 2019;150(19):194303. doi:10.1063/1.5096883.

[619] Rinsland CP, Malathy Devi V, Benner DC, Blake TA, Sams RL, Brown LR, et al. Multispectrum analysis of the ν_4 band of CH_3CN: Positions, intensities, self- and N_2-broadening, and pressure-induced shifts. J Quant Spectrosc Radiat 2008;109:974–94. doi:10.1016/j.jqsrt.2007.11.013.

[620] Müller HS, Belloche A, Lewen F, Drouin BJ, Sung K, Garrod RT, et al. Toward a global model of the interactions in low-lying states of methyl cyanide: rotational and rovibrational spectroscopy of the $\Delta\nu_4 = 1$ state and tentative interstellar detection of the $\Delta\nu_4 = \Delta\nu_8 = 1$ state In Sgr B2(N). J Mol Spectrosc 2021;378:111449. doi:10.1016/j.jms.2021.111449.

[621] Müller HSP, Brown LR, Drouin BJ, Pearson JC, Kleiner I, Sams RL, et al. Rotational spectroscopy as a tool to investigate interactions between vibrational polyads in symmetric top molecules: Low-lying states $\Delta\nu_8 \leq 2$ of methyl cyanide, CH_3CN. J Mol Spectrosc 2015;312:22–37. doi:10.1016/j.jms.2015.02.009.

[622] Carlos M, Gruson O, Richard C, Boudon V, Rotger M, Thomas X, et al. High-resolution spectroscopy and global analysis of CF_4 rovibrational bands to model its atmospheric absorption. J Quant Spectrosc Radiat Transf 2017;201:75–93. doi:10.1016/j.jqsrt.2017.06.039.

[623] Bizzocchi L, Tamassia F, Laas J, Giuliano BM, Esposti CD, Dore L, et al. Rotational and High-resolution Infrared Spectrum of HC_3N: global ro-vibrational analysis and improved line catalog for astrophysical observations. Astrophys J Suppl Ser 2017;233(1):11. doi:10.3847/1538-4365/aa9571.

[624] Thelen AE, Nixon CA, Chanover NJ, Cordiner MA, Molter EM, Teanby NA, et al. Abundance measurements of Titan's stratospheric HCN, HC_3N, C_3H_4, and CH_3CN from ALMA observations. Icarus 2019;319:417–32. doi:10.1016/j.icarus.2018.09.023.

[625] Villanueva GL, Magee-Sauer K, Mumma MJ. Modeling of nitrogen compounds in cometary atmospheres: fluorescence models of ammonia (NH_3), hydrogen cyanide (HCN), hydrogen isocyanide (HNC) and cyanoacetylene (HC_3N). J Quant Spectrosc Radiat Transf 2013;129:158–68. doi:10.1016/j.jqsrt.2013.06.010.

[626] Jiang XJ, Wang JZ, Gao Y, Gu QS. HC_3N observations of nearby galaxies. Astron Astrophys 2017;600:15. doi:10.1051/0004-6361/201629066.

[627] Tamassia F, Melosso M, Bizzocchi L, Canè E. The f HC_3N from 190 to 3360 cm^{-1} and global ro-vibrational analysis. J Quant Spectrosc Radiat Transf 2021;in Preparation.

[628] Jolly A, Benilan Y, Fayt A. New infrared integrated band intensities for HC_3N and extensive line list for the ν_5 and ν_6 bending modes. J Mol Spectrosc 2007;242(1):46–54. doi:10.1016/j.jms.2007.01.008. http://linkinghub.elsevier.com/retrieve/pii/S0022285207000252

[629] Miller-Ricci E, Seager S, Sasselov D. The atmospheric signatures of super-Earths: how to distinguish between hydrogen-rich and hydrogen-poor atmospheres. Astrophys J 2008;690:1056–67. doi:10.1088/0004-637x/690/2/1056.

[630] Wcisło P, Thibault F, Stolarczyk N, Jóźwiak H, Słowiński M, Gancewski M, et al. The first comprehensive dataset of beyond-Voigt line-shape parameters from ab initio quantum scattering calculations for the HITRAN database: He-perturbed H_2 case study. J Quant Spectrosc Radiat Transf 2021;260:107477. doi:10.1016/j.jqsrt.2020.107477.

[631] E. Roueff, H. Abgrall, P. Czachorowski, K. Pachucki, M. Puchalski, J. Komasa. The full infrared spectrum of molecular hydrogen. Astron Astrophys 2019;630:A58. doi:10.1051/0004-6361/201936249.

[632] Lu Z, Tabisz GC, Ulivi L. Temperature dependence of the pure rotational band of HD: interference, widths, and shifts. Phys Rev A 1993;47:1159–73. doi:10.1103/PhysRevA.47.1159.

[633] K. Sung, E. H. Wishnow, L. Manceron, B. Drouin, C. Nixon,. Progress report on the measurements of pressure-broadening of HD rotational transitions for Jovian atmospheres. Bull AAS 2020;52(6). https://baas.aas.org/pub/2020n6i103p06

[634] K. Sung, E. H. Wishnow, L. Manceron, B. Drouin, C. Nixon,. Laboratory study of HD R(0) - R(3) transitions broadened by H_2 for Jovian atmospheres. J Quant Spectrosc Radiat Transf 2021;In Preparation.

[635] Endres CP, Schlemmer S, Schilke P, Stutzki J, Müller HSP. The Cologne Database for Molecular Spectroscopy, CDMS, in the Virtual Atomic and Molecular Data Centre, VAMDC. J Mol Spectrosc 2016;327:95–104. doi:10.1016/j.jms.2016.03.005.

[636] Chandra S, Kegel WH, Le Roy RJ, Hertenstein T. Einstein A-coefficients for vib-rotational transitions in CS. Astron Astrophys Suppl 1995;114:175.

[637] Paulose G, Barton EJ, Yurchenko SN, Tennyson J. ExoMol molecular line lists - XII. Line lists for eight isotopologues of CS. Mon Not R Astron Soc 2015;454(2):1931–9. doi:10.1093/mnras/stv1543.

[638] Hou S, Wei Z. Line Lists for the $X^1\Sigma^+$ State of CS. Astrophys J Suppl Ser 2020;246(1). doi:10.3847/1538-4365/ab61ef.

[639] Sandor BJ, Todd Clancy R, Moriarty-Schieven G, Mills FP. Sulfur chemistry in the Venus mesosphere from SO_2 and SO microwave spectra. Icarus 2010;208(1):49–60. doi:10.1016/j.icarus.2010.02.013.

[640] de Kleer K, de Pater I, Ádámkovics M. Emission from volcanic SO gas on Io at high spectral resolution. Icarus 2019;317:104–20. doi:10.1016/J.ICARUS.2018.07.012.

[641] Boissier J, Bockelée-Morvan D, Biver N, Crovisier J, Despois D, Marsden BG, et al. Interferometric imaging of the sulfur-bearing molecules H_2S, SO, and CS in comet C/1995 O1 (Hale-Bopp). Astron Astrophys 2007;475(3):1131–44. doi:10.1051/0004-6361:20078380.

[642] Pickett HM. The fitting and prediction of vibration-rotation spectra with spin interactions. J Mol Spectrosc 1991;148:371–7. doi:10.1016/0022-2852(91)90393-O.

[643] Martin-Drumel MA, Hindle F, Mouret G, Cuisset A, Cernicharo J. A complete spectroscopic characterization of SO and its isotopologues up to the Terahertz domain. Astrophys J 2015;799(2):115. doi:10.1088/0004-637X/799/2/115.

[644] Lovas FJ, Suenram RD, Ogata T, Yamamoto S. Microwave spectra and electric dipole moments for low-J levels of interstellar radicals: SO, C2S, C3S, c-HC3, CH2CC, and c-C3H2. Astrophys J 1992;399:325. doi:10.1086/171928.

[645] Powell FX, Jr DRL. Microwave spectrum of the SO radical. J Chem Phys 2004;41(5):1413. doi:10.1063/1.1726082.

[646] Bernath PF, Johnson R, Liévin J. Line lists for the $b^1\Sigma^+$-$X^3\Sigma^-$ and $a^1\Delta$-$X^3\Sigma^-$ transitions of SO. J Quant Spectrosc Radiat Transf 2021;272. doi:10.1016/j.jqsrt.2021.107772.

[647] Setzer KD, Fink EH, Ramsay DA. High-Resolution Fourier-Transform Study of the $b^1\Sigma^+ \rightarrow X^3\Sigma^-$ and $a^1\Delta \rightarrow X^3\Sigma^-$ Transitions of SO. J Mol Spectrosc 1999;198(1):163–74. doi:10.1006/jmsp.1999.7943.

[648] Raddaoui E, Troitsyna L, Dudaryonok A, Soulard P, Guinet M, Aroui H, et al. Line parameters measurements and modeling for the ν_6 band of CH_3I: a complete line list for atmospheric databases. J Quant Spectrosc Radiat Transf 2019;232:165–79. doi:10.1016/J.JQSRT.2019.04.036.

[649] Papoušek D, Pracna P, Winnewisser M, Klee S, Demaison J. Simultaneous rovibrational analysis of the ν_2, ν_3, ν_5, and ν_6 bands of $H_3^{12}CF$. J Mol Spectrosc 1999;196:319–23. doi:10.1006/jmsp.1999.7875.

[650] Jacquemart D, Guinet M. Line parameters measurements and modeling for the ν_6 band of CH_3F: generation of a complete line list for atmospheric databases. J Quant Spectrosc Radiat Transf 2016;185:58–69. doi:10.1016/j.jqsrt.2016.08.010.

[651] Ramchani AB, Jacquemart D, Soulard P, Guinet M. Measurements and modeling of N_2-broadening coefficients for the ν_6 band of CH_3F, comparison with CH_3Br and CH_3Cl molecules. J Quant Spectrosc Radiat Transf 2016;185:58–69. doi:10.1016/j.jqsrt.2017.06.013.

[652] Adriani A, Bracco A, Grassi D, Moriconi ML, Mura A, Orton G, et al. Two-year observations of the Jupiter polar regions by JIRAM on board Juno. J Geophys Res Planets 2020;125. doi:10.1029/2019JE006098.

[653] Wenger C, Boudon V, Rotger M, Sanzharov JP, Champion JP. XTDS and SPVIEW: graphical tools for the analysis and simulation of high-resolution molecular spectra. J Mol Spectrosc 2008;251:102–13. doi:10.1016/j.jms.2008.01.011.

[654] Boudon V, Grigoryan T, Philipot F, Richard C, Kwabia Tchana F, Manceron L, et al. Line positions and intensities for the ν_3 band of 5 isotopologues of germane for planetary applications. J Quant Spectrosc Radiat Transf 2018;205:174–83. doi:10.1016/j.jqsrt.2017.10.017.

[655] C. Richard, V. Boudon, A. Rizopoulos, J. Vander Auwera and F. Kwabia Tchana. Line positions and intensities for the ν_2/ν_4 bands of 5 isotopologues of germane near 11.5 μm. J Quant Spectrosc Radiat Transf 2021;260:107474. doi:10.1016/j.jqsrt.2020.107474.

[656] Albert D, Antony BK, Ba YA, Babikov YL, Bollard P, Boudon V, et al. A decade with VAMDC: results and ambitions. Atoms 2020;8:76. doi:10.3390/atoms8040076.

[657] Ulenikov ON, Gromova OV, Bekhtereva ES, Raspopova NI, Kuznetsov AV, Sydow C, et al. High resolution analysis of GeH_4 in the dyad region: Rovibration energy structure of $^{70}GeH_4$ and line strengths of $^{M}GeH_4$ (M = 70, 72, 73, 74, 76). J Quant Spectrosc Radiat Transf 2019;236. doi:10.1016/j.jqsrt.2019.106581.

[658] Ulenikov ON, Gromova OV, Bekhtereva ES, Raspopova NI, Kuznetsov AV, Boudon V, et al. Comprehensive study of the pentad bending triad region of germane: positions, strengths, widths and shifts of lines in the $2\nu_2$, $\nu_2+\nu_4$ and $2\nu_4$ bands of $^{70}GeH_4$, $^{72}GeH_4$, $^{73}GeH_4$, $^{74}GeH_4$, $^{76}GeH_4$. J Quant Spectrosc Radiat Transf 2021;262. doi:10.1016/j.jqsrt.2021.107526.

[659] Calmonte U, Altwegg K, Balsiger H, Berthelier JJ, Bieler A, Cessateur G, et al. Sulphur-bearing species in the coma of comet 67P/Churyumov-Gerasimenko. Mon Not R Astron Soc 2016;462:S253–73. doi:10.1093/mnras/stw2601.

[660] Jackson WM, Scodinu A, Xu D, Cochran AL. Using the ultraviolet and visible spectrum of comet 122P/de vico to identify the parent molecule CS_2. Astrophys J 2004;607(2):L139–41. doi:10.1086/421995.

[661] Atreya SK, Edgington SG, Trafton LM, Caldwell JJ, Noll KS, Weaver HA. Abundances of ammonia and carbon disulfide in the Jovian stratosphere following the impact of comet Shoemaker-Levy 9. Geophys Res Lett 1995;22(12):1625–8. doi:10.1029/95GL01718.

[662] Chin M, Davis DD. Global sources and sinks of OCS and CS_2 and their distributions. Glob Biogeochem Cycles 1993;7(2):321–37. doi:10.1029/93GB00568.

[663] M.O. Andreae. Ocean-atmosphere interactions in the global biogeochemical sulfur cycle. Mar Chem 1990;30:1–29. doi:10.1016/0304-4203(90)90059-L.

[664] Beauchamp R, Bus J, Popp J, Boreiko C, Goldberg L. A critical review of the literature on carbon disulfide toxicity. Crit Rev Toxicol 1983;11(3):169–278. doi:10.3109/10408448309128255.

[665] S. Hernberg, T. Partanen, C. Nordman, P. Sumari. Coronary heart disease among workers exposed to carbon disulphide. Occup Environ Med 1970;27(4):313–25. doi:10.1136/oem.27.4.313.

[666] Karlovets EV, Gordon IE, Hashemi R, Kochanov RV, Hargreaves RJ, Rothman LS. Addition of the line list for carbon disulfide to the HITRAN database: line positions, intensities, and half-widths of the $^{12}C^{32}S_2$, $^{32}S^{12}C^{34}S$, $^{32}S^{12}C^{33}S$, and $^{13}C^{32}S_2$ isotopologues. J Quant Spectrosc Radiat Transf 2021;258. doi:10.1016/j.jqsrt.2020.107275.

[667] Karlovets EV, Gordon IE, Konnov D, Muraviev AV, Vodopyanov KL. Dual-comb laser spectroscopy of CS_2 near 4.6 μm. J Quant Spectrosc Radiat Transf 2020;256. doi:10.1016/j.jqsrt.2020.107269.

[668] Blanquet G, Walrand J, Blavier J-F, Bredohl H, Dubois I. Fourier transform infrared spectrum of CS_2: analysis of the $3\nu_3$ band. J Mol Spectrosc 1992;152(1):137–51. doi:10.1016/0022-2852(92)90124-7.

[669] Blanquet G, Walrand J, Bredohl H, Dubois I. High-resolution spectra of carbon disulfide $^{12}C^{32}S_2$ in the region of 2 μm. J Mol Spectrosc 1999;198(1):43–51. doi:10.1006/jmsp.1999.7932.

[670] Platz T, Matheis M, Hornberger C, Demtröder W. High-sensitivity overtone spectroscopy of carbon disulfide CS_2. J Mol Spectrosc 1996;180(1):81–4. doi:10.1006/jmsp.1996.0226.

[671] Person WB, Hall LC. Absolute infrared intensifies of CS_2 fundamentals in gas and liquid phases. An interpretation of the bond moments of CO_2 and CS_2. Spectrochim Acta 1964;20(5):771–9. doi:10.1016/0371-1951(64)80076-X.

[672] Montzka SA, Reimann S, Engel A, Krüger K, O'Doherty S, Sturges WT, et al. Scientific assessment of ozone depletion: Ozone-Depleting Substances (ODSs) and related chemicals. Global Ozone Research and Monitoring Project Report, Report No. 52. Geneva Switzerland: World Meterological Organization; 2011. ISBN 9966-7319-6-2

[673] Yokouchi Y, Nojiri Y, Toom-Sauntry D, Fraser P, Inuzuka Y, Tanimoto H, et al. Long-term variation of atmospheric methyl iodide and its link to global environmental change. Geophys Res Lett 2012;39(23):L23805. doi:10.1029/2012GL053695.

[674] Ishikawa J, Kawaguchi K, Maruyama Y. Analysis for iodine release from unit 3 of Fukushima Dai-ichi nuclear power plant with consideration of water phase iodine chemistry. J Nucl Sci Technol 2015;52(3):308–14. doi:10.1080/00223131.2014.951417.

[675] Perrin A, Haykal I, KwabiaTchana F, Manceron L, Doizi D, Ducros G. New analysis of the ν_6 and $2\nu_3$ bands of methyl iodide (CH_3I). J Mol Spectrosc 2016;324:28–35. doi:10.1016/J.JMS.2016.04.014.

[676] Kwabia-Tchana F, Attafi Y, Manceron L, Doizi D, Vander Auwera J, Perrin A. Line intensities for the ν_6 and $2\nu_3$ bands of methyl iodide ($^{12}CH_3I$). J Quant Spectrosc Radiat Transf 2019;222-223:130–7. doi:10.1016/j.jqsrt.2018.10.001.

[677] Sadiek I, Hjältén A, Senna Vieira F, Lu C, Stuhr M, Foltynowicz A. Line positions and intensities of the ν_4 band of methyl iodide using mid-infrared optical frequency comb fourier transform spectroscopy. J Quant Spectrosc Radiat Transf 2020;255:107263. doi:10.1016/j.jqsrt.2020.107263.

[678] Soboń G, Martynkien T, Mergo P, Rutkowski L, Foltynowicz A. High-power frequency comb source tunable from 2.7 to 4.2 μm based on difference frequency generation pumped by an yb-doped fiber laser. Opt Lett 2017;42(9):1748–51. doi:10.1364/OL.42.001748.

[679] Khodabakhsh A, Ramaiah-Badarla V, Rutkowski L, Johansson AC, Lee KF, Jiang J, et al. Fourier transform and Vernier spectroscopy using an optical frequency comb at 3–5.4μm. Opt Lett 2016;41(11):2541–4. doi:10.1364/OL.41.002541.

[680] Foltynowicz A, Ban T, Masłowski P, Adler F, Ye J. Quantum-noise-limited optical frequency comb spectroscopy. Phys Rev Lett 2011;107:233002. doi:10.1103/PhysRevLett.107.233002.

[681] Maslowski P, Lee KF, Johansson AC, Khodabakhsh A, Kowzan G, Rutkowski L, et al. Surpassing the path-limited resolution of Fourier-transform spectrometry with frequency combs. Phys Rev A 2016;93:021802. doi:10.1103/PhysRevA.93.021802.

[682] Rutkowski L, Masłowski P, Johansson AC, Khodabakhsh A, Foltynowicz A. Optical frequency comb Fourier transform spectroscopy with sub-nominal resolution and precision beyond the Voigt profile. J Quant Spectrosc Radiat Transf 2018;204:63–73. doi:10.1016/j.jqsrt.2017.09.001.

[683] Boughdiri A, Manceron L, Maaroufi N, Rotger M, Aroui H. Measurements of line intensities for some lines of methyl iodide in the ν_5 and $\nu_3+\nu_6$ bands. J Quant Spectrosc Radiat Transf 2018;221:147–54. doi:10.1016/j.jqsrt.2018.10.004.

[684] Raddaoui E, Soulard P, Guinet M, Aroui H, Jacquemart D. Measurements and modeling of air-broadening coefficients for the ν_6 band of CH_3I. J Quant Spectrosc Radiat Transf 2020;246:106934. doi:10.1016/J.JQSRT.2020.106934.

[685] Robson JI, Gohar LK, Hurley MD, Shine KP, Wallington TJ. Revised IR spectrum, radiative efficiency and global warming potential of nitrogen trifluoride. Geophys Res Lett 2006;33(10):L10817. doi:10.1029/2006GL026210.

[686] Prather MJ, Hsu J. NF_3, the greenhouse gas missing from Kyoto. Geophys Res Lett 2008;35(12):L12810. doi:10.1029/2008GL034542.

[687] Dillon TJ, Vereecken L, Horowitz A, Khamaganov V, Crowley JN, Lelieveld J. Removal of the potent greenhouse gas NF_3 by reactions with the atmospheric oxidants $O(^1D)$, OH and O_3. Phys Chem Chem Phys 2011;13:18600–8. doi:10.1039/C1CP22230A.

[688] Arnold T, Mühle J, Salameh PK, Harth CM, Ivy DJ, Weiss RF. Auto-

mated measurement of nitrogen trifluoride in ambient air. Anal Chem 2012;84(11):4798–804. doi:10.1021/ac300373e.
[689] Weiss RF, Mühle J, Salameh PK, Harth CM. Nitrogen trifluoride in the global atmosphere. Geophys Res Lett 2008;35(20):L20821. doi:10.1029/2008GL035913.
[690] Nikitin A, Champion J, Tyuterev V, Brown L, Mellau G, Lock M. The infrared spectrum of CH_3D between 900 and 3200 cm^{-1}: extended assignment and modeling. J Mol Struct 2000;517-518:1–24. doi:10.1016/S0022-2860(99)00235-5.
[691] Egorov O, Nikitin A, Rey M, Rodina A, Tashkun S, Tyuterev V. Global modeling of NF_3 line positions and intensities from far to mid-infrared up to 2200 cm^{-1}. J Quant Spectrosc Radiat Transf 2019;239:106668. doi:10.1016/j.jqsrt.2019.106668.
[692] Tyuterev V, Tashkun S, Rey M, Kochanov R, Nikitin A, Delahaye T. Accurate spectroscopic models for methane polyads derived from a potential energy surface using high-order contact transformations. J Phys Chem A 2013;117(50):13779–805. doi:10.1021/jp408116j.
[693] Nikitin A, Champion J, Tyuterev V. The MIRS computer package for modeling the rovibrational spectra of polyatomic molecules. J Quant Spectrosc Radiat Transf 2003;82(1):239–49. doi:10.1016/S0022-4073(03)00156-0.
[694] Nikitin A, Rey M, Champion J, Tyuterev V. Extension of the MIRS computer package for the modeling of molecular spectra: from effective to full ab initio ro-vibrational Hamiltonians in irreducible tensor form. J Quant Spectrosc Radiat Transf 2012;113(11):1034–42. doi:10.1016/j.jqsrt.2012.01.027.
[695] Boulaftali N, Sari-Zizi N, Wötzel U, Demaison J, Margulés L, Harder H, et al. The $\nu_4 = 1$ state of $^{14}NF_3$ at 493 cm^{-1} studied by high-resolution FTIR, centimeter-wave, and millimeter-wave spectroscopy. J Mol Spectrosc 2002;212(1):41–52. doi:10.1006/jmsp.2001.8505.
[696] Akkad K, Ben Sari-Zizi N, Bakri B, Demaison J, Bürger H, MKadmi E. Fourier transform infrared and millimeter-wave study of the $\nu_2 = 1$, 2 and the $\nu_2 = \nu_4 = 1$ rovibrational states of $^{14}NF_3$. J Mol Spectrosc 2003;218(1):36–47. doi:10.1016/S0022-2852(02)00028-0.
[697] Sari-Zizi NB, Najib H, Demaison J, Bakri B, Colmont J, Bürger H. High-resolution FTIR and MMW study of the $\nu_4 = 2$ (A_1,E) excited state of $^{14}NF_3$ near 985 cm^{-1}: the axial ground state rotational constants derived by the "loop-method". J Mol Spectrosc 2004;228(2):511–27. doi:10.1016/j.jms.2004.07.010.
[698] Höhe W, Häring U, Kreiner WA, Essig H, Ruoff A. Analysis of the ν_1 fundamental of NF_3 combining FT and laser side-band saturation spectroscopy. A secondary standard for the 1000-1060 cm^{-1} region. Can J Phys 1994;72(11-12):1051–9. doi:10.1139/p94-137.
[699] Najib H, Ben Sari-Zizi N, Demaison J, Bakri B, Colmont J-M, MKadmi E. High-resolution infrared and millimeterwave spectra of the $\nu_3 = 1$ vibrational state of $^{14}NF_3$ at 907 cm^{-1}. J Mol Spectrosc 2003;220(2):214–22. doi:10.1016/S0022-2852(03)00127-9.
[700] Hmimou S, Msahal H, Najib H. First high-resolution FTIR study of the $\nu_1 = \nu_4 = 1$ rovibrational state of $^{14}NF_3$ near 1523 cm^{-1}. Mol Phys 2010;108(6):787–94. doi:10.1080/00268971003662904.
[701] Najib H, Hmimou S, Msahal H. High-resolution infrared spectroscopy of the $\nu_1 + \nu_4$ Band of $^{14}NF_3$:reductions of the rovibrational Hamiltonian. J Chem 2012;9(218684):253–9. doi:10.1155/2012/218684.
[702] Ben Sari-Zizi N, Najib H. High-resolution infrared study of the $2\nu_3(A_1, E)$ and $\nu_1 + \nu_3$(E) bands of $^{14}NF_3$. J Mol Spectrosc 2006;240(2):210–26. doi:10.1016/j.jms.2006.09.011.
[703] Bolotova I, Ulenikov O, Bekhtereva E, Albert S, Bauerecker S, Hollenstein H, et al. High resolution analysis of the FTIR spectra of trifluoroamine NF_3. J Mol Spectrosc 2018;348:87–102. doi:10.1016/j.jms.2018.04.004.
[704] Molina LT, Wooldridge PJ, Molina MJ. Atmospheric reactions and ultraviolet and infrared absorptivities of nitrogen trifluoride. Geophys Res Lett 1995;22(14):1873–6. doi:10.1029/95GL01669.
[705] Rodina A, Egorov O, Nikitin A, Rey M, Serdyukov V, Sinitsa L, et al. Line list for NF_3 molecule in the 1750–1950 cm^{-1} region. J Quant Spectrosc Radiat Transf 2019;232:10–19. doi:10.1016/j.jqsrt.2019.04.028.
[706] Kochanov RV, Gordon IE, Rothman LS, Shine KP, Sharpe SW, Johnson TJ, et al. Infrared absorption cross-sections in HITRAN2016 and beyond: expansion for climate, environment, and atmospheric applications. J Quant Spectrosc Radiat Transf 2019;230:172–221. doi:10.1016/j.jqsrt.2019.04.001.
[707] Bernath P. The Atmospheric Chemistry Experiment (ACE). J Quant Spectrosc Radiat Transf 2017;186:3–16. doi:10.1016/j.jqsrt.2016.04.006. Satellite Remote Sensing and Spectroscopy: Joint ACE-Odin Meeting, October 2015
[708] Montzka SA, Dutton GS, Yu P, Ray E, Portmann RW, Daniel JS, Kuijpers L, Hall BD, Mondeel D, Siso C, Nance JD, Rigby M, Manning AJ, Hu L, Moore F, Miller BR, Elkins JW. An unexpected and persistent increase in global emissions of ozone-depleting CFC-11. Nature 2018;557:413–17. doi:10.1038/s41586-018-0106-2.
[709] Rigby M, Park S, Saito T, Western LM, Redington AL, Fang X, Henne S, Manning AJ, Prinn RG, Dutton GS, Fraser PJ, Ganesan AL, Hall BD, Harth CM, Kim J, Kim K-R, Krummel PB, Lee T, Li S, Liang Q, Lunt MF, Montzka SA, Mühle J, O'Doherty S, Park M-K, Reimann S, Salameh PK, Simmonds P, Tunnicliffe RL, Weiss RF, Yokouchi Y, Young D. Increase in CFC-11 emissions from eastern China based on atmospheric observations. Nature 2019;569:546–50. doi:10.1038/s41586-019-1193-4.
[710] Montzka SA, Dutton GS, Portmann RW, Chipperfield MP, Davis S, Feng W, Manning AJ, Ray E, Rigby M, Hall BD, Siso C, Nance JD, Krummel PB, Mühle J, Young D, O'Doherty S, Salameh PK, Harth CM, Prinn RG, Weiss RF, Elkins JW, Walter-Terrinoni H, Theodoridi C. A decline in global CFC-11 emissions during 2018-2019. Nature 2021;590:428–32. doi:10.1038/s41586-021-03260-5.
[711] Park S, Western LM, Saito T, Redington AL, Henne S, Fang X, Prinn RG, Manning AJ, Montzka SA, Fraser PJ, Ganesan AL, Harth CM, Kim J, Krummel PB, Liang Q, Mühle J, O'Doherty S, Park H, Park M-K, Reimann S, Salameh PK, Weiss RF, Rigby M. A decline in emissions of CFC-11 and related chemicals from eastern China. Nature 2021;590:433–7. doi:10.1038/s41586-021-03277-w.
[712] Mühle J, Ganesan AL, Miller BR, Salameh PK, Harth CM, Greally BR, et al. Perfluorocarbons in the global atmosphere: tetrafluoromethane, hexafluoroethane, and octafluoropropane. Atmos Chem Phys 2010;10(11):5145–64. doi:10.5194/acp-10-5145-2010.
[713] J. Harnisch and A. Eisenhauer. Natural CF_4 and SF_6 on earth. Geophys Res Lett 1998;25(13):2401–4. doi:10.1029/98GL01779.
[714] Li Z, Varanasi P. Measurement of the absorption cross-sections of CFC-11 at conditions representing various model atmospheres. J Quant Spectrosc Radiat Transf 1994;52(2):137–44. doi:10.1016/0022-4073(94)90002-7.
[715] Harrison JJ. New and improved infrared absorption cross sections for trichlorofluoromethane (CFC-11). Atmos Meas Tech 2018;11(10):5827–36. doi:10.5194/amt-11-5827-2018.
[716] Le Bris K, McDowell J, Strong K. Measurements of the infrared absorption cross-sections of HCFC-141b (CH_3CFCl_2). J Quant Spectrosc Radiat Transf 2012;113(15):1913–19. doi:10.1016/j.jqsrt.2012.05.004.
[717] Harrison JJ. Infrared absorption cross sections for air-broadened 1,1-dichloro-1-fluoroethane (HCFC-141b). J Quant Spectrosc Radiat Transf 2019;238:106489. doi:10.1016/j.jqsrt.2019.04.041.
[718] Varanasi P, Li Z, Nemtchinov V, Cherukuri A. Spectral absorption-coefficient data on HCFC-22 and SF_6 for remote-sensing applications. J Quant Spectrosc Radiat Transf 1994;52(3):323–32. doi:10.1016/0022-4073(94)90162-7. Special Issue Atmospheric Spectroscopy Applications
[719] Harrison JJ. New infrared absorption cross sections for the infrared limb sounding of sulfur hexafluoride (SF_6). J Quant Spectrosc Radiat Transf 2020;254:107202. doi:10.1016/j.jqsrt.2020.107202.
[720] Nemtchinov V, Varanasi P. Thermal infrared absorption cross-sections of CF_4 for atmospheric applications. J Quant Spectrosc Radiat Transf 2003;82(1):461–71. doi:10.1016/S0022-4073(03)00170-5.
[721] Harrison JJ. New infrared absorption cross sections for the infrared limb sounding of carbon tetrafluoride (CF_4). J Quant Spectrosc Radiat Transf 2021;260:107432. doi:10.1016/j.jqsrt.2020.107432.
[722] Cantrell CA, Davidson JA, McDaniel AH, Shetter RE, Calvert JG. Infrared absorption cross sections for N_2O_5. Chem Phys Lett 1988;148(4):358–63. doi:10.1016/0009-2614(88)87288-9.
[723] Wagner G, Birk M. New infrared spectroscopic database for chlorine nitrate. J Quant Spectrosc Radiat Transf 2003;82(1-4):443–60. doi:10.1016/S0022-4073(03)00169-9.
[724] Niemann HB, Atreya SK, Demick JE, Gautier D, Haberman JA, Harpold DN, et al. Composition of Titan's lower atmosphere and simple surface volatiles as measured by the Cassini-Huygens probe gas chromatograph mass spectrometer experiment. J Geophys Res (Planets) 2010;115(E12). doi:10.1029/2010JE003659.
[725] Sung K, Toon GC, Drouin BJ, Mantz AW, Smith MAH. FT-IR measurements of cold propene (C_3H_6) cross-sections at temperatures between 150 and 299 K. J Quant Spectrosc Radiat Transf 2018;213:119–32. doi:10.1016/j.jqsrt.2018.03.011.
[726] Sung K, Toon GC, Mantz AW, Smith MAH. FT-IR measurements of cold C_3H_8 cross sections at 7-15 μm for Titan atmosphere. Icarus 2013;226(2):1499–513. doi:10.1016/j.icarus.2013.07.028.
[727] Sung K, Steffens B, Toon GC, Nemchick DJ, Smith MAH. Pseudoline parameters to represent n-butane (n-C_4H_{10}) cross-sections measured in the 7-15 μm region for the Titan atmosphere. J Quant Spectrosc Radiat Transf 2020;251. doi:10.1016/j.jqsrt.2020.107011.
[728] Hewett D, Bernath PF, Wong A, Billinghurst BE, Zhao J, Lombardo NA, et al. N_2 and H_2 broadened isobutane infrared absorption cross sections and butane upper limits on Titan. Icarus 2020;344. doi:10.1016/j.icarus.2019.113460.
[729] Sung K, Toon GC, Crawford TJ. N_2- and (H_2+He)-broadened cross sections of benzene (C_6H_6) in the 7-15 μm region for the Titan and Jovian atmospheres. Icarus 2016;271:438–52. doi:10.1016/j.icarus.2016.01.012.
[730] Sung K, Toon GC, Crawford TJ. Corrigendum to "N_2- and (H_2+He)-broadened cross sections of benzene (C_6H_6) in the 7-15 μm region for the Titan and Jovian atmospheres" [Icarus, 271 (2016) 438-452]. Icarus 2017;281:476. doi:10.1016/j.icarus.2016.08.018.
[731] Hewett D, Bernath P, Zhao J, Billinghurst B. Near infrared absorption cross sections for ethane broadened by hydrogen and nitrogen. J Quant Spectrosc Radiat Transf 2020;242. doi:10.1016/j.jqsrt.2019.106780.
[732] Hewett DM, Bernath PF, Billinghurst BB. Infrared absorption cross sections of isobutane with hydrogen and nitrogen as broadening gases. J Quant Spectrosc Radiat Transf 2019;227:226–9. doi:10.1016/j.jqsrt.2019.02.008.
[733] Hewett DM, Bernath PF, Billinghurst BE. Erratum to "Infrared absorption cross sections of isobutane with hydrogen and nitrogen as broadening gases" [Journal of Quantitative Spectroscopy and Radiative Transfer 227 (2019) 226-229]. J Quant Spectrosc Radiat Transf 2020;242. doi:10.1016/j.jqsrt.2019.106771.
[734] Bernath P, Dodangodage R, Dulick M, Zhao J, Billinghurst B. Absorption cross sections for neopentane broadened by nitrogen in the 3.3 μm region. J Quant Spectrosc Radiat Transf 2020;251. doi:10.1016/j.jqsrt.2020.107034.
[735] Wong A, Hewett D, Billinghurst BB, Hodges JN, Bernath PF. He and H_2 broad-

ened propane cross sections in the 3 μm region at cold temperatures. J Quant Spectrosc Radiat Transf 2019;232:104–7. doi:10.1016/j.jqsrt.2019.04.038.
[736] Dodangodage R, Bernath PF, Zhao J, Billinghurst B. Absorption cross sections for ethane broadened by hydrogen and helium in the 3.3 micron region. J Quant Spectrosc Radiat Transf 2020;253. doi:10.1016/j.jqsrt.2020.107131.
[737] Wong A, Appadoo DRT, Bernath PF. IR absorption cross sections of propane broadened by H_2 and He between 150 K and 210 K. J Quant Spectrosc Radiat Transf 2018;218:68–71. doi:10.1016/j.jqsrt.2018.06.026.
[738] Wong A, Billinghurst B, Bernath PF. Helium broadened propane absorption cross sections in the far-IR. Mol Astrophys 2017;8:36–9. doi:10.1016/j.molap.2017.06.003.
[739] Wong A, Hargreaves RJ, Billinghurst B, Bernath PF. Infrared absorption cross sections of propane broadened by hydrogen. J Quant Spectrosc Radiat Transf 2017;198:141–4. doi:10.1016/j.jqsrt.2017.05.006.
[740] Beale CA, Hargreaves RJ, Bernath PF. Temperature-dependent high resolution absorption cross sections of propane. J Quant Spectrosc Radiat Transf 2016;182:219–24. doi:10.1016/j.jqsrt.2016.06.006.
[741] Buzan EM, Hargreaves RJ, Bernath PF. High resolution absorption cross sections for propylene in the 3 μm region at high temperatures. Mol Astrophys 2016;3:16–20. doi:10.1016/j.molap.2016.06.001.
[742] Es-sebbar E-t, Alrefae M, Farooq A. Infrared cross-sections and integrated band intensities of propylene: temperature-dependent studies. J Quant Spectrosc Radiat Transf 2014;133:559–69. doi:10.1016/j.jqsrt.2013.09.019.
[743] Es-sebbar E-t, Benilan Y, Farooq A. Temperature-dependent absorption cross-section measurements of 1-butene (1-C_4H_8) in VUV and IR. J Quant Spectrosc Radiat Transf 2013;115:1–12. doi:10.1016/j.jqsrt.2012.09.014.
[744] Alrefae M, Es-sebbar ET, Farooq A. Absorption cross-section measurements of methane, ethane, ethylene and methanol at high temperatures. J Mol Spectrosc 2014;303:8–14. doi:10.1016/j.jms.2014.06.007.
[745] Klingbeil AE, Jeffries JB, Hanson RK. Temperature-dependent mid-IR absorption spectra of gaseous hydrocarbons. J Quant Spectrosc Radiat Transf 2007;107(3):407–20. doi:10.1016/j.jqsrt.2007.03.004.
[746] Strand CL, Ding Y, Johnson SE, Hanson RK. Measurement of the mid-infrared absorption spectra of ethylene (C_2H_4) and other molecules at high temperatures and pressures. J Quant Spectrosc Radiat Transf 2019;222:122–9. doi:10.1016/j.jqsrt.2018.10.030.
[747] Ding Y, Su W-W, Johnson SE, Strand CL, Hanson RK. Temperature-dependent absorption cross section measurements for propene, 1-butene, cis-/trans-2-butene, isobutene and 1,3-butadiene in the spectral region 8.4-11.7 μm. J Quant Spectrosc Radiat Transf 2020;255. doi:10.1016/j.jqsrt.2020.107240.
[748] Ding Y, Strand CL, Hanson RK. High-temperature mid-infrared absorption spectra of methanol (CH_3OH) and ethanol (C_2H_5OH) between 930 and 1170 cm^{-1}. J Quant Spectrosc Radiat Transf 2019;224:396–402. doi:10.1016/j.jqsrt.2018.11.034.
[749] Ding Y, Peng WY, Strand CL, Hanson RK. Quantitative measurements of broadband mid-infrared absorption spectra of formaldehyde, acetaldehyde, and acetone at combustion-relevant temperatures near 5.7 μm. J Quant Spectrosc Radiat Transf 2020;248. doi:10.1016/j.jqsrt.2020.106981.
[750] Birk M, Wagner G. ESA SEOM-IAS – Measurement and ACS database O_3 UV region. Zenodo 2021. doi:10.5281/zenodo.1485587.
[751] Bak J, Xiong L, Birk M, Wagner G, Gordon IE, Chance K. Impact of using a new ultraviolet ozone absorption cross-section dataset on OMI ozone profile retrievals. Atmos Meas Tech (AMT) 2020;13:5845–54. doi:10.5194/amt-13-5845-2020.
[752] Gorshelev V, Serdyuchenko A, Weber M, Chehade W, Burrows JP. High spectral resolution ozone absorption cross-sections - Part 1: measurements, data analysis and comparison with previous measurements around 293 K. Atmos Meas Tech 2014;7:609–24. doi:10.5194/amt-7-609-2014.
[753] Hodges JT, Viallon J, Brewer PJ, Drouin BJ, Gorshelev V, Janssen C, et al. Recommendation of a consensus value of the ozone absorption cross-section at 253.65 nm based on a literature review. Metrologia 2019;56:034001. doi:10.1088/1681-7575/ab0bdd.
[754] Janssen C, Elandaloussi H, Gröbner J. A new photometric ozone reference in the Huggins bands: the absolute ozone absorption cross section at the 325 nm HeCd laser wavelength. Atmos Meas Tech 2018;11:1707–23. doi:10.5194/amt-11-1707-2018.
[755] Hearn AG. The Absorption of ozone in the ultra-violet and visible regions of the spectrum. Proc Phys Soc 1961;78(5):932–40. doi:10.1088/0370-1328/78/5/340.
[756] Hermans C, Vandaele AC, Fally S. Fourier transform measurements of SO_2 absorption cross sections: I. Temperature dependence in the 24 000-29 000 cm^{-1} (345-420 nm) region. J Quant Spectrosc Radiat Transf 2009;110:756–65. doi:10.1016/j.jqsrt.2009.01.031.
[757] Vandaele AC, Hermans C, Fally S. Fourier transform measurements of SO_2 absorption cross sections: II. Temperature dependence in the 29 000-44 000 cm^{-1} (227-345 nm) region. J Quant Spectrosc Radiat Transf 2009;110:2115–26. doi:10.1016/j.jqsrt.2009.05.006.
[758] Wagner G, Birk M. UV cross-sections of SO_2. In preparation; 2021.
[759] Bogumil K, Orphal J, Homann T, Voigt S, Spietz P, Fleischmann OC, et al. Measurements of molecular absorption spectra with the SCIAMACHY preflight model: instrument characterization and reference data for atmospheric remote-sensing in the 230–2380 nm region. J Photochem Photobiol A Chem 2003;157:167–84. doi:10.1016/S1010-6030(03)00062-5.
[760] Birk M, Wagner G. ESA SEOM-IAS - measurement and ACS database SO_2 UV region. Zenodo 2018. doi:10.5281/zenodo.1492581.
[761] Sioris CE, Boone CD, Nassar R, Sutton KJ, Gordon IE, Walker KA, et al. Retrieval of carbon dioxide vertical profiles from solar occultation observations and associated error budgets for ACE-FTS and CASS-FTS. Atmos Meas Tech 2014;7(7):2243–62. doi:10.5194/amt-7-2243-2014.
[762] Chimot J, Veefkind JP, Vlemmix T, de Haan JF, Amiridis V, Proestakis E, et al. An exploratory study on the aerosol height retrieval from OMI measurements of the 477 nm O_2–O_2 spectral band using a neural network approach. Atmos Meas Tech 2017;10:783–809. doi:10.5194/amt-10-783-2017.
[763] Kataoka F, Crisp D, Taylor T, O'Dell C, Kuze A, Shiomi K, et al. The Cross-Calibration of Spectral Radiances and Cross-Validation of CO_2 Estimates from GOSAT and OCO-2. Remote Sens 2017;9(12):1158. doi:10.3390/rs9111158.
[764] Hartmann J-M, Boulet C, Toon GC. Collision-induced absorption by N_2 near 2.16 μm: calculations, model, and consequences for atmospheric remote sensing. J Geophys Res Atmos 2017;122:2419. doi:10.1002/2016JD025677.
[765] Ortega I, Berg LK, Ferrare RA, Hair JW, Hostetler CA, Volkamer R. Elevated aerosol layers modify the O_2–O_2 absorption measured by ground-based MAX-DOAS. J Quant Spectrosc Radiat Transf 2016;176:34–49. doi:10.1016/j.jqsrt.2016.02.021.
[766] Spinei E, Cede A, Herman J, Mount GH, Eloranta E, Morley B, et al. Direct sun and airborne MAX-DOAS measurements of the collision induced oxygen complex, O_2–O_2 absorption with significant pressure and temperature differences. Atmos Meas Tech Discuss 2014;7(9):10015–57. doi:10.5194/amtd-7-10015-2014.
[767] Meadows VS. Reflections on O_2 as a biosignature in exoplanetary atmospheres. Astrobiology 2017;17(10):1022–52. doi:10.1089/ast.2016.1578.
[768] Abel M, Frommhold L. Collision-induced spectra and current astronomical research gas of H_2. Can J Phys 2013;91:0532. doi:10.1139/cjp-2012-0532.
[769] Godin PJ, Ramirez RM, Campbell CL, Wizenberg T, Nguyen TG, Strong K, et al. Collision-induced absorption of CH_4–CO_2 and H_2–CO_2 complexes and their effect on the ancient martian atmosphere. J Geophys Res Planet 2020;125(12):e06357. doi:10.1029/2019JE006357.
[770] Wordsworth R, Kalugina Y, Lokshtanov S, Vigasin A, Ehlmann B, Head J, et al. Transient reducing greenhouse warming on early Mars. Geophys Res Lett 2017;44:665. doi:10.1002/2016GL071766.
[771] Richard C, Gordon IE, Rothman LS, Abel M, Frommhold L, Gustafsson M, et al. New section of the HITRAN database: Collision-Induced Absorption (CIA). J Quant Spectrosc Radiat Transf 2012;113(11):1276–85. doi:10.1016/j.jqsrt.2011.11.004.
[772] Karman T, Gordon IE, van der Avoird A, Baranov YI, Boulet C, Drouin BJ, et al. Update of the HITRAN collision-induced absorption section. Icarus 2019;328:160–75. doi:10.1016/j.icarus.2019.02.034.
[773] Abel M, Frommhold L, Li X, Hunt KLC. Collision-induced absorption by H_2 pairs: from hundreds to thousands of Kelvin. J Phys Chem A 2011;115(25):6805–12. doi:10.1021/jp109441f.
[774] Fletcher LN, Gustafsson M, Orton GS. Hydrogen dimers in giant-planet infrared spectra. Astrophys J Suppl Ser 2018;235(1):24. doi:10.3847/1538-4365/aaa07a.
[775] Abel M, Frommhold L, Li X, Hunt KLC. Infrared absorption by collisional H_2–He complexes at temperatures up to 9000 K and frequencies from 0 to 20 000 cm^{-1}. J Chem Phys 2012;136(4):044319. doi:10.1063/1.3676405.
[776] Gustafsson M, Frommhold L. The H_2–H infrared absorption bands at temperatures from 1000 K to 2500 K. Astron Astrophys 2003;400(3):1161–2. doi:10.1051/0004-6361:20030100.
[777] Gustafsson M, Frommhold L. Infrared absorption spectra of collisionally interacting He and H atoms. Astrophys J 2001;546(2):1168. doi:10.1086/318311.
[778] Borysow A, Frommhold L. Theoretical collision-induced rototranslational absorption spectra for the outer planets: H_2–CH_4 pairs. Astrophys J 1986;304:849–65. doi:10.1086/164221.
[779] Bar-Ziv E, Weiss S. Translational spectra due to collision-induced overlap moments in mixtures of He with CO_2, N_2, CH_4, and C_2H_6. J Chem Phys 1972;57:34. doi:10.1063/1.1677970.
[780] Odintsova T, Serov E, Balashov A, Koshelev M, Koroleva A, Simonova A, et al. CO_2–CO_2 and CO_2–Ar continua at millimeter wavelengths. J Quant Spectrosc Radiat Transf 2021;258. doi:10.1016/j.jqsrt.2020.107400.
[781] Taylor RH, Borysow A, Frommhold L. Concerning the rototranslational absorption spectra of He–CH_4 pairs. J Mol Spectrosc 1988;129:45. doi:10.1016/0022-2852(88)90257-3.
[782] Samuelson RE, Nath NR, Borysow A. Gaseous abundances and methane supersaturation in Titan's troposphere. Planet Space Sci 1997;45(8):959–80. doi:10.1016/S0032-0633(97)00090-1.
[783] Borysow A, Frommhold L. Collision-induced rototranslational absorption spectra of CH_4-CH_4 pairs at temperatures from 50 to 300 K. Astrophys J 1987;318:940–3. doi:10.1086/165426.
[784] Gruszka M, Borysow A. Roto-translational collision-induced absorption of CO_2 for the atmosphere of Venus at frequencies from 0 to 250 cm^{-1}, at temperatures from 200 to 800 K. Icarus 1997;129:172. doi:10.1006/icar.1997.5773.
[785] Baranov Y, Vigasin A. Collision-induced absorption by CO_2 in the region of ν_1, $2\nu_2$. J Mol Spectrosc 1999;193(2):319–25. doi:10.1006/jmsp.1998.7743.
[786] Baranov Y, Fraser GT, Lafferty WJ, Vigasin A. Collision-induced absorption in the CO_2 fermi triad for temperatures from 211 K to 296 K. In: Camy-Peyret C, Vigasin A, editors. Weakly interacting molecular pairs: unconventional absorbers of radiation in the atmosphere. Springer; 2003. p. 149–58. doi:10.1007/978-94-010-0025-3.
[787] Baranov YI. Collision-induced absorption in the region of the $\nu_2 + \nu_3$ band of carbon dioxide. J Mol Spectrosc 2018;345:11–16. doi:10.1016/j.jms.2017.11.005.
[788] Borysow A, Frommhold L. Theoretical collision-induced rototranslational ab-

sorption spectra for modeling Titan's atmosphere: H_2–N_2 pairs. Astrophys J 1986;303:495–510. doi:10.1086/164096.
[789] Chistikov DN, Finenko AA, Lokshtanov SE, Petrov SV, Vigasin AA. Simulation of collision-induced absorption spectra based on classical trajectories and ab initio potential and induced dipole surfaces. I. Case study of N_2-N_2 rototranslational band. J Chem Phys 2019;151(19). doi:10.1063/1.5125756.
[790] Baranov YI, Lafferty WJ, Fraser GT. Investigation of collision-induced absorption in the vibrational fundamental bands of O_2 and N_2 at elevated temperatures. J Mol Spectrosc 2005;233(1):160–3. doi:10.1016/j.jms.2005.06.008.
[791] Lafferty WJ, Solodov AM, Weber A, Olson WB, Hartmann J-M. Infrared collision-induced absorption by N_2 near 4.3 μm for atmospheric applications: measurements and empirical modeling. Appl Opt 1996;35(30):5911. doi:10.1364/AO.35.005911.
[792] Sung K, Wishnow E, Venkataraman M, Brown LR, Ozier I, Benner DC, et al. Progress in the measurement of temperature-dependent N_2-N_2 collision-induced absorption and H_2-broadening of cold and hot CH_4. In: Proceedings of the AAS/division for planetary sciences meeting abstracts 48. In: AAS/Division for Planetary Sciences Meeting Abstracts, 48; 2016. p. 424.11.
[793] Baranov YI, Lafferty W, Fraser G. Infrared spectrum of the continuum and dimer absorption in the vicinity of the O_2 vibrational fundamental in O_2/CO_2 mixtures. J Mol Spectrosc 2004;228(2):432–40. doi:10.1016/j.jms.2004.04.010.
[794] Maté, B, Lugez C, Fraser GT, Lafferty WJ. Absolute intensities for the O_2 1.27 μm continuum absorption. J Geophys Res Atmos 1999;104(D23):30585–90. doi:10.1029/1999JD900824.
[795] Karman T, Koenis MAJ, Banerjee A, Parker DH, Gordon IE, van der Avoird A, et al. O_2-O_2 and O_2-N_2 collision-induced absorption mechanisms unravelled. Nat Chem 2018;10:549. doi:10.1038/s41557-018-0015-x.
[796] Spiering FR, van der Zande WJ. Collision induced absorption in the $a^1\Delta(v{=}2) \leftarrow X^3\Sigma_g^-(v{=}0)$ band of molecular oxygen. Phys Chem Chem Phys 2012;14(28):9923–8. doi:10.1039/c2cp40961e.
[797] Tran H, Boulet C, Hartmann J-M. Line mixing and collision-induced absorption by oxygen in the A-band: laboratory measurements, model, and tools for atmospheric spectra computations. J Geophys Res 2006;111:D15210. doi:10.1029/2005JD006869.
[798] Spiering FR, Kiseleva MB, Filippov NN, van Kesteren L, van der Zande WJ. Collision-induced absorption in the O_2 B-band region near 670 nm. Phys Chem Chem Phys 2011;13:9616–21. doi:10.1039/C1CP20403C.
[799] Thalman R, Volkamer R. Temperature dependent absorption cross-sections of O_2-O_2 collision pairs between 340 and 630 nm and at atmospherically relevant pressure. Phys Chem Chem Phys 2013;15(37):15371. doi:10.1039/c3cp50968k.
[800] Thibault F, Menoux V, Le Doucen R, Rosenmann L, Hartmann J-M, Boulet C. Infrared collision-induced absorption by O_2 near 6.4 μm for atmospheric applications: measurements and empirical modeling. Appl Opt 1997;36(3):563. doi:10.1364/ao.36.000563.
[801] Orlando JJ, Tyndall GS, Nickerson KE, Calvert JG. The temperature dependence of collision-induced absorption by oxygen near 6 μm. J Geophys Res Atmos 1991;96(D11) 20 755–20 760. doi:10.1029/91JD02042.
[802] Menoux V, Doucen RL, Boulet C, Roblin A, Bouchardy AM. Collision-induced absorption in the fundamental band of N_2: temperature dependence of the absorption for N_2-N_2 and N_2-O_2 pairs. Appl Opt 1993;32(3):263–8. doi:10.1364/AO.32.000263.
[803] Hartmann J-M, Boulet C, Tran DD, Tran H, Baranov Y. Effect of humidity on the absorption continua of CO_2 and N_2 near 4 μm: calculations, comparisons with measurements, and consequences for atmospheric spectra. J Chem Phys 2018;148(5):054304. doi:10.1063/1.5019994.
[804] Borysow A, Tang C. Far infrared CIA spectra of N_2–CH_4 pairs for modeling of Titan's atmosphere. Icarus 1993;105(1):175–83. doi:10.1006/icar.1993.1117.
[805] Vangvichith M, Tran H, Hartmann J-M. Line-mixing and collision induced absorption for O_2–CO_2 mixtures in the oxygen A-band region. J Quant Spectrosc Radiat Transf 2009;110(18):2212–16. doi:10.1016/j.jqsrt.2009.06.002.
[806] Karman T, Miliordos E, Hunt KL, Groenenboom GC, van der Avoird A. Quantum mechanical calculation of the collision-induced absorption spectra of N_2-N_2 with anisotropic interactions. J Chem Phys 2015;142(8):1–12. doi:10.1063/1.4907917.
[807] Frommhold L. Collision induced absorption in gases. Cambridge University Press; 2006.
[808] Borysow J, Moraldi M, Frommhold L. The collision induced spectroscopies: concerning the desymmetrization of classical line shape. Mol Phys 1985;56(4):913–22. doi:10.1080/00268978500102801.
[809] Schofield P. Space-time correlation function formalism for slow neutron scattering. Phys Rev Lett 1960;4(5):239–40. doi:10.1103/PhysRevLett.4.239.
[810] Borysow A, Frommhold L. Collision-induced rototranslational absorption spectra of N_2-N_2 pairs for temperatures from 50 to 300 K. Astrophys J 1986;311:1043. doi:10.1086/164841.
[811] Serov EA, Balashov AA, Tretyakov MY, Odintsova TA, Koshelev MA, Chistikov DN, et al. Continuum absorption of millimeter waves in nitrogen. J Quant Spectrosc Radiat Transf 2020;242:106774. doi:10.1016/j.jqsrt.2019.106774.
[812] Meshkov AI, De Lucia FC. Laboratory measurements of dry air atmospheric absorption with a millimeter wave cavity ringdown spectrometer. J Quant Spectrosc Radiat Transf 2007;108(2):256–76. doi:10.1016/j.jqsrt.2007.04.001.
[813] Maté B, Lugez CL, Solodov AM, Fraser GT, Lafferty WJ. Investigation of the collision-induced absorption by O_2 near 6.4 μm in pure O_2 and O_2-N_2 mixtures. J Geophys Res Atmos 2000;105(D17):22225–30. doi:10.1029/2000JD900295.
[814] Oparin DV, Filippov NN, Grigoriev IM, Kouzov AP. Effect of stable and metastable dimers on collision-induced rototranslational spectra: carbon dioxide - rare gas mixtures. J Quant Spectrosc Radiat Transf 2017;196:87–93. doi:10.1016/j.jqsrt.2017.04.002.
[815] Turbet M, Tran H, Pirali O, Forget F, Boulet C, Hartmann JM. Far infrared measurements of absorptions by CH_4+CO_2 and H_2+CO_2 mixtures and implications for greenhouse warming on early Mars. Icarus 2019;321(November 2018):189–99. doi:10.1016/j.icarus.2018.11.021.
[816] Turbet M, Boulet C, Karman T. Measurements and semi-empirical calculations of CO_2+CH_4 and CO_2+H_2 collision-induced absorption across a wide range of wavelengths and temperatures. Application for the prediction of early Mars surface temperature. Icarus 2020;346(February):113762. doi:10.1016/j.icarus.2020.113762.
[817] Mondelain D, Boulet C, Hartmann JM. The binary absorption coefficients for H_2+CO_2 mixtures in the 2.12-2.35 μm spectral region determined by CRDS and by semi-empirical calculations. J Quant Spectrosc Radiat Transf 2021;260:107454. doi:10.1016/j.jqsrt.2020.107454.
[818] Finenko AA, Gordon IE, Chistikov DN, Conway EK, Lokshtanov SE, Kalugina YN, et al. Trajectory-based simulation of CH_4-N_2 collision-induced band profiles relevant to the atmosphere of Titan. In: Proceedings of the AGU fall meeting abstracts; 2020. p. P067–0013. https://agu.confex.com/agu/fm20/webprogram/Paper686857.html. American Geophysical Union 2020 Fall Meeting (San Francisco, CA, 1-17 Dec 2020)
[819] Banerjee A, Mandon J, Harren F, Parker DH. Collision-induced absorption between O_2-CO_2 for the $a^1\Delta_g(v=1) \leftarrow X^3\Sigma_g^-(v=0)$ transition of molecular oxygen at 1060 nm. Phys Chem Chem Phys (Inc Faraday Trans) 2019;21(4):1805–11. doi:10.1039/C8CP06778C.
[820] Mondelain D, Kassi S, Campargue A. Accurate laboratory measurement of the O_2 collision-induced absorption band near 1.27 μm. J Geophys Res Atmos 2019;124(1):414–23. doi:10.1029/2018JD029317.
[821] Thomas G, Stamnes K. Radiative transfer in the atmosphere and ocean. Cambridge: Cambridge University Press; 1999. ISBN 9780521890618. doi:101063/11333301.
[822] Brasseur G, Solomon S. Aeronomy of the middle atmosphere. Dordrecht: Springer; 2005. ISBN 978-1-4020-3824-2. doi:101007/1-4020-3824-0.
[823] Fenn R, Clough S, Gallery W, Good R, Kneizys F, Mill J, et al. Optical and infrared properties of the atmosphere. In: Jursa A, editor. Handbook of geophysics and the space environment. Springfield: National Technical Information Service; 1985. p. 1038. ntrl.ntis.gov/NTRL/dashboard/searchResults/titleDetail/ADA167000.xhtml
[824] Downing HD, Williams D. Optical constants of water in the infrared. J Geophys Res 1975;80(12):1656–61. doi:10.1029/JC080i012p01656.
[825] Wagner R, Benz S, Möhler O, Saathoff H, Schnaiter M, Schurath U. Mid-infrared extinction spectra and optical constants of supercooled water droplets. J Phys Chem A 2005;109(32):7099–112. doi:10.1021/jp051942z.
[826] Warren SG, Brandt RE. Optical constants of ice from the ultraviolet to the microwave: a revised compilation. J Geophys Res 2008;113(D14):D14220. doi:10.1029/2007JD009744.
[827] Clapp ML, Worsnop DR, Miller RE. Frequency-dependent optical constants of water ice obtained directly from aerosol extinction spectra. J Phys Chem 1995;99(17):6317–26. doi:10.1021/j100017a010.
[828] Tisdale RT, Glandorf DL, Tolbert MA, Toon OB. Infrared optical constants of low-temperature H_2SO_4 solutions representative of stratospheric sulfate aerosols. J Geophys Res Atmos 1998;103(D19):25353–70. doi:10.1029/98JD02457.
[829] Lund Myhre CE, Christensen DH, Nicolaisen FM, Nielsen CJ. Spectroscopic study of aqueous H_2SO_4 at different temperatures and compositions: variations in dissociation and optical properties. J Phys Chem A 2003;107(12):1979–91. doi:10.1021/jp026576n.
[830] Lund Myhre CE, Grothe H, Gola AA, Nielsen CJ. Optical constants of HNO_3/H_2O and $H_2SO_4/HNO_3/H_2O$ at low temperatures in the infrared region. J Phys Chem A 2005;109(32):7166–71. doi:10.1021/jp0508406.
[831] Niedziela RF, Miller RE, Worsnop DR. Temperature- and frequency-dependent optical constants for nitric acid dihydrate from aerosol spectroscopy. J Phys Chem A 1998;102(32):6477–84. doi:10.1021/jp981299z.
[832] Richwine LJ, Clapp ML, Miller RE, Worsnop DR. Complex refractive indices in the infrared of nitric acid trihydrate aerosols. Geophys Res Lett 1995;22(19):2625–8. doi:10.1029/95GL02650.
[833] Toon OB, Tolbert MA, Koehler BG, Middlebrook AM, Jordan J. Infrared optical constants of H_2O ice, amorphous nitric acid solutions, and nitric acid hydrates. J Geophys Res 1994;99(D12):25631. doi:10.1029/94JD02388.
[834] Wagner R, Ajtai T, Kandler K, Lieke K, Linke C, Müller T, et al. Complex refractive indices of Saharan dust samples at visible and near UV wavelengths: a laboratory study. Atmos Chem Phys 2012;12(5):2491–512. doi:10.5194/acp-12-2491-2012.
[835] Pyle DM, Mather TA, Biggs J. Remote sensing of volcanoes and volcanic processes: integrating observation and modelling - introduction. Geol Soc Lond Spec Publ 2013;380:1–13. doi:10.1144/SP380.14.
[836] Deguine A, Petitprez D, Clarisse L, Gudmundsson S, Outes V, Villarosa G, et al. Complex refractive index of volcanic ash aerosol in the infrared, visible, and ultraviolet. Appl Opt 2020;59(4):884. doi:10.1364/AO.59.000884.
[837] Liu PF, Abdelmalki N, Hung H-M, Wang Y, Brune WH, Martin ST. Ultraviolet and visible complex refractive indices of secondary organic material produced by photooxidation of the aromatic compounds toluene and m-xylene. Atmos Chem Phys 2015;15:1435–46. doi:10.5194/acp-15-1435-2015.
[838] Liu P, Zhang Y, Martin ST. Complex refractive indices of thin films of sec-

ondary organic materials by spectroscopic ellipsometry from 220 to 1200 nm. Environ Sci Technol 2013;47(23):13594–601. doi:10.1021/es403411e.
[839] Lund Myhre CE, Nielsen CJ. Optical properties in the UV and visible spectral region of organic acids relevant to tropospheric aerosols. Atmos Chem Phys 2004;4(7):1759–69. doi:10.5194/acp-4-1759-2004.
[840] Alexander DTL, Crozier PA, Anderson JR. Brown carbon spheres in east asian outflow and their optical properties. Science 2008;321(5890):833–6. doi:10.1126/science.1155296.
[841] Sutherland RA, Khanna RK. Optical properties of organic-based aerosols produced by burning vegetation. Aerosol Sci Technol 1991;14(3):331–42. doi:10.1080/02786829108959495.
[842] Magi BI, Fu Q, Redemann J. A methodology to retrieve self-consistent aerosol optical properties using common aircraft measurements. J Geophys Res 2007;112(D24):D24S12. doi:10.1029/2006JD008312.
[843] Stagg B, Charalampopoulos T. Refractive indices of pyrolytic graphite, amorphous carbon, and flame soot in the temperature range 25° to 600°C. Combust Flame 1993;94(4):381–96. doi:10.1016/0010-2180(93)90121-I.
[844] Chang H, Charalampopoulos TT. Determination of the wavelength dependence of refractive indices of flame soot. Proc R Soc A Math Phys Eng Sci 1990;430(1880):577–91. doi:10.1098/rspa.1990.0107.
[845] Querry M. Optical constants of minerals and other materials from the millimeter to the ultraviolet. Technical Report. Aberdeen: Chemical Research, Development Engineering Center, CRDEC-CR-88009: Chemical Research Development and Engineering Center; 1987.
[846] Toon OB, B Pollack J, Sagan C. Physical properties of the particles composing the Martian dust storm of 1971-1972. Icarus 1977;30(4):663–96. doi:10.1016/0019-1035(77)90088-4.
[847] Khare B, Sagan C, Arakawa E, Suits F, Callcott T, Williams M. Optical constants of organic tholins produced in a simulated Titanian atmosphere: from soft x-ray to microwave frequencies. Icarus 1984;60(1):127–37. doi:10.1016/0019-1035(84)90142-8.
[848] Ramirez S, Coll I, da Silva A, Navarro-Gonzalez R, Lafait J, Raulin F. Complex refractive index of Titan's aerosol analogues in the 200-900 nm domain. Icarus 2002;156(2):515–29. doi:10.1006/icar.2001.6783.
[849] Imanaka H, Cruikshank DP, Khare BN, McKay CP. Optical constants of Titan tholins at mid-infrared wavelengths (2.5–25 μm) and the possible chemical nature of Titan's haze particles. Icarus 2012;218(1):247–61. doi:10.1016/j.icarus.2011.11.018.
[850] Henning T, Mutschke H. Low-temperature infrared properties of cosmic dust analogues. Astron Astrophys 1997;327:743–54.
[851] Zeidler S, Posch T, Mutschke H. Optical constants of refractory oxides at high temperatures. Astron Astrophys 2013;553:A81. doi:10.1051/0004-6361/201220459.
[852] Begemann B, Dorschner J, Henning T, Mutschke H, Gurtler J, Kompe C, et al. Aluminum oxide and the opacity of oxygen-rich circumstellar dust in the 12–17 micron range. Astrophys J 1997;476(1):199–208. doi:10.1086/303597.
[853] Henning T, Begemann B, Mutschke H, Dorschner J. Optical properties of oxide dust grains. Astron Astrophys Suppl Ser 1995;112:143–9. http://adsabs.harvard.edu/abs/1995A&AS..112..143H
[854] Posch T, Kerschbaum F, Fabian D, Mutschke H, Dorschner J, Tamanai A, et al. Infrared properties of solid titanium oxides: exploring potential primary dust condensates. Astrophys J Suppl Ser 2003;149(2):437–45. doi:10.1086/379167.
[855] Triaud A.. Database of optical constants for cosmic dust, unpublished data. 2012. http://www.astro.uni-jena.de/Laboratory/OCDB/mgfeoxides.htmlC.
[856] Fabian D.. Database of optical constants for cosmic dust, unpublished data. 2012. http://www.astro.uni-jena.de/Laboratory/OCDB/crsilicates.htmlC.
[857] Fabian D, Henning T, Jäger C, Mutschke H, Dorschner J, Wehrhan O. Steps toward interstellar silicate mineralogy. Astron Astrophys 2001;378(1):228–38. doi:10.1051/0004-6361:20011196.
[858] Fabian D, Posch T, Mutschke H, Kerschbaum F, Dorschner J. Infrared optical properties of spinels, a study of the carrier of the 13, 17 and 32 micron emission features observed in ISO-SWS spectra of oxygen-rich AGB stars. Astron Astrophys 2001;373(3):1125–38. doi:10.1051/0004-6361:20010657.
[859] Jäger C, Dorschner J, Mutschke H, Posch T, Henning T. Steps toward interstellar silicate mineralogy VII. Spectral properties and crystallization behaviour of magnesium silicates produced by the sol-gel method. Astron Astrophys 2003;408(1):193–204. doi:10.1051/0004-6361:20030916.
[860] Zeidler S, Posch T, Mutschke H, Richter H, Wehrhan O. Near-infrared absorption properties of oxygen-rich stardust analogs: the influence of coloring metal ions. Astron Astrophys 2011;526:A68. doi:10.1051/0004-6361/201015219.
[861] Posch T, Kerschbaum F, Mutschke H, Fabian D, Clément D, Dorschner J. Features of oxide dust particles in circumstellar shells of AGB stars. In: Proceedings of the exploiting the ISO data archive, infrared astronomy in the internet age; 2002. p. 14. Siguenza, Spain, June 24-27 http://adsabs.harvard.edu/abs/2003ESASP.511..141P
[862] Kou L, Labrie D, Chylek P. Refractive indices of water and ice in the 0.65- to 2.5-μm spectral range. Appl Opt 1993;32(19):3531. doi:10.1364/AO.32.003531.
[863] Sinyuk A, Torres O, Dubovik O. Combined use of satellite and surface observations to infer the imaginary part of refractive index of Saharan dust. Geophys Res Lett 2003;30(2). doi:10.1029/2002GL016189.
[864] Dingle JH, Zimmerman S, Frie AL, Min J, Jung H, Bahreini R. Complex refractive index, single scattering albedo, and mass absorption coefficient of secondary organic aerosols generated from oxidation of biogenic and anthropogenic precursors. Aerosol Sci Technol 2019;53(4):449–63. doi:10.1080/02786826.2019.1571680.
[865] Zarzana KJ, De Haan DO, Freedman MA, Hasenkopf CA, Tolbert MA. Optical properties of the products of α-dicarbonyl and amine reactions in simulated cloud droplets. Environ Sci Technol 2012;46(9):4845–51. doi:10.1021/es2040152.
[866] Niedziela RF, Norman ML, DeForest CL, Miller RE, Worsnop DR. A temperature- and composition-dependent study of H_2SO_4 aerosol optical constants using fourier transform and tunable diode laser infrared spectroscopy. J Phys Chem A 1999;103(40):8030–40. doi:10.1021/jp991323o.
[867] Biermann UM, Luo BP, Peter T. Absorption spectra and optical constants of binary and ternary solutions of H_2SO_4, HNO_3, and H_2O in the mid infrared at atmospheric temperatures. J Phys Chem A 2000;104(4):783–93. doi:10.1021/jp992349i.
[868] Palmer KF, Williams D. Optical constants of sulfuric acid; Application to the clouds of Venus? Appl Opt 1975;14(1):208. doi:10.1364/AO.14.000208.
[869] Norman ML, Qian J, Miller RE, Worsnop DR. Infrared complex refractive indices of supercooled liquid HNO_3/H_2O aerosols. J Geophys Res Atmos 1999;104(D23):30571–84. doi:10.1029/1999JD900902.
[870] Querry MR, Tyler IL. Reflectance and complex refractive indices in the infrared for aqueous solutions of nitric acid. J Chem Phys 1980;72(4):2495–9. doi:10.1063/1.439445.
[871] Remsberg EE, Lavery D, Crawford B. Optical constants for sulfuric and nitric acids. J Chem Eng Data 1974;19(3):263–5. doi:10.1021/je60062a003.
[872] Hasenkopf CA, Beaver MR, Trainer MG, Langley Dewitt H, Freedman MA, Toon OB, et al. Optical properties of Titan and early earth haze laboratory analogs in the mid-visible. Icarus 2010;207(2):903–13. doi:10.1016/j.icarus.2009.12.015.
[873] Bohren C, Huffman D. Absorption and scattering of light by small particles. New York: John Wiley and Sons; 1983. ISBN 9783527618156. doi:101002/9783527618156.
[874] Wakeford HR, Sing DK. Transmission spectral properties of clouds for hot Jupiter exoplanets. Astron Astrophys 2015;573:A122. doi:10.1051/0004-6361/201424207.
[875] Massie S, Hervig M. HITRAN 2012 refractive indices. J Quant Spectrosc Radiat Transf 2013;130:373–80. doi:10.1016/j.jqsrt.2013.06.022.
[876] Skinner FM, Gordon IE, Hill C, Hargreaves RJ, Lockhart KE, Rothman LS. Referencing sources of molecular spectroscopic data in the era of data science: application to the HITRAN and AMBDAS databases. Atoms 2020;8(2):16. doi:10.3390/atoms8020016.
[877] Harris CR, Millman KJ, van der Walt SJ, Gommers R, Virtanen P, Cournapeau D, et al. Array programming with NumPy. Nature 2020;585(7825):357–62. doi:10.1038/s41586-020-2649-2.
[878] Tran H, Ngo NH, Hartmann JM. Efficient computation of some speed-dependent isolated line profiles. J Quant Spectrosc Radiat Transf 2013;129:199–203. doi:10.1016/j.jqsrt.2013.06.015.
[879] Tran H, Ngo NH, Hartmann JM. Erratum to “Efficient computation of some speed-dependent isolated line profiles” [Journal of Quantitative Spectroscopy and Radiative Transfer 129 (2013) 199-203]. J Quant Spectrosc Radiat Transf 2014;134:104. doi:10.1016/j.jqsrt.2013.10.015.
[880] Clough SA, Iacono MJ, Moncet J-L. Line-by-line calculations of atmospheric fluxes and cooling rates: application to water vapor. J Geophys Res Atmos 1992;97(D14):15761–85. doi:10.1029/92JD01419.
[881] Mlawer EJ, Payne VH, Moncet JL, Delamere JS, Alvarado MJ, Tobin DC. Development and recent evaluation of the MT_CKD model of continuum absorption. Philos Trans R Soc Lond Ser A 2012;370(1968):2520–56. doi:10.1098/rsta.2011.0295.
[882] Paynter D, Ramaswamy V. Investigating the impact of the shortwave water vapor continuum upon climate simulations using GFDL global models. J Geophys Res Atmos 2014;119(18):10720–37. doi:10.1002/2014JD021881.
[883] Serov EA, Odintsova TA, Tretyakov MY, Semenov VE. On the origin of the water vapor continuum absorption within rotational and fundamental vibrational bands. J Quant Spectrosc Radiat Transf 2017;193:1–12. doi:10.1016/j.jqsrt.2017.02.011.
[884] Vigasin AA. Water vapor continuum: Whether collision-induced absorption is involved? J Quant Spectrosc Radiat Transf 2014;148:58–64. doi:10.1016/j.jqsrt.2014.06.019.
[885] Clough SA, Kneizys FX, Davies RW. Line shape and the water vapor continuum. Atmos Res 1989;23(3):229–41. doi:10.1016/0169-8095(89)90020-3.
[886] Baranov Y, Lafferty W. The water-vapor continuum and selective absorption in the 3–5 μm spectral region at temperatures from 311 to 363K. J Quant Spectrosc Radiat Transf 2011;112(8):1304–13. doi:10.1016/j.jqsrt.2011.01.024.
[887] Ptashnik IV, McPheat RA, Shine KP, Smith KM, Williams RG. Water vapor self-continuum absorption in near-infrared windows derived from laboratory measurements. J Geophys Res 2011;116(D16):D16305. doi:10.1029/2011JD015603.
[888] Baranov YI. The continuum absorption in H_2O+N_2 mixtures in the 2000–3250 cm^{-1} spectral region at temperatures from 326 to 363 K. J Quant Spectrosc Radiat Transf 2011;112(14):2281–6. doi:10.1016/j.jqsrt.2011.06.005.
[889] Baranov YI, Lafferty WJ. The water vapour self-and water-nitrogen continuum absorption in the 1000 and 2500 cm^{-1} atmospheric windows. Philos Trans R Soc A Math Phys Eng Sci 2012;370(1968):2578–89. doi:10.1098/rsta.2011.0234.
[890] Ptashnik IV, McPheat RA, Shine KP, Smith KM, Gary Williams R. Water vapour foreign-continuum absorption in near-infrared windows from

laboratory measurements. Philos Trans R Soc A Math Phys Eng Sci 2012;370(1968):2557–77. doi:10.1098/rsta.2011.0218.
[891] Ptashnik IV, Klimeshina TE, Solodov AA, Vigasin AA. Spectral composition of the water vapour self-continuum absorption within 2.7 and 6.25 μm bands. J Quant Spectrosc Radiat Transf 2019;228:97–105. doi:10.1016/J.JQSRT.2019.02.024.
[892] Birk M, Wagner G, Loos J, Shine KP. 3 μm Water vapor self- and foreign-continuum: new method for determination and new insights into the self-continuum. J Quant Spectrosc Radiat Transf 2020;253:107134. doi:10.1016/j.jqsrt.2020.107134.
[893] Campargue A, Kassi S, Mondelain D, Vasilchenko S, Romanini D. Accurate laboratory determination of the near-infrared water vapor self-continuum: as test of the MT_CKD model. J Geophys Res Atmos 2016;121(21):13180–203. doi:10.1002/2016JD025531.
[894] Lechevallier L, Vasilchenko S, Grilli R, Mondelain D, Romanini D, Campargue A. The water vapour self-continuum absorption in the infrared atmospheric windows: new laser measurements near 3.3 and 2.0 µm. Atmos Meas Tech 2018;11(4):2159–71. doi:10.5194/amt-11-2159-2018.
[895] Mondelain D, Aradj A, Kassi S, Campargue A. The water vapour self-continuum by CRDS at room temperature in the 1.6 µm transparency window. J Quant Spectrosc Radiat Transf 2013;130:381–91. doi:10.1016/j.jqsrt.2013.07.006.
[896] Mondelain D, Manigand S, Kassi S, Campargue A. Temperature dependence of the water vapor self-continuum by cavity ring-down spectroscopy in the 1.6 µm transparency window. J Geophys Res Atmos 2014;119(9):5625–39. doi:10.1002/2013JD021319.
[897] Mondelain D, Vasilchenko S, Čermák P, Kassi S, Campargue A. The self- and foreign-absorption continua of water vapor by cavity ring-down spectroscopy near 2.35 µm. Phys Chem Chem Phys (Inc Faraday Trans) 2015;17(27):17762–70. doi:10.1039/C5CP01238D.
[898] Odintsova TA, Tretyakov MY, Pirali O, Roy P. Water vapor continuum in the range of rotational spectrum of H_2O molecule: new experimental data and their comparative analysis. J Quant Spectrosc Radiat Transf 2017;187:116–23. doi:10.1016/j.jqsrt.2016.09.009.
[899] Odintsova TA, Tretyakov MY, Zibarova AO, Pirali O, Roy P, Campargue A. Far-infrared self-continuum absorption of $H_2{}^{16}O$ and $H_2{}^{18}O$ (15–500 cm^{-1}). J Quant Spectrosc Radiat Transf 2019;227:190–200. doi:10.1016/j.jqsrt.2019.02.012.
[900] Vasilchenko S, Campargue A, Kassi S, Mondelain D. The water vapour self- and foreign-continua in the 1.6 µm and 2.3 µm windows by CRDS at room temperature. J Quant Spectrosc Radiat Transf 2019;227:230–8. doi:10.1016/j.jqsrt.2019.02.016.
[901] Shine KP, Campargue A, Mondelain D, McPheat RA, Ptashnik IV, Weidmann D. The water vapour continuum in near-infrared windows - current understanding and prospects for its inclusion in spectroscopic databases. J Mol Spectrosc 2016;327:193–208. doi:10.1016/j.jms.2016.04.011.
[902] Paynter DJ, Ramaswamy V. An assessment of recent water vapor continuum measurements upon longwave and shortwave radiative transfer. J Geophys Res Atmos 2011;116(D20). doi:10.1029/2010JD015505.
[903] Baranov YI, Lafferty WJ, Ma Q, Tipping RH. Water-vapor continuum absorption in the 800- 1250 cm^{-1} spectral region at temperatures from 311 to 363 K. J Quant Spectrosc Radiat 2008;109:2291–302. doi:10.1016/j.jqsrt.2008.03.004.
[904] Paynter DJ, Ptashnik IV, Shine KP, Smith KM, McPheat R, Williams RG. Laboratory measurements of the water vapor continuum in the 1200-8000 cm^{-1} region between 293 K and 351 K. J Geophys Res (Atmos) 2009;114(D21). doi:10.1029/2008JD011355.
[905] Serio C, Masiello G, Esposito F, di Girolamo P, di Iorio T, Palchetti L, et al. Retrieval of foreign-broadened water vapor continuum coefficients from emitted spectral radiance in the H_2O rotational band from 240 to 590 cm^{-1}. Opt Express 2008;16(20):15816. doi:10.1364/OE.16.015816.
[906] Mast JC, Mlynczak MG, Cageao RP, Kratz DP, Latvakoski H, Johnson DG, et al. Measurements of downwelling far-infrared radiance during the RHUBC-II campaign at Cerro Toco, Chile and comparisons with line-by-line radiative transfer calculations. J Quant Spectrosc Radiat Transf 2017;198:25–39. doi:10.1016/j.jqsrt.2017.04.028.
[907] Rizzi R, Maestri T, Arosio C. Estimate of radiosonde dry bias from far-infrared measurements on the antarctic plateau. J Geophys Res Atmos 2018;123(6):3205–11. doi:10.1002/2017JD027874.
[908] Odintsova TA, Tretyakov MY, Simonova AA, Ptashnik IV, Pirali O, Campargue A. Measurement and temperature dependence of the water vapor self-continuum between 70 and 700 cm^{-1}. J Mol Struct 2020;1210. doi:10.1016/j.molstruc.2020.128046.
[909] Dekker H, D'Odorico S, Kaufer A, Delabre B, Kotzlowski H. Design, construction, and performance of UVES, the echelle spectrograph for the UT2 Kueyen telescope at the ESO paranal observatory. In: Iye M, Moorwood AF, editors. Optical and IR Telescope Instrumentation and Detectors. Society of Photo-Optical Instrumentation Engineers (SPIE) Conference Series, 4008; 2000. p. 534–45. doi:10.1117/12.395512.